HIGH ENERGY SPARK IGNITION IN NON-PREMIXED FLOWING COMBUSTORS

A Dissertation
Presented to
The Academic Faculty

by

Brandon A. Sforzo

In Partial Fulfillment
of the Requirements for the Degree
Doctor of Philosophy in the
School of Aerospace Engineering

Georgia Institute of Technology
December 2014

High Energy Spark Ignition in Non-Premixed Flowing Combustors

Approved by:

Dr. Jerry Seitzman, Advisor
School of Aerospace Engineering
Georgia Institute of Technology

Dr. Jeff Jagoda
School of Aerospace Engineering
Georgia Institute of Technology

Dr. Wenting Sun
School of Aerospace Engineering
Georgia Institute of Technology

Dr. Suresh Menon
School of Aerospace Engineering
Georgia Institute of Technology

Mr. Randal McKinney
Combustion Systems Aero.
Pratt & Whitney

Date Approved: August 21, 2014

To Gina

ACKNOWLEDGMENTS

I have faced very few challenges in life where I felt alone. Overcoming these obstacles is indeed gratifying, but the tasks in which others have pushed, or pulled me through hardships provide not only a sense of accomplishment but also one of humility. The foremost recognition goes to my parents, Gary and Colleen, for whom I am eternally grateful. Their acts of love and sacrifice have allowed me to be where I am today, and they have instilled the virtues that made me *who* I am today. Thank you, Mom and Dad.

This thesis, my years of research, and my overall experience of graduate school at Georgia Tech would not have been as enriching or even possible without the presence of many people.

Firstly, I would like to acknowledge the help and guidance from my advisor, Dr. Jerry Seitzman. As a teaching assistant I knew I wanted to work with Dr. Seitzman because his care for and dedication to the students was evident. I am grateful for the trust he has placed with me, the wisdom he shares, and the example he sets for all his students as an admirable teacher and mentor. I am especially thankful that he pushed me to work hard, and was beside me during the stressful times (like this thesis).

I would like to thank Dr. Jeff Jagoda for being part of my research experience as a co-advisor in the spark ignition project. His attention to detail kept me focused and his delightful sense of humor kept meetings lively.

I am particularly thankful for the support of Randy McKinney and his colleagues at Pratt & Whitney. Randy has guided us through the ignition project and has continued his dedication by being part of my thesis committee.

I also acknowledge the support I received from other members of the faculty,

iv

particularly Dr. Suresh Menon and Dr. Wenting Sun for being engaged in my thesis work and providing critical feedback. I am grateful for their commitment in being part of my committee.

Key help from individuals has also made my work much easier, if not, possible. Gratitude to the AE machine shop guys, Scott Eliot, Scott Mosley, and Red, for helping me fabricate my experimental facility. I would like to thank Shane Getchell and Bobby Noble for helping me build my facility. Sasha Bibik and Ianko, thanks for getting me through some difficult technical pinches. Additionally, thank you to Metin Ozcan for contributing to the surrogate modeling portions of my work.

This research experience was strengthened by fellow spark ignition investigators with whom I could commiserate, Jae Kim and Alex Lambert; thank you for your contributions and support with this work.

My career in the combustion lab would not have been the same without the family-like camaraderie from fellow graduate students, especially senior students for their support and brutality during quals preparation, (in no particular order), Jackie, Prabs, Andrew Marshall, Matt Quinlan, Karthik, Yash, Jack Crawford, Chris Foley, Ben Wilde, Jim Cornacchio, John Bennewitz, Danny Bloomer, Aimee, Ben Emmerson, Mike Malanowski, Mike Aguilar, Travis, Nishant, and Sampath.

I owe a very special debt of gratitude to my lifelong friend, Dr. Thomas Ober. Tom and I have encouraged and challenged each other in our professional and personal endeavors for many years, and without his scholarly example I doubt I would have pursued a doctorate at all. I sincerely hope that we will continue our friendship and support for many years to come.

Above all, I owe everything to God. I have found His support through my loved ones, the community around me, my coworkers and in the work I do. During this research I have obtained, with His support to persevere, a better understanding of the intricacies of the natural world.

TABLE OF CONTENTS

vii

viii

LIST OF TABLES

LIST OF FIGURES

xiii

LIST OF SYMBOLS

Abbreviations

LHC Latin hypercube experimental design

P-JICF Pulsed Jet in Crossflow

PSR   Perfectly stirred reactor

SVM   Support vector machine

Greek Symbols

α Significance level for t-statistic

α_j Jet duty cycle

Γ Vortex circulation

ν Kinematic viscosity

ϕ Global equivalence ratio

$\phi(x)$ SVM transform function

ϕ_{bottom} Equivalence ratio in the kernel flow

ϕ_{top} Equivalence ratio in the main flow

ρ Density

ρ_j Jet fluid density

ρ_{cf} Crossflow fluid density

τ_{mid} Delay for middle of kernel to cross h_s

τ_{thru} Delay for convecting portion of kernel to completely cross h_s

τ_{top} Delay for top edge of kernel to cross h_s

$\tau_{transit}$ Nominal time between discharge and kernel reaching h_s; time input for modeling

ε Error term in regression model

ξ SVM slack variable

Roman Symbols

$\bar{v}$ Mass averaged mean velocity in the test section

$\dot{m}_{entrain}$ Mass entrainment rate in numerical simulation

$\hat{P}(ign)$ Predicted probability of ignition

$\hat{Y}$ Predicted logical outcome from pattern classifier

$\mathbf{w}$ SVM hyperplane normal vector

$\mathbf{x}_i$ Single SVM training datum

$\mathcal{T}$ SVM training set

A Jet trajectory scaling coefficient

a_i Probability of ignition regression model coefficients

C SVM penalty parameter

D Mass diffusion coefficient

d Nozzle exit diameter

xvi

dt Time interval for saving properties in cantera

$E_{supplied}$ Accumulated supplied energy to the igniter

F Flammability factor

f Jet pulsing frequency

f_{lean} Lean flammability limit

f_{rich} Rich flammability limit

h_s Splitter plate height

I Current flow through igniter

J P-JICF momentum ratio

$K(x, y)$ SVM kernel function

m Jet trajectory exponential scaling coefficient

m_i Initial kernel mass

N_{succ} Number of successful ignition events

N_{total} Total number of ignition attempts

$P(\eta)$ Probability density function (PDF) of the mixture fraction

$P(ign)$ Probability of ignition

q_{loss} Volumetric heat loss

q_{sp} Supplied spark energy

r Ratio of jet and crossflow velocities, $U_j/\bar{v}$

t^* Normalized pulse time

T_i Inflow temperature

t_p Pulse time duration

U_j Jet velocity

U_{cf} Crossflow velocity

V Voltage across igniter leads

Y Logical outcome from reduced order model

y_i SVM training categorical value

Y_{alpha} Mass fraction for species α

endt   Final evaluation time in cantera

mentrain Mass entrainment rate from environment to the reactor in cantera

pin   Input pressure in cantera

Tin   Input temperature in cantera

Xin   Initial kernel composition in cantera

SUMMARY

In many practical combustion devices, including those used in gas turbine engines for aircraft and power generation, a high energy spark kernel is necessary to reliably ignite the turbulently flowing flammable gases. Complicating matters, the spark kernel is sometimes generated in a region where a non-flammable mixture is present, or where there is no fuel at all. This requires the spark kernel to travel to a flammable region before rapid combustion can begin in non-premixed or stratified flows. This transit time allows for chemical reactions to take place within the kernel as well as mixing with surrounding gases. Despite these demanding conditions, the majority of research in ignition has been for low energy sparks and premixed conditions, not resembling those found in many combustion devices. Similarly, there is little work addressing this issue of spark kernel evolution in the non-premixed flowing environment, and none available that control the time allowed for transit.

The goal of this thesis is to understand the development of a spark kernel issued into a non-premixed flow and the sensitivities of the ignition process. To this effect, a stratified flow facility for ignition experiments has been fabricated utilizing a high speed schlieren and emission imaging system for visualizing the kernel motion and ignition success. Additionally, OH chemiluminescence and CH PLIF were used to track chemical species during the ignition process. This facility is also used to control the important variables regarding the flow and spark kernel interaction to quantify the influence on ignition probability.

A reduced order model employing a perfectly stirred reactor (PSR) has also been developed based on experimental observations of the entrainment of fluid into the evolving kernel. The simulations provide additional insight to the chemical development in the kernel under different input conditions. This model was enhanced

by introducing random perturbations to the input variables, mimicking a practical situation. A computationally efficient support vector machine was trained to replicate the numerical model outputs and predict ignition probabilities for nominal input conditions, providing comparison to experimental results.

Experimental and numerical results show that initial mixing with non-flammable fluid quickly reduces the ability for the kernel to ignite the flammable flow, resulting in a strong influence of the inlet temperature and the kernel transit time on the probability of ignition. Once the kernel reaches the flammable mixture, entrainment of this flow occurs, which requires on the order of a vortex turn-over time before chemistry can begin. Initial chemical reactions include endothermic fuel decomposition, further reducing the kernel temperature prior to heat release, creating a competition between the cooling effect of additional mass entrainment and the delayed heat release reactions. CH PLIF results show that flame chemistry is initially confined to a thin region that corresponds to the interface layer where the flammable gases mix with the hot kernel fluid from the vortex entrainment of ambient gas.

The dependence of the ignition probability to variations in flow conditions is captured reasonably well by the reduced order model, validating the PSR approach and the probability prediction tool. The development of this reduced order model is a major contribution of this work with the ability to predict the effects of the important physical ignition processes, which can be used when considering an ignition system's feasibility. This work will provide knowledge to guide the use and design practices in industry, as well as a simple model to test ignition feasibility based on mixing, entrainment, and chemical reactions.

Furthermore, the flow facility is well characterized, and a database has been developed that can provide validation points for future computational simulations. Future modeling will be important to further understand fluid dynamic effects that are difficult to measure experimentally, and study a broader range of conditions.

CHAPTER 1

INTRODUCTION

Combustion is a self sustaining chemical process that releases thermal energy, some of which is used to overcome the activation energy required to begin subsequent reactions [1]. Prior to a stabilized flame, an initial energy input is required to begin the reaction cascade. By far, the most common approach to this obstacle is some kind of spark ignition, a form of forced ignition. Forced ignition is the process where an external source of thermal energy or radical species is introduced to cause the initiation of a burning state. Conversely, autoignition (or spontaneous ignition) requires no external source of energy, but is defined by a gradual rise in reactivity until a critical state is reached when rapid burning begins [2]. Both types of ignition have been studied extensively, but the focus of this work is on forced ignition.

1.1 Motivation

Forced ignition is used in most practical combustion devices such as industrial boilers, internal combustion (IC) engines, gas turbine engines, and even gas barbeque grills. Under ideal conditions, combustors can be ignited quite easily using the spark ignition system. However, regulations limiting emissions and industrial standards requiring high efficiencies have necessitated alternative combustion strategies, lean combustion being the most prominent. These lean mixtures are less reactive and therefore more difficult to ignite [3, 4]. Gas turbine, lean-premix-prevaporized (LPP) engines rely on lean overall equivalence ratios to reduce the emission signature, yet look to avoid autoignition [5]. Advances in forced ignition knowledge can therefore lead to improved devices and operations. Likewise, undesirable instances of forced ignition can occur

1
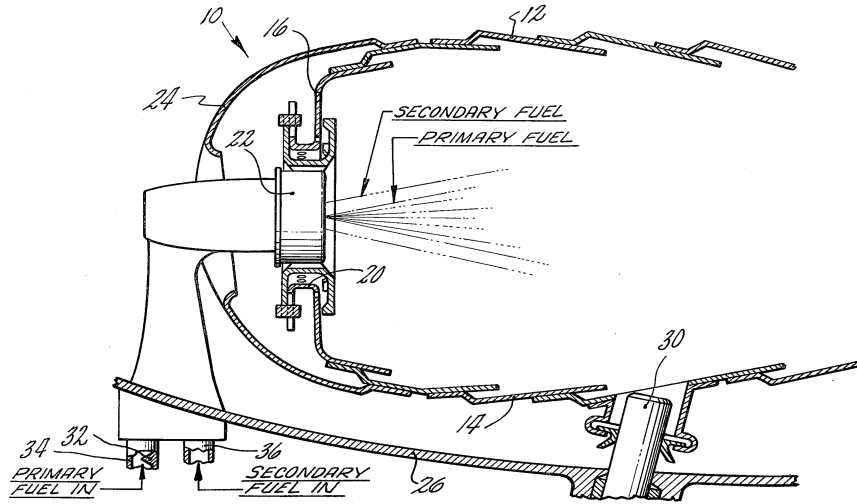
Figure 1.1: *Annular combustor with (30) igniter mounted through the (26) outer casing and (14) outer liner. [9].*

in some situations, like in the handling of hydrogen storage [6] which is of growing concern due to increased focus on alternate energy sources. Therefore, advances in the fundamental understanding of forced ignition can improve safety [5, 7].

One of the basic requirements of an aircraft gas turbine engine is for reliable and smooth ignition on initial startup [8]. In such an engine, fuel is introduced at the injector before mixing with air and flowing into the primary zone of the combustor. This results in a non-homogeneous mixture of liquid and gaseous fuel with air, turbulently flowing through the combustor toward the outlet. The typical configuration of a combustor can be seen in Fig. 1.1, where flow convects from left to right.

Experiments have been performed on some realistic combustor configurations to determine the most successful location for the igniter. The results suggested that a location near the centerline, close to the nozzle is preferred for ignition [10]. This location is not practical due to poor access for maintenance, aerodynamic disruption, and the stabilized flame during operation severely reduces the longevity of the igniter. A consequence of traditional igniter plug placement is that fuel may not continuously circulate to the spark location and the igniter location may experience temporal

fluctuations in flammability [11]. As a result, an ignition kernel must convect from the igniter plug to a region where combustion reactions are possible.

Additionally, in aircraft engines operating in potentially unstable flight conditions where flameout is possible, like in icing, turbulent air, takeoffs or landings, an operational ignition system should quickly relight the engine with no thrust interruption, this is called ignition stand-by protection [12]. At high altitudes, relight is challenged by the low ambient temperature, affecting fuel volatility [12], and low atmospheric pressure causing a change in the reactivity and heat losses from the ignition kernel [13], further challenging the reliability of ignition. High performance (military) aero-engines can also include an afterburner/augmentor. Changes to augmentor designs, including higher operating temperatures and heightened survivability requirements have also increased the importance of having a reliable ignition system [14]. The high temperature and high velocity conditions in the augmentor environment are not ideal for convenient placement of these systems, and relying on autoignition is not a currently employed strategy due to large operational envelopes and reliability concerns.

1.2 Literature Review

1.2.1 Premixed Ignition

Forced ignition has been studied primarily in premixed fuel-air scenarios due to their simplicity, usually in a quiescent combustion chamber, which is representative of an (IC) engine [3, 15, 16], and to a lesser extent in flowing test sections [11, 17–19], analogous to the situation in a gas turbine combustor.

(a) *Fuel jet in air coflow*

(b) *Stratified flow*

(c) *Opposed-jet counterflow*

(d) *Internal combustion with fluctuations (species and/or temperature)*
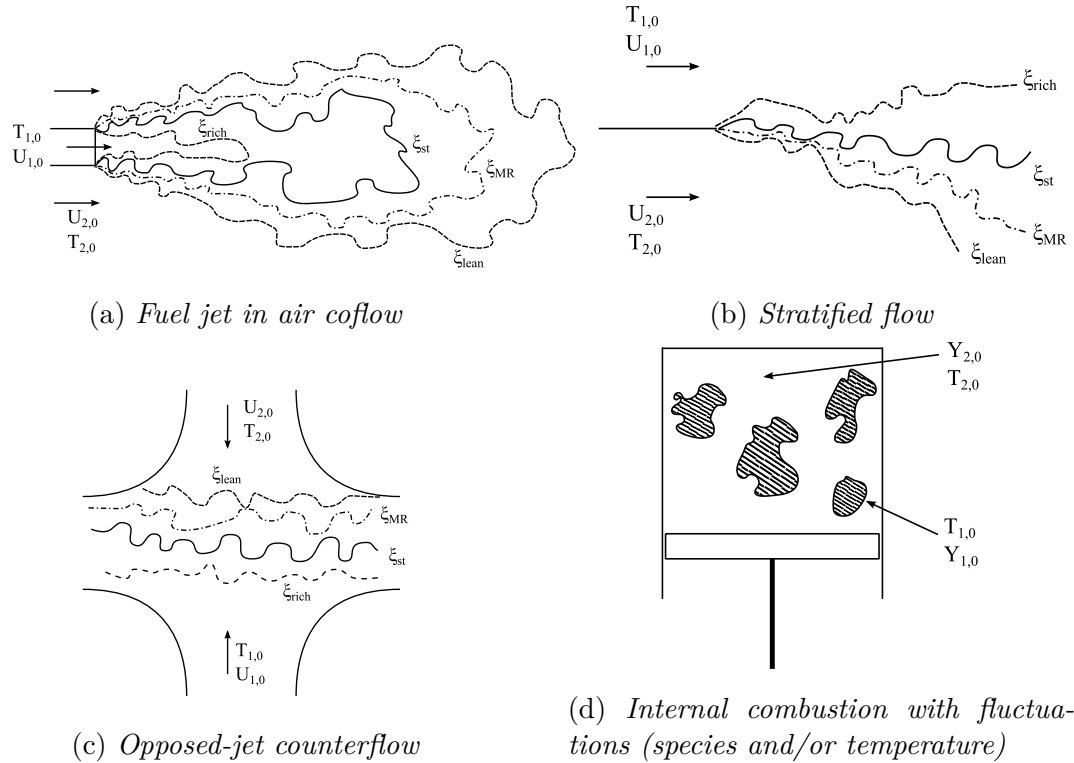
Figure 1.2: *Types of turbulent ignition configurations. 1: fuel; 2: oxidizer. (Adapted from [5])*

1.2.2 Non-Premixed Ignition

Little systematic work has been performed in the realm of turbulent non-premixed ignition. Mastorakos [5] highlights the varieties of non-premixed configurations that have been investigated, as seen in Fig. 1.2, and indicates the extent of the research performed on forced ignition of non-premixed flames is much less than the efforts that have examined autoignition in these types of scenarios.

The opposed flow scenario depicted in Fig. 1.2c has been the focus of the turbulent non-premixed work of Ahmed [7]. The results indicated in Fig. 1.3 illustrate the difficulties of igniting high strain/turbulent flames, even when using a high energy igniter (up to $300mJ$). Although the flow properties were measured to correlate the results, the spark characteristics were the main variables that could be adjusted. It is important to note that the mixture fraction and strain rate were not controlled but

4
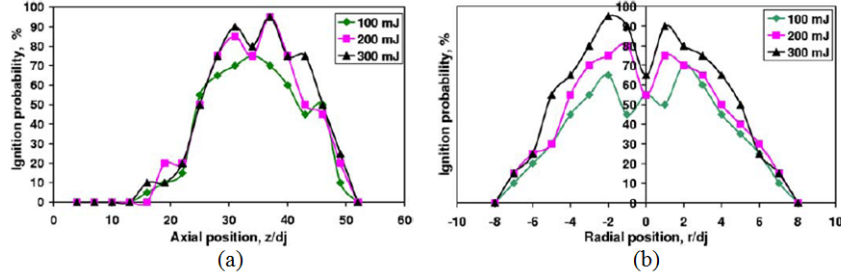
Figure 1.3: *Effect of spark energy on ignition probability. (a) Along the jet centerline; (b) radially. Spark: $500\mu s$, $1\,mm$ gap. [7]*

only measured at the time of ignition. This work, though addressing non-premixed flow, does not provide control over the mixture fraction or the duration between spark kernel creation and the interaction of the spark kernel with a flammable mixture. Having control over these variables is the focus of the proposed effort.

1.2.2.1 Ignition Definition

Theoretical work to understand the fundamental processes of spark ignition was carried out by Lewis et al. [15] for quiescent gas mixtures, under the assumption that ignition is successful if enough energy is supplied to overcome losses and allow for growing heat release.

Ignition in flowing systems was pioneered by Swett [20] where various effects of environmental and spark related parameters were studied. To analyze the spark ignition process, a simplified energy equation (Eq.1.1) that is one dimensional and includes unsteady, diffusion, and chemical source terms can be used[21].

$$c_{p,m}\frac{\partial\left(\rho T\right)}{\partial t} + c_{p,m}\frac{\partial\left(\rho uT\right)}{\partial x} = -\sum_{\alpha=1}^{N} h_\alpha w_\alpha + \rho D\frac{\partial T}{\partial x}\sum_{\alpha=1}^{N} c_{p,\alpha}\frac{\partial Y_\alpha}{\partial x} + q_{sp} - q_{loss} \qquad (1.1)$$

In this equation, u is the velocity of the mixture with density ρ, pressure p, and mass fraction Y_α for species α with a mass diffusion coefficient D. The spark energy supplied is represented by q_{sp}, and q_{loss} is the volumetric heat or equivalent heat due

5

to species lost, such as in wall interaction. Many sources use a minimum ignition energy (MIE) type analysis to determine the energy needed to overcome the loss terms and raise the kernel volume temperature to the flame temperature, allowing successful ignition [15, 17–19]. Typically, successful ignition is defined by light-back, where a spark kernel followed by flame propagation downstream leads to blow off, or in the case of upstream propagation, ignition leads to a stable flame [11].

1.2.3 Ignition Probability

Recent work has emphasized the probabilistic nature of successful initiation of a self-sustaining flame [22]. Therefore the MIE type of threshold is not a discrete change due to a change in a single variable [6]. It is necessary to report a probability at a given condition by gathering the results of many ignition attempts. This stochastic property of ignition may be due to high sensitivity to an unsteady flow variable, or a variation in the spark breakdown process. One approach to characterizing the varying ignition probability uses a flammability factor, F, defined in Eq. 1.2, as the area beneath the probability density function (PDF) of the fuel mass fraction between the static flammability limits [11]. This attempts to incorporate the mixture reactivity into the probability of ignition.

$$F = \int_{f_{lean}}^{f_{rich}} P\left(\eta\right) d\eta \tag{1.2}$$

where, f_{rich} and f_{lean} are the respective rich and lean static flammability limits, and $P(\eta)$ is the pdf of the mixture fraction.

1.2.4 Sunken Fire Igniter

Early qualitative empirical findings showed that the high energy plasma igniter could be a useful device for gas turbine combustors [3]. This may have led to the development of sunken fire ejection igniters, and a subsequent shift away from automotive

6
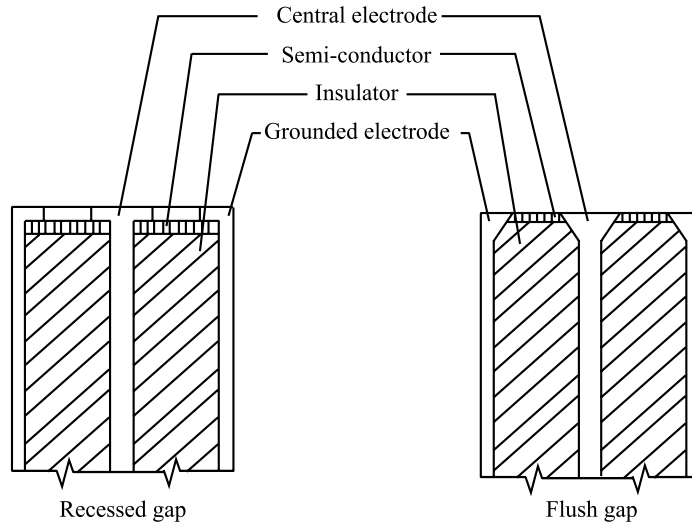
Figure 1.4: *Two types of surface discharge igniters.(Adapted from [8])*

derivative igniters for gas turbine [23]. Reactivity enhanced by ion and radical supply was later shown to reduce ignition delays from milliseconds to sub-microseconds [24]. Commercially available power supplies and igniters relying on forced ignition come in several varieties. These differ in the housing of the electrode gap where the spark kernel is generated as well as the discharge characteristics. The most common is a surface discharge igniter [12], which is characterized by a central conducting electrode separated from an outer casing which is grounded and serves as the second electrode. The two electrodes are separated by a ceramic insulator, coated with a semiconductor to facilitate breakdown [8]. Fig. 1.4 compares two types of surface discharge igniters: a recessed gap and a flush gap igniter. The subtle differences between the igniter designs influence the discharge and the subsequent kernel development, for example some designs result in a mere quarter of the supplied energy being deposited into the flow [25].

The sunken fire surface discharge igniter creates a high pressure region within the cavity that forces the spark kernel into the flow. This ejection can be represented by a pulsed jet in a crossflow, the mechanics of which have been computationally

7

simulated [26], which is discussed further in Chapter 2. The pulsed characteristic can cause enhanced mixing, as a function of the ejection velocity, and has been found to generate vortex rings that penetrate into the flow further than a steady jet [27]. Subtle changes in the pulsing frequency can affect the penetration and mixing characteristics. Pulsed jet in crossflow studies have also focused on adjusting pulsing variables to adjust the penetration distance and mixing to desired values [28]. This previous work highlights some of the important fluid dynamical effects of having an ejection of gas into a crossflow and how that changes mixing between the two gases.

Since a majority of the research performed in the area of forced ignition has been under premixed conditions, it fails to address the dynamics involved in the evolution of a spark kernel prior to its introduction to a flammable mixture. Additionally, the common use of high energy, short duration igniters, changes these dynamics, and defines the influential variables that allow for successful ignition. Therefore it is important to investigate the roles of the flow and spark variables in the evolution of the spark kernel and effect on the probability of ignition in a realistic configuration.

1.2.5 Ignition Modeling

Computational modeling of the ignition process can provide insight to the physical processes relating to successful and failed ignition attempts. This is especially useful if the model is validated against experimental observations. Models can also be used to look at compositional information that is difficult to measure experimentally. For example, during early times in a kernel's evolution when highly ionized species exist, simulations can capture the non-equilibrium composition, which can greatly influence the ignition process [29–33]. Specifically, radicals such as O and OH existing after the energy deposition can enhance chain reactions during ignition [34], and O,H, and N atoms have been shown to affect flame speeds, indicating an influence on reaction rates [35].

A number of efforts have focused on understanding the plasma physics associated with gas discharges [36]. For example, a number of premixed ignition studies exploring quiescent background conditions have employed numerical models where the deposited electrical energy was distributed within either a cylindrical or spherical volume in space [37–41], while the temporal energy deposition profile was specified or matched to experimental data. Simple initialization using only the deposited spark energy as an input, which has been shown to be influential to the development of the ignition kernel [42, 43] and the probability of ignition [7], has been shown to be sufficient in capturing the ignition kernel development [44]. Ignition simulations have mostly focused on premixed ignition in either quiescent [40, 45], or flowing conditions [44], but have yet to address non-premixed modeling including mixing with non-flammable flows.

1.3 Thesis Objectives and Organization

Given the lack of previous work in this area, the overall goal of the current work is to provide a better understanding of the flow parameters that control the probability of successful ignition in the non-premixed or partially premixed environment of a gas turbine engine combustor. Specifically, this thesis focuses on:

1. Identifying the most influential variables for forced ignition in a turbulent non-premixed flowing environment.

2. Providing a database of ignition results within the turbulent non-premixed flowing environment.

3. Developing and validating a reduced order model for ignition in a non-premixed, flowing environment.

Chapter 2 presents background and previous work that illuminates unique aspects of the thesis. The first section describes the current understanding of pulsed jets in

9

crossflow, a configuration that represents the flow field of a sunken fire igniter. The second section presents the theory behind support vector machines, as they are used in the reduced order modeling presented here. The design of the experimental facility and related diagnostic approaches used to study ignition kernel development and ignition probability are presented in Chapter 3. Similarly, the development and implementation of the reduced order model for simulating ignition is provided in Chapter 4. Results from experimental spark kernel development and ignition sensitivity studies are presented and discussed in Chapter 5. Simulation results of ignition kernels in stratified flows based on the reduced order model are found in the first half of Chapter 6, and simulated ignition probability results are discussed in the latter half. Finally, conclusions drawn from the discussions in Chapters 5–6 and suggestions for future work are presented in Chapter 7.

CHAPTER 2

BACKGROUND

Two major items are discussed in this chapter that will be helpful to the reader when considering the discussions to follow. Firstly, the fluid dynamics of a pulsed jet issuing into a crossflow are presented. The pulsed jet-in-crossflow has many parallels to the experimentally observed features of the spark kernel ejecting from the sunken fire igniter. Historical findings are presented which relate to the structural creation and evolution of a vortex ring, and the implications this has on the problem at hand. Additionally, the concept of support vector machines is reviewed as a method of classifying data into predicted categorical outcomes. The mathematical construct of these support vector machines is presented, supporting the application of this method to the prediction of ignition outcomes from reduced order simulations, which is used in Chapter 6.

2.1 Vortex Ring Dynamics

This section describes the characteristics of a vortex ring created by a pulsed jet in a crossflow (P-JICF), a physical representation of the ignition kernel issued from a sunken fire igniter. Understanding the P-JICF and the vortex ring characteristic of this flow will be important to the discussions and interpretations in this thesis. The fluid dynamics of the vortex ring results in important ignition controlling phenomena.

2.1.1 Formation

Early studies into pulsed jets aimed to investigate the mechanism by which the vortex rings were created. Originally called "puffs" [46], the vortices were identified as

11

(a)   (b)   (c)
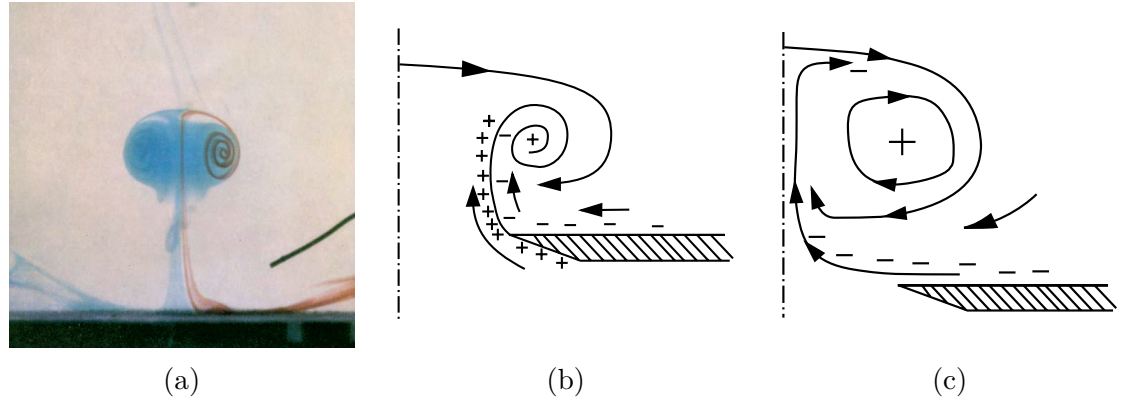
Figure 2.1: *Vortex ring formation at a sharp edged orifice. Image shows blue dye originating from within the cavity and red dye at the outside wall. Schematic shows the production and convection of opposite vorticity (-) to that of the main ring (+). (Adapted from [49])*

strongly turbulent fluid elements moving and mixing with their surroundings. These elements were found to enhance mixing between the jet fluid and the crossflow. The transition from the pulsed jet to a vortex ring was explained in detail by Didden [47], where water was used as the fluid. The high velocity gradient at the exit of the nozzle during the pulse generates circulation (Γ) which induces the vortex roll-up. The vortex sheet involutes and captures a substantial portion of the ambient fluid near the exit plane. This captured fluid remains in the vortex bubble indefinitely. [48] Furthermore, circulation of the opposite sign from the main vortex ring is also generated at the wall and causes mass to flow into the orifice. The circulation flows created are depicted in Fig. 2.1 (after [49]). This figure illustrates how the fluid very near the wall becomes wrapped in the vortex ring. This roll-up mechanism is important for understanding how the sunken fire ignitor's spark kernel forms and issues into the crossflow.

2.1.2 Entrainment

In the case of the spark kernel, entrainment of surrounding fluid is important to the ignition process. Little work has been done to develop a relation for the entrainment rate at these early times. Nevertheless, the amount of fluid entrainment

during this early time, also known as vortex ring formation, is caused by Biot-Savart induction [50].

Additionally, Olcay & Krueger [50] showed the entrainment that occurs is highly dependent on the time history profile of the mass ejection from the jet orifice. Their experiments compared vortex rings created using different pulse velocity profiles, where the medium was water with no crossflow. Planar fluorescence images were obtained, with fluorescent dye added to the jet mass to show the boundary between fluid originating from the jet and fluid entrained from the surroundings. Those results are shown in Fig. 2.2 for two triangular velocity histories. The images are sequenced in time, where $t^* = t/t_p$ and t_p is the pulse length of the mass ejection. The top images show the progress of a vortex ring where the input velocity pulse began with a sharp rise $(0 < t^* < 0.1)$, which was then followed by a gradual, negatively sloped (NS) decay until $t^* = 1$. The bottom row is the mirror of that profile, i.e., a gradual, positively sloped increase in velocity until $t^* = 0.9$, and then a sharp end to the pulse. The increased amount of darker regions within the vortex roll-up region for the high jet acceleration case indicates an increase in early mass entrainment, caused by the high velocity gradients in the inner nozzle leading to stronger vorticity [50]. This work illustrates the large entrainment effect caused by subtle discharge changes.

Early entrainment rates change significantly by later times when the kernel has moved several diameters away from the source [48]. The mechanism by which fluid is entrained at these later times is no longer due to roll-up but is described in part by the spatial distribution of vorticity relative to the translating vortex bubble [49]. The entrainment rate slows as near-wall effects cease, resulting in non-constant mass growth when considering the pulse moving into the far-field. Several models exist to explain the mass convection, including a concept where the kernel is comprised of fluid originating from the jet, entrained mass wrapped around the vortex core, and added mass that exists in front of the vortex ring due to continuity, as well as fluid

13

(a) $t^* = 0.5$ (b) $t^* = 1.0$ (c) $t^* = 1.5$ (d) $t^* = 2.0$

(e) $t^* = 0.5$ (f) $t^* = 1.0$ (g) $t^* = 1.5$ (h) $t^* = 2.0$
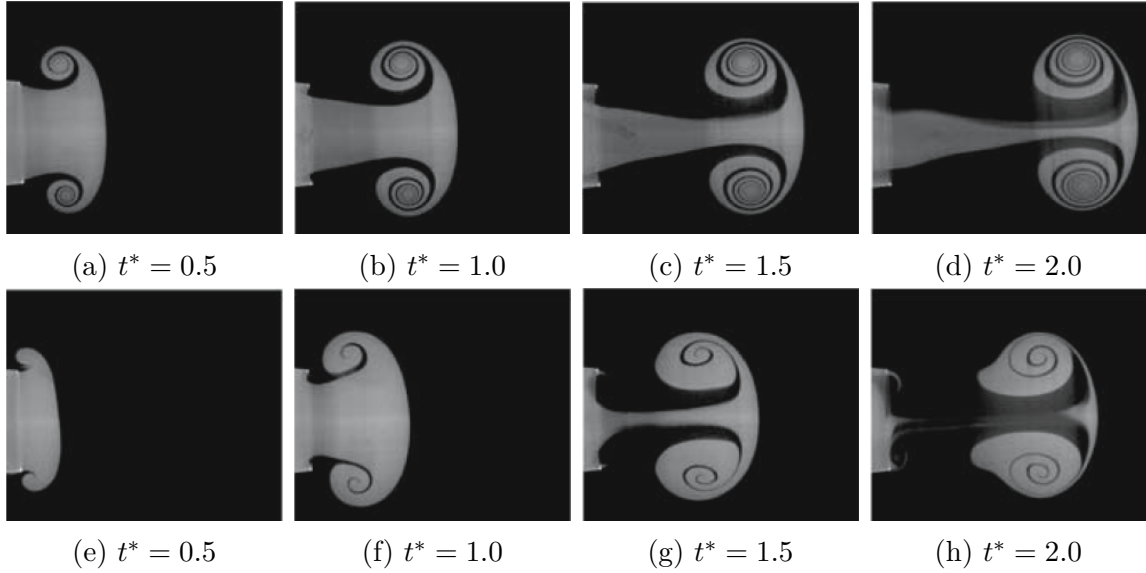
Figure 2.2: *Flow visualization of vortex rings generated with two different pulse velocity time profiles. The top images correspond to an abrupt rise in velocity with a negatively sloped (NS) decay, while the bottom row vortex was generated with a positively sloped (PS) rise in jet velocity with an abrupt cutoff.(Adapted from [50])*

moving behind the ring [51]

2.1.3 Characterization

Previous works investigating the P-JICF have quantified several inflow parameters and their influence on the resulting vortex ring. The characteristics of interest range from the vortical structure to the degree of interaction between the vortices. A key parameter for characterizing pulsed jets is the non-dimensional pulsing frequency, or Strouhal number, as defined in Eq. 2.1. This parameter relates to the interactions between consecutive pulses. Here, f is the pulsing frequency, d is the nozzle exit diameter, and U_j is the jet velocity.

$$St = \frac{fd}{U_j} \tag{2.1}$$

An early model for the propagation of the vortex ring proposed that vorticity diffused from the vortex core [49]. The vorticity that diffuses out affects the layer

near the surface of the vortex bubble, which was initially irrotational. The thin layer is also the source of fluid that trails the vortex bubble and becomes a wake region [48]. Support for this proposal was provided by the observation that at a fully pulsed condition (where no interaction between rings occurred) for $Sr = 0.28$ there are two branches of the jet material; one protrudes far into the flow, and the other trails the bubble remaining near the wall [27].

Additionally the stroke ratio,

$$\frac{L}{d} = \frac{\alpha_j}{St} \tag{2.2}$$

was shown to be important to the pulse characteristic and the jet penetration distance. For $\frac{L}{d} < 4$, the pulsed mass rolls into a tightly compact vortex ring. For $4 < \frac{L}{d} < 20$, the pulse splits into a deep penetrating vortex ring (not as spatially compact as previously), and a near-wall trail of fluid [52]. Additionally, the structure and trajectory of the pulse are affected by the Reynolds number (Re_j), as defined in Eq. 2.3. Pulses with high ($Re_j = 6200$) Reynolds numbers (and fixed stroke ratio) form more diffusive puffs, while tighter vortex rings with less trailing fluid are observed for lower Re_j values. These observations will be important to consider when observing the characteristics in the ejected kernel from the sunken fire igniter.

$$Re_j = \frac{U_j d}{\nu} \tag{2.3}$$

2.1.4 Jet Trajectory

Compared to steady jets, which have been investigated thoroughly [53], the pulsed jet can penetrate up to five times deeper into the crossflow [54]. This may be an advantage for using a pulsed igniter over a continuous ignition jet source, or torch type device, if high penetration distances into the crossflow are desired.

15

Previous work also reveals that the vortex rings resulting from low frequency pulsations were able to carry fluid from the jet further into the crossflow than high frequency pulses or steady jets [52,55]. This can also be enhanced with a shorter duty cycle (α_j) and using square wave excitation [56,57]. This distinction is necessary when speaking of rapidly pulsed jets, where subsequent pulses have the ability to interact, thus reducing their trajectory. Additionally, penetration enhancement also observed for zero-mass flux (synthetic) jets [58,59].

Much research has been conducted in understanding the scaling laws that correspond to the trajectory and development of a steady jet in crossflow. For steady jets, the trajectory is modeled by correlations with forms similar to that shown in Eq. 2.4. There, r is the ratio of jet velocity to crossflow velocity ($r = U_j/\bar{v}$), and A and m are empirical correlations with ranges, $m = 0.25 - 0.28$ and $A = 1.5 - 2.05$ [54], for jet and crossflow with a common density.

$$\frac{y}{rd} = A \left(\frac{x}{rd} \right)^m \tag{2.4}$$

This correlation was extended for heated jets where the jet and crossflow have unlike densities. Here the penetration is a function of the momentum ratio [60], defined as

$$J = \frac{\rho_j U_j^2}{\rho_{cf} U_{cf}^2} \tag{2.5}$$

Where, ρ_j, ρ_{cf}, and U_{cf}, are the jet density, crossflow density, and crossflow velocity, respectively.

Furthermore, the relation is adjusted when accounting for penetration enhancement with a pulsing jet. Pasumarti et. al. [61] performed simulations for a P-JICF, validated against the experimental data from Johari [52]. The obtained representation

16

of the pulsed jet trajectory becomes:

$$\frac{y}{d} = k \left(\sqrt{\frac{\rho_j U_j^2}{\rho_{cf} U_{cf}^2}} \frac{L}{D} \right)^{1/4} \left(\frac{x}{d} \right)^{1/4} \tag{2.6}$$

This correlation is relevant for considering the penetration when the crossflow velocity is increased, or the inflow temperature adjusted. Furthermore, this equation can be used to see the effects of adjusting the pulsing frequency or duration.

2.2 Numerical Prediction

A significant task of this thesis is to develop a simple prediction capability for ignition probability in a non-premixed flow. As discussed further in Chapter /refnumerical, a method of machine learning was identified as a computationally inexpensive method for evaluating ignition success based on input conditions. Specifically, a model only needs to choose between two possible outcomes.

2.2.1 Support Vector Machines

An SVM is a type of model that uses a custom algorithm for classifying data. The algorithm is created using supervised learning, where training data are provided which consist of paired data points with the desired output [62, 63]. The SVM is well suited for the problem at hand because it specializes at mapping data that fall into one of two categorical outcomes. For our case, these are successful or failed ignition attempts as simulated by the reduced order model. The training data, which are pre-categorized, are used to build the algorithm which will then be applied to mapping new points. The SVM at this point is deterministic, in contrast to other machine learning methods that apply probability to the classification.

Simply put, the training of the support vector machine constructs a hypersurface in p-dimensional parameter space used to classify data points (of p-dimensionality).
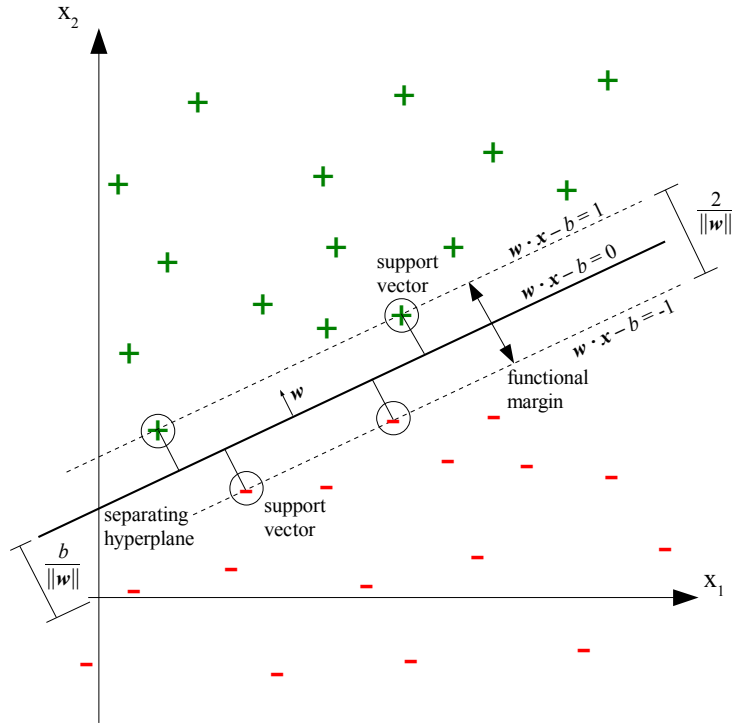
Figure 2.3: *Schematic depicting the separating hyperplane for a support vector machine classifier.*

The surface is constructed to best divide the training data between the two input classes. This optimal location is determined by maximizing the separation (functional margin) between the hyperplane and the nearest points of the two categories, as seen in Fig. 2.3. In the figure, the kernel function $(K(x, y))$ of the boundary is linear, and depicted for two dimensions. The two categories of data are $+$ and $-$ (signifying +1 and -1) with the support vector points circled. In this depiction the two categories are perfectly separated, where the linear boundary is defined with no incorrectly categorized points. Relaxation of this constraint is discussed later, but first we consider a linear boundary.

2.2.1.1 Linear Formulation

The formulation for defining a hyperplane follows [64], where the linear SVM is defined for perfectly separable data categories. Provided n points that constitute a set of

18

training data, $\mathcal{T}$, which are of the form

$$\mathcal{T} = \{(\mathbf{x}_i, y_i) \,|\, \mathbf{x}_i \in \mathbb{R}^p, y_i \in \{-1, 1\}\}_{i=1}^n \qquad (2.7)$$

where the points, $\mathbf{x}_i$, are p-dimensional, each belonging to a category y, which is either -1 or 1. In the same space, a hyperplane is defined as

$$\{x \colon f(x) = \mathbf{x} \cdot \mathbf{w} - b = 0\} \qquad (2.8)$$

where $\mathbf{w}$ is a vector normal to the surface such that $\frac{b}{\|\mathbf{w}\|}$ determines the offset from the origin. With the imposed condition that $\mathcal{T}$ is linearly separable, two parallel hyperplanes to the separating hyperplane can be selected, with the distance between these two hyperplanes defined as the functional margin $(2M)$. The two offset hyperplanes are described by

$$\mathbf{x} \cdot \mathbf{w} - b = 1 \qquad (2.9)$$

and

$$\mathbf{x} \cdot \mathbf{w} - b = 1 \qquad (2.10)$$

Therefore, the distance between these two parallel hyperplanes is $\frac{2}{\|\mathbf{w}\|}$, and the optimization problem to find the best separating hyperplane is as follows:
Find $\mathbf{w}$ and b to minimize $\|\mathbf{w}\|$, such that for all data points $(\mathbf{x}_i, y_i)$,

$$y_i \left(\mathbf{x} \cdot \mathbf{w} - b\right) \geq 1 \qquad (2.11)$$

which constrains the plane to existing only for separable data. For computational simplicity, the minimization problem is applied to finding $\mathbf{w}$ and b to minimize $\frac{1}{2} \|\mathbf{w}\|^2$, under the same constrain of Eq. 2.11.

19

2.2.1.2 Nonseparable Data

Suppose the training data cannot be bisected with a hyperplane to create two distinct regions each containing only one data category. This mixed data is expected for complex problems such as the spark ignition reduced order modeling. It is therefore helpful to understand the optimization problem in this case, considering that if the hyperplane cannot cleanly divide the training data, it will likely not categorize the input points faithfully compared to the reduced order model. The best dividing hyperplane in this situation is similar to the derivation above, though, using soft margin allows for mis-categorized training points [65]. In this formulation, the constraint of Eq. 2.11 is relaxed, and non-negative slack variables ξ_i are introduced which measure the degree of mis-classification as seen in Fig. 2.4. The revised form of Eq. 2.11 is as follows

$$y_i \left(\mathbf{x} \cdot \mathbf{w} - b \right) \geq 1 - \xi_i \tag{2.12}$$

for $1 \leq i \leq n$. In this form, the optimization is to find $\mathbf{w}$, b, and ξ, to minimize

$$\frac{1}{2} \left\| \mathbf{w} \right\|^2 + C \sum_{i=1}^{n} \xi_i \tag{2.13}$$

for any $i = 1, \cdots, n$, subject to Eq. 2.12, where C is a penalty parameter for having a separating plane that mis-categorizes data points.

2.2.1.3 Nonlinear Data

For certain parameter responses, a planar classification is not appropriate. It may be likely that a linear model is not appropriate for certain physical responses (e.g. equivalence ratio effects). Thus, the maximum-margin hyperplane is modified using the kernel method [66]. As a result, the hyperplane optimization is solved as before, using the following kernel function theory:

20
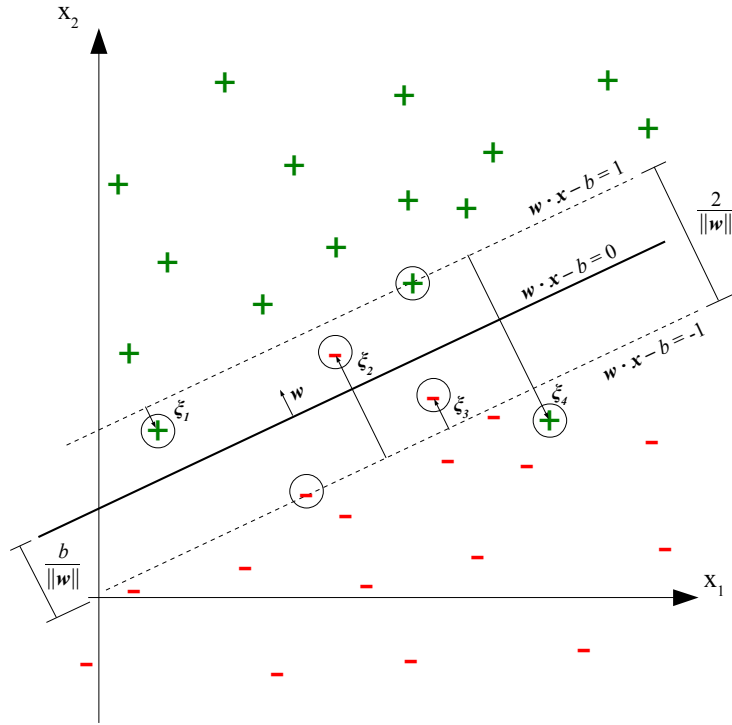
Figure 2.4: *Schematic depicting the separating hyperplane with a soft margin. The non-separable data have slack variables ξ_i to quantify the degree of misclassification.*

A class of functions are used, $K(x, y)$, which is applied such that $\mathbf{x}$ is mapped to a new linear space S by way of the function $\phi(x)$. The mapping function *phi* is defined such that

$$K(x, y) = \phi(x) \cdot \phi(y) \tag{2.14}$$

where the dot product occurs in the space S. For our purposes, the polynomial class of kernel functions is all that is necessary. In this case, for some positive integer d,

$$K(x, y) = (1 + \phi(x) \cdot \phi(y))^d \tag{2.15}$$

where $\phi(x)$ is a transform function that need not be explicitly represented. The solutions to the mathematical optimization problems will not be discussed further as this theory is applied in Chapter 6. The specific choices for training data and

21

methods of validation are presented in Section 4.2.2, which relate to the general concept outlined above.

CHAPTER 3

EXPERIMENTAL METHODS AND CONSIDERATIONS

This chapter describes the experimental apparatus and the diagnostic approaches used in this work. The first section presents a detailed description and characterization of the stratified flow facility used for the experimental work. The second section focuses on the implementation of the diagnostic techniques that were used to study spark kernel development and ignition. Data reduction techniques used to process the acquired raw data are also described.

3.1 Stratified Flow Facility

An experimental, systematic study of turbulent non-premixed forced ignition requires a facility that allows control of the relevant flow variables and measurement of the ignition process. The ignition process is a sequence of events influenced by the design of the facility. To represent a non-premixed turbulent flow, the following sequence must occur in the facility for each ignition attempt:

1. a plasma kernel is created;

2. the kernel convects in pure air (or a non-flammable mixture);

3. the kernel is quickly introduced to a flammable fuel/air mixture.

In addition to the process sequence, it is important to define what constitutes successful ignition. Following the light-back definition [11], other reviewed literature, and typical aero-engine flow conditions, successful ignition shall be defined here as a flame kernel that grows and propagates in a flowing *flammable* mixture beyond 2 *ms* following the spark discharge event. If the kernel is not observed after 2 *ms* following

23

the discharge then for practical purposes, it would not be able to grow and stabilize, and therefore fail to ignite the burner.

Control of certain flow parameters was required for the operation of the flow facility and in the investigation. Therefore, considerations for the following variables needed to be incorporated in the design:

- Mean flow velocity $(\bar{v})$

- Equivalence ratio(s) (ϕ)

- Preheat temperature (T_i)

- Convection time of the kernel before it reaches the flammable mixture $(\tau_{transit})$

- Igniter

Inlet flow turbulence was also considered as a variable of interest, to relate to kernel development and ignition success. It was decided to keep this as a measured variable, as it scaled with mean velocity, instead of designing a method of control.

3.1.1 Conceptual Design

Considering the requirements defined above, a conceptual design was generated by outlining features which address each objective and ranking the combinations of those options. A schematic of the experimental flow facility is shown in Fig. 3.1. Other conceptual designs were considered, including an annular co-flow design, which relies on the expansion of the kernel to control the delay time until interaction with the flammable flow. This, and the other concepts considered do not allow as much control over the variables listed above as the concept in Fig. 3.1. Times for the kernel to convect in this design were defined based on early experiments characterizing the kernel trajectory, described below. Desired kernel travel times depicted were chosen
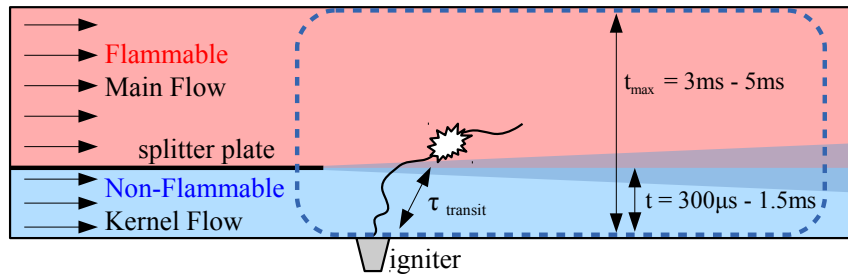
Figure 3.1: *Conceptual design of the stratified flow facility. Time scales were decided upon based on experimental data.*

based on typical flow times in commercial combustors. Trajectory data for the spark kernel were used to size the facility design.

3.1.2 Facility Implementation

Based on the requirements of the facility, the conceptual design was developed into the detailed design seen in Fig. 3.2. Detailed drawings of the facility can be found in Appendix A. The structure was designed and built of 6.35 mm thick carbon steel plate, and is not designed to operate at elevated pressure. Most of the plates were cut by water jet out of plate stock at the GTRI machine shop. Welding and finalization of parts was carried out at the GT aerospace machine shop. Existing flow monitoring and air heating infrastructure was adapted for this facility. The installed facility is seen in Fig. 3.2b.

3.1.2.1 Infrastructure

The facility is supplied from a single air source that can be electrically preheated up to 540 K. A small amount of fuel (e.g., methane) could also be added to the supply approximately 60 cm upstream of the facility, allowing for a non-zero equivalence ratio in the kernel flow (ϕ_{bottom}). After passing through a perforated plate (2.4mm dia. holes, 30 % open area), the flow enters a plenum before being split into two streams by a thin splitter plate (0.6mm thickness). The upper stream is the main
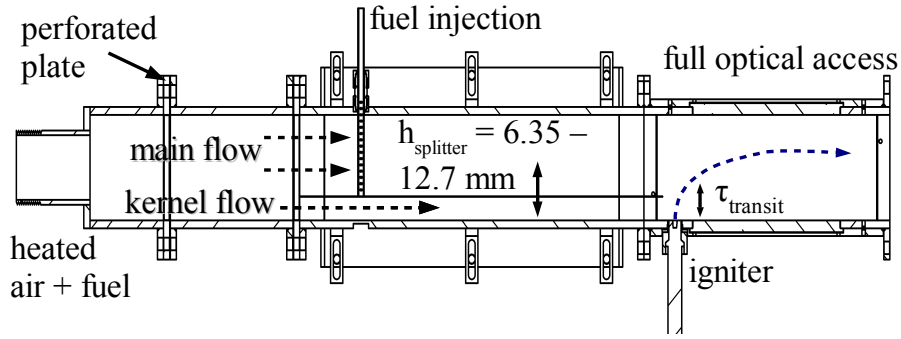
(a) *Detailed design of facility.*
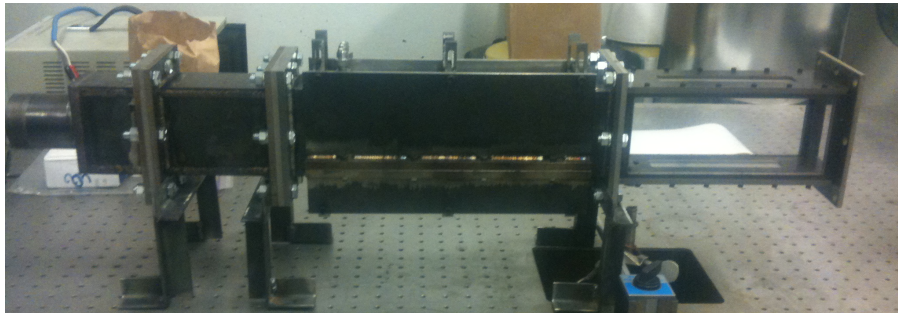
(b) *Photograph of completed facility*

Figure 3.2: *Detailed design schematic and photograph of the stratified flow facility for use in non-premixed ignition experiments.*

flow and the lower stream is the non-flammable kernel flow. The splitter height (h_s) can be adjusted to control the distance between the igniter and the main flow. The splitter plate can also be adjusted up and downstream to ensure a minimum possible mixing layer thickness at the point of kernel interaction. The main flow region has fuel bars where additional gaseous fuel can be introduced to produce a flammable mixture. The two flows then enter the test section, which has quartz window side walls, as well as windows in the top and bottom walls, for optical access. The outlet of the facility opens to the laboratory, creating approximately atmospheric pressure conditions in the test section. A vent draws exhaust away from the facility approximately 30 *cm* from the end of the test section.

Table 3.1: *Ranges for operating parameters in the stratified flow facility.*

$\bar{v}$	$10 - 40 \; m/s$
T_i	$435 - 475 \; K$
h_s	$6.4 - 12.7 \; mm$
ϕ_{top}	$0 - 1.4$
ϕ_{bottom}	$0 - 0.05$

3.1.2.2 Controls

The flow of air and fuel in the system is manually controlled by way of gate and needle valves. The flow rates through the supply air and main flow fuel lines are measured using sub-critical orifices with differential pressure transducers. The pressure transducers and orifices were calibrated using a Ritter drum-type gas meter. Fuel injected to the bottom flow is supplied by a pressurized cylinder and metered using an Omega FMA-1842 mass flow meter, which was also calibrated using the drum-meter.

Signals from transducers are input to a National Instruments compactRIO and processed using a LabVIEW virtual instrument to report ϕ_{top}, ϕ_{bottom}, T_i, and $\bar{v}$. The readings were corrected for zero offset at the beginning of each run.

Inflow temperature (T_i) is measured just upstream of the facility using an unshielded type K thermocouple. The temperature reading, as reported in the LabVIEW panel, was verified using a handheld thermocouple reader. The temperature in the test section was also measured using a handheld thermocouple and reader at several preheat settings, which compared well to the values recorded in LabVIEW. Following the facility connection and control operability, the flow parameters were roughly tested to match the designed ranges as listed in Tab. 3.1. These parameters and their variability were further verified as shown below.

27

3.1.3 Characterization

3.1.3.1 Igniter Characterization

The igniter used in these experiments is a commercially available model, characterized by a sunken fire surface discharge gap with a capacitance based exciter. This equipment produces a high energy, short duration spark, as characterized by the voltage-current plot in Fig 3.3. The integrated energy deposited was calculated from the V-I plot according to Eq. 3.1. The plot shows that the electrical energy is supplied in $\mathcal{O}(10\mu s)$. The supply of high energy ($\sim 1.25 \ J$) is assumed to have a high deposition efficiency due to the short discharge duration [44]. This pulse duration and frequency effectively result in a duty cycle of $\alpha_j = 0.001\%$. The equipment regulates the igniter pulsing to 15 Hz, which corresponds to, $St \approx 6 \times 10^{-4}$, according to Equation 2.1. This low value is a result of the high pulsing energy causing a relatively high ejection velocity combined with a low pulsing frequency. This results in distinct, non-interacting, jet pulsing. Additional characterization experiments were performed, including kernel trajectory measurements under quiescent conditions. These data aided in the sizing of the facility design, described below, and understanding the variability in the operation of the igniter. Kernel penetration distance distributions are presented in Fig. 3.4 to demonstrate the shot-to-shot variability in kernel characteristics and the variability between igniters. These data were taken unconfined, with no crossflow to observe if any variability existed under quiescent conditions. As discussed in Chapter 2, the discharge is dependent on the breakdown characteristics which could be variable, resulting in a variable trajectory. Only igniter 3 was used in the actual ignition experiments, as it provided a higher mean velocity kernel. Generally, the

$$E_{supplied} = \int V(t)I(t)dt \qquad (3.1)$$
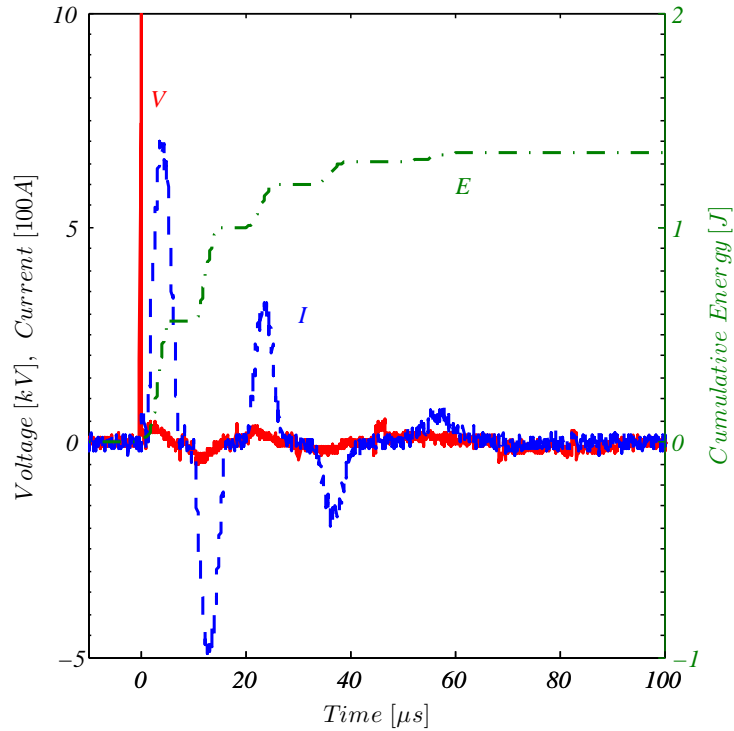
Figure 3.3: *Voltage (V) and current (I) traces for sunken fire igniter. Total supplied energy (E) is also plotted as according to Eq. 3.1*

3.1.3.2 Velocity Flowfield

Facility characterization experiments were performed to understand the uniformity of the flow entering the test section. Pitot probe measurements were used to determine the velocity distribution in the tunnel. Figure 3.5 depicts a velocity profile at the downstream location where the igniter is placed. The profile shows good uniformity and boundary layers in expected locations. The overall flow rate based on the probe data compares well with values obtained using a critical orifice flow meter in the air supply system, with mean velocity values agreeing to within 5 %.

Turbulence intensity was measured using a single element hotwire under various inflow conditions at several locations in the test section. Though the turbulence is not a controlled parameter, it has been characterized for several $\bar{v}$ conditions to understand trends as flow parameters are changed. Velocity profiles as measured by

29
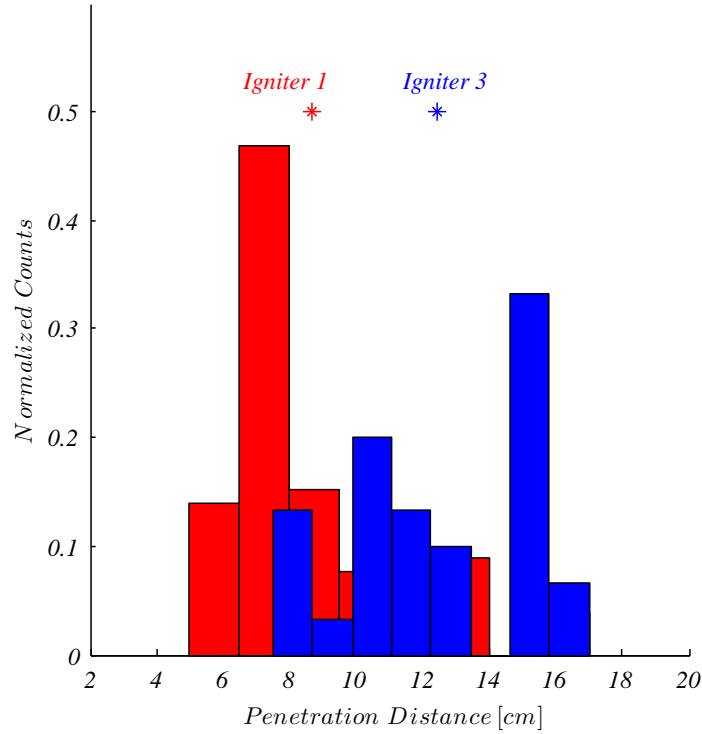
Figure 3.4: *Variability between igniters as measured by penetration distances of the spark kernels. The distributions illustrate the spread of values kernels from a single igniter may have, and the differences between mean values of different igniters.*

hotwire are presented in Fig. 3.6. Hotwire velocity time histories and the corresponding spectra for sampling locations can be found in Appendix B.

Based on the velocity profiles shown, some mean velocity non-uniformity (about 15%) is attributed to the wake region deficit downstream of the splitter plate. Temporal fluctuations were measured to be $v_{RMS}/\bar{v} < 15\%$ at each location.

3.1.3.3 Fuel Distribution

Natural gas was chosen as the fuel in these experiments due to availability and its combustion characteristics. The natural gas was shown to be comprised primarily ($\sim 95\%$) of CH_4, based on compositional information from the supplier. The natural gas for the main flow is injected from fuel bars fabricated from perforated steel tubing, as shown in the drawings in Appendix A. The degree of fuel distribution uniformity

30
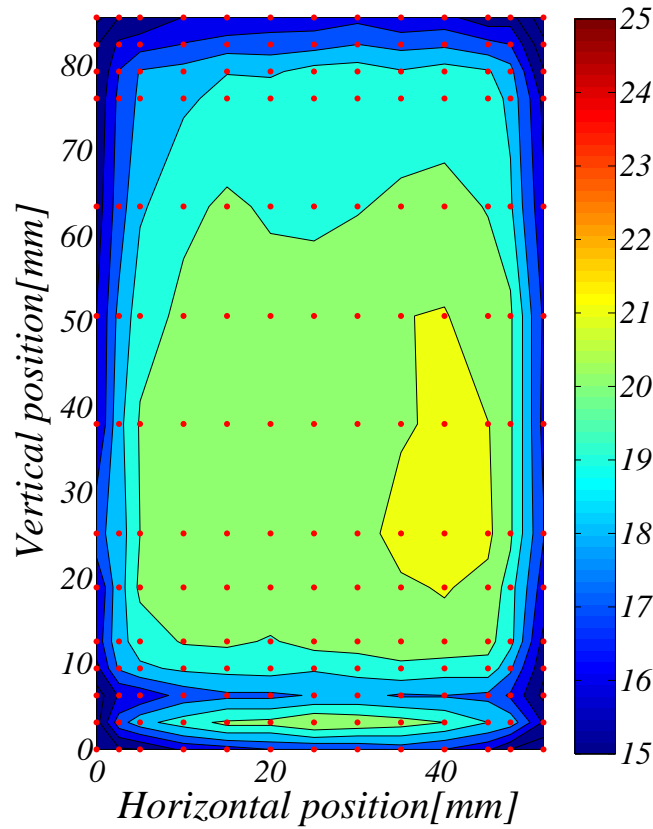
Figure 3.5: *Velocity ($\bar{v}$) [m/s] profile inside test section 13mm downstream of the splitter plate. Red dots indicate sampling locations with the nominal velocity set to 20 m/s.*

in the main flow was determined by traversing a gas sampling probe across the test section inlet and measuring the fuel content with a gas analyzer. Several iterations of fuel bars and supply lines were attempted with non-uniformity prevalent due to slight differences in pressure losses from the fuel supply manifold to the fuel bars. Flexible steel braided fuel hoses of equal length resulted in the most uniform fuel supply. With this configuration, the fuel distribution was found to be uniform $\pm 5\%$ of the mean concentration throughout the main flow region, as seen in Fig. 3.7. Additionally, the fuel mixing layer thickness at the trailing edge of the splitter plate is $\sim 2\ mm$ at the point of kernel interaction, as seen with schlieren.

31

(a) $x = -3\ mm$ (b) $x = 25.4\ mm$ (c) $x = 38.1\ mm$
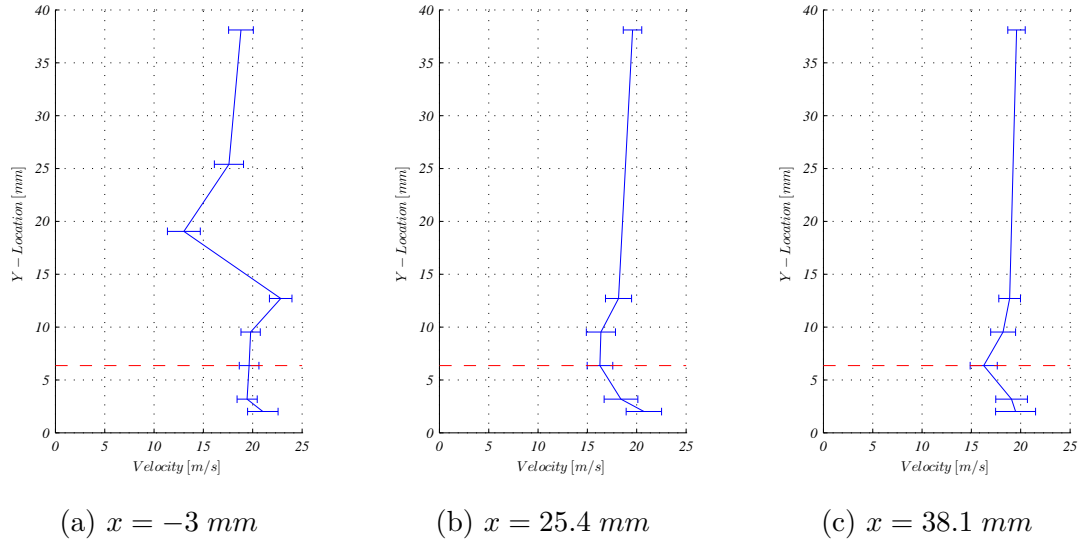
Figure 3.6: *Velocity profiles taken at three downstream locations along the mid-plane for $\bar{v} = 20\ m/s$ with errorbars representing RMS velocity values. Downstream locations are measured from the igniter opening which is located $12.7\ mm$ downstream from the splitter plate trailing edge. The dashed line depicts the height of the splitter plate.*

3.2 Diagnostics

3.2.1 Schlieren

The kernel was viewed through the quartz windows on the sides of the test section using a single pass collimated schlieren system in an X configuration as seen in Fig. 3.8. The setup uses a $50\,W$ halogen lamp whose light passes through a $0.4\,mm$ diameter pin hole and is then collimated by a $0.2\,m$ diameter, $1\,m$ focal length off-axis parabolic mirror. The reflected collimated light is then directed through the test section and toward a second (identical) parabolic mirror. This mirror refocuses the light to a point. The schlieren stop was produced by a glass slide with an opaque spot, roughly the size of the focal point of the light beam with the flow facility not running.

A high speed CMOS camera (Photron Fastcam SA5 or SA3) focused on the test section was used to record the data at framing rates >50 kHz. An $80\,mm$ telephoto photographic lens was mounted on the camera. A nanosecond response photodiode

32
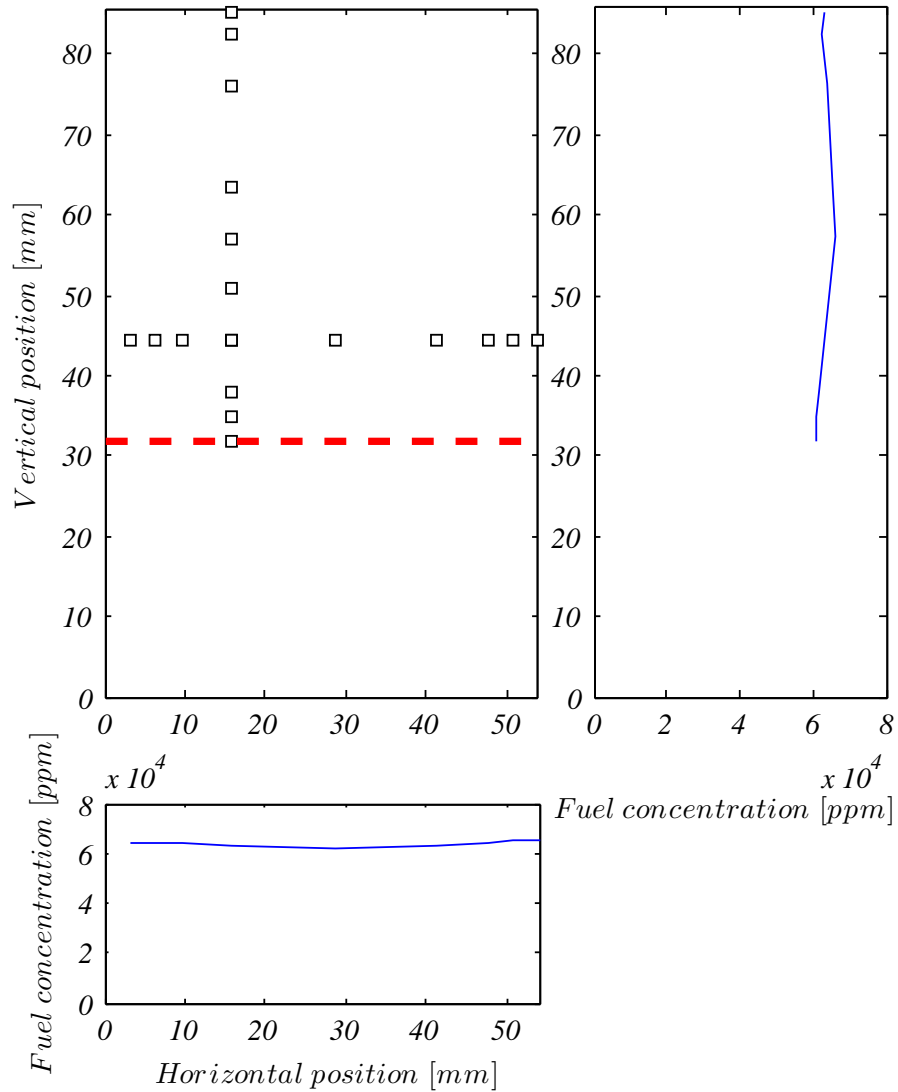
Figure 3.7: *Plots of fuel concentration levels along a horizontal and a vertical traverse in a cross plane of the test section taken $\sim 6\ mm$ upstream of the splitter plate. The splitter plate was set to $h_s = 32\ mm$.*
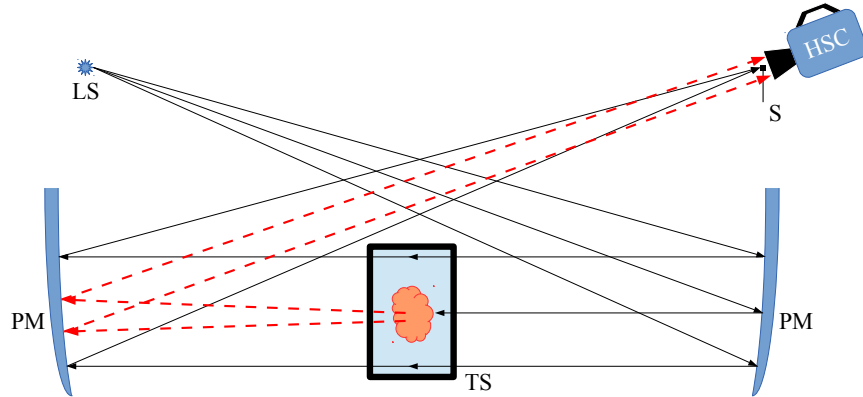
Figure 3.8: *Schlieren optical raytrace schematic: a cross-stream view. A point light source (LS) provides broadband light which is collected and collimated by a parabolic mirror (PM) toward the test section (TS). Light passing through and schliered light (dashed in red) is redirected by a second parabolic mirror (PM). Unrefracted light is refocused onto an opaque schlieren stop (S), while schliered light passes toward a high speed camera (HSC).*

was directed at the igniter to signal the spark event to a digital delay and pulse generator (Stanford Research Systems SRS DG535) which was used to trigger the camera and other devices explained below.

The schlieren imaging allows for visualization of the index of refraction gradients which arise from density gradients [67]. This visualization can be used to observe the kernel trajectory and interaction dynamics with the stratified flow. Additionally, the growth of the kernel can be related to the amount of mass entrained [68]. Therefore, the schlieren imaging data was used to estimate mixing rates of the kernel with the environment.

3.2.2 Chemiluminescence

Ignition of a fuel-air mixture induced by the spark kernel can be sensed by monitoring optical emissions associated with combustion reactions, i.e., chemiluminescence. Whether selected to look at emission from specific electronically excited chemical species or broadband, the signals can inform the temporal or spacial location of flame chemistry and/or heat release.

3.2.2.1 OH* Chemiluminescence

OH^* chemiluminescence is often used for flame characterization [69, 70]. Here, OH^* is measured using a photomultiplier tube (PMT) fitted with a narrow band filter centered at $307nm$. This approach can be used to track the time history of flame chemistry following a spark event. The PMT signal output is connected to a high speed oscilloscope to monitor and record the light intensity as depicted in Fig. 3.9. Unwanted emission observation from any flame outside the test section (e.g., the flame produced from a previous spark kernel) is prevented by blocking the exit of the test section and directing the PMT to collect light emitted only from within the test section. This can be used to determine the earliest (detectable) occurrence of OH^* signal after the spark breakdown.

3.2.2.2 Broadband Detection

Broadband flame kernel emission can also be recorded using a high speed CMOS camera (Photron SA3) to compare spatial kernel development to results obtained with the PMT. Synchronized high speed imaging and PMT data are used to compare the OH flame chemistry indicator to the visible emission features. This equipment configuration is also depicted in Fig. 3.9.

Independent of the PMT, the high speed camera can be used to take images of the developing kernel triggered to set intervals following the spark event. Fig. 3.9 shows the trigger information flow through the data capture equipment. The photodiode, pulse generator, and high speed camera all have a very short internal delay, known to be on the order of nanoseconds. To verify this synchronization, an oscilloscope was used to monitor the trigger signal provided by the pulse generator, and the exposure signal from the high speed camera. Delay within the camera could be adjusted to correct for misalignment.

When recording emission with the high speed camera, each trial can capture 135

www.manaraa.com
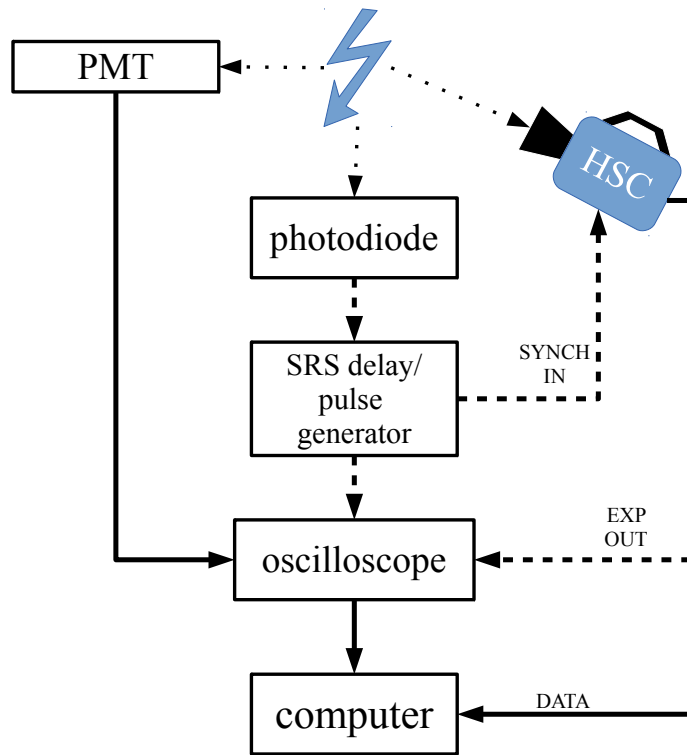
Figure 3.9: *Schematic depicting the flow of information through the data acquisition system components. The dotted lines represent light emission, the dashed lines represent trigger signals, and the solid lines represent data streams. The oscilloscope was used for synchronization adjustments.*

images synchronized to the spark event. The images are post processed using a MATLAB program. The program uses a combination of cropping to the desired field of view and edge tracking to determine if a growing flame kernel exists in the image.

3.2.3 Image Processing: Edge tracking

Schlieren image data was primarily processed using MATLAB image processing toolbox. There are several variations on how the data was manipulated, but the core functions remained the same. Images were saved in the Photron Fastcam Viewer (PFV) software in an uncompressed avi format. The files were each loaded in matlab using the combination of "mmreader.m" and "read.m." Edge tracking was an important aspect in measuring the size and movement of the kernels in the images. The

36

images were first binarized by using "im2bw" and a chosen intensity threshold. The threshold was kept constant for all frames, and for all videos from the same experimental run. The black and white image was filled in so no internal holes existed. This provides a more representative kernel area because schlieren only produces light where density gradients exist. So the center of the kernel can be dark even though it is hot. The function "bwboundaries.m" was used to create the line along the boundary of the kernel, which was then typically plotted over the original grayscale image so the internal structure could be visible. Additional cropping and intensity adjustments were performed as needed so the regions of interest were identifiable. The corresponding progression of images through these steps is depicted in Fig. 3.10. A similar process was applied to the images gathered to detect for a successful ignition event. The successful imaging of a flame was indicated by a large bounded area as determined through the edge detection scheme.

3.2.4 CH Planar Laser-Induced Fluorescence

Planar laser-induced fluorescence (PLIF) is performed to identify regions of the ignition kernel where flame chemistry begin. A Light Age PAL 101 alexandrite laser is used, whose output is tuned with a birefringent element to $\sim 774.4\ nm$. The fundamental beam is passed through a frequency-doubling crystal to achieve the desired harmonic of $\sim 387.2\ nm$. A detailed explanation and schematic of the laser is presented in [71]. The laser beam is directed as several beam steering mirrors before passing through sheet forming optics and directed into the top of the test section, as depicted in Fig. 3.11. When operated in Q-switched single pulse mode, the power output of the laser is typically 15 $mJ/pulse$ and the pulse half max width is $\sim 60 - 80\ ns$.

The laser is operated at 15 Hz to match the repetition rate of the spark igniter, and allow for seamless transition between internal clock triggering and external triggering

37

(a) *Grayscale image*

(b) *Binary*

(c) *Traced edge*

(d) *Edge applied to grayscale*
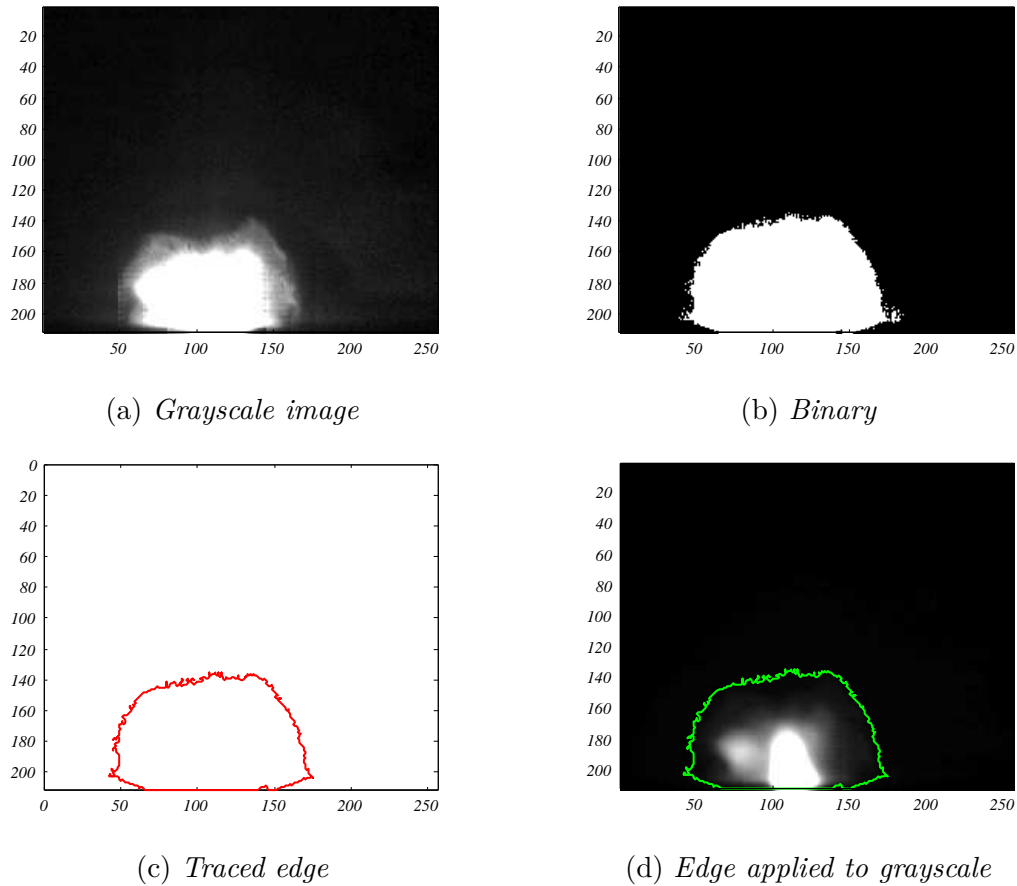
Figure 3.10: *Sequence of images depicting the process of edge tracking applied for schlieren data. (1) The grayscale image is loaded in matlab from the avi file. (2) An intensity threshold is applied to binarize the image. (3) An edge is plotted from the boundary between black and white in the binary image. (4) The edge is applied to the grayscale image after brightness adjustments.*

from the igniter. The exciter box and discharge of the igniter are not trigger-able and are monitored to synchronize the other equipment with the laser pulses. A photodiode monitors the bright spark discharge, which is received at the external trigger to a SRS DG535 pulse gate and delay generator, as depicted in Fig. 3.12. A zero delay TTL signal is sent to the Berkeley Nucleonics Corporation (BNC) 575 pulse generator. This device controls the triggering of the PAL flash-lamps (PAL lamp), PAL Q-switch (Q1), intensified CCD camera's gate width (PI cam), SA5 exposure, and SA3 exposure. The relative timing and synchronization of these events are adjusted and confirmed by oscilloscope prior to every data acquisition. General timing delays are

38
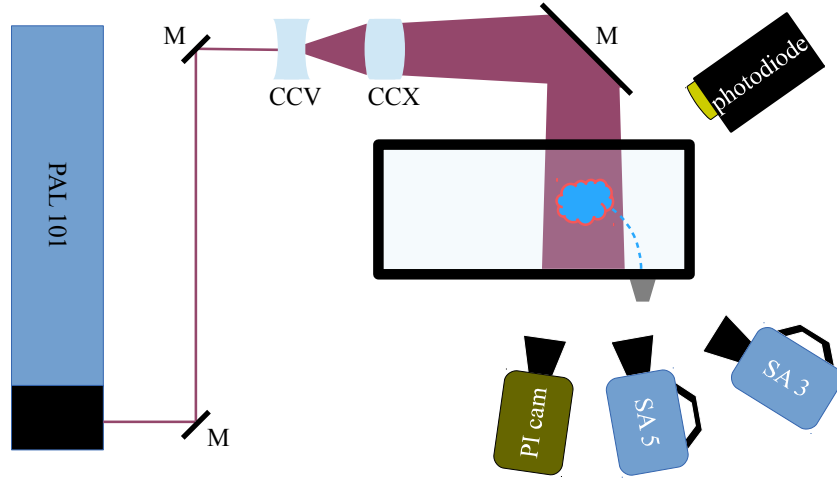
Figure 3.11: *Schematic of the PLIF component configuration. The second harmonic beam is emitted from the side of the PAL 101 laser and steered by dichroic mirrors (M). The beam passes through a cylindrical concave lens (CCV) to expand and then through a cylindrical convex lens (CCX) to reduce the expansion. The sheet is then reflected into the test section where it excites CH and the fluorescence is imaged by the PI cam. The SA5 simultaneously captures schlieren images, and the SA3 records broadband emission at later times to determine ignition success. Timing of the laser and record events is based on signal originating from the photodiode detecting the spark event.*

depicted in Fig. 3.13.

3.2.4.1 PLIF Imaging

PLIF images of the kernel were taken using an intensified Acton PI 512 $\times$ 512 camera. The camera intensifier is an 18 mm Gen III HB film-less intensifier, which has a quantum efficiency of $\sim$ 45 % in the spectral region corresponding to the CH fluorescence. The camera was equipped with a a 55 mm Nikor lens (f/1.4). Elastic scattering was filtered using a 3 mm thick GG 420 Schott Glass filter. All images with the PI camera were taken with a gate width of 200 ns.

3.2.4.2 Image Registration

One goal of performing the CH PLIF is to investigate where flame chemistry reactions occur in the ignition kernel. Simultaneous fluorescence and schlieren images
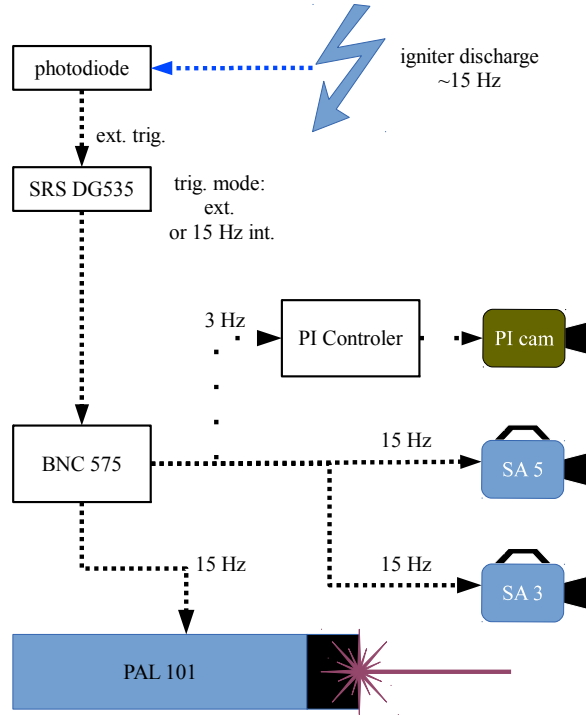
Figure 3.12: *Schematic depicting the flow of trigger signals through the CH PLIF system. The dashes represent a nominal* 15 *Hz signal while the dotted line represents a* 3 *Hz signal. An oscilloscope was used for synchronization adjustments.*
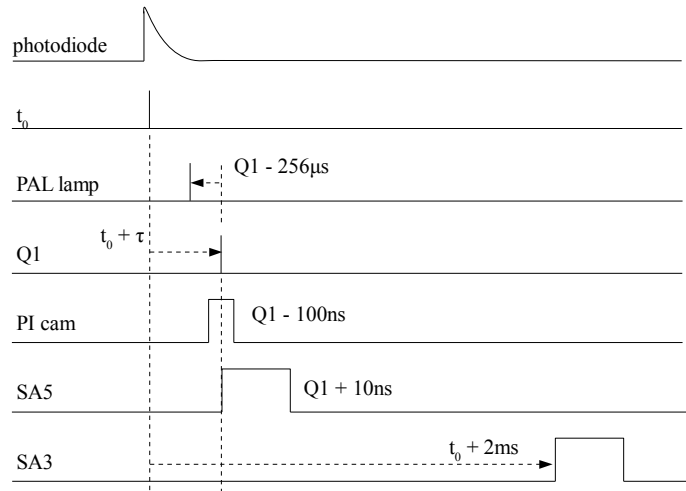
Figure 3.13: *Timing diagram depicting the signal delays programed in the BNC 575 pulse generator.*

were acquired to assist in this study, however the images need to be superimposed to provide a meaningful spatial comparison. The perspective difference of the two cameras requires a careful image registration procedure to allow for this superposition. A calibration target is used to obtain a spatial reference from each camera, in the same orientation and under the same optical conditions used for the ignition experiments. The target, which consists of a transparency with 0.5 mm dia. circles arranged in a grid with 2 mm on-center spacing adhered to a 6.4 mm thick quartz window, was imaged with the PI camera and the SA5, as seen in Fig. 3.14. The camera resolutions are, at their maxima, 512 × 512 for the PI camera and 1024 × 1024 for the SA5. The image registration is performed in MATLAB, using a control point method, with the function "cpselect," where the control points are selected, as seen in the images. The locations of the control points are manually selected based on the image regions of interest where the kernel and torch (described later) are imaged. The schlieren image is defined as the fixed reference, and a transformation matrix is generated for the control points of the PLIF image using the function "cp2tform," which is applied to the PLIF image with the function "imtransform." The pixel dimensions of the schlieren image are also fed into this function so the newly registered PLIF image has the same resolution, with the values of any newly created blank regions set to zero. The two images are combined by making the monochromatic schlieren image the red layer of an RGB image and making the monochromatic PLIF image the green layer. The resulting superimposed registration image is seen in Fig. 3.15. The control points of the targets match well and agree to within a fraction of the dot size, ($< 0.1\,mm$). At the mean convection velocity of the flow used in the PLIF experiments ($\sim 20\,m/s$) the kernel will move this distance in 5 μs, which is less than the schlieren exposure of 33 μs. Thus the streaking due to schlieren image integration is greater than the registration uncertainty.

41

(a) *SA5 (Schlieren)* (b) *PI camera (PLIF)*
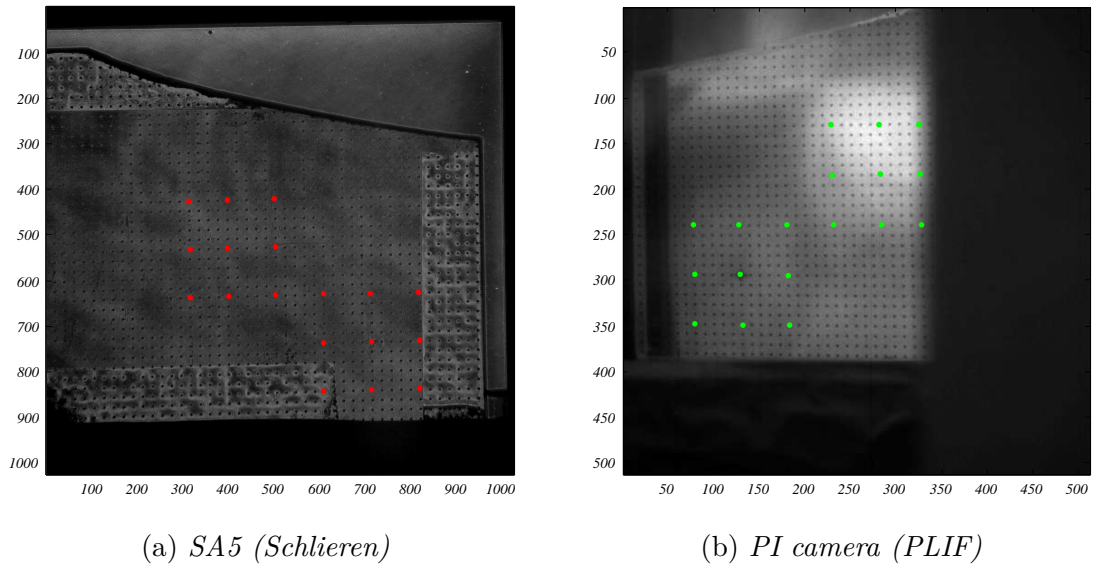
Figure 3.14: *Calibration target images taken with the PI camera and the SA5 to allow for image registration.*
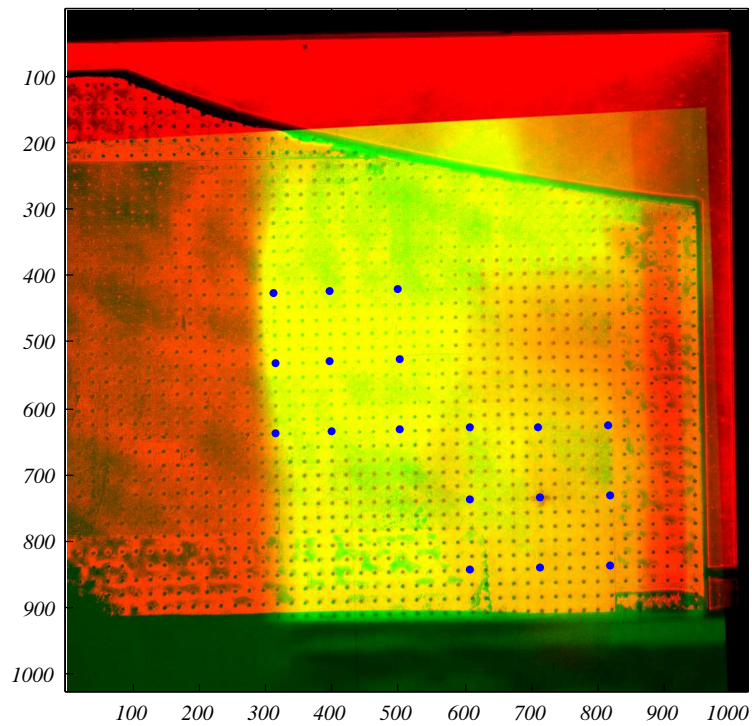
Figure 3.15: *Post-processed image of both calibration targets, registered, and superimposed. Schlieren image intensity on red layer and PLIF intensity on green layer of this RGB image.*

42

www.manaraa.com
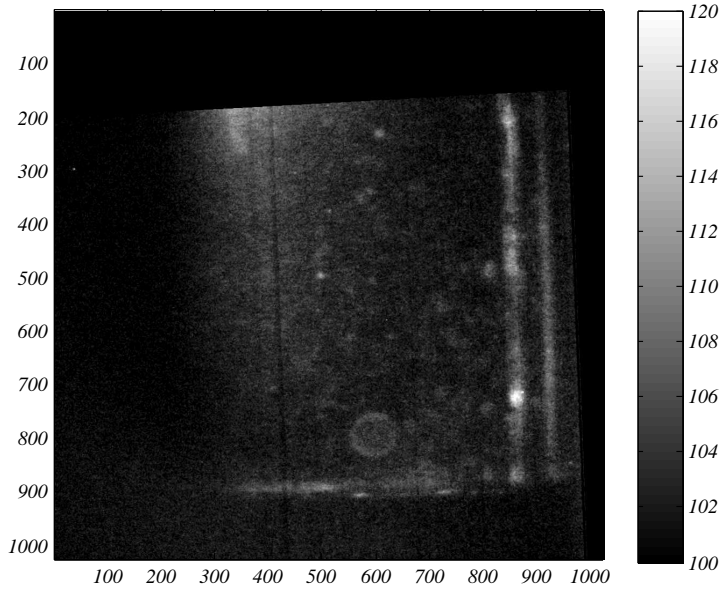
Figure 3.16: *Averaged background signal from 30 images taken with the PI camera, and the PLIF laser operating. The image has been registered to the schlieren image coordinates.*

3.2.4.3 Background Signal

To isolate the CH PLIF signal from other (background) signals, images are captured with the PI camera with only the laser operating (no spark, and no fuel). An example of this background signal can be seen in Fig 3.16, which is the average of 30 single-shot images; the average background intensity in the viewable region is 102. The bright signal at the top of the image is likely due to scattering as the sheet passes through the top window. The linear region of high intensity near $x = 900$ is caused by laser scattering from the test section flange. This provides a background image to subtract from subsequent PLIF images to remove scattering that occurs in the test section. This background image is only subtracted from images acquired with the PLIF laser operating.

43

3.2.4.4 Bunsen Excitation

Preliminary CH PLIF imaging tests were conducted using a partially premixed propane torch to ensure the equipment synchronization and to tune the laser to the optimal wavelength for CH excitation. This tuning ensures the highest signal and provides CH PLIF signal images for qualitative reference. For this preliminary experiment, the propane torch is placed in the test section with the top window removed to allow for the hot exhaust gases to escape. The broadband emission captured with the SA3 camera can be seen in Fig. 3.17; this is the same camera perspective as the emission imaging used to determine the success or failure of each ignition attempt. The emission, PLIF, and schlieren images are acquired with the timing sequence described above, controlled by the 15 Hz internal clock of the SGS535 instead of the igniter discharge. The resulting schlieren and PLIF images, after image registration, are shown in Fig. 3.18. Elastic scattering from the excitation laser sheet is visible at the bottom wall of the test section in the the lower portion of Fig. 3.18b. This wall scattering was blocked from the PI (PLIF) camera in subsequent imaging experiments, using black cinefoil, and the remaining background signal subtracted as discussed above. Superposition of the registered schlieren and PLIF images, following intensity balancing and the color layering process described above, results in the image shown in Fig 3.19. The schlieren indicates where the largest density gradients exist in the propane jet flame, while the CH PLIF highlights the primary heat release zone. The success of the registration process is confirmed by the relative placement of the two signals. The PLIF signal falls along the outer boundary of the high intensity schlieren signal (more so on the top edge, but also along the bottom). The largest density gradient, marked by the schlieren, occurs on the unburned side of the flame [2], while the CH PLIF marks the subsequent reaction zone. The high intensity of the schlieren on the bottom (near $y = 700$) shows the density gradient on the burned side of the flame [2]. This is not as apparent for the top side due to the buoyant flow.

44
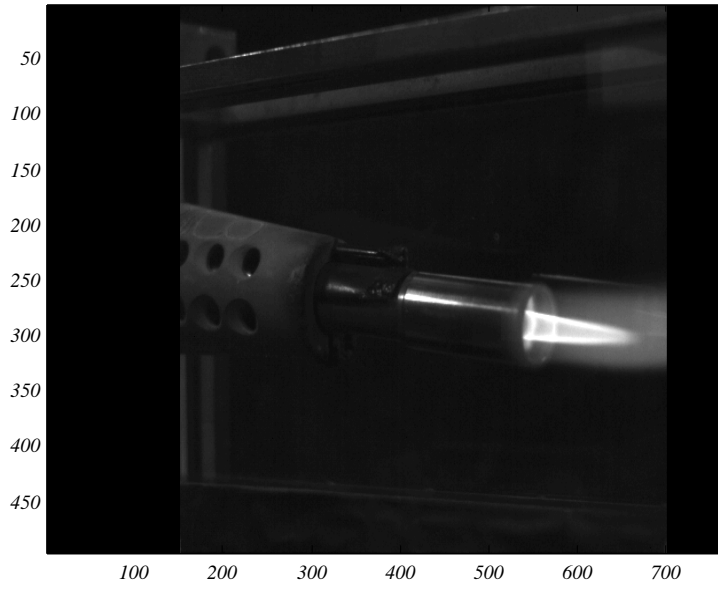
Figure 3.17: *Image of broadband emission from partially premixed torch flame.*

(a) *Schlieren*
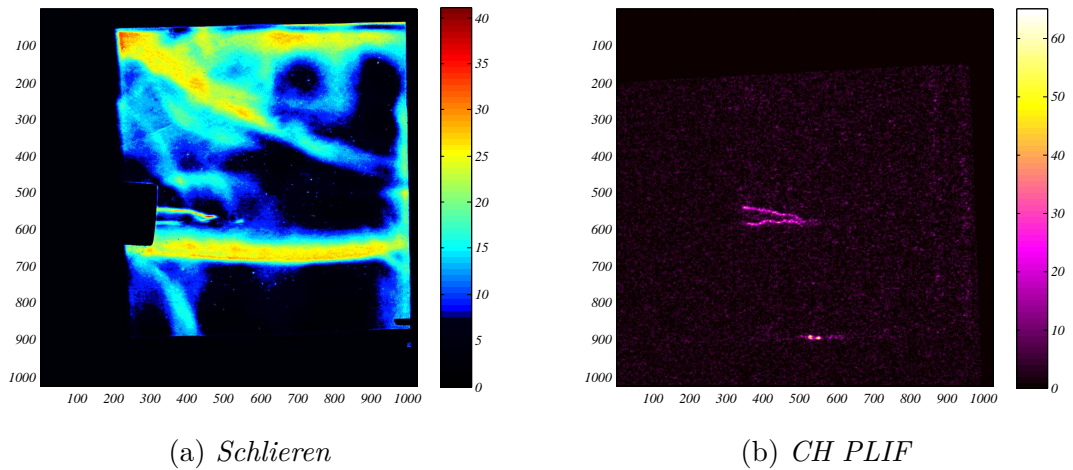
(b) *CH PLIF*

Figure 3.18: *Separate schlieren and CH PLIF images of a partially premixed torch flame, registered to the same coordinates.*

45
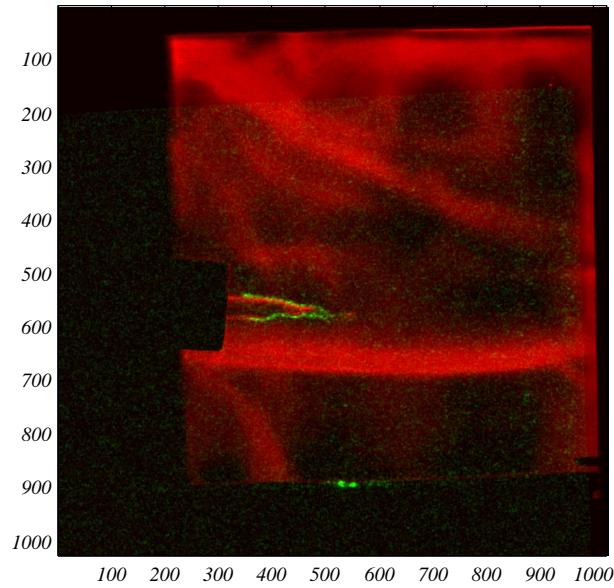
Figure 3.19: *Post-processed image of torch flame schlieren and PLIF images. Schlieren image intensity on red layer and PLIF intensity on green layer of this RGB image.*

3.3 Experimental Design

Part of performing the experimental trials is choosing which conditions to run. An intelligent design of cases will include points that are orthogonal to each other in the multi-dimensional variable design space. By meeting this objective, the most information about how all the variables affect the response is obtained for the least number of expensive experiments.

3.3.1 Screening Tests

A set of exploratory screening cases were designed to determine the most influential input parameters. These full ranges of the inputs were interrogated in order to explore the extremes of the design space, and observe main effects. Most trends were assumed to be simply representable by a linear fit, except trends with equivalence ratio. For that reason, an interior condition was needed for those variables. Splitter height (h_s) was also chosen to have three levels to be able to capture any non-linear trends. The

46

other variables were designed to be screened with only two levels.

The experimental design was automatically populated based on the number of variables being investigated in JMP statistical software. The variable levels of interest were provided and populated in the general design. The specific levels and type of design is discussed further in section 5.3.1. The output from JMP provided the nominal values to use in the experiments, though the actual conditions that were measured during testing were recorded and used during analysis.

3.3.2 Higher Order Parameters

Beyond the initial experimental cases designed to determine the most influential design parameters, a more comprehensive set of experiments was desired to capture the higher order relations. A space filling experimental design was chosen to increase the chances of capturing the higher order trends and cross correlations between the remaining variables. These parameters were interrogated across their experimental ranges according to a discretized Latin hypercube (LHC) design. The number of experimental trials was first decided based on time and cost constraints and the ranges of the variables entered. The LHC has the benefit of sampling each dimension evenly and not repeating locations. Additionally, the design is orthogonal, so the most information can be regressed from the number of points chosen.

47

CHAPTER 4

NUMERICAL METHODS

This chapter explains the development and implementation of a simple numerical model used in this work. The first section introduces the reactor model and the associated design choices. The structure of the model is based primarily on results and observations of the ignition kernel and process discussed in Ch. 5. The second half of the current chapter describes the methods associated with introducing randomness into the model. The intended goal of this effort is to connect the reduced order model to the experiments through a common response variable.

4.1 Reduced-Order Model

A reduced-order physics-based model is used to study the effects of mixing and chemical reactions that occur from the time the spark kernel is created to when ignition occurs (if it does). The model is based on coupled thermal and chemical analysis simulations built to represent the same physical sequence of events that occur in the experiments so non-premixed ignition is addressed in a verifiable manner. The model consists of a constant pressure, perfectly stirred reactor (PSR), with two inflow compositions representing the non-flammable and flammable flows, as illustrated in Fig. 4.1. The perfectly stirred model assumes the mixing rate of entrained fluid with kernel fluid is much faster than the time required for chemical reactions. While this assumption is not realistic, it can provide an approximation of how the entrained mass affects the kernel. The model was implemented in CANTERA [72]. The code for the executable functions to simulate the two stages of the PSR can be found in Appendix C.

48
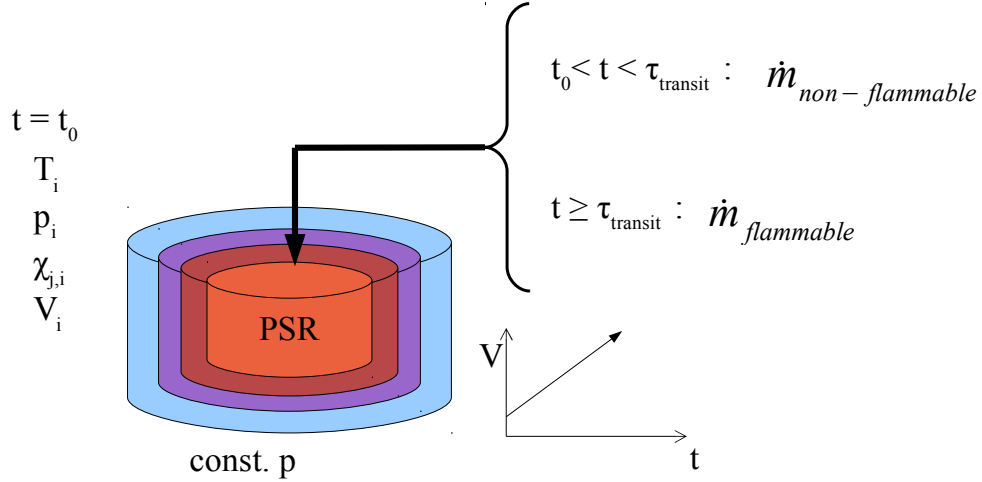
Figure 4.1: *Reactor model for an ignition kernel including mass entrainment and a transition to a flammable mixture. The reactor has no outlet and increases in volume to maintain constant pressure as mass is added.*

4.1.1 Non-Flammable Reactor

The function code for the first reactor is presented in section C.1 as "KernelReactor.m". The simulation begins by defining a gas phase to initialize the reaction model. This phase is characterized by the chemical mechanisms and constants used to calculate the reaction rates and thermodynamic state. The first stage of the PSR includes only air related species at elevated temperatures, requiring an air plasma mechanism. The chemical mechanism is the same as outlined by Schulz et al. [73] using rate coefficients from [74–76] and thermodynamic coefficients from NASA CEA [77], which is defined up to $20,000\ K$.

The gas phase state is initially computed as equilibrium air ($T = Ti$, $p = 1\ atm$, $\chi_{N_2} = 0.79$, $\chi_{O_2} = 0.21$). The spark discharge energy ($1.25\ J$) as measured in section 3.1.3.1 is added to the internal energy of the air contained within the volume of the igniter cavity, $\mathcal{O}\left(0.1 cm^3\right)$. The equilibrium state is again computed for the air phase. This high energy gas is then expanded (isentropically) to $p = 1\ atm$, simulating the kernel expanding from the sunken igniter.

The first stage of the PSR is initialized with a portion of this gas, with a vol-

www.manaraa.com

ume (0.02 cm^3) extrapolated from experimental schlieren images to $t = 0$ s, further explained in section 5.1.2. The PSR is adjacent to the environment which contains the initial air phase ($T = Ti$ K, $p = 1$ atm, $\chi_{N_2} = 0.79$, $\chi_{O_2} = 0.21$). When the time-stepping begins mass is added to the PSR at a constant rate to simulate entrainment of mass into the kernel; there is no outflow from the reactor, so the volume continuously adjusts to maintain constant pressure. This gas is sourced from the environment phase, so is composed of the initial air state. The rate of mass addition was estimated from schlieren imaging by observing the kernel area's rate of change, discussed in section 5.1.2. This entrainment mass is to simulate the mixing of the kernel with the kernel flow of Fig. 3.2a.

4.1.1.1 Input Parameters

The specific inputs to the first stage of the reactor are listed in the preface to the MATLAB code in section C.1. The first input is dt, the time interval between each saved property set for the kernel reactor. This is not the minimum step size for convergence of the kinetics solver. The subfunction "advance" determines the rate of change of volume, mass of each species, and the total energy in the reactor by integrating the system of ordinary differential equations. This integration is performed from the time of the input conditions to the final time specified by dt. During this time interval, many time steps may be made within the "advance" function in order to achieve the specified or default convergence criteria. The input variable "endt" is the final evaluation time performed in the kernel function. This does not necessarily dictate the time that the next stage begins, but simply how long the current reactor continues its calculations. If a given set of initial temperatures and pressures are to be reused for numerous $\tau_{transit}$ simulations, the kernel reactor is only run once for the longest time required as to save computation expense. The input "mentrain" directly corresponds to the amount of mass added to the kernel reactor from the surrounding

50

environment in a given time interval. This variable was chosen to be a constant, approximated from experiments. Though the observations showed some nonlinear volume growth, suggesting a varying entrainment rate, the standard functions in Cantera did not handle these. The environment temperature, which is the same as the initial kernel temperature, is "Tin" in the code, and was matched directly from input temperatures from experiments. Though experimental measurements could only be performed under atmospheric conditions, the code has the ability to vary "pin." The pressure is set to one atmosphere when matching the experiments. As noted above, the composition of air in the environment is set internally to $\chi_{N_2} = 0.79$ and $\chi_{O_2} = 0.21$. This also dictates the composition in the kernel volume prior to energy deposition. The input variable "Xin" allows a non-equilibrium composition to be specified at the onset of the reactions, to simulate superequilibrium in the early plasma.

4.1.2 Flammable Reactor

The function code for the second reactor is presented in section C.1. In experiments, the kernel reaches the flammable layer after a nominal transit time ($\tau_{transit}$). Likewise, after a specified time, the entrained gas becomes a flammable fuel-air mixture at a fixed equivalence ratio. This is performed by running the ignition reactor code and using the output structure from the first stage as an input to the current function. As explained earlier, the output structure from the first stage may contain extra data, so the variable "tau" is used to select the appropriate state from the first function.

The second stage of the PSR employs a standard hydrocarbon-air chemical mechanism [78]. All remaining ions (and electrons) at this time are replaced with their corresponding neutral state (eg., N^+ to N), as an appropriate ionized fuel-air ignition mechanism was not identified. This produces a negligible change in the chemical enthalpy since the charged species concentrations are at trace levels at $\tau_{transit}$ for the

51

conditions studied here. This conversion from the NASA based mechanism to the UCSD mechanism is performed by "nasa2ucsd.m" which is presented in section C.3. The transformed composition vector with the temperature, pressure, and volume from the first stage reactor is then used to initialize the second stage. The flammable environment is defined by first defining the phases for the two constituents at atmospheric conditions: air ($\chi_{N_2} = 0.79$ and $\chi_{O_2} = 0.21$) and methane ($\chi_{CH_4} = 1$). The input variable "ER" is used to determine the ratio of the oxidizer and fuel and therefore determine the composition of the environment gas. This environment is set to the same "Tin" and "pin" as it is assumed these parameters are constant between the two flows.

Similar to the first stage reactor, the mass entrainment between the environment is input to "mentrain" and is a constant value. Though the code allows a step change at this point if desired, the entrainment rate was kept constant and set to the value used in the first function. At this point, the time stepping begins and the kernel properties are again calculated by the "advance" function. At each time step the kernel properties are saved and exported at the end of the simulation, once "endt" has been reached.

The temperature and chemical composition evolution from second stage are analyzed following the simulation as the indicators of successful ignition. This is further discussed in section 6.1.2.

4.2 Modeling Ignition Probability

In Ch. 1, ignition is introduced as a stochastic event, implying that for a given set of conditions, the outcome is sensitive to random fluctuations. Experimental investigations are subject to similar fluctuations as *in situ* ignition attempts, but this random noise must be artificially introduced in numerical simulations. Several ways of introducing and evaluating this variability are presented.

52
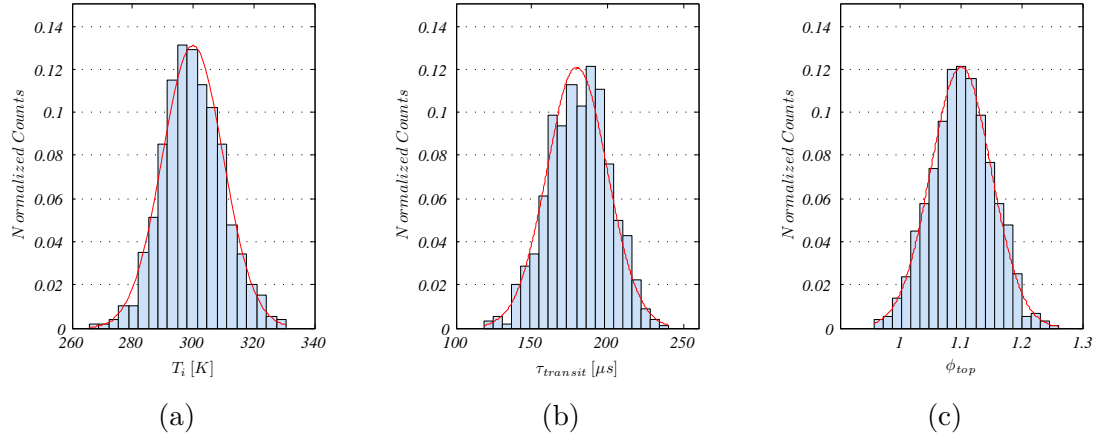
Figure 4.2: *Example generated input values for transit time and equivalence ratio, which approximate a normal distribution (outline).*

4.2.1 Random Input Generator

It was assumed that the experimental flow variables of interest were normally distributed about the measured input values, therefore, corresponding distributions are required as inputs to the numerics to appropriately model the effects. Perturbations were introduced to the simulation input variables (inflow temperature, transit time and equivalence ratio) using a random number generator that approximates normally distributed parameters. The generator function code is presented in section C.4 and uses the "rand" function at its core. The "monteNorm" function is called with inputs for the mean, standard deviation, and the desired number of output values. For one point, the generator sums 100, uniformly distributed, independent random variables to create one approximately normally distributed random variable. This variable is adjusted so that the distribution of the variables match the desired input mean and standard deviation (σ) of the test condition. A sample of generated normally distributed random variables is seen in Fig. 4.2. Though the function has the ability to generate any number of random variables, one thousand cases was used for each nominal test condition so a statistically significant ignition probability, $P(ign)$, could be calculated and compared to the experimentally determined probabilities.

53

4.2.1.1 Variation Inputs

4.2.2 Classifying Ignition

As described above, the reduced order simulation concludes with property histories that evidence the success or failure of ignition. A single run has only one of those two outcomes. This suggests that an even simpler model could be implemented that categorizes successes and failures based on the inputs. Additionally, performing thousands of simulations to provide an ignition probability for a single nominal condition was known to be computationally expensive, so a pattern classifier was sought to quickly evaluate a set of inputs. The pattern classifier is a type of machine learning that needs training data. The data provides the algorithm with enough information to make subsequent evaluations.

4.2.2.1 Training Data

Training points for the pattern classifier are needed that sufficiently encompass the mean variable design space, with enough added range to capture the variability. These training points are generated in JMP using the built-in Latin Hypercube (LHC) design of experiment function. As a space filling design, the minimum and maximum variable space values, and the number of design points is sufficient to generate the points. The simulation is run using these input values that fill the variable design space. This produces a list of points with success or failure results. The pattern classifier is trained using a large fraction of these input/result pairs, the remaining portion is used to validate the classifier prediction capability. Example validation results are presented in Tab. 4.1, where Y is the logical result from the simulation and $\hat{Y}$ is the predicted outcome from the pattern classifier. Out of the 20 points presented, only one was incorrectly categorized, highlighted in red.

Table 4.1: *Twenty example test points with outcomes from the numerical model and predictive classifications from the SVM.*

$T_i\ [K]$	$\tau_{transit}\ [\mu s]$	ϕ_{top}	Y	$\hat{Y}$
523.9	251.4	1.08	0	0
359.0	239.4	0.47	0	0
285.0	140.7	1.32	0	0
506.3	186.3	1.57	0	0
437.7	202.7	1.34	0	0
310.8	95.6	1.23	1	1
423.7	221.6	0.71	0	0
315.0	106.1	0.91	1	0
433.1	240.6	0.96	0	0
453.4	204.3	0.91	0	0
368.4	100.6	1.00	1	1
385.7	103.0	0.91	1	1
455.1	77.8	1.53	1	1
482.1	84.0	0.84	1	1
473.5	81.0	0.75	1	1
330.1	167.5	1.49	0	0
395.3	163.9	0.99	0	0
469.1	99.2	1.14	1	1
417.6	206.8	0.72	0	0
320.5	200.5	0.85	0	0
$\vdots$	$\vdots$	$\vdots$	$\vdots$	$\vdots$
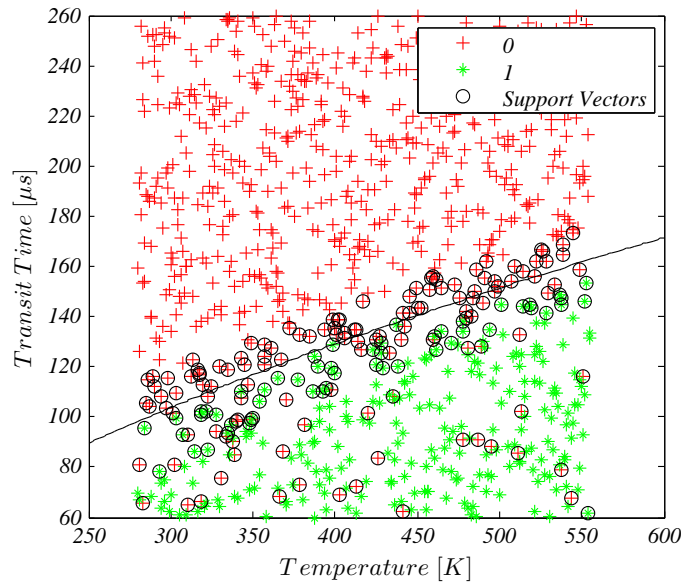
Figure 4.3: *Example view of training data used to inform the kernel function of "svmtrain." The points labeled "0" are simulated points that resulted in failed ignition, while "1" points are successes. The circled points are those used as support vectors. This example only used temperature and transit time to inform the SVM, so there are many points on the wrong side of the boundary, representing failed attempts due to an equivalence ratio effect.*

4.2.2.2 Support Vector Machine

The most widely used pattern classifier, where binary outcomes are required, is a support vector machine (SVM). Described further in Chapter 2, the support vector machine is a type of supervised learning that fits a kernel function to the set of training data. The SVM was implemented using the standard MATLAB function, "svmtrain." Provided training data, the tool creates a tuned set of coefficients for the specified kernel function. For the experiments here, a quadratic kernel function was selected. An example of the training data and the resulting classification line created can be seen in Fig. 4.3. The training of this SVM only used temperature and transit time so a 2D visualization could be created, as a result many points fall on the incorrect side of the line due to equivalence ratio effects. Following the training of the SVM, to evaluate a set of points, the function "svmclassify" is used which requires the previously created structure and the design points to classify.

56

CHAPTER 5

SPARK KERNEL EVOLUTION AND IGNITION SENSITIVITY

This chapter presents the experimental findings for forced ignition in the stratified flow facility. It begins with an examination of the kernel generation and evolution measurements and results. This is followed by the investigation of the most influential parameters on the probability of ignition.

5.1 Kernel Development

The kernel transit and evolution were observed for various conditions to see if noticeable development phenomena correlated with ignition success. This kernel of hot gases was visualized using the high speed schlieren imaging system described in Section 3.2. These images provide information on the trajectory and growth of the kernel.

Initial ejection visualization experiments were performed in an open environment with no crossflow. As seen in Fig. 5.1, the ejected kernel emits (measurable) visible light for at least 400 μs following the initial breakdown. This suggests that, for no crossflow, the kernel is sufficiently hot or contains enough high energy species to viably ignite a flammable mixture that it encounters for a delay up to at least several hundred microseconds.

5.1.1 Trajectory

Similar experiments were performed prior to the construction of the facility to characterize the trajectory of the ignition kernel after leaving the igniter in a cross-flow.
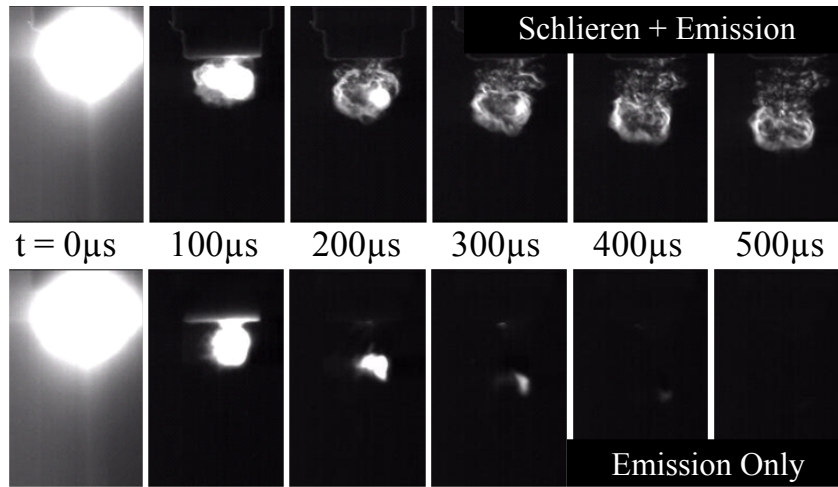
Figure 5.1: *Time progression of two separate kernel ejections from igniter. Top sequence depicts schlieren and emission. Bottom sequence depicts emission only.*

These results were used in the sizing of the experimental facility described in Section 3.1. The igniter was placed at the exit of a small flow facility described in Kim et al. [68] with a mean exit velocity of 25 m/s. The high speed camera captured images at 5,000 fps, and recorded ten discharge events. Between four and five frames were captured for each convecting kernel. Figure 5.2 presents four frames from one of the ten kernels. Each image was processed with an edge detection algorithm (described in Ch. 3), and the resulting kernel edges from all the frames and discharge events were superimposed into one image as seen in Fig. 5.3; the igniter cavity is located at (0,0). These results indicate that the height required to prevent the kernel from interacting with the top wall of the facility is approximately 80 mm within the time span of interest ($\sim 5\ ms$).

5.1.1.1 Kernel Transit Times

Following the design and construction of the facility, the kernel trajectory was again characterized in the stratified flow tunnel. One correlation of interest is between the splitter plate height and the transit time, i.e, the nominal time required for the kernel

58
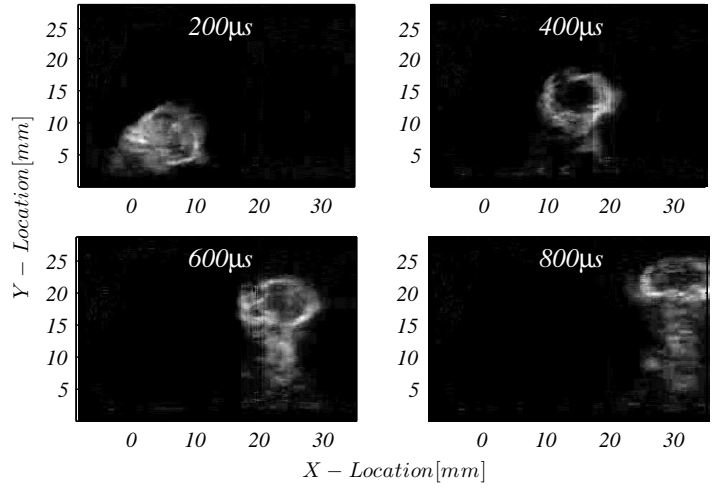
Figure 5.2: *Four schlieren frames from a single kernel convecting kernel in a 25 m/s crossflow. The igniter is located at (0,0) and crossflow is left to right. Times indicate delay following discharge event.*
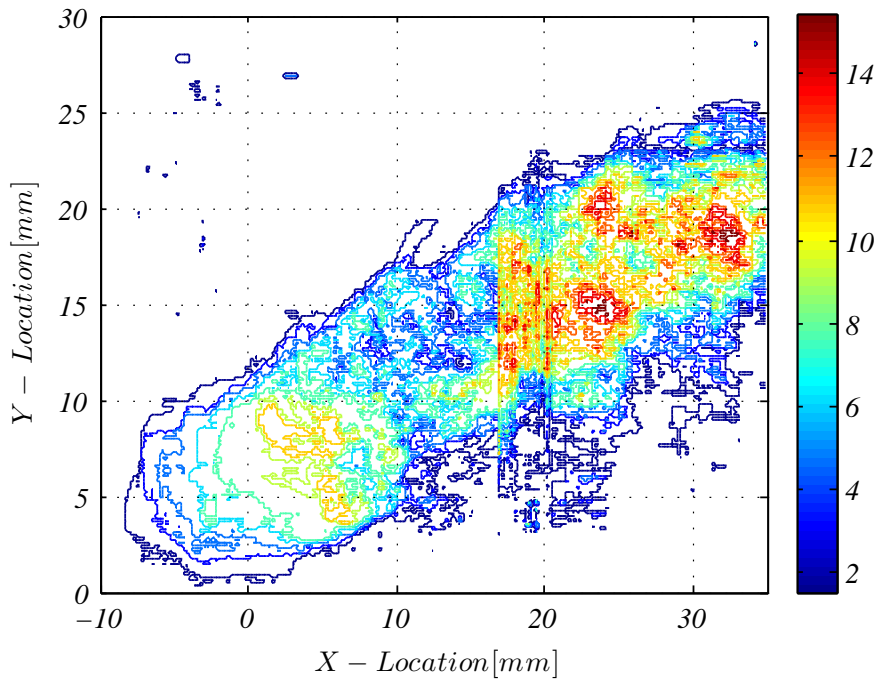
Figure 5.3: *Superposition of approximately ten kernel trajectories from a high-speed movie in a 25 m/s crossflow. The igniter is located at (0,0) and flow is left to right. Color bar indicates the number of times a kernel edge is observed at a given location.*

59

to reach the mixing layer. This is directly related to the ejection velocity of the kernel from the igniter, as discussed in Section 3.1.

Figure 5.4 depicts a sequence of schlieren images taken with the high speed camera at 50,000 frames per second. These were obtained with a crossflow of 20 m/s air in the flow facility and $h_s = 6.4 \ mm$. The bright regions in the images correspond to the plasma emission. The schlieren boundary of the kernel is visible at later times (as the emission signal decreases) and provides the interface for determining the transit time. The schlieren sequence also depicts the kernel fluid motion occurring as it convects away from the igniter, indicating that mixing is an important process. This is visible when unique features on the surface of the kernel are tracked from frame to frame and show the kernel fluid mixing. The previous results of emission duration combined with these observations suggest that the kernel has at least a few hundred microseconds to convect *and mix* with the flammable fluid, while energetic species are still present. The kernel may still be able to cause ignition at later times, because there can be non-emitting (e.g., ground state) radicals and high temperatures remaining within the kernel. For this particular splitter plate height, the top of the kernel (τ_{top}) is able to reach in 40 μs with some uncertainty based on the interval between frames. In this figure, the indicated transit times are based on the amount of time elapsed between the kernel deposition and the point when the top edge of the kernel reaches the splitter plate height.

Spark event schlieren images were analyzed to compare the range of crossing times required for the kernel to progress to different vertical locations with respect to the splitter plate. Because ignition depends on the kernel interacting with the flammable mixture, these crossing times represent a characteristic time for this interaction to start. The edge detection image processing described in Section 3.2.3 was used on the high speed schlieren images to collect the edges of the kernels and to determine the crossing times. Figure 5.5 shows sequences of five kernel ejections with the splitter

60
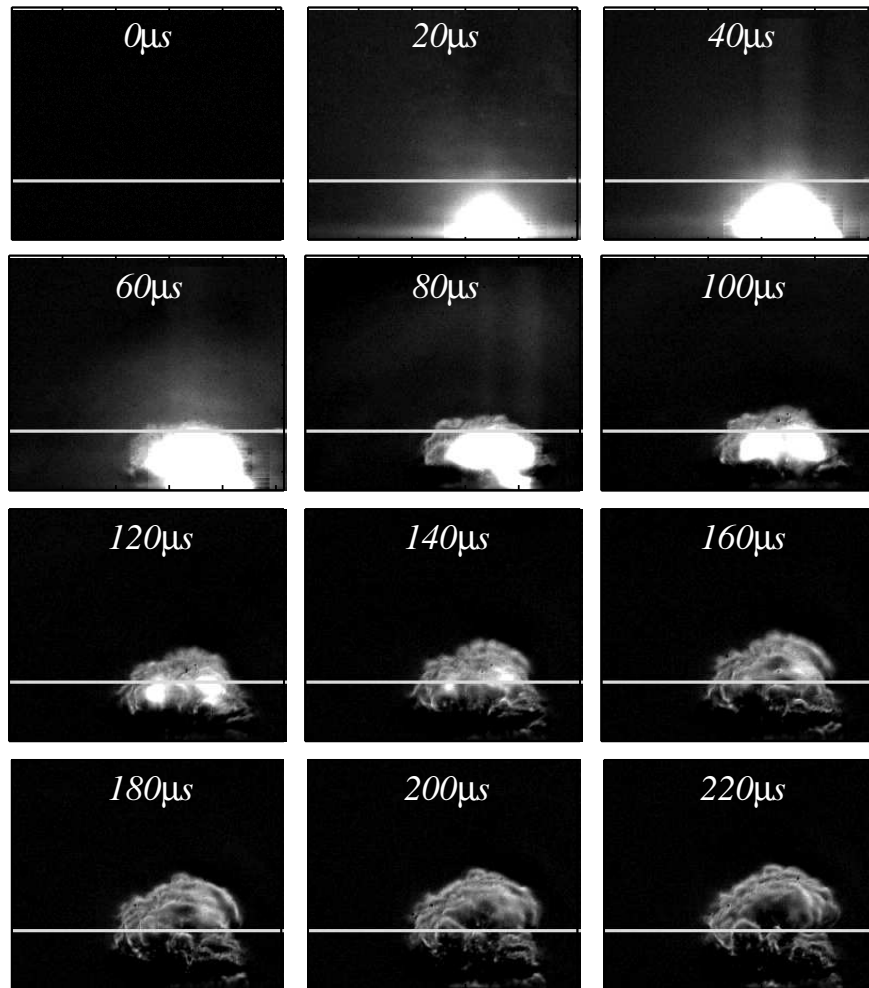
Figure 5.4: *Time progression of a kernel ejected from igniter. Schlieren visualization depicts kernel reaching splitter boundary (overlaid white line) at 40 $\mu s \pm 10$ μs, where the splitter was set to $h_s = 6.4$ mm.*

plate height represented for each test. The general similarity in kernel progression suggests that the vertical displacement of the splitter plate has little influence on the time required for the kernel to transit a specified distance from the igniter. The edges determined from the software algorithm are also included in the figures. Edges from images at early times $(0 - 40 \ \mu s)$ were not tracked because the bright spark emission obscures the schlieren results.

The locations of the kernel's top edge, centroid, and bottom were recorded for each time delay in each sequence and are plotted in Fig. 5.6. A quadratic best-fit (least squares) model for the vertical location as a function of time was determined for each of the three kernel location metrics in order to provide a measure of the mean crossing times. The tight grouping of the points for the top edge and centroid locations at earlier times helps define the variability of the three possible time choices for the nominal value of $\tau_{transit}$. The significant scatter for time required for the the bottom of the kernel to pass a given height is due to the structure of the kernel's trailing edge. This portion of the kernel often shows trailing tendrils that extend well beyond the main portion of the convecting kernel.

This trajectory information for the different parts of the kernel indicate the time scales required for the kernel to reach (and then mix) with gas from the flammable layer. The values of crossing times for the investigated plate heights, in increments of $\sim 1.6 \ mm$ up to $12.7 \ mm$, are listed in Table 5.1. The three transit times are reported, where τ_{top} is the time for the top of the kernel to reach the flammable layer, τ_{mid} is the crossing time of the kernel centroid, and τ_{thru} is the time when the bottom of the kernel passes above the splitter plate. This information was also used to determine that the kernel ejection velocity, as averaged over the first $100 \ \mu s$, is $\mathcal{O}(100 \ m/s)$. The jet momentum ratio (Eq. 2.5) is a function of this ejection velocity and affects the kernel penetration and entrainment characteristics as discussed in Chapter 2.
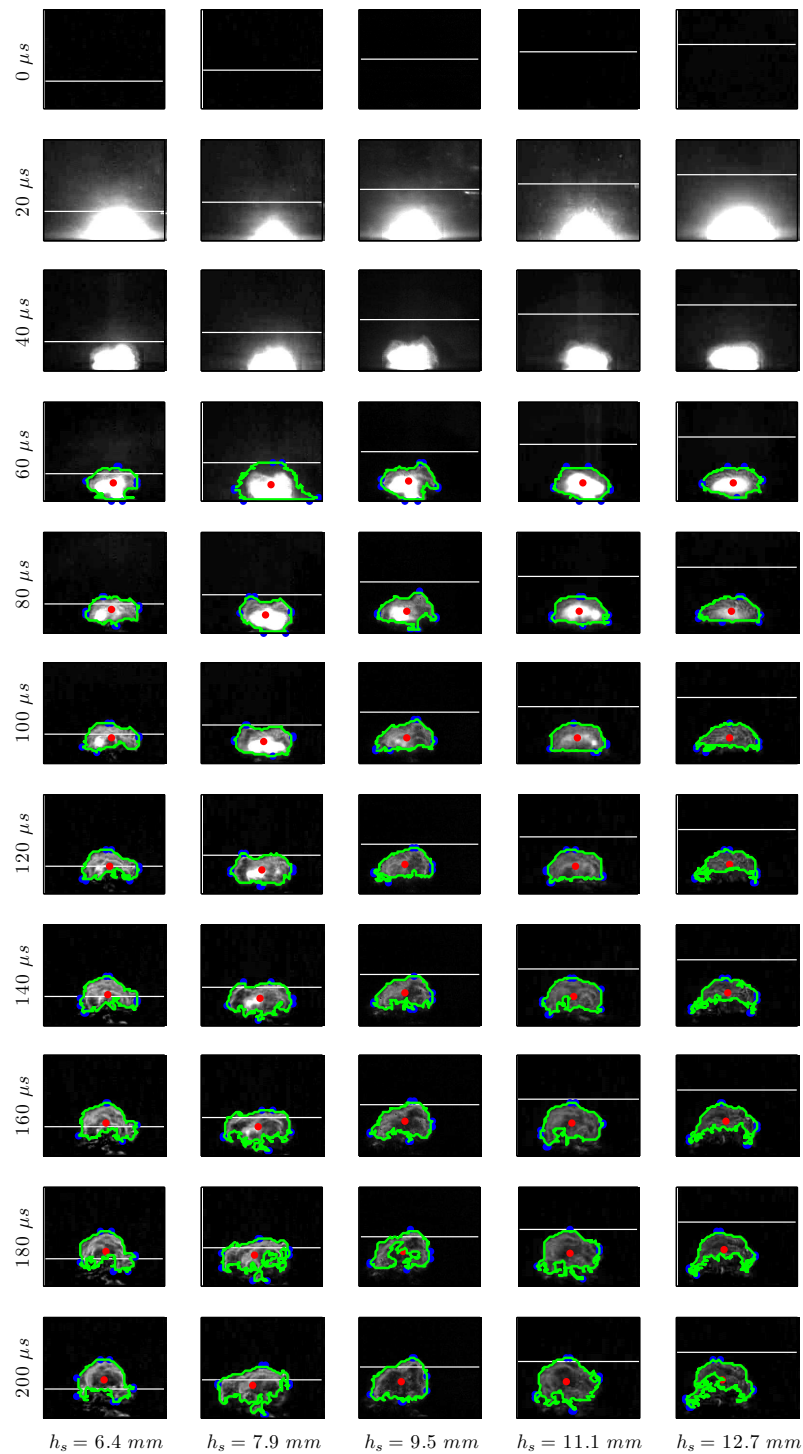
Figure 5.5: *Time progression sequence of five kernels ejected from the igniter. Each kernel was observed in the facility at the indicated splitter height settings. The white lines depict the heights of the splitter plates. The kernels shown with edge tracking lines (green), centroid (red) and the extrema locations (blue). Early times were not tracked because the bright emission obscures the schlieren results.*
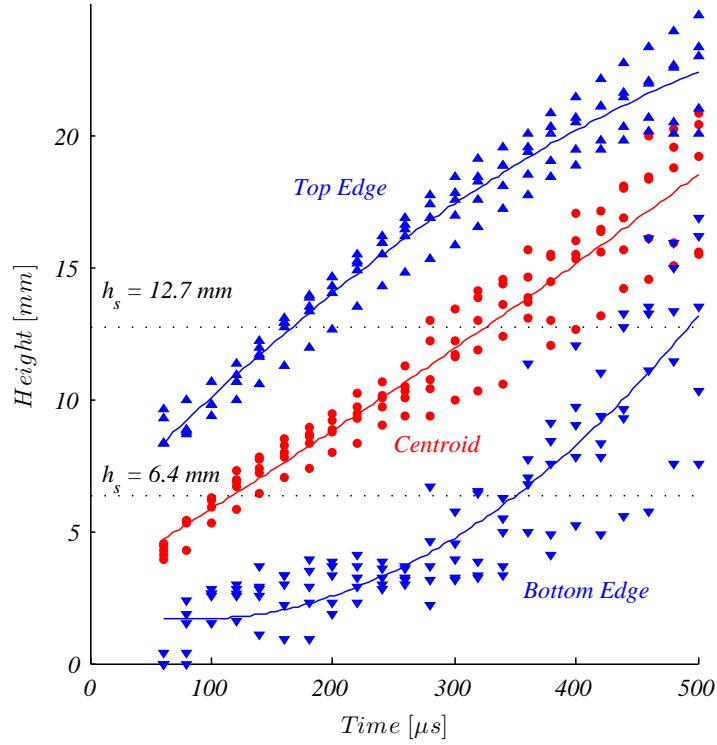
Figure 5.6: *Kernel location heights from wall at different times for five kernel events. Dashed lines depict the extreme heights of the splitter plate.*

Table 5.1: *Transit times of three kernel locations (top, middle, and bottom) **to** the flammable region boundary for different splitter heights as determined from schlieren imaging.*

h_s [mm]	τ_{top} (μs)	τ_{mid} (μs)	τ_{thru} (μs)
6.4	40 ± 10	120 ± 15	350 ± 150
7.9	55 ± 10	175 ± 20	410 ± 75
9.5	85 ± 15	230 ± 30	450 ± 100
11.1	125 ± 15	280 ± 40	475 ± 150
12.7	165 ± 15	335 ± 40	500 ± 200

64

5.1.1.2 Trajectory Variability

Observations of the kernel ejection were performed in the stratified facility with a flammable mixture present in the main flow. High speed schlieren imaging was used to visualize trajectories (x vs. y) in the facility with $\bar{v} = 20 \ m/s$, as seen in Fig. 5.7. The kernel centroid trajectories are plotted for four kernel ejection events, and the ignition success of each kernel is indicated. Ignition success was determined from the output of a photodiode detecting broadband emission from the propagating flame that occurs only during a successful event.

The kernel paths are similar, especially at early times (i.e., for vertical distances less than 25 mm). Since the maximum splitter plate height is 12.7 mm, there is little shot-to-shot variation in the kernel trajectory as it passes through the initial non-flammable layer of the stratified flow. Further downstream, there is some variability in the kernel trajectory, with one trajectory deviating from the other three by as much as 8 mm at 90 mm downstream of the igniter tip. However it is important to note that the variation in kernel trajectory does not correlate to the eventual success of the ignition process. The kernel trajectory should be strongly influenced by the kernel ejection process and the deposited spark energy that induced the kernel ejection. These results suggest that shot-to-shot variations in the energy deposition and the ejection process are not significant and are therefore not a likely source of any significant ignition variability observed in the experiments.

5.1.2 Kernel Entrainment

The high speed schlieren imaging provides the traits of the kernel ejection process. Additionally, the kernel centroid appears to decelerate as it convects away from the igniter. Based on the high speed schlieren imaging, the kernel also resembles a vortex ring, which would facilitate mixing and entrainment with the environment, as discussed in Chapter 2. The kernel volume growth rate was estimated by measur-

65
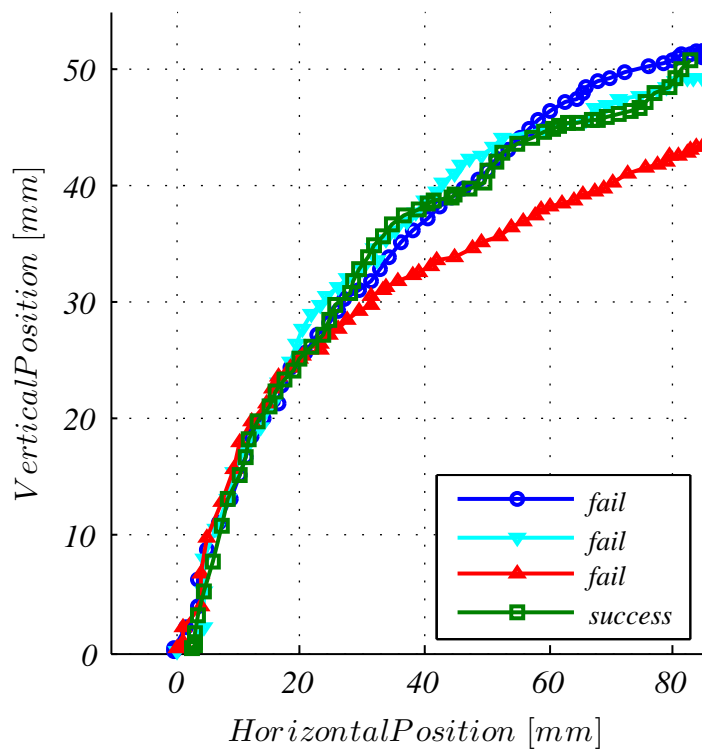
Figure 5.7: *Trajectories of four kernels in a crossflow, highlighting the kernel that results in successful flame propagation, which is not the trajectory outlier.*

ing the area in the schlieren images seen in Fig. 5.1, and assuming symmetry about a vertical axis. The resulting volume approximations are seen in Fig 5.8. A least-squares linear fit was applied to the volume data to deduce a volumetric growth rate of $0.00018 \ m^3/s$. Using an air kernel equilibrium density at $2000 \ K$ of $\rho = 0.176 \ kg/m^3$, the average mass entrainment was estimated to be $\sim 3 \times 10^{-5} \ kg/s$ over a period of $2 \ ms$. This averaged value does not explain the sources of variability for entrainment rate, but as presented in Chapter 2, even subtle differences in the ejection profile can have profound effects on the entrainment characteristics. Even if the spark energy is consistent, the arc location may subtly influence the duration of mass discharge, thus leading to variations in mass entrainment. This is especially important for the early distances from the orifice, when the fluid being entrained is non-flammable.

Features on the kernel were also tracked to monitor the rotation of the vortices and approximate the time required for initial entrainment. Characteristic protrusions on the top surface of the kernel at early times in Fig. 5.1 rotated to the bottom of the kernel after $\sim 100 \ \mu s$. Any unique features originating near the top and to the left of center rotate across the surface toward the bottom in an anti-clockwise fashion; features on the top right of the kernel move clockwise. This motion also supports the vortex ring geometry hypothesis. According to the linear trend in Fig. 5.8, the mass entrainment into the kernel is equivalent to the initial mass, $m_i \approx 3.5 \times 10^{-9} \ kg$, being added to the kernel every $\sim 100 \ \mu s$. If the time scale of the kernel rotation observations is correct, each rotation adds approximately the same mass as was originally in the kernel.

5.2 Ignition Initiation

Beyond the creation and initial development of the spark kernel, the connection to ignition and eventual flame propagation was studied. The common approach of observing the presence of chemiluminescence as an indicator of combustion chemistry
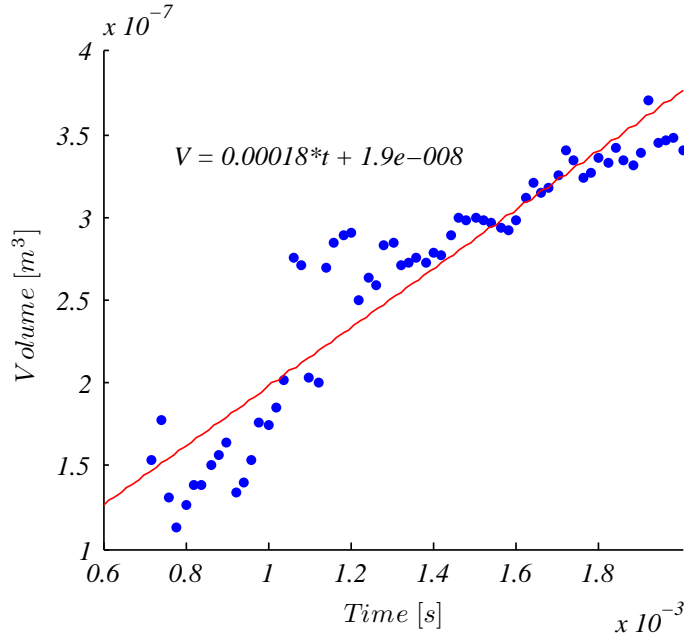
Figure 5.8: *Kernel volume development as calculated by assuming rotational symmetry about the vertical axis. The kernel area was measured using edge tracking on schlieren images. A least squares fit linear trendline was applied to determine the growth rate.*

was used as described in Section 3.2. OH chemiluminescence was measured with the PMT for various data collection lengths and temporal resolutions to test the data acquisition capability of observing successful ignition on the oscilloscope. Successful and unsuccessful ignition kernels were also compared by their schlieren signatures. Lastly, the CH PLIF results are analyzed to provide information on the evolution of the ignition kernel and its conversion into a propagating flame.

5.2.1 OH Chemiluminescence

Experiments were conducted for a test section velocity of $20m/s$ with the splitter plate in the lowest position ($6.35mm$ above the tunnel floor). As previously discussed, this resulted in a kernel top transit time of $\sim 40\mu s$ from when the kernel is produced to when its leading edge *reaches* the flammable main flow. Fig. 5.9 shows the emission signal obtained with the PMT for two main flow conditions: the first with air only (labeled $\phi_{top} = 0$), and for a flammable mixture (labeled $\phi_{top} = 1.3$).
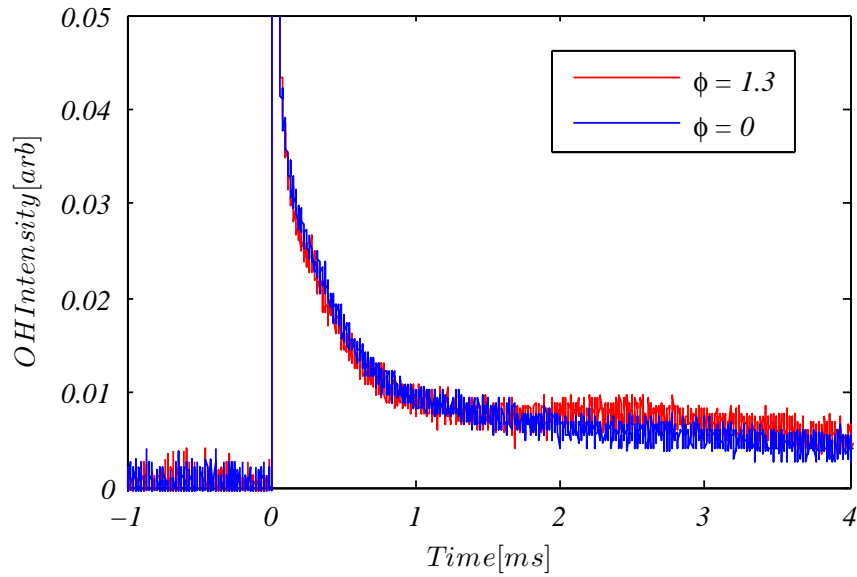
Figure 5.9: *OH* emission within the test section for two cases. The slight rise in the $\phi = 1.3$ signal at 2 ms indicates successful flame emission.*

The rich condition was chosen because initial tests in the facility and visible observations indicated this equivalence ratio produced a reasonable number of successful ignitions. In both cases, there is a sudden rise in the light intensity at t=0, associated with the bright broadband emission of the spark discharge (and not likely due to OH* emission). The signal peaks under 1 μs after breakdown[1] and then rapidly decays, though the kernel continues to emit for at least a few hundred microseconds. The failure of the PMT output to decay to zero for up to $5ms$ in the $\phi = 0$ case may be a limitation of the detection electronics. For the $\phi_{top} = 1.3$ case, the initial signal behavior is similar, However, the important difference is the slight rise in the signal starting at $\sim 1.5\ ms$. This is an indication that a new source of ultraviolet light, i.e., OH chemiluminescence, is now present. At this time, it is likely that a large enough flame reaction zone exists to be detectable by the PMT

---

[1]To emphasize the tail of the decreasing signal, the figure is not scaled to show the peak of the signal.
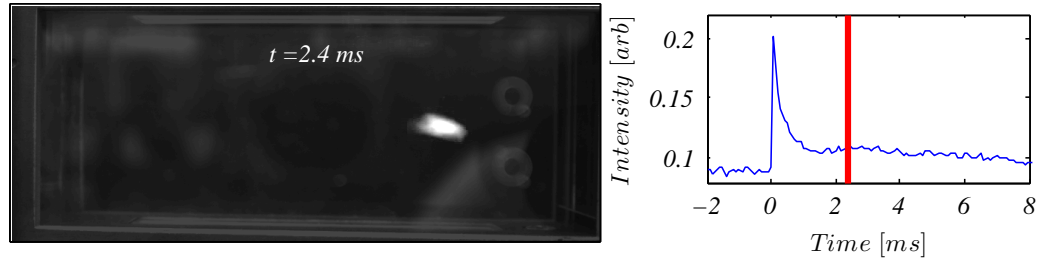
Figure 5.10: *Simultaneously captured, high speed emission image and OH* emission by PMT. The high intensity spikes in OH indicate plasma emission from each spark event, and the contour rises in OH signal that indicate flame chemistry, as seen in the image on the left.*

5.2.2 Emission Imaging

In addition to the PMT measurements of OH chemiluminescence, a high speed camera was used to explore the flame chemiluminescence. As described in Section 3.2, the camera was synchronized to the PMT signal for correlated data acquisition. Fig. 5.10 shows a single high speed camera image with a delay of 2 ms after the spark breakdown and an exposure of 2 ms, along with the corresponding synchronized PMT signal data. The delay for the image corresponds to a time where the PMT signal has begun to increase again. The location, shape and size of the bright region in the image support the interpretation that the increase in emission beyond $1 - 2$ ms is due to emission from the convecting kernel. In addition, the imaging shows that this flame continues to grow with time. Therefore, a spark event that resulted in OH* emission beginning by 2 ms and continuing to grow defines successful ignition for the purposes here, and are in line with the definition from Section 3.1.

Figure 5.11 shows a 2 ms exposure image, triggered to begin 2 ms after the spark discharge, acquired for the following flow conditions: $\bar{v} = 20$ m/s, $T_i = 456$ K, $\phi_{top} = 1$, $\phi_{bottom} = 0$, and $h_s = 6.4$ mm. This streak image shows significant time-integrated emission from a single spark discharge corresponding to a flame kernel that has ignited and grown as it convects downstream from right to left (the growing edges of the emission region are highlighted). Based on the definition of emission existing

70
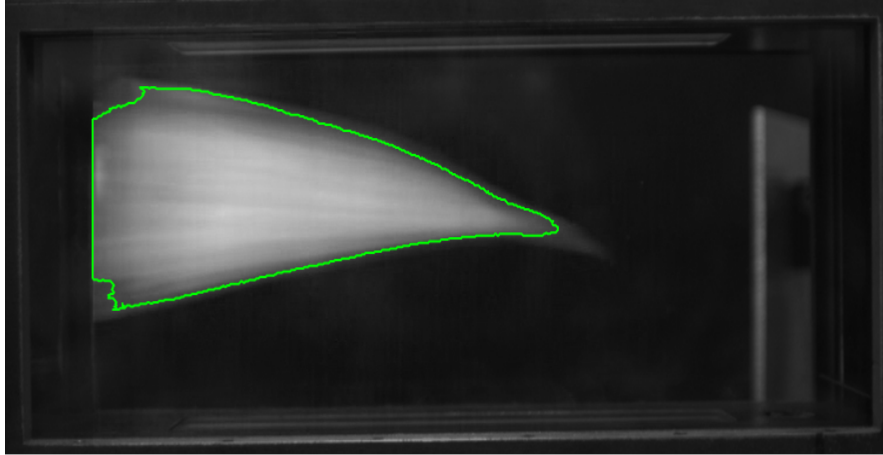
Figure 5.11: *Example long-exposure emission image showing developing flame kernel, edges highlighted in green; failed ignition attempts show no emission (flow is from right to left).*

at $2\ ms$ and continuing to grow, this image represents a spark event that successfully ignited. For a given experimental test, i.e., a series of spark events at the same nominal test conditions, a number of such images are recorded; some show similar levels of emission, and others show no flame emission. The fraction of successful images, see Eq. 5.1 where the number of successful ignitions is N_{succ} and the total number of images is N_{total}, is a measure of the ignition probability for that condition. For the test represented by Figure 5.11 and based on 135 events captured, the probability of successful ignition was determined to be 52%. This proved to be a robust and time efficient method for determining probability. The results presented below are based on this approach.

$$P(ign) = N_{succ}/N_{total} \tag{5.1}$$

5.2.3 Schlieren Comparison

To examine the difference between kernels that lead to successful and unsuccessful ignition events, high speed schlieren images were further analyzed. The flow conditions were set to $T_i = 266\ K$, $\phi_{top} = 1.3$, $h_s = 6.4\ mm$, $\bar{v} = 20\ m/s$, and $\phi_{bottom} = 0$. Four

71

convecting, developing kernels were observed and the images of each were processed using edge tracking to determine the extent of the kernels. The edges of these kernels were superimposed, and the results are presented in Fig 5.12. In each of these sequential images, the grayscale kernel with the edge marked in cyan represents a successful ignition event, while the three other superimposed kernel edges (in different colors) represent events that were unsuccessful in producing a self-sustained flame. While the region imaged at each delay time was identical, the images in this sequence represent a smaller region, and the viewed position was moved to track the convecting kernel and emphasize the differences in development between the successful and unsuccessful kernels.

The compact nature of the cyan kernel at 67 μs is similar to the blue kernel but differs from the red and green traces. This is also noticeable at 333 μs, but the greatest divergence in size and shape of the cyan kernel from the others is between 600 and 867 μs. The cyan kernel continues to grow while the others decrease in size, signifying a meaningful developmental difference at or before this time. This demonstrates that the disparity between successful and unsuccessful kernels is visible in differences in schlieren characteristics as early as 600 μs. Prior to this visible transition, the differences between the kernels is not apparent here.

5.2.4 CH PLIF Results

Further information on where the hot kernel begins to show evidence of flame reactions, and in what part of the kernel this occurs, was obtained from CH PLIF images. Simultaneous schlieren images were acquired to show how the reaction zones correspond to the kernel density gradients as explained in Section 3.2. Several experiments were performed to understand the types of signals recorded under different testing conditions. Prior to gathering and interpreting CH PLIF images, other images were collected in various modes of synchronizing the laser or having a lack of fuel. This

72
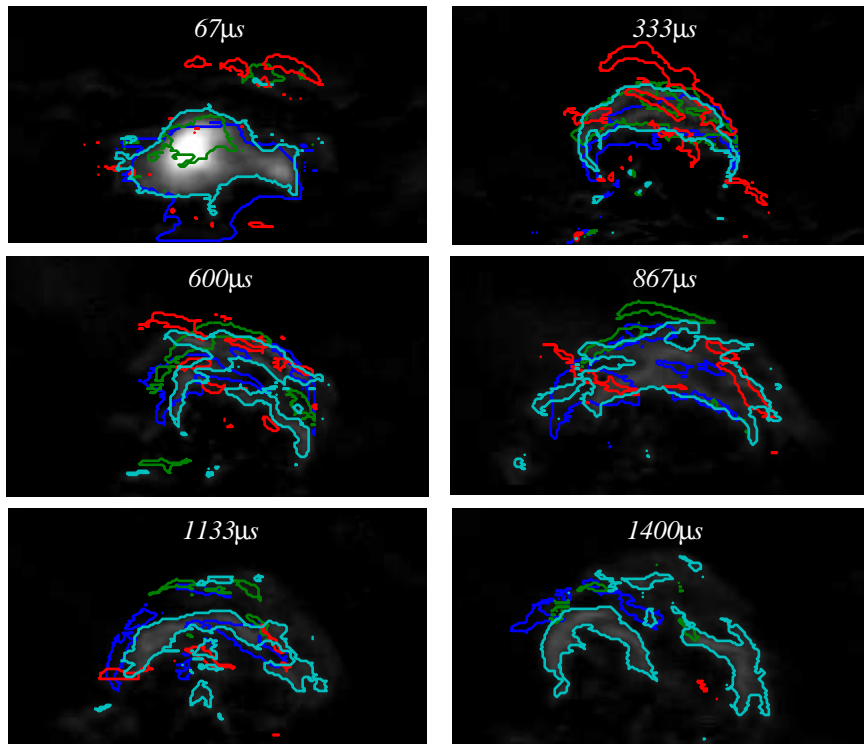
Figure 5.12: *Time progression of four kernel developments. The grayscale background image corresponds to the cyan outline and is a kernel that successfully developed into a flame. The three other outlines are from kernels that were unsuccessful. The images were centered on the kernel and the position moves with respect to the facility.*

aids in determining the characteristics of the PLIF signal and discriminating in from other signals like broadband emission and elastic scattering.

5.2.4.1 Kernel emission

Sets of images at various delay times were acquired without the CH PLIF excitation laser operating in order to determine the background emission recorded by the CH PLIF camera. The images were acquired at Q1 delays of 300, 450 and 600 μs, with and without fuel in the main flow. Where, Q1 is the trigger time for the q-switch, resulting in laser emission. At each condition, thirty images were collected and averaged; the results are shown in Fig. 5.13. As explained in Chapter 3, the PLIF camera images were spatially transformed to register them to the schlieren camera. The registered images' coordinates are in pixels and are zoomed in with respect to the visible area of Fig 3.15. These averaged images give a general sense of where emission occurred, and the signal source. No background subtraction was applied to these images, as the PLIF laser was not in operation. Therefore, these images depict emission, directly imaged or from scattering off the facility walls, as well as the camera background noise.

The early time data (300 μs) show a strong concentrated signal without fuel added (Fig. 5.13a), suggesting this is residual broadband emission from the hot plasma. The average signal count in this region, near pixel location (750,800) is $\sim$ 130. For the fueled case (Fig. 5.13b), the average signal count in the high intensity region drops to $\sim$ 120. This reduction in the emission could be due to enhanced cooling or recombination of the high energy emitting species in the kernel when subjected to the endothermic fuel decomposition reactions. A larger region of signal ($\sim$ 115 counts) seen in both the fuel and unfueled images is likely due to scattering of the kernel emission off the facility windows and walls.

In both the fueled and unfueled cases, the kernel emission signal decreases by the

74

450 μs delay, although it appears the area of counts in the range of 110 is larger for fueled kernels of Fig. 5.13d. By the 600 μs delay, the emission is essentially gone for the unfueled case of Fig. 5.13e, but remains well above the background levels for the fueled result of Fig. 5.13f. The trend of initial strong broadband emission from the hot plasma decaying through the non-flammable fluid followed by an increase of emission due to flame chemiluminescence agrees with the observations in Section 5.2.1.

5.2.4.2 CH radicals

As described in Section 3.2.4, images of the kernel were captured at 300, 450, and 600 μs following the spark discharge. Examples are seen in Fig. 5.14, with simultaneously recorded schlieren images superimposed. Weak signal with the PLIF camera was observed at the 300 μs delay, as seen in Fig 5.14a. The peak signal for the CH PLIF camera is only ~ 130 counts, which is roughly the background signal reported in the previous section. This indicates the lack of CH fluorescence (and therefore, a measurable CH concentration) at that delay.

Broadband emission images were recorded with the schlieren and CH PLIF data. The same broadband emission camera as used in ignition probability data gathering (SA3) integrated signal for $2-4\ ms$ following the discharge, to determine if the flame successfully propagated for the other synchronously captured images of the kernel. The right column shows set diagrams of what was observed from the simultaneous images. The numbers indicate the observed count of kernels that fall within that boundary, e.g., in Fig. 5.14b nine total kernels were observed to propagate to a successful flame. The PI camera captured emission signal for six of these successful kernels, while the other three revealed no emission signal at 300 μs.. Of the 11 failed events, three exhibited some emission signal observed with the PI camera. As noted above, CH PLIF signal was not observed at 300 μs, but this emission signal was

75

(a) 300 μs: no fuel   (b) 300 μs: fuel

(c) 450 μs: no fuel   (d) 450 μs: fuel

(e) 600 μs: no fuel   (f) 600 μs: fuel
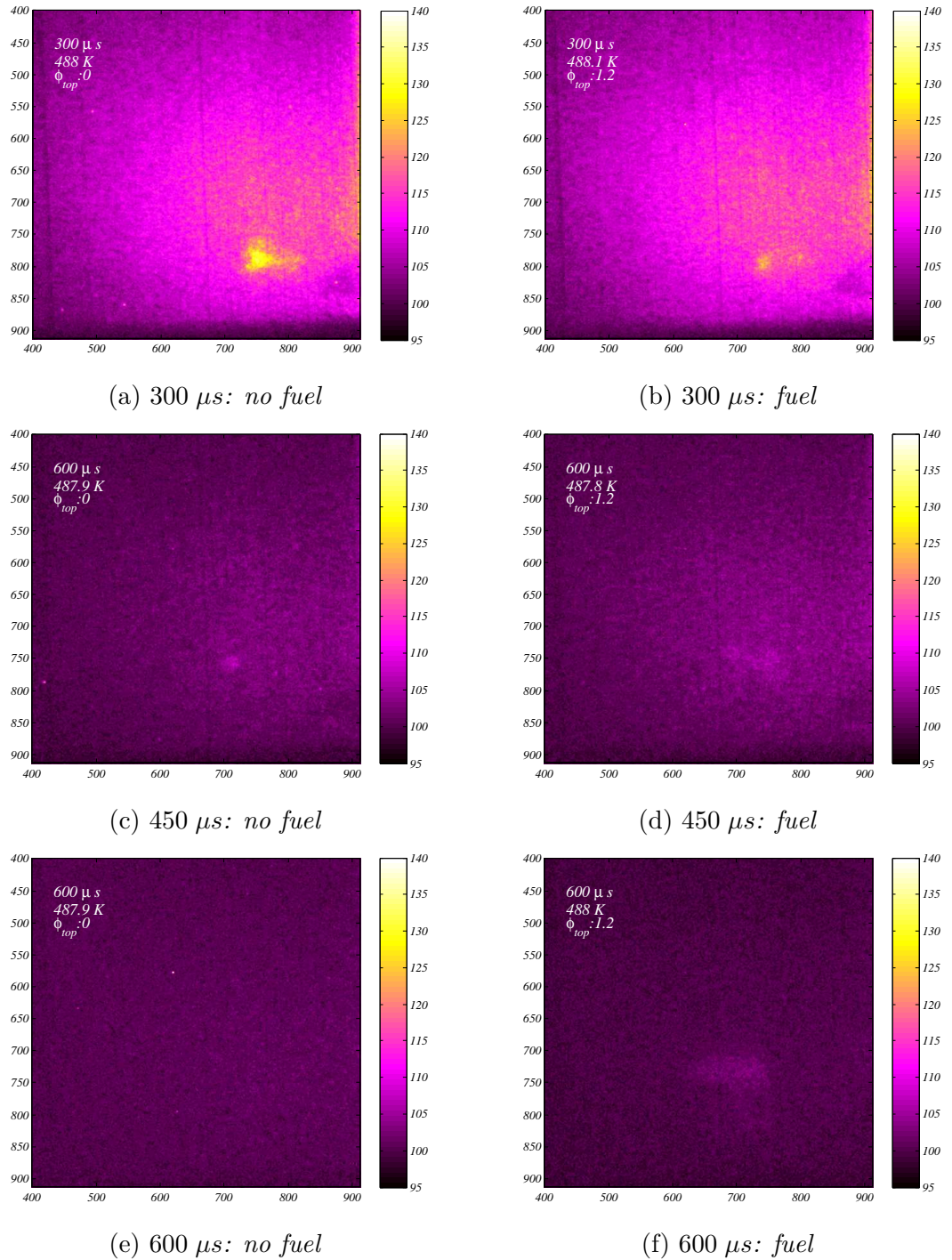
Figure 5.13: *Images recorded at several delay times following the spark discharge. Time sequenced images in the left column have no fuel in the 20 m/s air flow, while images in the right column have fuel added ($\phi_{top} = 1.2$). Neither set had the excitation laser operating.*

(faint green), which correlates well with successful flame propagation; 66% of successful kernels had emission observed at 300 μs. This may suggest that if observable kernel emission lasts longer than 300 μs it is likely to have the thermal energy required to propagate into a self-sustaining flame. At 450 μs, PLIF signal is observed, but it cannot be determined if emission does not appear when PLIF is seen, on account of the PLIF signal having higher signal strength. Therefore, PLIF is plotted as a subset of emission in Fig. 5.14d. One instance of emission with no PLIF signal was observed for a kernel that developed into a successful flame. At 600 μs there are many more images where PLIF signal is detectable. This could be due to higher CH concentrations due to the beginning of a self-sustaining flame, or just the region of flame chemistry has grown, increasing the chances that the ignition region intersects with the laser sheet. More interestingly at this time, all PLIF signals recorded continued to develop into self sustaining flames. One can conclude that by 600 μs if PLIF signal is observed that the flame is likely to become a successful flame. This is not to say that all kernels that develop into successful flames should exhibit CH PLIF signal at this time, as seen in Fig. 5.14f, where 8 of the kernels did not show PLIF signal (or emission). The lack of PLIF signal may be due to the kernel trajectory laying outside of the laser sheet, or CH concentrations being too low to observe.

The CH PLIF signals were prevalent at 600 μs, resulting in several cases where fluorescence signal was observed. Similarities in the PLIF signals can be observed in Fig. 5.15. Both of the composite images correspond to kernels that continued to propagate successfully. These images and result presented in Fig. 5.14e share similar CH PLIF structures. At 600 μs, the high strength signal appears to form thin, ring-like structures that are inside the outer boundaries of the schlieren. The schlieren images define the outer extent of the kernel based on the temperature difference between the hot kernel and the colder cross-flow. Furthermore, the rings match well with the locations in the kernel where vortices appear to exist in the schlieren images,

77
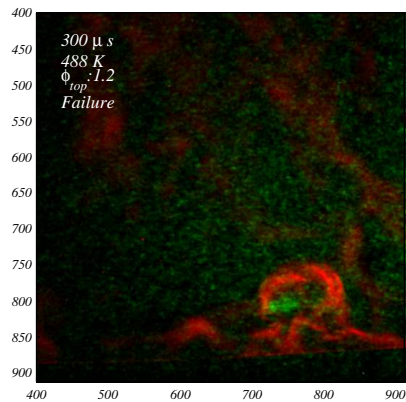
(a) 300 μs emission signal

(b) 300 μs

(c) 450 μs PLIF signal

(d) 450 μs
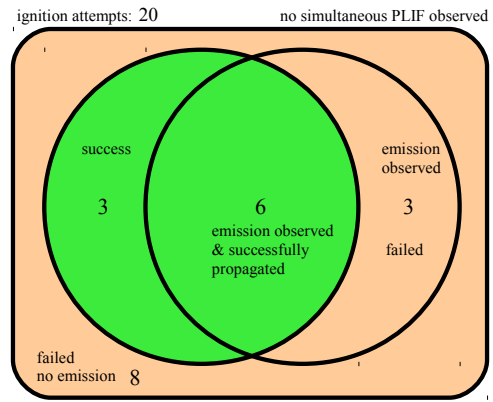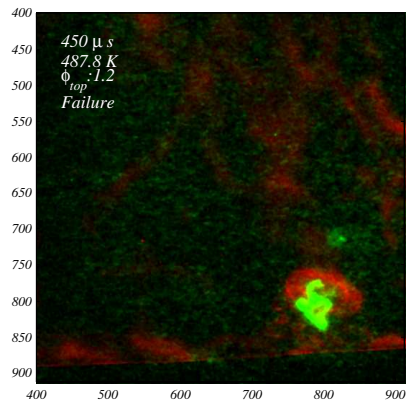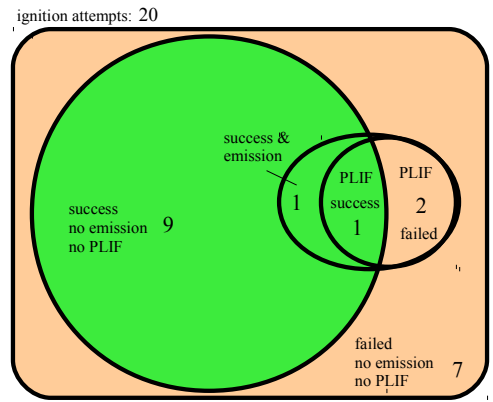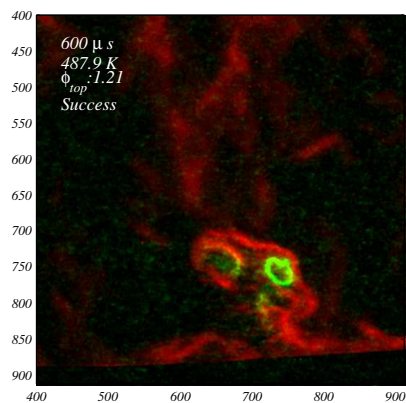
(e) 600 μs PLIF signal
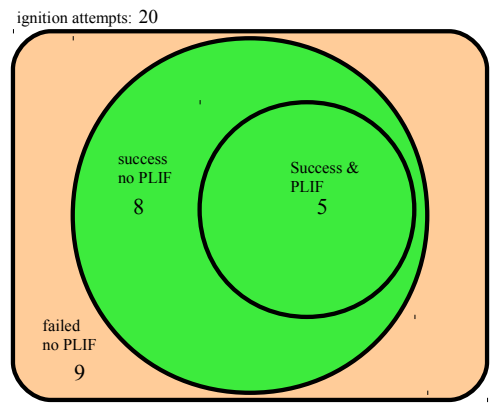
(f) 600 μs

Figure 5.14: *Schlieren images with PLIF signal superimposed at three delay times after the discharge. Grayscale schlieren data is applied to the red layer, and grayscale PLIF applied to the green layer. PLIF signal was not observed simultaneously with schlieren at 300 μs, but emission signal was observed.*
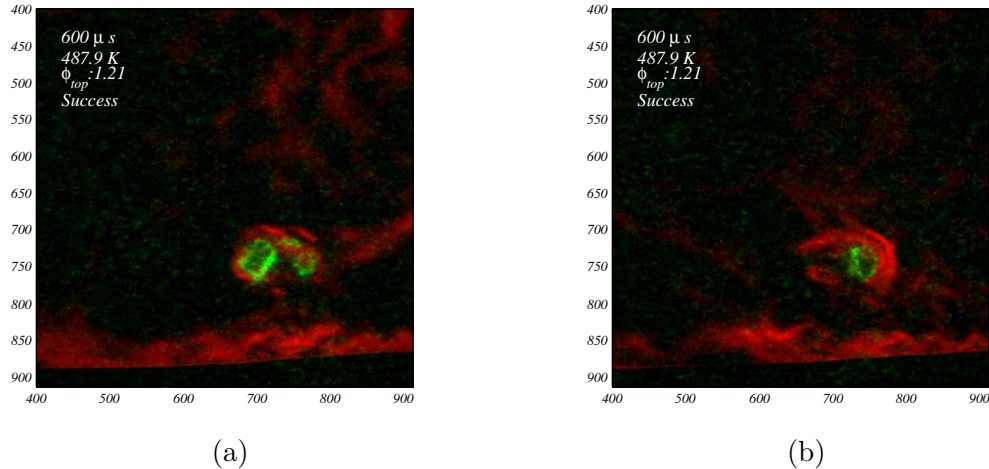
Figure 5.15: *Schlieren images with PLIF signal superimposed at* 600 *μs after the discharge.*

as described in Section 2.1.

Additional CH PLIF images were captured without synchronous schlieren and emission data. The PLIF camera was capable of recording 30 full frame images, but the other cameras could only capture the first 10 spark events. Therefore, more PLIF images were acquired during a test run than the simultaneous schlieren and emission images. This removes the ability to say whether a particular kernel developed into a self-propagating flame, and there is no direct schlieren image for spatial comparison. Still, the additional image provides increase the number of CH PLIF images that can be analyzed.

CH fluorescence signal was observed in this way at 300 μs, as seen in Fig. 5.16a. The geometry of this thin curved reaction zone suggests that fuel conversion is occurring for the reactants being entrained into the kernel. A representative (but non-simultaneous) schlieren image for 300 μs delays is superimposed with this PLIF signal in Fig. 5.16b, as a reference for where this reaction zone could be located with respect to the vortex ring. Additional indications for where the reaction zones occur can be seen in Fig. 5.17, where the maximum value at each pixel location from 60 individual images recorded at each delay time is represented. Again, these images represent the surplus of PLIF images over schlieren images. The compilation of signals for a 300 μs

delay (Fig. 5.17a) depicts the reaction zones being confined to two distinct regions. By 450 μs the reaction zone locations are more distributed, possibly due to the self-induced turbulence of the kernel moving the propagating reaction zone throughout the kernel, or the result of different reaction regions initiating. The variability in the reaction regions continues at 600 μs.

The narrow region (low spatial variability) of where reactions were observed at the early time combined with the low probability that PLIF signal was observed means that CH producing reactions are beginning to have a significant rate on this time scale. Considering that the kernel first interacts with fuel at $\sim 40 - 120$ μs after the discharge, flame chemistry is observed as early as $\sim 180 - 260$ μs following fuel interaction. Time scales for mixing, approximated in Section 5.1.2, also predict $\mathcal{O}(100$ $\mu s)$ for a fractional amount of the kernel mass entrainment. This predicts that ~ 150 μs passes between mixing of flammable fluid with hot kernel matter to when sufficient CH concentrations exist to produce a detectable PLIF signal (with reference to the torch signal). Furthermore, the reactions begin and exist in regions of high mixing, where the kernel entrains the flammable fluid into the vortex ring, as opposed to occurring on the extreme edges of the kernel where initial interaction occurs. This may be due to the high temperatures located in the vortex core, the amount of residence time required after initial fuel encounter to when reactions can be observed, or that strain rates on the outer edges of the kernel extinguish the propagation of reactions. Additional CH PLIF images depicting the regions of flame chemistry can be found in Appendix B.2.

5.3 Ignition Probability

The background literature reviewed in Section 1.2.3 indicates the stochastic nature of the ignition process. Additionally, this work examines the influence of several variables on the probability of successful ignition, leading to many possible combinations

80

(a) *CH PLIF* (b) *Representative schlieren with PLIF*
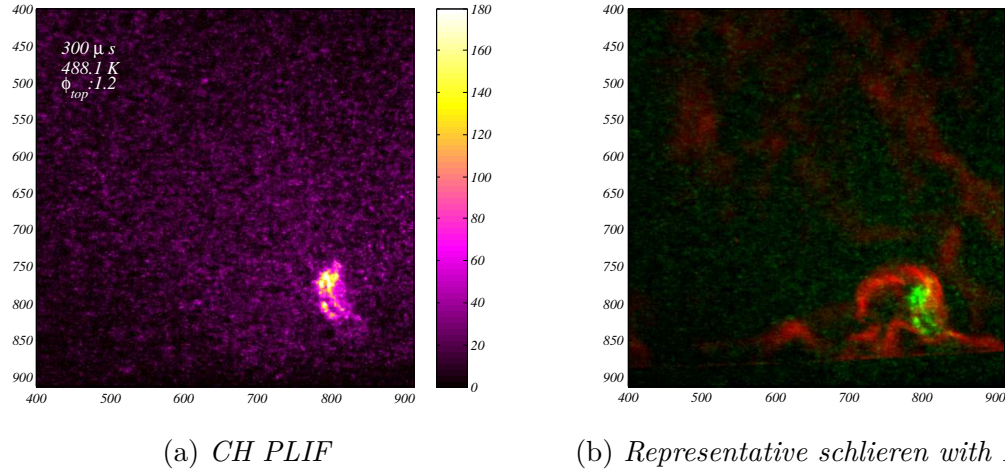
Figure 5.16: *CH PLIF at* 300 *μs after the discharge. The schlieren signal superimposed is not the same kernel, as synchronous schlieren was not recorded, but provides a general reference as representative of the location of the kernel at that time.*

of test points. A design of experiments was used to generate a set of screening test cases, which provided a low order regression of the main effects of each variables on the response: ignition probability. These screening experiments are described in this section along with an exploration into the main effects of the most influential flow variables on ignition probability.

5.3.1 Screening Experiments

The flow variables of interest, and which are controllable in the experiments as laid out in Section 3.1, are inlet temperature (T_i), mass averaged mean velocity ($\bar{v}$), main flow equivalence ratio (ϕ_{top}), kernel flow equivalence ratio (ϕ_{bottom}), and splitter plate height (h_s). It was surmised that the effects of splitter plate and equivalence ratio (based on adiabatic flame temperature trends) on ignition probability would be non-monotonic, and therefore would need *at least* three levels of interrogation. Even with this rough design, $2^3 \times 3^2 = 72$ test conditions would be required for a full factorial investigation. This number of expensive experiments, in terms of time and resources, are not justified by the unrefined trends that result from two and three level variations of continuous parameters, like the ones investigated here. Therefore, a set of screening

81

(a) 300 μs

(b) 450 μs
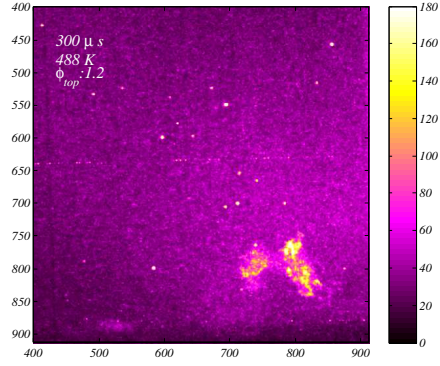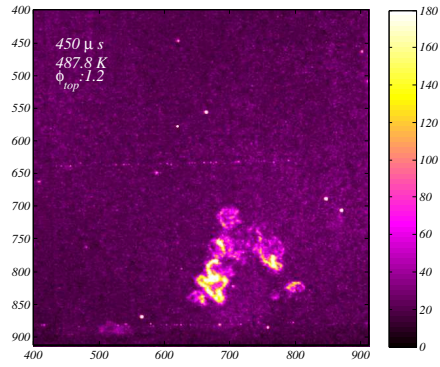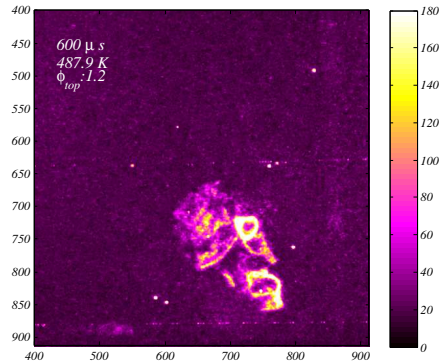
(c) 600 μs

Figure 5.17: *Maximum levels of PLIF signal observed at each location in the viewable region at three delay times after the discharge. Each image represents 60 compiled PLIF recordings.*

82

cases generated with a proven experimental design method was chosen to reduce the number of experiments while providing enough results to decisively remove the less influential parameters.

Considering the goal of the screening experiments is to investigate the low order correlation between the input variables and the ignition probability for further investigation, it is important to perform these experiments at the extrema of each variable range, resulting in an interpolated relation that is more credible. Following this, testing values for $\bar{v}$, T_i, and h_s were chosen based on the operating range allowed in the facility, as outlined in Table 3.1. Equivalence ratios were chosen to reflect the operating range of interest. As previously noted, some variables known to cause a non-linear response, such as ϕ_{top} and h_s, were given three levels, and $\bar{v}$ was given three levels because it was easily adjusted.

A Chakravarti [79] screening design of experiments (DOE) which is valid for mixed level orthogonal design for up to three two-level variables and six three-level variables was generated using JMP software for the three two-level and three three-level design at hand. This resulted in the set of cases that sample the design space using only 18 cases, as opposed to $2^2 \times 3^3 = 108$ cases for the full factorial design. The cases and results for these conditions are presented in Table 5.2.

These data were used to construct a response model using a least squares fit method. The model is of the form of Eq. 5.2 , which was limited to capturing the linear response of the variables and the expected non-monotonic response of the main equivalence ratio. The generated parameter estimates result in a model that captures much of the variability in the data as evidenced by a coefficient of determination (R^2) of 91%. This agreement between the screening results and the generated model can be seen in the actual-by-predicted plot of Fig. 5.18, where complete agreement between the experimental data and the generated model would be seen by data points

83

Table 5.2: *Flow conditions and ignition probabilities for the 18 screening test cases.*

$\bar{v}$ [m/s]	ϕ_{top}	ϕ_{bottom}	T_i [K]	h_s [mm]	P(ign)
20	0.8	0.05	300	6.4	0.7%
10	0.8	0	300	6.4	0.0%
40	1.4	0.05	533	6.4	91.5%
10	1.1	0.05	533	6.4	86.7%
20	1.4	0	533	6.4	88.1%
40	1.1	0	533	6.4	68.9%
30	1.05	0	300	9.5	0.0%
10	1.4	0.05	300	9.5	0.0%
20	1.1	0.05	533	9.5	52.2%
10	1.1	0	533	9.5	30.4%
40	0.8	0.05	533	9.5	21.5%
20	0.8	0	533	9.5	14.4%
40	1.1	0.05	300	12.7	0.0%
20	1.1	0	300	12.7	0.0%
10	1.4	0	533	12.7	0.0%
10	0.8	0.05	533	12.7	4.4%
40	0.8	0	533	12.7	0.0%
20	1.4	0.05	533	12.7	16.3%
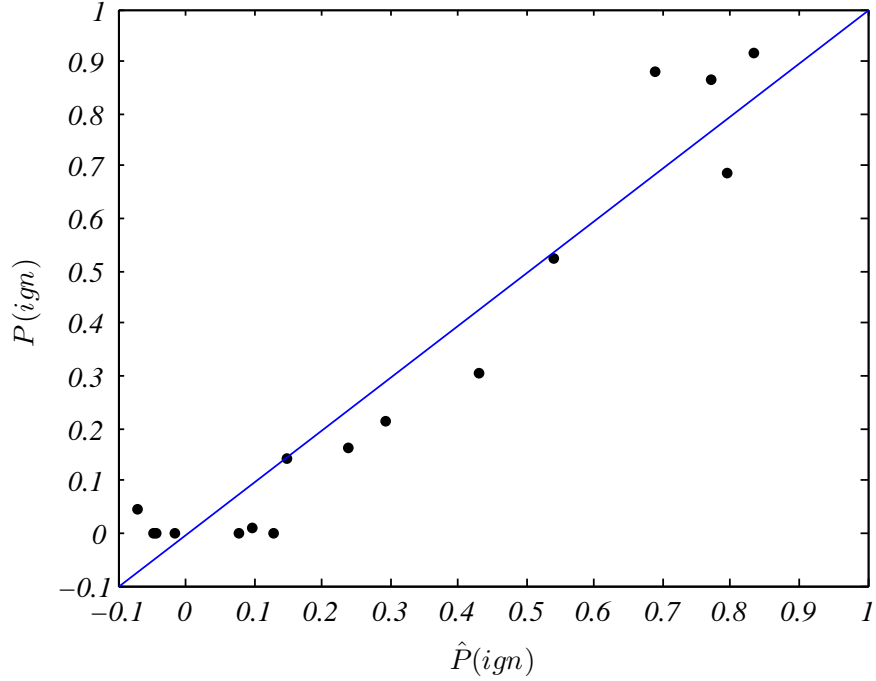
Figure 5.18: *Agreement between the screening data and the generated screening model of the form found in Eq. 5.2.*

falling on the illustrated line with a slope of one.

$$\hat{P}(ign) = a_0 + a_1\, h_s + a_2\, \bar{v} + a_3\, T_i + a_4\, \phi_{top} + a_5\, \phi_{top}^2 + a_6\, \phi_{bottom} + \varepsilon \qquad (5.2)$$

The t-ratio is the test statistic for each parameter of a hypothesis that the parameter estimate is zero. The t-ratio was calculated for each parameter estimate to determine if the correlation to $\hat{P}(ign)$ is significant. Figure 5.19 portrays a tornado plot of the parameters, sorted by the absolute value of their t-ratios with vertical lines for the $\alpha = 0.05$ significance level. This illustrates that the most influential variables in these ignition experiments were splitter height (i.e., kernel transit time), inflow temperature, and the main flow equivalence ratio. For these tests, where cross stream velocity is much less than the kernel ejection velocity, the weak dependence

85
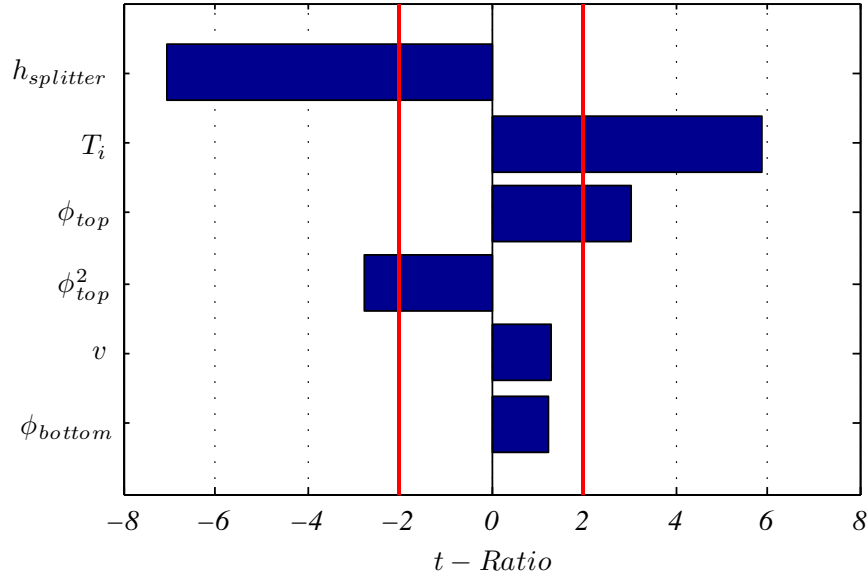
Figure 5.19: *Parameters sorted by t-ratio representing their influence in the model. The vertical lines depict the 0.05 significance level (α).*

on the cross-flow velocity suggests free-stream generated turbulence may not be a significant consideration in the presence of the strong kernel vorticity observed in the schlieren imaging (e.g., Fig. 5.4). The weak dependence on ϕ_{bottom} is an indication that small amounts of fuel, within the range tested, do not provide enough radicals or heat release to substantially raise $P(ign)$.

These findings allowed the following experiments to focus on the effects of temperature, splitter height, and main equivalence ratio on ignition probability. This ultimately reduced the number of experiments when exploring the design space with these continuous variables.

5.3.2 Effect of Equivalence Ratio and Splitter Height

Additional data were taken to observe the main effects of these most influential variables. Transit time, via splitter height, was previously shown to be the most influential parameter and trials were conducted to explore the dependence of the ignition probability. Other parameters were fixed at $\bar{v} = 20 \ m/s$ and $T_i = 300 \ K$. As observed

86

using high speed schlieren in Section 5.1 and presented in Table 5.1, a splitter plate height of 6.4 mm corresponds to a kernel top transit time (τ_{top}) to the flammable region of $\sim 50\ \mu s$ whereas a splitter height of 12.7 mm corresponds to $\sim 260\ \mu s$. The combined effect of splitter plate height and equivalence ratio can be seen in Figure 5.20.

For these cases, successful ignition is not observed at equivalence ratios below $\phi_{top} = 0.9$, and the ignition probability peaks at a slightly fuel rich condition. A similar trend occurs between equivalence ratio and minimum ignition energy, as well as adiabatic flame temperature, for methane flames [4]. It is hypothesized that the peak of ignition probability occurs at a more rich condition due to the initial kernel consisting of only air-derived species. Thus when the kernel fluids mixes with the main zone (flammable) mixture, the resulting mixture is leaner than the main zone fluid.

Additionally, Fig. 5.20 shows that increasing the splitter plate height is detrimental to ignition probability. The ignition probability is essentially zero for a splitter plate height of 12.7 mm and peaks below 1% for $h_s = 9.5\ mm$, well within the experimental noise. As seen previously, the divergence in development between a successful kernel and unsuccessful can be seen around 600 μs, meaning that the conditions that separate the two outcomes has already occurred even before noticeable changes are seen in the schlieren images. This indicates that some change occurs which determines if a kernel will be successfully ignite the flow relatively early ($< 600\ \mu s$), which is supported by the early time scales of the CH PLIF signal visibility.

More notably, for these room temperature conditions, less than 10% of the spark discharges lead to successful kernels even at the optimum equivalence ratio and minimum splitter height of $h_s = 6.4\ mm$. For the most probable case ($\phi = 1.1$, $h_s = 6.4\ mm$), the compounded probability over one second of ignition attempts at 15Hz(a standard discharge repetition rate) is only 60%. In other words, there is a

87
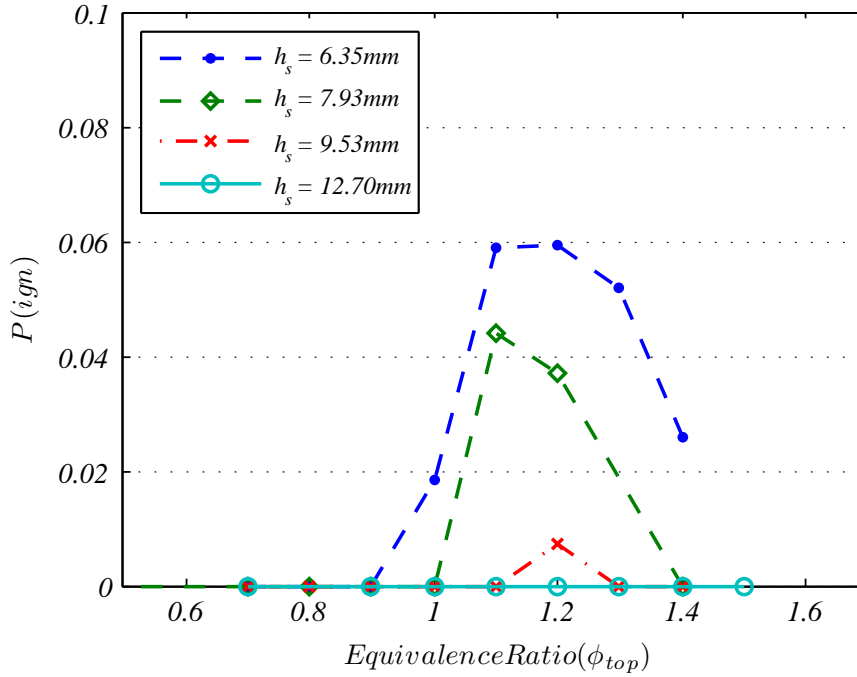
Figure 5.20: *Ignition probabilities at several splitter plate heights for varying equivalence ratios and* 300 *K inflow temperature.*

reasonable probability that ignition would not occur within one second if an engine combustor were operated at these conditions.

5.3.3 Effect of Inflow Temperature and Splitter Height

The main effect of preheating on ignition probability was also investigated since it was shown to be highly influential by the screening experiments. The equivalence ratio that resulted in highest P(ign) during the low temperature tests ($\phi = 1.1$) and the same velocity ($\bar{v} = 20 \ m/s$) were chosen. The results of increasing the temperature can be seen in Fig. 5.21 for the minimum and maximum splitter plate heights. For $h_s = 6.4 \ mm$, the probabilities increased somewhat linearly from 300 K to the highest preheat of 575 K. At $h_s = 12.7 \ mm$, Fig. 5.21 shows that the probability of successful ignition remains nearly zero, even with substantial preheating. As presented in the vortex ring dynamics of Chapter 2, the vortex roll-up causes high initial entrainment near the wall. This fluid does not contribute to heat release and therefore hinders
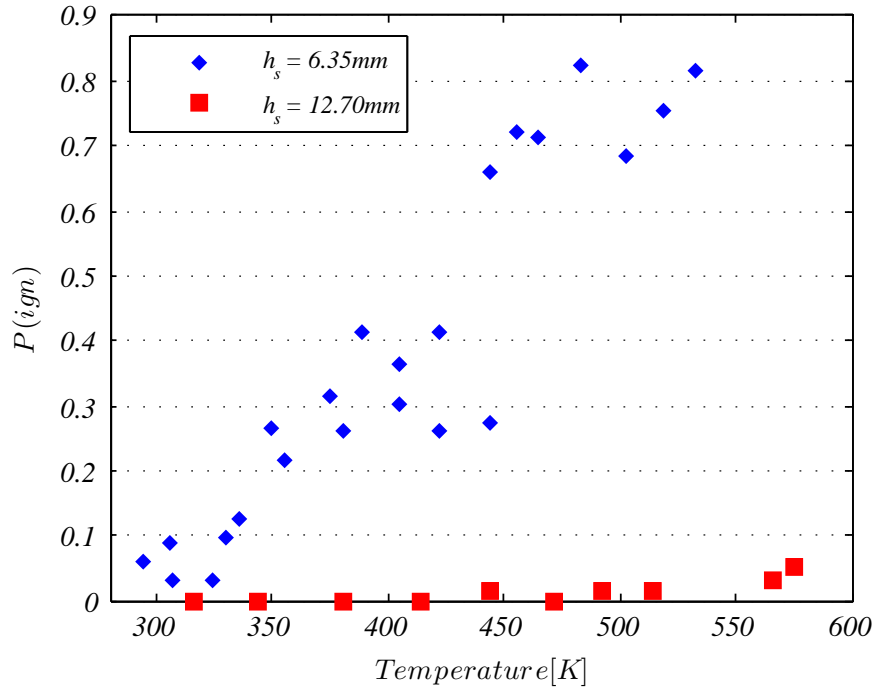
Figure 5.21: *Probability of ignition at increased inlet temperatures, taken at h_s = 6.4 & 12.7 mm.*

ignition.

For the maximum preheating case and the lowest splitter plate height, the combined probability of ignition after $1s$ of attempts at 15 Hz pulsing is ∼100%. At the maximum splitter plate height of 12.7 mm, however, the compounded probability of ignition after 1 s is below 10%. Temperature sensitivity was also investigated for other equivalence ratios resulting in similar trends. Overall, preheating increased the effective ignition limits, i.e., a wider range of equivalence ratios. This observation can be explained in at least two ways. First, the kernel will have a higher temperature, and possibly more radicals, when it enters the main flow, because it was initially diluted with higher temperature air. Second, the flammable mixture is hotter, and therefore more easily ignited.

89
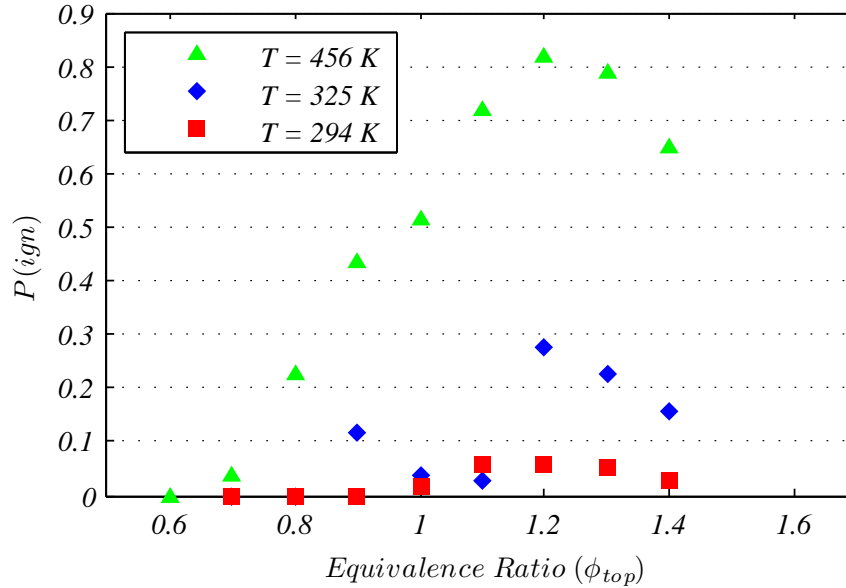
Figure 5.22: *Ignition probability for varying equivalence ratio, taken at several inlet temperatures. For these sets, $\bar{v} = 20 \ m/s$ and $h_s = 6.35 \ mm$.*

5.3.4 Effect of Equivalence Ratio and Preheat

Additionally, several inlet temperatures were chosen and equivalence ratios were varied for v = 20 m/s and $h_s = 6.35mm$; Fig. 5.22 summarizes the results. These findings support those from Fig. 5.21, where increasing the temperature has a linear effect over the range of preheat used. Moreover, it is seen that preheating broadens the range of equivalence ratios where successful ignition is observed. Previously, in the ambient temperature cases of Fig. 5.20, no successful ignition events were seen at any $\phi < 0.9$. Here, at $T_i = 456K$, successful ignition was visually witnessed at $\phi_{top} = 0.6$, and recorded above $\phi_{top} = 0.7$. Furthermore, at $\phi_{top} = 0.9$ the probability of successful ignition has risen to 43%. This finding supports the statement that the higher preheat increases the reactivity of the reactants thus increasing ignition probability.

5.4 Multiple Regression Study

Having determined the key flow variables that influence ignition probability, higher order sampling can capture interactions and highlight additional physical subtleties. This section focuses on the generation and execution of experimental cases aimed at thoroughly sampling the design space without exhaustively performing a full factorial set of experiments. Those parameters previously highlighted in Section 5.3.1 are the influential effects of splitter height, preheating, and the expected trend from the main flow equivalence ratio.

5.4.1 Design of Experiments

Early experiments used to characterize the diagnostic capabilities and gather preliminary data consisted of perturbing one variable at a time to observe the effects. Though simple and easily performed, this method of data collection fails to sample large portions of the design space, missing locations that exhibit the effects of parameter interactions. An experimental design that thoroughly samples the design space while being cost effective was desired. These requirements motivated the use of a Latin hypercube (LHC) design, a type of space filling design [80]. Though other space filling designs fulfill similar requirements, familiarity with LHC also influenced the choice. The LHC is characterized by using the desired number of experimental runs as an input. Time restrictions constrained the number of experiments that could be performed in the flow facility, thus 50 cases were permitted. The LHC design evenly divides the sampling range for each parameter by the number of cases to be performed. The added characteristic of this design is that each design point is equidistant from neighboring design points in the N-dimensional hyperspace, where N is the number of parameters. JMP software was used to generate the design as represented in Table 5.3.

Table 5.3: *Representation of test conditions as prescribed by the latin hypercube experimental design.*

case	ϕ_{top}	T_i [K]	h_s [mm]
1	0.665	377.0	11.53
2	1.073	494.0	9.07
3	1.400	367.2	9.20
4	0.780	303.9	11.40
5	0.878	528.1	8.55
6	1.188	347.7	12.31
7	0.714	474.5	7.78
8	1.367	479.4	8.29
9	1.220	406.2	8.68
10	0.633	372.1	6.35
$\vdots$	$\vdots$	$\vdots$	$\vdots$

Though the prescribed LHC design evenly spaces neighboring design points, it is time consuming to adjust the parameters, some more than others. Splitter height adjustment required complete shutdown of the facility and disassembly of the test section, a time intensive process. Unique splitter levels for all 50 cases was not an option. Additionally, precision control of T_i and ϕ_{top} to the degree specified in Table 5.3 was unrealistic. These points were generated under the assumption of absolute control of these continuously variable parameters. Operability constraints required some amount of discretization of these points, as provided in Table 5.4, based on the cost of adjustment (h_s) and control of inputs (T_i and ϕ_{top}). As a result, the cases performed are found in Table. 5.5, where the parameter levels are binned for ease of experimental operation. These cases have been reordered in the sequence they were performed, where the splitter height was positioned for a set of cases and the inlet temperature was ramped.

Table 5.4: *Selected values for discritizing latin hypercube experimental design in Tab. 5.3.*

ϕ_{top} values	$T_i\ [K]$ values	$h_s\ [mm]$ values
0.6	294	6.4
0.7	316	7.9
0.8	339	9.5
0.9	361	11.1
1	383	12.7
1.1	405	
1.2	427	
1.3	450	
1.4	472	
	494	
	516	
	539	

5.4.2 Higher Order Relations

A similar analysis of model fitting used for screening cases was attempted on the LHC design experimental results. Despite the attempt to perform a sufficient number of experiments to fill the design space, the addition of all previous data points taken is helpful if the two sets were reduced under the same methods and the conditions were recorded accurately. The use of the experimental design to explore the variable space was useful to ensure that all regions of the design space were sampled. The complete set of data are represented in Fig. 5.23 with their relation to ignition probability, with the recent LHC design points highlighted with circles. These scatter plots provide visualization for the main effects of each of the critical variables. This presentation of the data illustrates the boundaries that appear for each variable that suggests physical limitations preventing higher ignition probability. The drastic influence of splitter height is particularly apparent based on the drop-off in $P(ign)$ at splitter plates higher than 6.4 mm with any other combination of temperature and equivalence ratio.

To further illustrate the interactions of these variables on the ignition probability,

93

Table 5.5: *Test conditions performed as prescribed by Tab. 5.3, discretized in accordance with the selected parameter levels in Tab. 5.4, with associated ignition probabilities.*

case	ϕ_{top}	$T_i\,[K]$	$h_s\,[mm]$	$P(ign)$	case	ϕ_{top}	$T_i\,[K]$	$h_s\,[mm]$	$P(ign)$
50	1.1	316	6.4	0.047	21	1	383	9.5	0.289
10	0.6	383	6.4	0.000	48	1.1	450	9.5	0.004
42	1.1	383	6.4	0.292	19	0.9	472	9.5	0.033
33	0.8	427	6.4	0.626	35	0.6	494	9.5	0.026
34	1.4	427	6.4	0.567	2	1.1	494	9.5	0.067
26	0.8	516	6.4	0.304	20	1.3	494	9.5	0.148
23	1.2	516	6.4	0.789	4	0.8	294	11.1	0.000
22	0.9	294	7.9	0.000	40	1.3	294	11.1	0.004
38	0.7	339	7.9	0.000	47	1	316	11.1	0.004
41	1.3	339	7.9	0.015	46	1.3	361	11.1	0.004
31	0.9	361	7.9	0.015	1	0.7	383	11.1	0.000
25	0.6	405	7.9	0.000	49	1.1	405	11.1	0.004
14	1	405	7.9	0.044	29	1.4	427	11.1	0.015
9	1.2	405	7.9	0.144	27	0.7	450	11.1	0.000
37	1.2	450	7.9	0.259	43	1	450	11.1	0.015
7	0.7	472	7.9	0.019	15	0.8	516	11.1	0.004
44	0.9	472	7.9	0.100	45	1	516	11.1	0.085
8	1.4	472	7.9	0.241	11	1.2	539	11.1	0.170
5	0.9	539	7.9	0.293	6	1.2	339	12.7	0.000
24	0.8	316	9.5	0.000	13	0.9	361	12.7	0.007
12	1.3	316	9.5	0.012	18	1.3	405	12.7	0.004
17	0.6	339	9.5	0.000	16	0.8	427	12.7	0.015
28	1.1	339	9.5	0.015	32	1.2	450	12.7	0.004
3	1.4	361	9.5	0.052	36	0.7	494	12.7	0.000
30	0.7	383	9.5	0.311	39	1	494	12.7	0.015
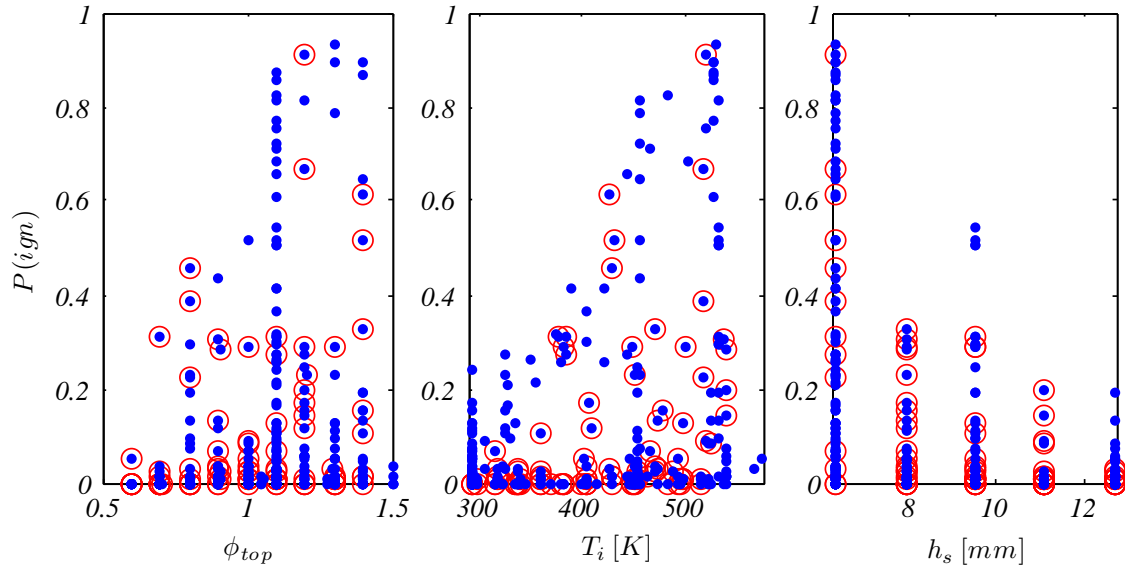
Figure 5.23: *Scatterplots of the most influential parameters with the corresponding ignition probabilities for all gathered data. The circled points are those cases from the LHC design.*

they are combined into the presentation shown in Fig. 5.24. This figure contains all 342 test cases performed with the corresponding ignition probabilities. It is clear from this plot that high ignition probabilities can only be achieved through high preheat temperatures, low splitter heights, and slightly rich equivalence ratios. Large points on the graph represent higher splitter heights and mainly result in low probabilities. To significantly raise the probability for these higher splitter heights, the temperature would need to further increased.

Part of the difficulty in analyzing ignition probabilities is the mathematical constraint on the response variable: $0 \leq P(ign) \leq 1$. This can, and does, result in a large number of cases that exist outside the feasible space of ignition probability for the selected ranges of input parameters. From the data visualizations and the previous screening tests, the splitter height is clearly a contributor to this high quantity of very low probability cases. For this reason, a partition tree was used to determine the most explanatory cutoffs for the data. A split of the data at $h_s = 7.9\ mm$ results in a 22% description of the variability in $P(ign)$. As a result, the group of $h_s \geq 7.94\ mm$ contains 69% of the data points whose mean ignition probability $(\bar{P}(ign))$ is only

95
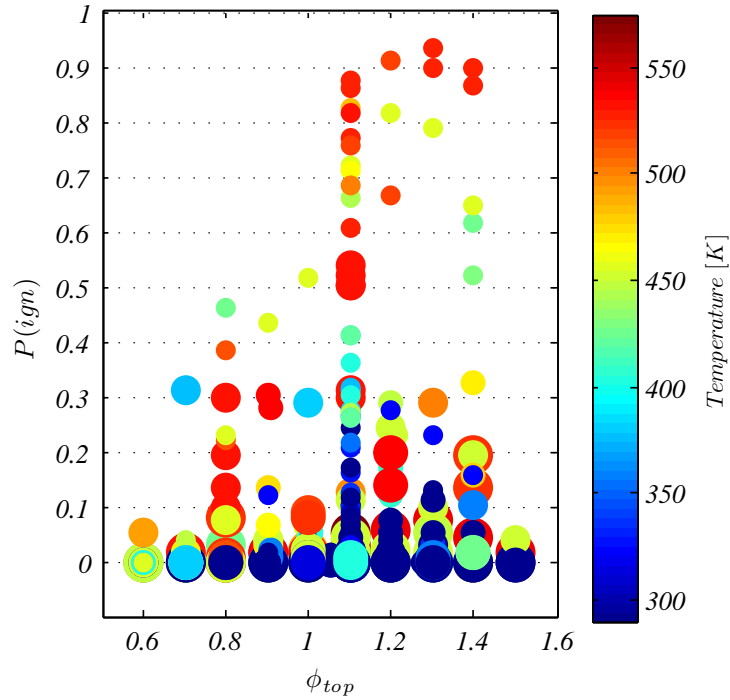
Figure 5.24: *Ignition probabilities from all data gathered. The axes represent ϕ_{top}, while the color represents T_i and the size of the marker corresponds to h_s.*

0.043. The other group with $h_s = 6.4\ mm$ has a significant increase of mean ignition probability to $\bar{P}(ign) = 0.25$. The split of these two groups of data can be seen in Fig. 5.25. Removing a large portion of points that result in zero ignition probability is beneficial to the predictive capability of a fit model, especially if the partition was based on an input variable. Since we are still interested in the effect of splitter height, $h_s = 6.4$ and $7.9\ mm$ are maintained for a linear model fit of that variable. Additionally, since the cases of interest have been opened beyond the LHC experiments, it is worthy to include the effects of $\bar{v}$ and ϕ_{bottom}. Although their influence is expected to be weak, they may have some descriptive power that can assist the model. With these considerations in mind, the restricted data set was used to create an empirical polynomial model using a least squared error method, as performed for the screening cases earlier. The result is Eq. 5.3, which has $R^2 = 95\%$.
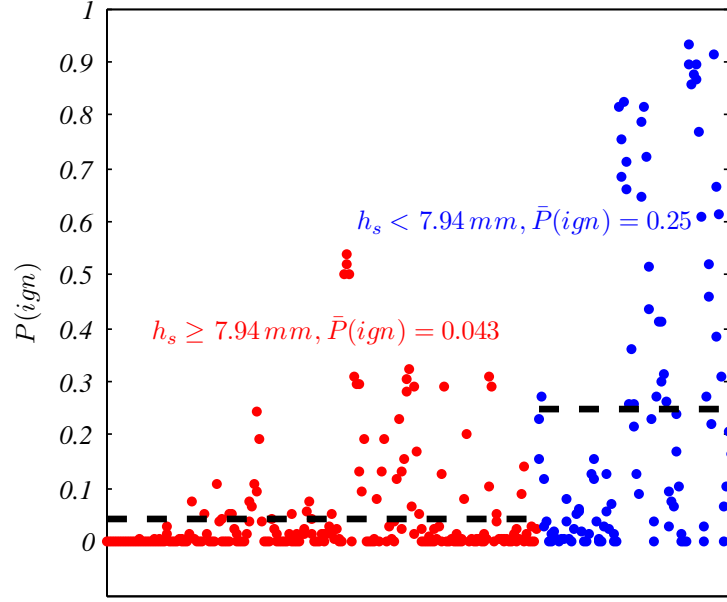
Figure 5.25: *All data points represented by their ignition probabilities. The cases have been split into two groups, one where $h_s \geq 7.94$ mm and a group where $h_s < 7.94$ mm. The mean ignition probabilities for each grouping are represented by the dashed lines.*

$$\hat{p} = 5.99 - 0.027\,T + 5.73 \times 10^{-5}\,T^2 - 6.67 \times 10^{-8}\,T^3$$
$$-13.1\,\phi_{top} + 7.00\,\phi_{top}^2 - 1.66\,\phi_{top}^3 + 1.13\,\phi_{bottom}$$
$$+0.012\,\bar{v} - 0.00061\,\bar{v}^2 + 8.15 \times 10^{-6}\,\bar{v}^3 \qquad (5.3)$$
$$+0.35\,h_s - 0.0021\,Th_s + 0.458\,\phi_{top}h_s + 0.029\,T\phi_{top}$$
$$-0.00626\,T\phi_{top}^2 + 3.7697 \times 10^{-6}\,T^2 h_s - 0.00176\,T\phi_{top}h_s$$

Similar to the screening cases, an actual-by-predicted chart was used to observe the quality of prediction of the model as compared to the actual results for $P(ign)$. As seen in Fig. 5.26 the model results reside close to the line which represents perfect prediction, with some random scatter. Despite the removal of the cases that used higher splitter heights, the results still contain points that result in near zero ignition probability. These cases may represent limits from other input parameters like an

97
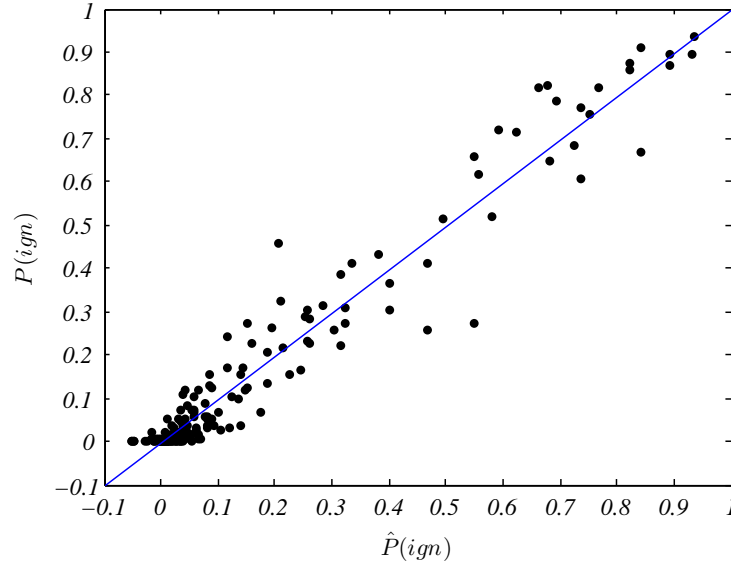
Figure 5.26: *Agreement between the experimental ignition probabilities and the empirical model found in Eq. 5.3. The line represents a perfectly predictive model.*

equivalence ratio near the flammability limit or the effect of low temperatures. To further visualize the trends that are captured by the empirical model, a prediction profile was created for a specific case as seen in Fig 5.27. The profiles show the trend in $\hat{P}(ign)$ if that particular variable is changed while holding others constant. This is further evidence that the influence of $\bar{v}$ and ϕ_{bottom} on $P(ign)$ are less significant than the other input parameters.

It is important to note the interaction terms that appear in the predictive expression. In particular, $T\phi_{top}$ is the most influential term in the calculation of $\hat{P}(ign)$. This term means that as temperature increases, the slope of the influence of equivalence ratio increases, and vice versa. This is the case between all three of the most influential variables, highlighting that the terms are influential on each other's ability to affect $P(ign)$. The physical significance of this is more difficult to pinpoint, but does suggest the connection between these variables. For example, interaction between temperature and main flow equivalence ratio supports the argument that as temperature is increased, the reactivity of the flammable flow is increased, thus increasing the sensitivity to ϕ_{top}. Likewise, if equivalence ratio is decreased closer to

98
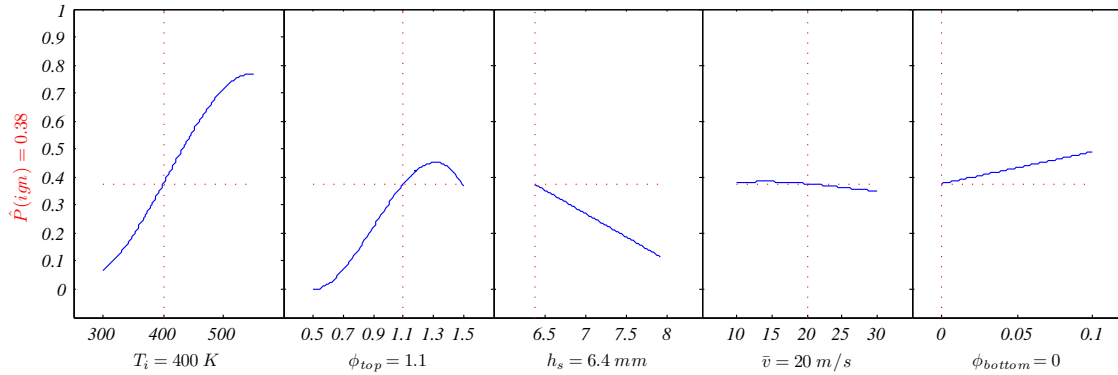
Figure 5.27: *Prediction profile for empirical model (Eq. 5.3). The vertical lines represent the input parameter set points and the horizontal lines show the resulting $\hat{p}(ign)$, which for this case is 0.38. The curves show the trend in $\hat{p}(ign)$ if that particular variable is changed while holding others constant.*

the flammability limit, the ignition probability is going to be low regardless of preheat temperature.

5.5 Summary of Results

The spark kernel initiation and development was studied experimentally to observe the fluid (schlieren) and chemical (OH*, CH PLIF) evolution as it transits, mixes, and either transitions into a successful flame, or fails. These experiments included high speed schlieren imaging, OH chemiluminescence, broadband emission, and CH PLIF. Experiments were also performed to observe the kernel once it reached the flammable flow to quantify ignition success sensitivities to operating conditions. Below is a summary of the significant results of this study.

1. The kernel entrainment (volume growth) scales well with the rotation rate of the features on the vortex ring.

2. Variations in kernel trajectory were not indicative of ignition success or failure for individual spark events.

3. Flame chemistry begins in regions of high mixing rates.

99

4. Fuel decomposition and oxidation chemistry leading to detectable CH concentrations is observed within 200 μs (and possibly earlier) after the kernel encounters fuel

5. Screening experiments reveal that the most influential variables in our study on ignition probability are splitter height, inflow temperature, and equivalence ratio.

6. Increases in splitter height produce an increase in mixing with the non-flammable flow, cooling the kernel and significantly reducing the ignition probability.

7. Preheat of the inflow keeps the kernel hotter by mixing warmer non-flammable flow as well as increases the reactivity of the flammable flow.

8. Transit times determined from schlieren, in conjunction with emission and PLIF results suggest that the spark kernel only has $\mathcal{O}(300\ \mu s)$ to convect to *and mix* with the flammable mixture before the ignition probability is drastically hindered.

CHAPTER 6

NON-PREMIXED IGNITION MODEL AND

PROBABILITY PREDICTION

This chapter presents the work performed using numerical modeling based on methods explained in Chapter 4. First, studies were carried out that explored the evolution of the kernel in the constant pressure reactor model under different conditions. In an effort to extract comparable parameters to experiments, randomness was introduced to the model so ignition probabilities could be calculated. The modeling of ignition probabilities using a vector machine is presented here, as well as the comparison to experimental results.

6.1 Numerical Kernel Evolution

Many properties of the spark kernel are difficult to interrogate experimentally due to physical or equipment limitations. Thus, a reduced order model was used to examine the evolution of kernel temperature and composition and to gain insight into what was occurring in the experiments. The model, detailed in Chapter 4, was developed based on the controlling processes found in the experiments described in Chapter 5. Mixing is an important process central to the development of the model as well as to control of other input parameters that simulated the experimental flow conditions. Initial conditions for the reactor were approximated from spark energy measurements found in Section 3.1, and schlieren observations from Section 5.1 on growth of the kernel.

6.1.1 Non-Flammable Region Sensitivities

Initial model investigations focused on observing the sensitivity of the kernel development in the initial, non-flammable flow to different input parameters. This investigation addresses the importance of each input variable and the level of precision required for the simulations.

6.1.1.1 Mass Entrainment Sensitivity

The mass entrainment rate of surrounding fluid (the environment) into the kernel (reactor) is a key input to the model. The value for this variable was estimated from schlieren measurements as explained in Section 5.1.2. Additionally, the measurements of the kernel growth suggest a non-constant mass growth, implying that the entrainment rate changes. For the sake of simplicity, the entrainment rate in the model was chosen to be constant. Additionally, as discussed in Chapter 2, the entrainment rate near the wall (within a several jet diameters) is different than the far-field rate. Thus, it is important to characterize the sensitivity of the kernel evolution to this parameter and decide if the chosen value provides reasonable results.

To that end, the simulation was carried out for the non-flammable region by using pure air entrainment into the reactor for different entrainment rates. The environmental conditions were set to $T_i = 300 \ K$ and $p = 1 \ atm$. Three entrainment rates were chosen: 3 mg/s; 30 mg/s, which was the value determined from the experiments; and 300 mg/s. The kernel evolution results are presented in Fig. 6.1. The rate of entrainment significantly impacts the degree of evolution that occurs in the kernel. In Fig. 6.1a for the lowest entrainment rate, the temperature decreases gradually and remains above 3000 K after 200 μs of development. On the other hand for the highest entrainment rate, in Fig. 6.1c, the temperature drops sharply to below 1000 K in less than 40 μs. These two temperature histories are not consistent with the experimental results (Section 5.1). Figure 6.1b illustrates a developing kernel

102
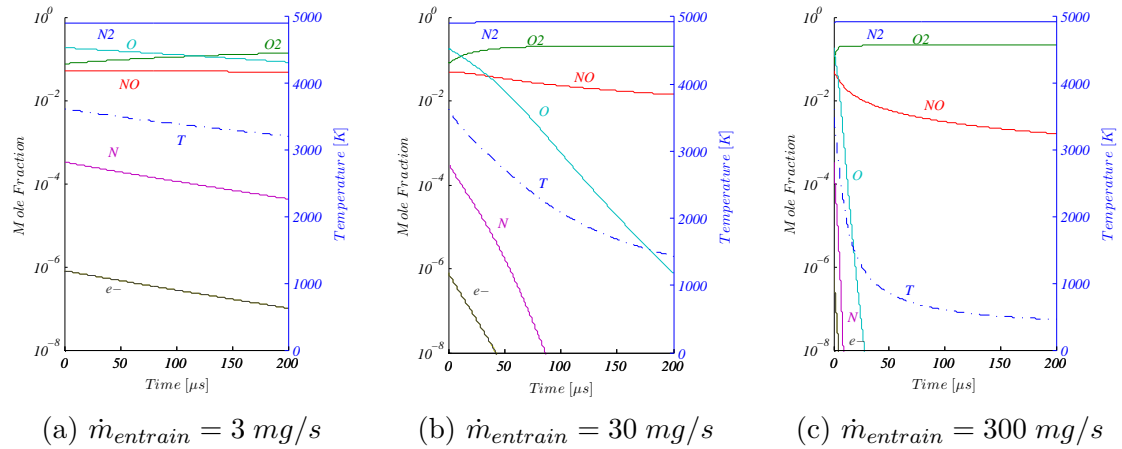
Figure 6.1: *Sensitivity study of the evolution of reactor contents with different mass entrainment rates. Initialization is with equilibrium air at $T_i = 300\ K$ and $p = 1\ atm$.*

that is more consistent with the experimental temperature profile and represents the measured entrainment rates. It is clear that the development of the kernel is sensitive to the choice of entrainment, that an order of magnitude difference results in either no development, or a very quick transition to a cold kernel.

Additional implications resulting from these developmental differences can be seen in the ignition reactions that take place in the reactor after the kernel begins to entrain flammable fluid. This is addressed in a later section discussing ignition results.

6.1.1.2 Equilibrium Investigation

The evolution of the kernel composition and temperature in the non-flammable region is mainly due to mass entrainment. This is because the reactor is assumed to be adiabatic, with constant inflow (entrainment) and no outflow, and at fixed (atmospheric) pressure. This is not to say that inflow is the only determinant of evolution within the kernel. Slow reactions can delay the creation or destruction of certain species. The degree of non-equilibrium was investigated for two initial environment temperatures ($T_i = 300$ and $500\ K$) by simulating the kernel development with $\dot{m}_{entrain} = 30\ mg/s$ air at $p = 1\ atm$, and performing an equilibrium composition calculation at each of

103

the developing temperatures. The resulting comparisons can be seen in Fig 6.2.

In both cases, the composition is close to the equilibrium composition, or the same values (e.g., O). This indicates that the chemical reactions at these times and temperatures are sufficiently fast to adjust to the inflow of entrained air. The largest deviation from equilibrium in both cases is the concentration of the NO radical. It is well known that NO recombination is a slow process [2], and explains the super-equilibrium state in the reactors. The $T_i = 500 \ K$ case in Fig. 6.2b is closer to equilibrium, likely due to the higher temperatures accelerating the chemical rates. The subtle differences between the simulated development and the equilibrium calculation are important to note due to the strong influence that radical species can have on ignition [35]. Because the simulations suggest the kernel is nearly in chemical equilibrium at the time when it reaches the flammable mixture, it is likely that the state of the kernel is simply a function of the amount of mass entrained. Thus in the simulations, the mass entrainment rate and transit time are interchangeable with respect to determining the kernel conditions just before the fuel entrainment begins.

6.1.2 Simulated Ignition Results

The simulations were continued from the previous section that focused on the evolution of the non-flammable kernel. For a given T_i, p_i, $\dot{m}_{entrain}$ and transit time of interest, the conditions from the non-flammable kernel evolution investigation are the "initial" conditions for the reactor when the entrainment of flammable fluid begins.

Initial simulations were performed to observe how the the measured ignition sensitivities were reflected in the numerical results. Three sets of conditions were simulated to study the effects of transit time and increased inflow temperature on ignition at fixed entrainment rates. The input conditions for these cases are presented in Table 6.1. As noted previously, these simulations begin by selecting the appropriate kernel data point from the non-flammable reactor.

104

(a) $T_i = 300\ K$ (b) $T_i = 500\ K$
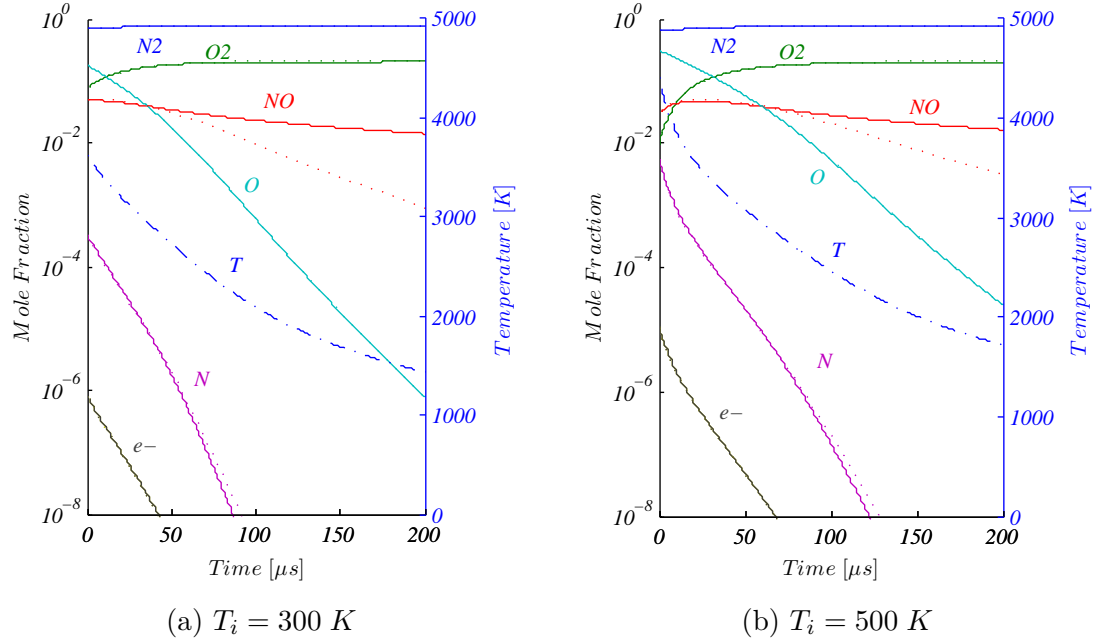
Figure 6.2: *Investigation of plasma kernels non-equilibrium state, for two initial temperatures. Simulation was performed with $\dot{m}_{entrain} = 30\ mg/s$ and $p = 1\ atm$. Equilibrium compositions were calculated for each temperature gathered from the simulation and are plotted as the dotted lines.*

Table 6.1: *Input values for three numerical modeling cases*

case	$\dot{m}_{entrain}\ [mg/s]$	$\tau_{transit}\ [\mu s]$	$T_i\ [K]$	ϕ_{top}
1	30	50	300	0.9
2	30	125	300	0.9
3	30	125	500	0.9

105

In Fig. 6.3 the temperature evolution from the first stage of the reactor is included as dotted lines to indicate the condition of the kernel when it arrives to the flammable flow region. The dashed lines show the kernel temperatures after the entrainment of the flammable mixture has begun, for cases where ignition is successful. The solid line indicates failure to ignite. For case 1, the flammable methane-air mixture was introduced after 50 μs, when the kernel temperature has dropped to $\sim 2740\ K$. As cold reactants are entrained, the temperature continues to drop for a short time, but levels off at $\sim 2100\ K$, indicating ignition has occurred. In case 2, the kernel also transited through air for 125 μs before the entrainment switches to the methane-air mixture. At that time, the kernel temperature was $\sim 1950\ K$. After this point, the temperature continues to decrease as the kernel is diluted, and ignition fails to occur. In contrast, case 3, which has the same 125 μs transit time but a higher entrained mass temperature, leads to successful ignition as the kernel temperature stops dropping. At the time when the kernel begins entraining the flammable mixture for case 3, the kernel is hotter ($\sim 2220\ K$) than in case 2, resulting in higher reaction rates.

The difference between successful and unsuccessful ignition is further illustrated in Fig. 6.4, which shows the evolution of the CH_4 and OH mole fractions in the kernel for the three cases studied. In case 2, where ignition fails to occur, the CH_4 level rapidly rises and approaches the methane mole fraction of the entrained fluid. In contrast for the cases where ignition occurs (1 and 3), the CH_4 is rapidly consumed. The intermediate radical OH provides another indication that cases 1 and 3 would develop a self-sustained flame. The OH mole fraction rises rapidly in both cases, and settles at a high level, $\sim 1\%$. The OH mole fraction also initially rises when fuel is introduced to the kernel for case 2, but is quickly quenched with continued mass entrainment. Initial endothermic fuel–decomposition reactions in conjunction with the cold mass entrainment lower the kernel temperature sufficiently that the OH mole fraction does not achieve the level required to sustain the exothermic flame chemistry.

106

Therefore, successful ignition after the transition to flammable mixture entrainment can be defined by a marked change in the temperature profile, rapid consumption of fuel, and a sustained high level of flame radicals (e.g., OH) or product species (e.g., CO_2).

This phase of brief endothermic reactions occurring shortly after fuel introduction to the kernel agrees with the observations of Fig. 5.13. On average, fueled kernels exhibit lower levels of emission (at the delay of 300 μs) than unfueled kernels, suggesting a lower temperature caused by the addition of fuel.

It is useful to contrast these results with those for a typical autoignition problem, which lacks the continuous entrainment process included here. For a mixture with an equivalence ratio ($\phi = 1$) similar to the flammable flow modeled here, and a pressure and temperature similar to the kernel in case 2 ($p = 1\ atm$ and $T = 2000\ K$), the autoignition delay is $\mathcal{O}\left(1\mu s\right)$ [81]. Thus one might expect the case 2 kernel to rapidly ignite. For case 2, we do initially see a rapid rise in OH when the fuel is introduced, indicating (endothermic) fuel-conversion reactions have begun. However 10 μs later, when the OH mole fraction begins to decrease, the effective equivalence ratio inside the kernel has reached only $\phi \sim 0.13$, and the heat release rate is too low to overcome the temperature drop due to mass entrainment.

6.1.3 Pressure Effects

The reduced order model is capable of handling pressures other than 1 atm as input. The simulation was performed for several input pressures as seen in Fig. 6.5. These trials were conducted with $T_i = 300\ K$, $\phi_{top} = 0.9$, and $\tau_{transit} = 125\ \mu s$, and pressures of 0.5, 1.0, 2.0, and 5.0 atm. Initially, the input pressure values were the only variation to the simulation code, with the resulting temperature histories seen in Fig. 6.5a. It is clear from the profiles that at lower pressures the initial temperatures are much higher. Additionally, the lower pressures have much steeper

107
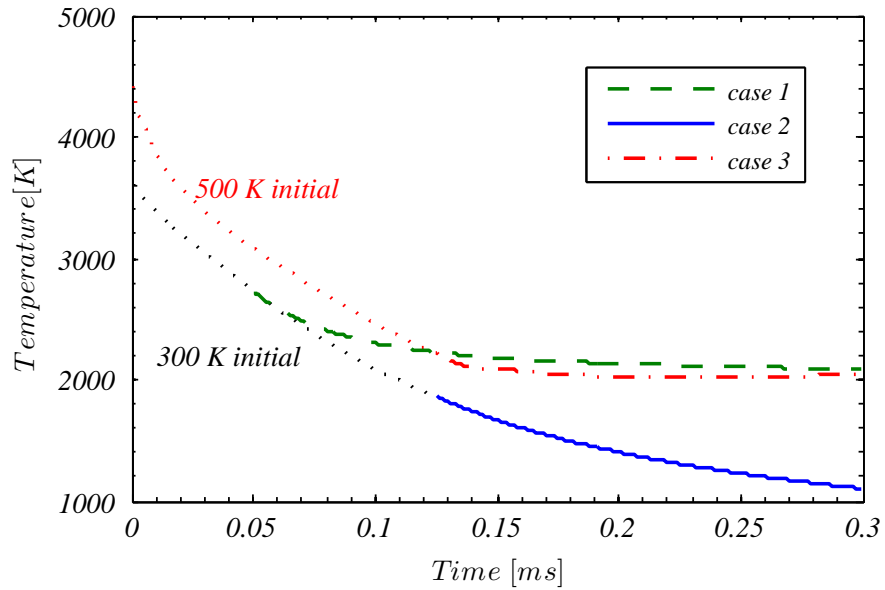
Figure 6.3: *Temperature development of three numerical simulation cases, as listed in Tab. 6.1, depicting the results from both first and second reactors.*
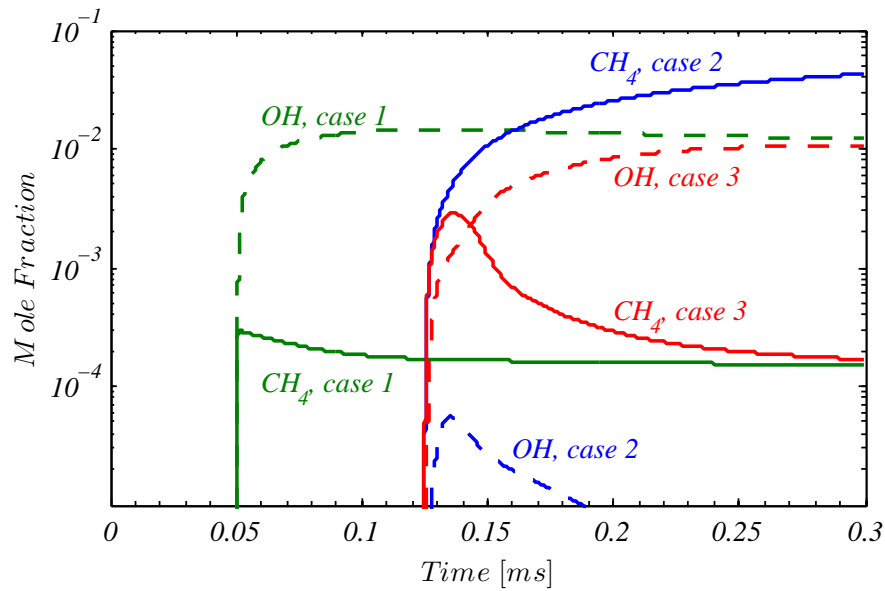
Figure 6.4: *Selected species (CH_4 & OH) time history for three cases listed in Tab. 6.1.*

temperature decays than the higher pressure cases. This combined effect of high initial temperature but quickly dropping temperature cause the 0.5 atm case to fail. This rapid temperature drop-off is due to the same mass entrainment rates being used despite the initial mass of the kernel having decreased in the lower density (low pressure) environment. Interestingly, the 1.0 and 2.0 atm cases have nearly the same temperature when introduced to the flammable mixture. Because the cooling due to entrainment is more rapid in the 1.0 atm case, it fails to ignite. This is further evidence for competing effects existing in the kernel between entrainment cooling and endothermic reactions being balanced by exothermic reactions. In the 2.0 atm case, the kernel was able to remain hot enough until exothermic reactions began due to the weaker entrainment cooling.

These simulations with fixed entrainment rate, independent of density, are unlikely to be realistic. Therefore, further simulations used a mass entrainment rate that was normalized by the ratio of the kernel density at the changed pressure condition to that at $p = 1$ atm conditions. The resulting profiles can be seen in Fig. 6.5b, with the $p = 0.5$ atm case resulting in successful ignition. This success can be explained simply by the increased initial temperature and therefore higher temperature at the time of fuel introduction. This higher initial temperature is the result of the same energy being deposited in the same kernel volume, despite the mass in the igniter cup being reduced for lower pressures (and lower densities). After energy deposition, the kernel has a higher energy density and therefore a higher temperature. Thus the influence of operating pressure on the igniter energy deposition process should be important.

To remove the dependence on the initial energy density, the initial energy density was scaled by the ratio $\rho_i/\rho_{1\,atm}$, where ρ_i is the initial density of the kernel before deposition, and $\rho_{1\,atm}$ is the initial density of the kernel at the 1.0 atm case. As can be seen in Fig. 6.6a, the species traces for the four pressures are essentially the same,

109

(a) *Several pressures* (b) *Entrainment Adjusted*
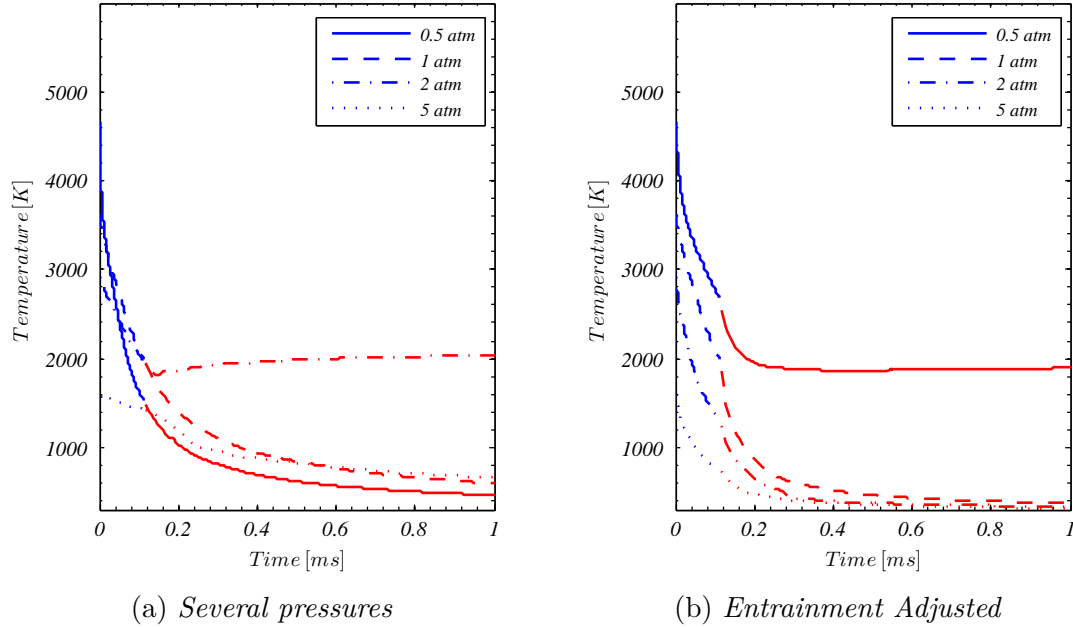
Figure 6.5: *Reduced order model run at several pressure conditions.*

showing little dependence of the kernel's composition due to the pressure influencing reaction rates. This collapse in results can also be seen in Fig. 6.7, specifically the agreement in the initial temperature due to these density related adjustments. Though hardly visible in the temperature profile, indicators of ignition almost taking place for the 5.0 *atm* case are visible in Fig. 6.6b as the concentration of CO increased quickly at the introduction of fuel. These results show that much of the dynamics of the model are dictated by the mixing of the hot kernel with entrained fluid.

6.2 Numerical Probability Prediction

As noted previously, measurements of composition and temperature evolution are difficult to gather experimentally, and consequently are not available for comparison to the model. The main parameter accessible from the experiments is the probability of ignition ($P(ign)$) for a set of given operating conditions. A result of the way ignition success is defined here, a given spark only has two possible outcomes: success or failure. The ignition attempts at an experimental condition are not so distinguished

(a) *Air plasma composition*

(b) *Ignition kernel composition*
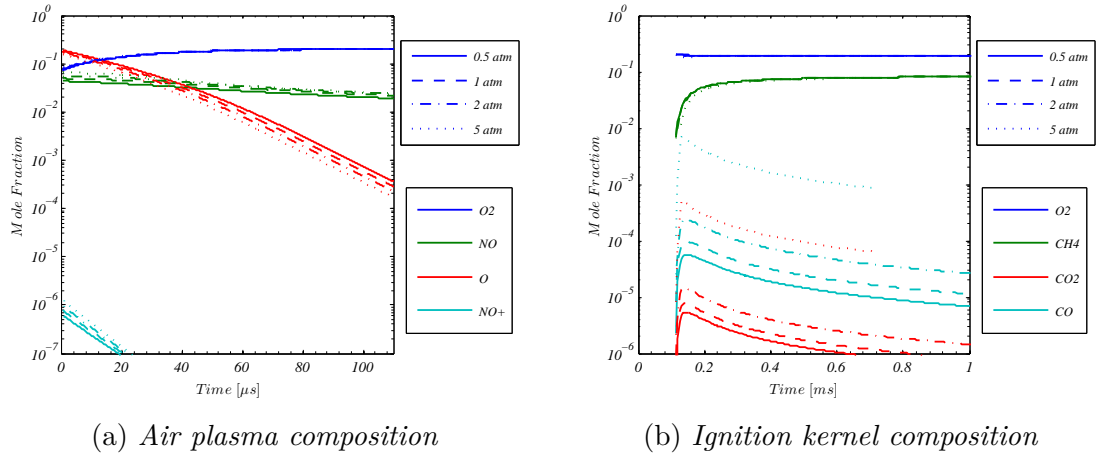
Figure 6.6: *Compositions from reduced order model run at several pressure conditions, with adjusted mass entrainment rates and adjusted post-spark energy density.*
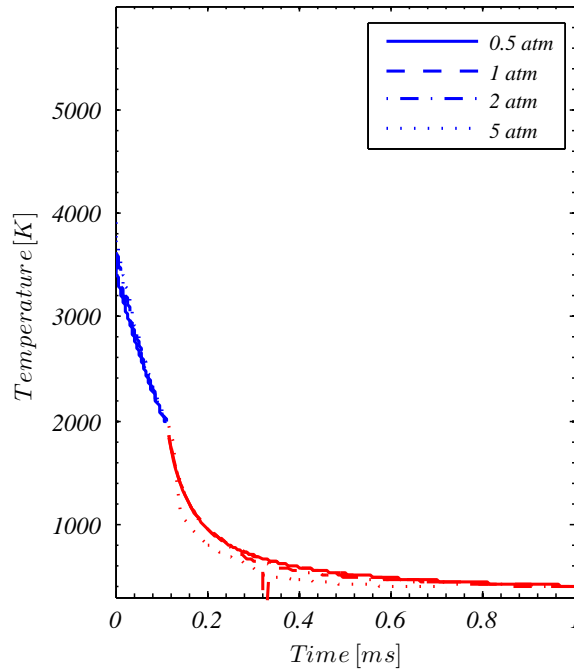
Figure 6.7: *Temperature profiles for simulations at four different pressures. The simulation has been adjusted to compensate for differences in initial density.*

111

from one condition to another. This is due to random fluctuations in the flow and to the spark discharge, causing localized condition changes that the kernel is subjected to. To replicate the experimental response parameter of $P(ign)$ in the simulations, random perturbations must be introduced.

6.2.1 Monte Carlo Trials

The most direct way to incorporate randomness in the evaluation of ignition at a given nominal condition is to generate and simulate many individual cases that have the input variables perturbed from the mean condition according to a distribution. Using the method outlined in Section 4.2.1, variability in specific parameters estimated from experimental data was incorporated in the prediction tool. It was assumed that each of the input parameters were independent, normally distributed, random variables.

Direct simulations of cases derived from a single mean condition, by random perturbation, were performed to calculate a synthesized ignition probability, and then compared to analogous experimental results. For each experimental pair listed in Table 6.2, a matched condition was used for the simulations. Estimations were made to correlate h_s to $\tau_{transit}$, based on data in Table 5.1. The conditions were randomly perturbed to create 500 cases that were run through the simulation. Experiments I and Ia correspond to Simulation I, and, as seen in Table 6.2, the probabilities are low in both the experiments and the simulation. The increase in temperature in condition II resulted in an increase in $P(ign)$ in both experiments and simulation, but not to the same degree. This suggests that the choice in transit time was not representative for $h_s = 6.4~mm$, and a shorter time may be more appropriate. Lastly, condition III had elevated T_i and an increase in h_s, while the choice of $\tau_{transit}$ was kept the same to better match the $P(ign)$ values.

The resulting $P(ign)$ for this case compares well between the experiments and the simulation, suggesting that the appropriate choice for $\tau_{transit}$ in the simulations should

112

Table 6.2: *Comparison between experimental ignition probabilities and that calculated from 500 simulated cases which were perturbed from the mean condition.*

Experiment	T_i [K]	ϕ_{top}	h_s [mm]	$P(ign)$
I	325	1.1	6.4	0.03
Ia	327	1.1	6.4	0.10
II	519	1.2	6.4	0.91
IIa	518	1.2	6.4	0.67
III	539	0.9	7.9	0.28
IIIa	538	0.9	7.9	0.30
Simulation	T_i [K]	ϕ_{top}	$\tau_{transit}$ [μs]	$P(ign)$
I	325 ± 5	1.1 ± 0.1	150 ± 15	0.05
II	519 ± 5	1.2 ± 0.1	150 ± 15	0.35
III	538 ± 5	0.9 ± 0.05	150 ± 15	0.26

be close to τ_{mid} in the simulations. Furthermore, for the $h_s = 6.4 \ mm$ condition, the kernel requires approximately 100 μs from the time it reaches the splitter plate height to mix before flame chemistry begins.

6.2.2 Tailored Support Vector Machine

Simulating hundreds of cases that represent fluctuations about a single nominal design point proved to computationally expensive. The 500 cases evaluated for a single resulting $P(ign)$ value required 8+ hours to complete on a dual core 2.0 GHz personal computer. Support vector machines (SVM) are a trained algorithm that categorizes input cases as described in Ch. 2. The implementation of the SVM in Matlab is explained in Section 4.2.2. The first implementation of the classification scheme is by training with data from a specific section of the design space, with representative experimental data available for comparison. The goal here is to produce a tailored SVM to faithfully predict the trend of varying one input parameter. The experimental cases had fixed parameter values except for one, which was varied to observe the trend. The corresponding training cases also included a small range of values for the other two variables in order to capture the trends due to random fluctuations in those

113

Table 6.3: *Ranges for LHC design of simulation inputs. The outcomes were used as training data in a tailored SVM that predicts $P(ign)$ for varying temperature.*

T_i	$280 - 555 \; K$
$\tau_{transit}$	$60 - 180 \; \mu s$
ϕ	$0.9 - 1.3$

variables.

6.2.2.1 Prediction of Temperature Influence

One of the important parameters that influences ignition probability is the incoming flow temperature. An LHC design of experiments was used to create 500 cases whose parameters fell in the ranges listed in Table 6.3. These cases were simulated in Cantera and 450 of the outcomes were used to train an SVM. The remaining 50 were used to validate the predictive ability of the SVM, which resulted in 100 % agreement. The SVM used a quadratic kernel function to map the training data.

The mean variable conditions of $\phi_{top} = 1.1$, $\tau_{transit} = 135 \; \mu s$, and a range of $T_i = 300 - 600$ were perturbed according to the Monte Carlo scheme with the spread parameters of $\sigma_T = 5 \; K$, $\sigma_\tau = 20 \; \mu s$, and $\sigma_\phi = 0.05$. At each mean condition, 2000 perturbed cases were created and evaluated using the SVM to calculate a $P(ign)$. The experimental data is followed very closely by the simulation prediction, as seen in Fig. 6.8 for the $h_s = 6.4 \; mm$ set of data. The simulation line has been smoothed with a five point moving average to remove some variations that would otherwise disappear if more points were generated in the Monte Carlo distribution. The agreement between the simulation prediction and the experiments is a result of the choices in the mean values for the two "fixed" variables, which have a small amount of variability, and the choice of how much spread to incorporate in the distribution of all parameters.

Though this SVM was specifically trained with data that captured the transit time range for $h_s = 6.4 \; mm$, cases were evaluated for the longer delay times of $\tau_{transit} =$

114

160 & 195 μs, representing the higher splitter heights of h_s = 9.5 & 12.7 mm, respectively. As seen in Fig. 6.8, the simulated prediction line follows the trend in the experimental points for the h_s = 9.5 & 12.7 mm cases. This suggests that the dependence of ignition success on the transit time is linear for the range of values in ϕ_{top} and T_i, and predicted the outcomes well, even though the SVM extrapolated to evaluate the data for longer delays. The trend can be seen in Fig. 6.9 that the boundary is linear and does not shift much for varying ϕ_{top}, meaning that the surface in the variable space is relatively planar.

Because each ignition event is either a success or failure, there is a discrete boundary within the design space separating conditions where events are all successful or all are failures. Using the SVM, an evaluation of points that fill the design space reveals where that boundary is, as illustrated in Fig. 6.9. An example distribution of points is also plotted to show how a given evaluation of randomly perturbed points can fall on both sides of the line, resulting in $P(ign) \neq 0, 1$. The resulting ignition probability is a function of the ratio of the closeness of the mean value to the discrete boundary and the distribution spread of the points. This distribution of points resulting in a $P(ign)$ is the same effect that occurs in experiments as the ignition event should be deterministic for exact inputs, but is affected by random perturbations.. The effect is seen in the slope of the results in Fig. 6.8. This slope is only a function of the spread of the points with respect to the proximity to the boundary. Therefore, an experimental set of $P(ign)$ results, where one variable was swept, contains information about the variability of all the controlling parameters. In Fig. 6.9, even though the group of points is being swept across a range of temperatures, the random variability in $\tau_{transit}$ is primarily responsible for the profile of $P(ign)$.

An effect of this interlinking of the spreads of all parameters is that higher variability may be desirable to improve chances of ignition, though certainly safer if you can ensure the design in a good region. If an experimental design point falls on the
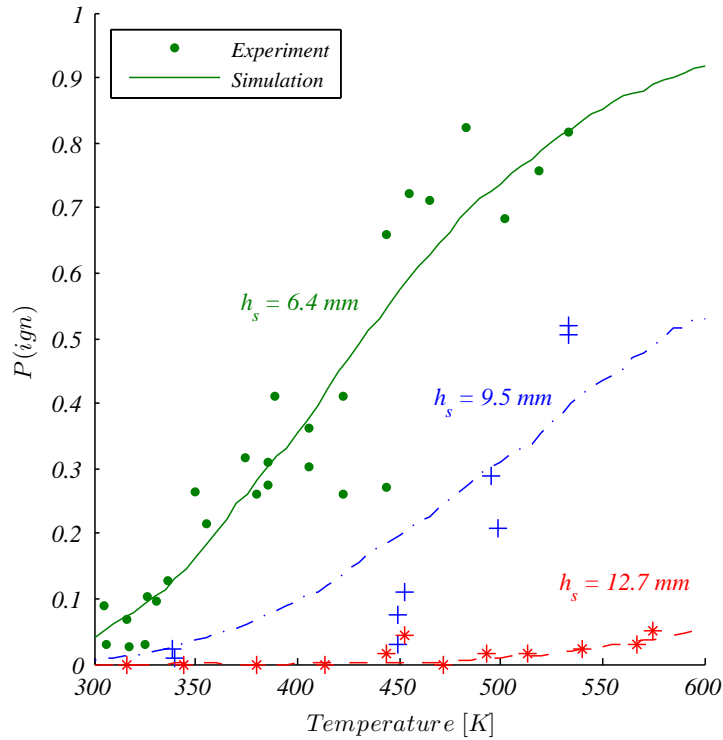
Figure 6.8: *Inflow temperature dependence of experimentally measured and predicted ignition probabilities for specified splitter plate height and fixed equivalence ratio ($\phi_{top} = 1.1$).*

unsuccessful side of the line, and there is no spread in any of the input parameters, $P(ign) = 0$. But, if there is an increase in the variability, the ignition probability will increase. Conversely, if a design point is in the successful regime, it is beneficial to reduce the variability, thus increasing $P(ign)$ closer to 100%.

6.2.2.2 Prediction of Equivalence Ratio Influence

An additional SVM was trained to specifically predict the trends when ϕ_{top} is swept with a small range of T_i and $\tau_{transit}$. The ranges for the 500 training data conditions are found in Table 6.4, which were generated using an LHC design. Again, with this tailored SVM, cases were evaluated that had selected mean conditions that matched the experimental inputs. The simulation prediction line in Fig. 6.10 for $T_i = 455~K$ represents the data well.

Unlike the sweeping temperature SVM, the SVM for predicting results for the

116
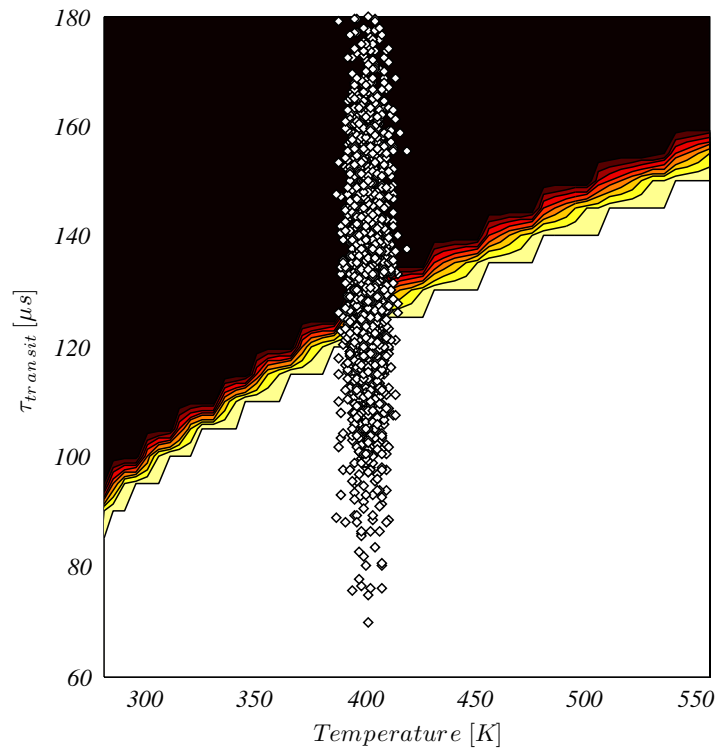
Figure 6.9: *Evaluation of points that fill the design space of the SVM for ramping tempera-ture. The top left region represents all cases that fail, and the bottom right are all successful. The series of lines portray the sensitivity to the adjustment of T_i.*

Table 6.4: *Ranges for LHC design of simulation inputs. The outcomes were used as training data in a tailored SVM that predicts $P(ign)$ for varying equivalence ratio.*

T_i	$435 - 475\ K$
$\tau_{transit}$	$60 - 180\ \mu s$
ϕ	$0.4 - 1.6$

sweeping equivalence ratio is unable to correctly replicate the trend from the experiments for other temperatures ($325\ K$ and $519\ K$). The function that describes the ignition boundary surface of Fig. 6.11 is clearly not planar, specifically not planar for the variation in T_i, which is normal to the page. It is also clear that the function for the surface variation in T_i is not correct outside the range of values used in this SVM training set, and consequently, the SVM is unable to correctly predict $P(ign)$ for other temperatures.

6.2.3 Comprehensive Design Space Predictor

The predictive capabilities of the tailored SVMs seemingly reliable, provided they are trained with data that represent the design space of interest. The simplicity of the individual functions and the capability to reproduce representative $P(ign)$ values and trends is a testament to the accuracy of the Cantera model and the support vector machine having an appropriate kernel function. The capability of the simple quadratic function capturing the ignition boundary suggests that this surface should extend throughout the broader design space, and could be captured by a SVM which is appropriately trained. The benefit of having a single SVM for the entire design space is that individually tailored classifiers do not need to be trained with simulation results that are expensive to run.
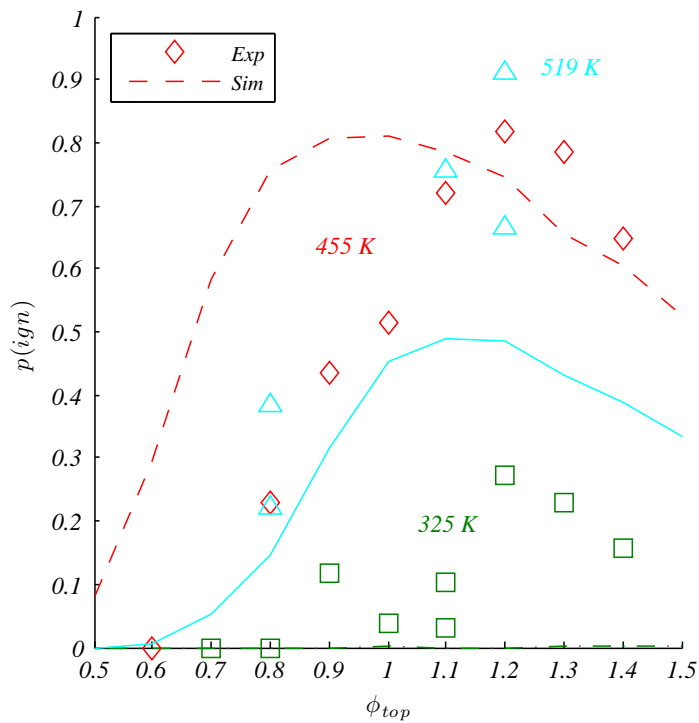
Figure 6.10: *Comparison between predicted and measured ignition probabilities for fixed splitter plate height (6.4 mm) and sweeping ϕ_{top} at several $T_i = 455$ K. Simulation cases were evaluated using the SVM tailored to sweeping equivalence ratio.*
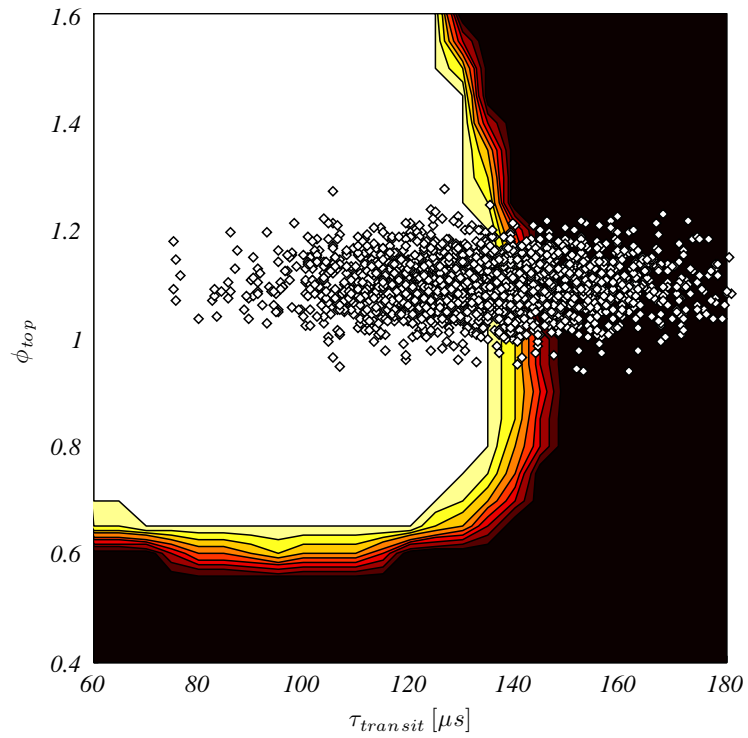
Figure 6.11: *Evaluation of points that fill the design space of the SVM for sweeping equivalence ratio. The top left region (white) represents cases that succeed, and cases in the dark region fail. The contours show the variability in the boundary location due to temperature, with increasing temperature causing the line to encompass more area.*

Table 6.5: *Ranges for reactor model input variables, the outcomes of which were used to inform the comprehensive SVM.*

T_i	$280 - 555\ K$
$\tau_{transit}$	$60 - 260\ \mu s$
ϕ	$0.4 - 1.6$

6.2.3.1 Predictive Convergence

One thousand simulations were performed in CANTERA, with ranges for inputs specified by Table 6.5, which encompass all of the corresponding experimental ranges. The inputs and outcomes of 900 cases were used to train the SVM, which then predicted the remaining 100 cases as verification, with 96% accuracy. The thousand cases were determined to be sufficient by checking the convergence of the predictive trend with classifiers that were trained with less simulated data points. As seen in Fig. 6.12, the predictions by the SVMs that were trained with 500 and 1000 cases match each other closely and also represent the experimental data well. This quantity of points is sufficient for the domain specified in Table 6.5 because the resulting density of points provides enough support vectors to accurately define the correct ignition boundary surface.

6.2.3.2 Comparison of support vector machines

The comprehensive SVM was used to evaluate the same sets of data that was evaluated by the tailored SVM for ramping temperature. The comparison between the evaluations of these sets of design points can be seen in Fig. 6.13. Both evaluation schemes follow the trends in the data, and compare well with each other. This suggest that the increase in size of the design space and the points that train the SVM did not affect the function that represents the ignition boundary in the T_i dimension. As suggested earlier, the ability of the tailored SVM to predict the profiles at other

121
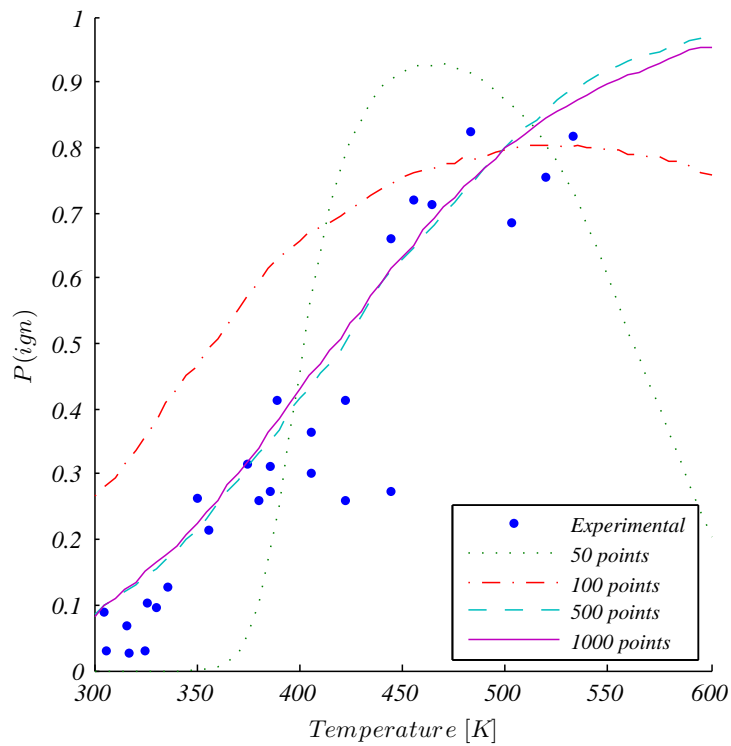
Figure 6.12: *Convergence of prediction capability for the SVM when informed by an increasing number of training cases. The predictions by the SVMs that were trained with 500 and 1000 cases match each other well and also follow the corresponding experimental data.*

122

(a) *Tailored to $\tau_{transit} = 135 \ \mu s$*   (b) *Comprehensive*
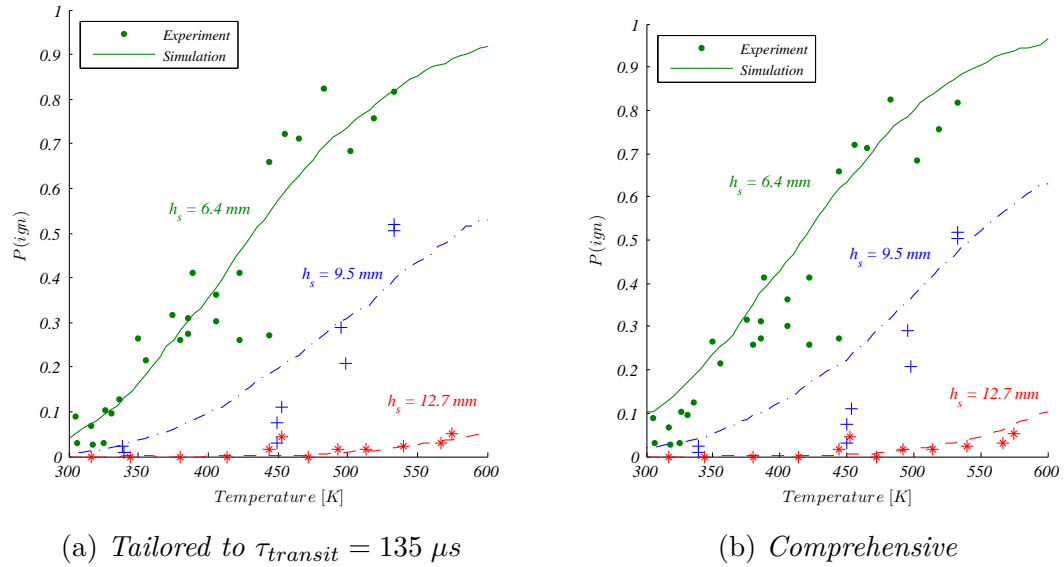
Figure 6.13: *Comparison of predictive capability of a SVM which was trained by cases that fall within a narrow range of $\tau_{transit}$ and ϕ_{top} values, and a SVM which was trained with cases simulated from a broader design space.*

heights meant that the surface was planar and extrapolated well. It is not surprising that the comprehensive SVM, which is informed by points at a wider range of $\tau_{transit}$ resulted in a good fit to all the data. The match between the two prediction models confirms that the ignition boundary surface is planar for T_i and $\tau_{transit}$ for the narrow range of ϕ_{top}.

Conversely, the ability for the comprehensive SVM exceeds that of the tailored SVM for sweeping equivalence ratio, as seen in Fig. 6.14. Though the predictions for the $T_i = 455 \ K$ cases are similar in trend, the tailored SVM does not follow experimental trends for the other temperatures. The small range in temperature of the cases for the tailored SVM did not provide enough information for the surface to have the appropriate shape in that dimension, and the trained surface did not extrapolate correctly. The predictive ability is redeemed when the training data are from a broader range of input variables, which can be seen in Fig. 6.14b. The comprehensive SVM was able to predict the trend of increasing $P(ign)$ for increasing temperatures.
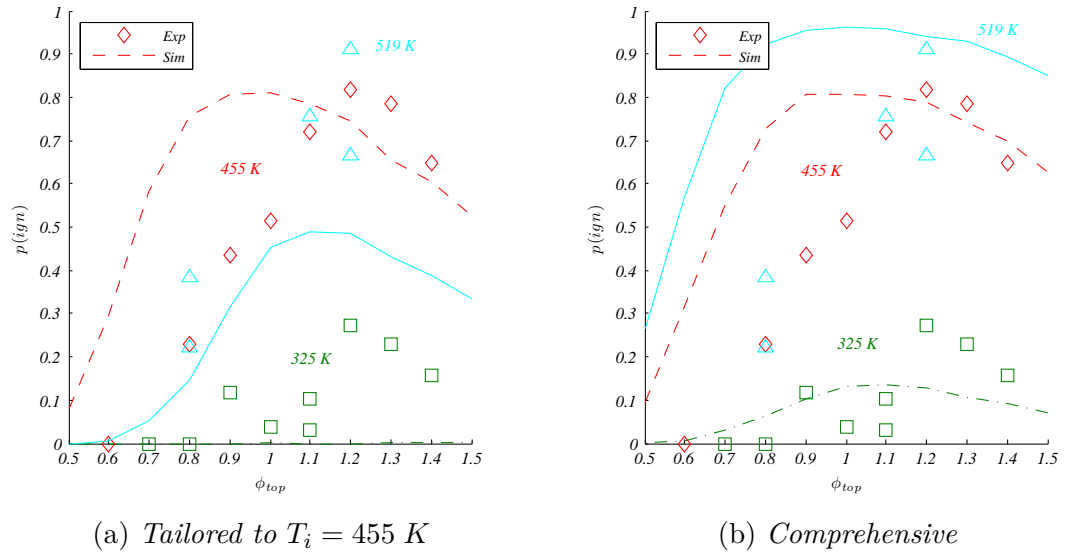
Figure 6.14: *Comparison of predictive capability of a SVM which was trained by cases that fall within a narrow range of T_i and ϕ_{top} values, and a SVM which was trained with cases simulated from a broader design space.*

6.2.3.3 Ignition Boundary Surface

The ability of the comprehensive SVM to match the experimental results for $P(ign)$ indicate that the physical ignition boundary surface is represented in the classifier. A three dimensional grid of points in T_i, $\tau_{transit}$ and ϕ_{top} design space spanning the experimental ranges, was evaluated using the comprehensive SVM. The surface that stretches between the regions of points that succeed and those that fail is the ignition boundary, and is depicted in Fig. 6.15. A single nominal condition with the associated distribution of variables is also represented, and spans the surface. The points that exist on the left side of the surface succeed, and those on the right fail. Though this surface is specific to the results of the Cantera model, it predicts the experimental results well with the estimated values of parameter variability. The characterization of this surface can serve as a powerful tool in conjunction with estimates of the variabilities of the controlling parameters. Given nominal conditions, an accurate estimate of the ignition probability can be made with these simple tools.

124
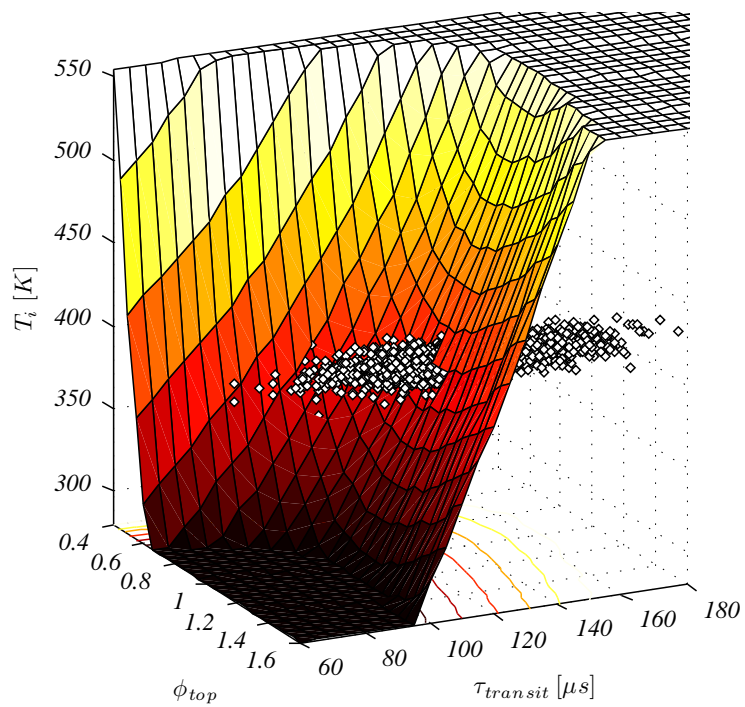
Figure 6.15: *Evaluation of the points that fill the design space by using the comprehensive SVM. The region on the left side of the boundary represents design space where ignition is successful, and failures occur to the right of the surface. A distribution of points is depicted, showing the chosen parameter variability and the relative sensitivities in the boundary.*
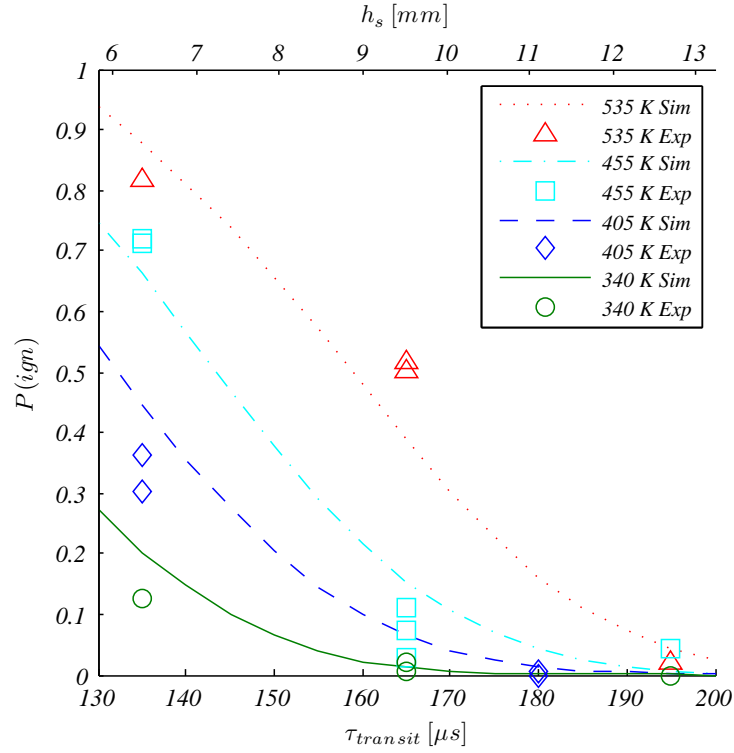
Figure 6.16: *Predicted P(ign) values for sweeping $\tau_{transit}$ using the comprehensive SVM.*

6.2.3.4 Prediction of Splitter Plate Height Influence

The comprehensive SVM was used to evaluate ignition probabilities for sweeping values of $\tau_{transit}$, at several levels of T_i, with $\phi_{top} = 1.1$. Again, these probabilities are based on 2000 evaluated cases at each nominal condition. Though the experimental data is sparse for this investigation, the trends match well as seen in Fig. 6.16. The same correlations between splitter height and transit time were used here as discovered in Fig. 6.8, where $h_s = 6.4 \ mm : \tau_{transit} = 135 \ \mu s$, and $h_s = 12.7 \ mm : \tau_{transit} = 195 \ \mu s$. The ability of the SVM to make these predictions even though the trend is in a new dimension supports the evidence that the model is representative.

126

6.3 Summary of Results

A thermochemical reactor model was developed to simulate the physical processes that occur following energy deposition and kernel ejection from a sunken fire igniter. Initialization of the model was based on the conditions determined in the experiments so that the results could be compared. The model represents the chemical processes as the kernel convects through a non-flammable and then a flammable gas, all while entraining the surrounding fluid. The development of this kernel was studied through the simulation to examine trends in sensitivities to different input parameters.

Additionally, randomized inputs were incorporated to the simulation to generate a probability of ignition based on a set of mean condition inputs. The evaluation of a statistically significant number of points for each nominal condition was performed by a support vector machine. This algorithm was trained using results from simulations that either spanned the design space or were focused to particular ranges.

The following are the significant contributions resulting from this study relating to the kernel development and the ignition probability implementation.

6.3.1 Kernel Development

1. Chemical rates are fast in the initial air plasma kernel due to high temperatures, making an equilibrium assumption reasonable at early times and allowing compositional changes to be primarily due to entrainment of surrounding fluid.

2. High flow temperatures lead to higher initial kernel temperatures and higher reactivity of the fuel-air mix, both enhancing the ignition process.

3. Entrainment of the flammable gas initially causes a brief decrease in temperature due to dilution of the kernel and endothermic fuel-decomposition reactions.

4. Pressure changes have little effect on chemical kinetics in either the air plasma

127

mechanism or the ignition reactions, though, energy deposition and mass entrainment changes due to altered pressure may have profound effects.

6.3.2 Modeled Ignition Probability

1. Experimental determination of transit time aided in correlation to splitter height for comparison of results, resulting in $\tau_m id$ being a good choice for model input, which allows time required for mixing.

2. Experimental approximations of parameter variability served well in generating input distributions, and in a case where the variability in one parameter is unknown, can be inferred by matching probabilities.

3. Support vector machines are a good method of evaluating ignition conditions, either when tailored to a specific range of inputs, or trained comprehensively.

4. The probability of ignition value is related to the ratio of the distance between nominal operating point and the discrete ignition boundary to the amount of variability in the input parameters.

CHAPTER 7

CONCLUSIONS

This work has been motivated by the lack of available information explaining non-premixed ignition in a flow, which is important for improving high performance combustion systems, such as aircraft engine combustors. Additionally, highly reliable ignition systems can allow for operations in challenging regimes, easing emission compliance and costs. The design and implementation of a stratified flow facility to study ignition induced by a sunken fire ignitor has been described. Details of the diagnostic techniques employed were also provided, including, schlieren, OH* chemiluminescence, broadband emission, and CH PLIF. In addition to studying the evolution of the kernel and its transition to a propagating flame, experiments were conducted to determine the most influential flow variables to the ignition process. Furthermore, a reduced order model was developed to characterize the ignition kernel based on experimental observations that mixing of the kernel with surrounding fluid is a key issue controlling the ignition process. As such, the model used a perfectly stirred reactor with entrainment of non-flammable and flammable gases. Random variability was introduced to the model to simulate realistic conditions and simulate ignition probabilities. This chapter summarizes the contributions of this thesis. The results are outlined in the context of their impact on applications and relation to the motivations discussed in Chapter 1. Lastly, recommendations for future work, based on the results of the current work, are put forward.

7.1 Thesis Contributions

Specifically, two branches of results are presented here. Firstly, conclusions relating to the initialization, and development of a plasma kernel as it evolves (or does not) to a self-sustaining flame, then, contributions in quantifying the influence of flow parameters on the probability of ignition are then discussed.

7.1.1 Kernel Evolution

The work here details development of a plasma kernel as it is ejected from a sunken fire igniter into a stratified crossflow following a short duration ($\sim 1 \ \mu s$) high energy ($\mathcal{O}(1 \ J)$) breakdown discharge. Schlieren observations of the convecting plasma kernel show characteristics of a rotating vortex ring during transit. This ring serves to entrain the surrounding gas into the vortex core, especially at early times as the kernel is issuing from the cavity. At these early times, the entrainment of the non-flammable fluid is key to the success or failure of ignition. The conditions of this entrained flow (e.g., temperature) and how long the entrainment lasts ($\tau_{transit}$) determine the effectiveness of the kernel when it arrives at the flammable mixture. Numerical simulations of these early times using the plasma mechanism result in a similar picture. The inflow temperature and duration of entrainment directly affects the temperature and radical concentrations of the kernel when transitioning to the flammable flow. The compositional changes are primarily due to entrainment as the chemical rates are sufficiently high that chemical equilibrium is nearly maintained. Additionally, when subjected to a range of pressures (0.5-5 atm), there appears to be little direct influence of pressure on chemical reaction rates. Rather, the major influence on kernel evolution and ignition is through density changes that can impact the initial energy density of the kernel or the relative entrainment rate.

In the current experimental facility, the entraining and cooling kernel reaches the

130

flammable flow as early as 40 μs following the discharge event. At this time, the kernel begins to entrain flammable fluid into the vortex ring, which allows interaction with the hot kernel gases to begin. The combination of entrainment and molecular mixing takes $\mathcal{O}(100\ \mu s)$ to sufficiently mix reactants into the hot kernel, and chemistry begins shortly after, as CH PLIF is observed as early as 300 μs. The fact that flame chemistry originates within the internal mixing region of the kernel supports the choice for a mixing based model used to simulate the ignition scenario in the sunken fire igniter flow. Emission signal can be observed at these early times (300 μs) and correlate to the eventual success of ignition. Schlieren imaging shows little distinction between kernels bound for successful ignition and those which fail until $\sim 1\ ms$, due to little heat release taking place before this time. When the fuel flow is introduced in the reduced order model, the simulated chemical evolution is revealed. The initial (few μs) fuel entrainment causes a rapid decrease in temperature as the entrained gas cools the kernel and endothermic reactions take place. The kernel must begin this step with enough thermal energy to overcome these losses required before heat release begins. Beyond this time, the competition between heat release from the recently entrained reactants and the cooling effect of continuous entrainment dictate whether the ignition is successful and self-sustaining reactions proceed. This outcome is limited to the modeled physics within the kernel and does not consider challenges that may exist for propagation or stabilization when the flame reaches the freestream.

The kernel transit time input to the reduced order model was informed by experimental measurements. The time when the centroid of the kernel has passed the flammable boundary has produced comparable results to experiments and proves to be a good choice for an input as it allows for mixing in the experiment. As a result, the developmental trends observed in the simulation match the evidence provided by the experiments. Additionally, the basis for the model came from observations on how important mixing is to the kernel ejection process. The development of this reduced

order model is a major contribution of this work with the ability to predict the effects of the important physical ignition processes, which can be used when considering an ignition system's feasibility. This work will provide knowledge to guide the use and design practices in industry, as well as a simple model to test ignition feasibility based on mixing, entrainment, and chemical reactions.

7.1.2 Ignition Probability

Much of the evidence seen in the ignition probability experiments compliment the observations on the kernel development processes. Initial screening experiments revealed that inflow temperature, transit time (via splitter height), and equivalence ratio are the most influential of the controlled variables within the tested ranges. Increased cross stream velocities could conceivably decrease the jet momentum ratio enough to influence the kernel trajectory, affecting transit time, and influencing ignition trends. Additionally, higher levels of free stream turbulence could augment the mixing between the free stream and the kernel, therefore changing the dominant ignition mechanism. Though, for the current flow regime, the competition between the effects of splitter height and temperature show that entrainment of the non-flammable gas is detrimental to the chances of successful ignition, and beyond a certain height (12.7 mm), no amount of available preheat could resurrect that possibility. The preheat temperature was also influential, as it served to heat the air provided to the initial spark volume, reduce the effects of entrainment cooling, and increase the reactivity of the flammable mixture. This understanding of the most influential flow variables on ignition success can inform the design and implementation of ignition systems in environments such as gas turbine combustors, leading to more reliable ignition.

Random perturbations were introduced to the inputs of the reduced order model with results comparable to experiments. Distributions for inputs were assumed to

be Gaussian and the spreads were estimated from experimental data. Comparison between the modeled probabilities and the experimental results aided in determining the relationship between the computational transit time input and the splitter height. Though well characterized in Chapter 5, this connection did not account for the time required to mix reactants into the core of the kernel, allowing for flame chemistry to begin. The reduced order model was used to simulate many data points located throughout the design space for the results to be used to train a support vector machine. This algorithm, once trained and validated, was used to quickly evaluate input points as either success or failure, with good results. The results were representative when based on comprehensive training data, or on a focused set of points. The evaluations by the SVM matched trends seen in the experiments, for example, in ramping temperature results. The simulation SVM essentially creates a boundary in the design space where successes occur on one side of the boundary, and failures on the other. The use of the SVM allowed the evaluation of points to comprise the visualization of the boundary. The output of $P(ign)$ from the SVM evaluated cases is the result of the ratio of the proximity of the nominal input conditions to the boundary compared to the spread in those variables.

Many ignition probability experiments were performed to understand the trends in ignition for the variables as well as to rule out certain parameters. The input conditions for all of these experiments and the successful ignition results are presented in Appendix B. An available database for these types of conditions is not currently available to the scientific community and will be useful to computational efforts in this field. This provision of results necessitated the furnishing of detailed characterizing information about the facility in use as well as well described data from each experiment, which is also provided in the appendix.

7.2 Recommendations for Future Work

Despite the comprehensive work presented here, further work is required to more fully understand spark ignition in non-premixed flows. Several additional areas of investigation exist that were not covered here, both in experimental work and simulations.

7.2.1 Experimental

A few experimental opportunities exist to study the development of the kernel. Though the CH PLIF images presented in this work let to some important findings, additional data collection can result in higher confidence in the statistical findings of the chemical markers. Simultaneous schlieren with the PLIF images resulted in a useful comparison of CH signal to where it occurred in the kernel. Additionally, the evolution of the kernel taken with PLIF would be an interesting set of data. This would require the use of a high speed laser and imaging system to capture the development of a single spark event. The current study focused on ignition of methane-air mixtures. More complex fuels can also be studied using this flow facility. For example, the facility also can be easily adapted to accept liquid fuels to see if additional complexities arise when evaporation is required. This effort could distinguish the ease of ignitability or the preheat temperature required to reliably obtain successful ignition in more complex fuel species. Some of the work presented in this thesis could be revisited to add ignition probability parameters of interest. Namely, variables relating to the spark igniter can be investigated, like deposited energy, spark duration, or even changing design features of the igniter cavity. Further quantification of energy deposition variability would compliment these investigations. Expansion of the tested variable ranges can also determine if other controlling mechanisms exist, for example: at much higher velocities and turbulence intensities, the entrainment dominance may give way to mixing caused by the freestream. In this situation, conditions

134

may be more favorable inside the kernel to initialize reactions, but upon propagation into the freestream the flame front may not be sustainable. This work also focused on ignition using a sunken fire igniter, which results in the characteristic vortex ring kernel, driving mass entrainment. Variations on igniter geometries, including surface discharge igniters not contained within a cavity can provide some insight to how the ejection and entrainment can be adjusted.

7.2.2 Numeric

A simplification made to the reduced order model can be relaxed for future numerical work, that being the use of constant entrainment rates. This was simple to implement and therefore a good first approximation. Based on the discussion in Chapter 2, evidence is available for the case that entrainment is not constant. The current model can also be evaluated to vary the equivalence ratio as a function of time, which may be more realistic for non-uniform fuel distribution or a stratified flow. The current PSR model enforces the properties of a uniform kernel. This simplification may bias the results since experiments depict some regions of high mixing and less in others. Therefore enhancements to the model could include changing the reactor model from a perfectly stirred reactor to a partially stirred reactor, a staged model, or even include some mass outflow to represent the fluid that is trailed behind the kernel. Higher discharge energies or shorter delay times may be of interest to determine how to improve ignition probability for certain regimes. This would require the identification and use of a chemical mechanism that includes ionized fuel species. Investigation of these challenging conditions may include pressures other than one atmosphere, and will require further study into the energy deposition process and the density related effects.

Additionally, a higher order computational model, simulating the kernel development in 3D, would be a good companion effort to the reduced order model. This

study of the fluid dynamics can provide a better estimate of the entrainment rates by use of a conserved scalar. The modeling can also give insight to where reactions begin allowing comparison to experimental findings, such as CH PLIF data.

Lastly, with the addition of more complex fuels to the modeling repertoire, the adaptation for the model to handle liquid fuels would be advantageous. The capability to account for evaporation energy in the model can open the model to a new range of problems, as well as allowing observation of the complex chemical species evolution. Liquid fuel consideration would require an evaporation sub-model and potentially alterations to the reactor mixing characteristics, using a partially stirred reactor instead of the current *perfectly* stirred reactor. This modeling alternative fuels investigation can compliment experimental trials with more complex or liquid fuels. These improvements to the model aim to capture the important physics of the problem, allow direct comparison to experimental results, and once validated, provide useful predictive tools for igniter or engine designers and operators. The model can inform engine designers *a priori* of conditions that are difficult to ignite or provide a probability.

APPENDIX A

FACILITY DESIGN

A.1 Facility Assembly

INFLOW SECTION

CONDITIONER SECTION

STRAIGHTENER SECTION

TEST SECTION

ITEM NO.	PART NUMBER	DESCRIPTION	Default/QTY.
1	TestSection		1
2	window		2
3	windowCover		2
4	topCap		1
5	plifWindow		2
6	bottomCap		1
7	igniterAdapter		1
8	StraightenerSection		1
9	FlowConditioner		1
10	InflowSection		1
11	Igniter		1
12	SSFLATSKT 0.19-24X0.1875-HX-N		1
13	testSectionflangeDown	DOWNSTREAM FLANGE ON TEST SECTION	1
14	testSectionflangeUp	UPSTREAM FLANGE ON TEST SECTION	1

138

Top drawing - Straightener Section

ITEM NO.	PART NUMBER	DESCRIPTION	QTY.
1	StraightenerSection		1
2	straightenerFlangeUp	UPSTREAM FLANGE ON STRAIGHTENER	1
3	straightenerFlangeDown	DOWNSTREAM FLANGE ON STRAIGHTENER	1
4	splitterPlate		1
5	straightenerUpperWall		2
6	straightenerLowerWall		2
7	rail	RAIL	6
8	topFuelBar		3
9	bottomFuelBar		2
10	topFuelManifold		1
11	BottomFuelManifold		1

INCH

UNLESS OTHERWISE SPECIFIED:
BREAK AND DEBURR ALL EDGES R/C 0.01
SURFACE FINISH = 125
DO NOT SCALE DRAWING
DIMENSIONING AND TOLERANCING PER ASME Y14.5M 1994 & Y14.3 1999

THIRD ANGLE PROJECTION

APPROVALS: DATE:
DRAWN BAS 2/14/2012
CHECKED
ISSUED

GEORGIA INSTITUTE OF TECHNOLOGY - SCHOOL OF AEROSPACE ENGINEERING

TITLE: STRAIGHTENER SECTION

SIZE **C** | DWG. NO. FLOW FACILITY ASSEMBLIES | REV **A**

SCALE: 1:2 & NOTED | SHEET 4 OF 6

REVISIONS
REV.	DESCRIPTION	DATE	REV. BY	CHECK. BY	APPR. BY
A	INITIAL RELEASE	2/14/2012	BAS		

PROPRIETARY AND CONFIDENTIAL

Bottom drawing - Conditioner Section

ITEM NO.	PART NUMBER	DESCRIPTION	QTY.
1	conditioningSection		1
2	conditionerFlangeDown	DOWNSTREAM FLANGE ON CONDITIONER	1
3	perforatedPlateDown		1
4	perfPlateFlangeDown	DOWNSTREAM FLANGE OUTSIDE PERFORATED PLATE	1
5	conditionerFlangeUp	UPSTREAM FLANGE ON CONDITIONER	1
6	perforatedPlateUp		1
7	perfPlateFlangeUp	UPSTREAM FLANGE OUTSIDE PERFORATED PLATE	1

INCH

UNLESS OTHERWISE SPECIFIED:
BREAK AND DEBURR ALL EDGES R/C 0.01
SURFACE FINISH = 125
DO NOT SCALE DRAWING
DIMENSIONING AND TOLERANCING PER ASME Y14.5M 1994 & Y14.3 1999

THIRD ANGLE PROJECTION

APPROVALS: DATE:
DRAWN BAS 2/14/2012
CHECKED
ISSUED

GEORGIA INSTITUTE OF TECHNOLOGY - SCHOOL OF AEROSPACE ENGINEERING

TITLE: CONDITIONER SECTION

SIZE **C** | DWG. NO. FLOW FACILITY ASSEMBLIES | REV **A**

SCALE: 1:2 & NOTED | SHEET 5 OF 6

REVISIONS
REV.	DESCRIPTION	DATE	REV. BY	CHECK. BY	APPR. BY
A	INITIAL RELEASE	2/14/2012	BAS		

139

www.manaraa.com

REV.	DESCRIPTION	DATE	REV. BY	CHECK. BY	APPR. BY
A	INITIAL RELEASE	2/14/2012	RAS		

ITEM NO.	PART NUMBER	DESCRIPTION	QTY.
1	inflowPipe	2" NPT THREADDED PIPE FOR INFLOW SECTION	1
2	inflowFlange	DOWNSTREAM FLANGE ON INFLOW SECTION	1
3	inflowSideWall	SIDE WALL OF INFLOW SECTION	2
4	inflowTopWall	TOP WALL OF INFLOW SECTION	2
5	inflowBackWall	BACK WALL TO INFLOW SECTION	1

GEORGIA INSTITUTE OF TECHNOLOGY - SCHOOL OF AEROSPACE ENGINEERING

TITLE:

INFLOW SECTION

INCH

THIRD ANGLE PROJECTION

UNLESS OTHERWISE SPECIFIED:
BREAK AND DEBURR ALL EDGES R/C 0.01
SURFACE FINISH = 125
DO NOT SCALE DRAWING
DIMENSIONING AND TOLERANCING PER ASME Y14.5M 1994 & B43 1999

APPROVALS: DATE:
DRAWN   RAS   2/14/2012
CHECKED
ENG

SIZE **C** DWG. NO. FLOW FACILITY ASSEMBLIES REV **A**

SCALE: 1:2 & NOTED   SHEET 6 OF 6

140

A.2 Test Section

SECTION A-A

DETAIL B
SCALE 4 : 1

TYP 45°
TYP .02±.050

.25±.005

SECTION A-A

OPTICAL SURFACE - POLISH THIS AND PARALLEL SURFACE
TO OPTICAL STANDARD

INCH

FUSED QUARTZ

POLISHED

GEORGIA INSTITUTE OF TECHNOLOGY -
SCHOOL OF AEROSPACE ENGINEERING

TITLE:
WINDOW

SIZE DWG. NO.   REV
C   TEST SECTION   A

SCALE: 1:1 & NOTED   SHEET 2 OF 8

SECTION C-C

TYP R.031±.002

.25±.005
.375±.05

8XR.125±.005

OPTICAL SURFACE - POLISH THIS AND PARALLEL SURFACE
TO OPTICAL STANDARD

INCH

FUSED QUARTZ

POLISHED

GEORGIA INSTITUTE OF TECHNOLOGY -
SCHOOL OF AEROSPACE ENGINEERING

TITLE:
PLIF WINDOW

SIZE DWG. NO.   REV
C   TEST SECTION   A

SCALE: 2:1 & NOTED   SHEET 3 OF 8

142

TEST SECTION

GEORGIA INSTITUTE OF TECHNOLOGY - SCHOOL OF AEROSPACE ENGINEERING

TITLE: TEST SECTION

SIZE C — DWG. NO. TEST SECTION — REV A

SHEET 4 OF 8

WINDOW COVER

GEORGIA INSTITUTE OF TECHNOLOGY - SCHOOL OF AEROSPACE ENGINEERING

TITLE: WINDOW COVER

MATERIAL: AISI 1020

SIZE C — DWG. NO. TEST SECTION — REV A

SHEET 5 OF 8

143

SECTION H-H

2X DETAIL I
SCALE 4 : 1

SECTION J-J

2X DETAIL K
SCALE 4 : 1

144

DETAIL R
SCALE 16 : 1

SCALE 2:1

SECTION P-P

IGNITER ADAPTER

TEST SECTION
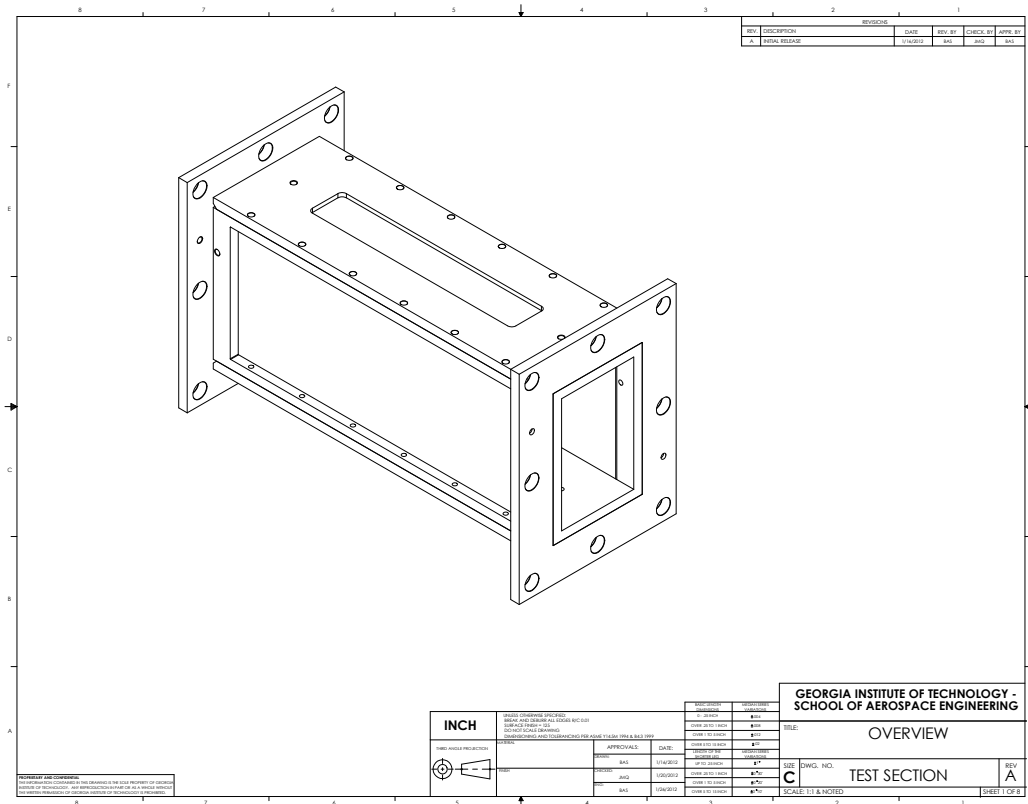
GEORGIA INSTITUTE OF TECHNOLOGY -
SCHOOL OF AEROSPACE ENGINEERING

AISI 1020

SHEET 8 OF 8

OVERVIEW

T S WELDMENT

GEORGIA INSTITUTE OF TECHNOLOGY -
SCHOOL OF AEROSPACE ENGINEERING

SHEET 1 OF 7

145

DETAIL A
SCALE 6 : 1

30°

.1±.010

.002 | A | B
C

3.875±.005

.002 | A
B

.25±.005
0
A

.002

.5±.005
0

**GEORGIA INSTITUTE OF TECHNOLOGY -
SCHOOL OF AEROSPACE ENGINEERING**

INCH

THIRD ANGLE PROJECTION

TITLE:

UPRIGHT

SIZE | DWG. NO. | REV
C | T S WELDMENT
SCALE: 1:1 & NOTED | SHEET 2 OF 7

.002 | A | B
0

2.125±.001

.002 | A
0

10.031±0.10

.002

.25±.005
0

NOTE:
BOTTOM WALL DESIGN SAME AS TOP WALL

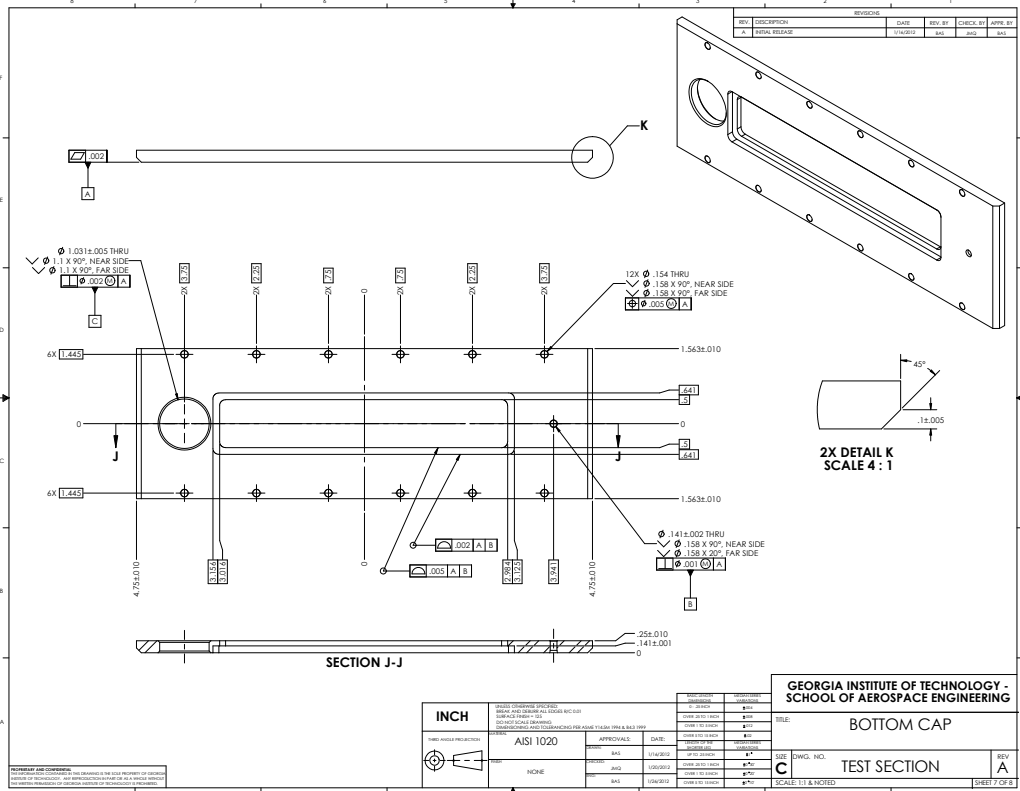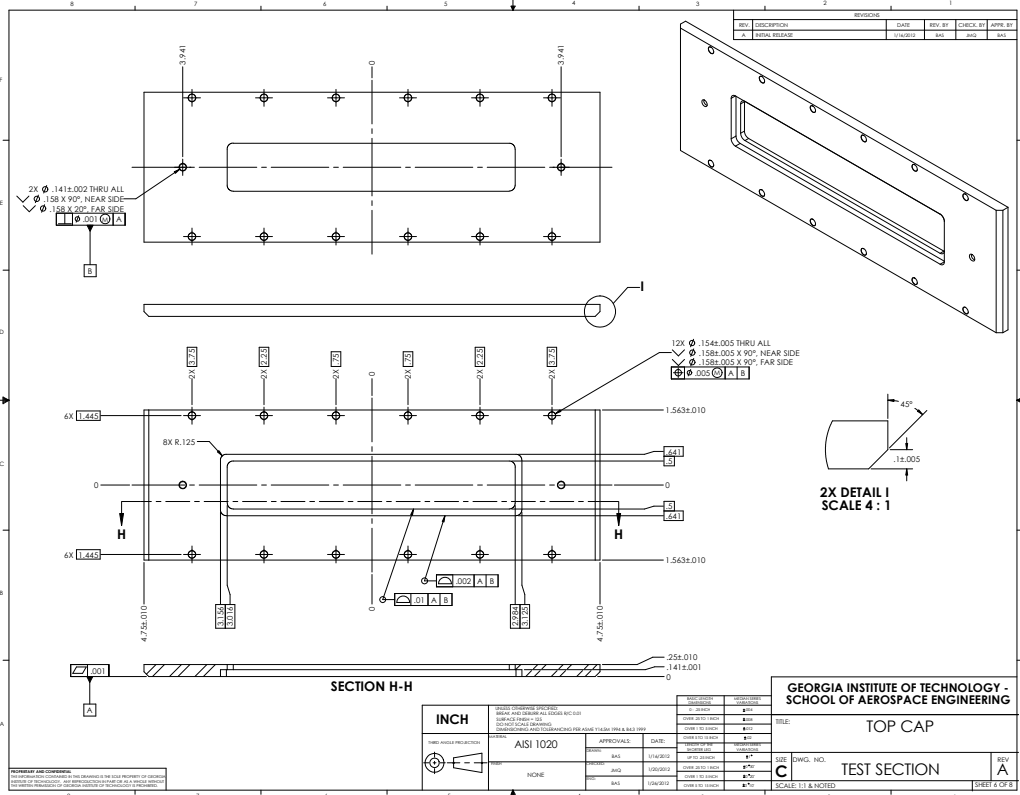**GEORGIA INSTITUTE OF TECHNOLOGY -
SCHOOL OF AEROSPACE ENGINEERING**

INCH

THIRD ANGLE PROJECTION

TITLE:

TOP WALL

SIZE | DWG. NO. | REV
C | T S WELDMENT
SCALE: 1:1 & NOTED | SHEET 3 OF 7

SECTION L-L

$.25^{+.000}_{-.005}$

DETAIL M
SCALE 6 : 1

NOTES:
PRESS FIT Ø.125" X .5" DOWEL PINS

2X Ø .123±.001 THRU
.145 X 20°, NEAR SIDE
.145 X 90°, FAR SIDE

8X Ø .406±.010 THRU
Ø .415 X 60°, NEAR SIDE
Ø .415 X 60°, FAR SIDE

2.938±.050

3X 2.563

UNILATERALLY OUT

TYP 45°
TYP .1±.010

2.313±.050

**GEORGIA INSTITUTE OF TECHNOLOGY -
SCHOOL OF AEROSPACE ENGINEERING**

TITLE: TEST SECTION FLANGE - DOWN

INCH

AISI 1020

SIZE C | DWG. NO. T S WELDMENT | REV

SCALE: 1:1 & NOTED | SHEET 4 OF 7

SECTION N-N

$.25^{+.000}_{-.005}$

DETAIL O
SCALE 6 : 1

2X Ø .1406±.0020 THRU
.158 X 90°, NEAR SIDE
.158 X 20°, FAR SIDE

8X Ø .406±.010 THRU
Ø .415 X 60°, NEAR SIDE
Ø .415 X 60°, FAR SIDE

4X R.01

2.938±.050

3X 2.563

UNILATERALLY OUT

TYP 45°

2.313±.050

**GEORGIA INSTITUTE OF TECHNOLOGY -
SCHOOL OF AEROSPACE ENGINEERING**

TITLE: TEST SECTION FLANGE - UP

INCH

AISI 1020

SIZE C | DWG. NO. T S WELDMENT | REV

SCALE: 1:1 & NOTED | SHEET 5 OF 7

147

ITEM NO. table (Sheet 6):

ITEM NO.	PART NUMBER	DESCRIPTION	QTY.
1	testSectionBottomWall	BOTTOM WALL	1
2	testSectionUpright	UPRIGHT SUPPORT MEMBER	4
3	testSectionTopWall	TOP WALL	1
4	testSectionflangeUp	UPSTREAM FLANGE ON TEST SECTION	1
5	testSectionflangeDown	DOWNSTREAM FLANGE ON TEST SECTION	1

GEORGIA INSTITUTE OF TECHNOLOGY - SCHOOL OF AEROSPACE ENGINEERING

TITLE: ASSEMBLY

SIZE C DWG. NO. T S WELDMENT REV

SCALE: 1:1 & NOTED SHEET 6 OF 7

INCH

ITEM NO.	PART NUMBER	DESCRIPTION	QTY.
1	testSectionBottomWall	BOTTOM WALL	1
2	testSectionUpright	UPRIGHT SUPPORT MEMBER	4
3	testSectionTopWall	TOP WALL	1
4	testSectionflangeUp	UPSTREAM FLANGE ON TEST SECTION	1
5	testSectionflangeDown	DOWNSTREAM FLANGE ON TEST SECTION	1

GEORGIA INSTITUTE OF TECHNOLOGY - SCHOOL OF AEROSPACE ENGINEERING

TITLE: WELD GUIDE

SIZE C DWG. NO. T S WELDMENT REV

SCALE: 1:1 & NOTED SHEET 7 OF 7

INCH

A.3 Straightener Section

STRAIGHTENER SECTION

4X DETAIL B
SCALE 6 : 1

SECTION A-A

4X DETAIL C
SCALE 6 : 1

4X DETAIL D
SCALE 6 : 1

NOTES:
⚠ PART - STRAIGHTENER WELDMENT - BOTTOM WALL
⚠ PART - STRAIGHTENER WELDMENT - SIDE WALL
⚠ PART - STRAIGHTENER WELDMENT - TOP WALL

GEORGIA INSTITUTE OF TECHNOLOGY -
SCHOOL OF AEROSPACE ENGINEERING

TITLE:
STRAIGHTENER SECTION

INCH
AISI 1020

SIZE C | DWG. NO. STRAIGHTENER SECTION | REV A
SCALE: 1:2 & NOTED | SHEET 2 OF 5

2X DETAIL L
SCALE 2 : 1

GEORGIA INSTITUTE OF TECHNOLOGY -
SCHOOL OF AEROSPACE ENGINEERING

TITLE:
UPPER WALL

INCH
AISI 1020

SIZE C | DWG. NO. STRAIGHTENER SECTION | REV A
SCALE: 1:2 & NOTED | SHEET 3 OF 5

المنارة للاستشارات

www.manaraa.com

Engineering drawing — Sheet 4 of 5: LOWER WALL

REVISIONS

REV.	DESCRIPTION	DATE	REV. BY	CHECK. BY	APPR. BY
A	INITIAL RELEASE	1/17/2012	BAS		

2X DETAIL K
SCALE 2 : 1

3X Ø .281±.010 THRU
Ø .3 X 60°, NEAR SIDE
Ø .3 X 60°, FAR SIDE
⌖ Ø .002 Ⓜ A B C

2.238±.010
3X 1.988
.25±.005

4X .206±.005 THRU ALL
Ø .218 X 60°, FAR SIDE
⌖ Ø .002 Ⓜ A B C
4X S

GEORGIA INSTITUTE OF TECHNOLOGY -
SCHOOL OF AEROSPACE ENGINEERING

INCH

UNLESS OTHERWISE SPECIFIED
BREAK AND DEBURR ALL EDGES R/C 0.01
SURFACE FINISH = 125
DO NOT SCALE DRAWING
DIMENSIONING AND TOLERANCING PER ASME Y14.5M 1994 & 843 1999

TITLE: LOWER WALL

MATERIAL: AISI 1020

APPROVALS: DATE:
DRAWN: BAS 1/17/2012
CHECKED:

FINISH: NONE

SIZE: C   DWG. NO. STRAIGHTENER SECTION   REV: A

SCALE: 1:2 & NOTED   SHEET 4 OF 5

PROPRIETARY AND CONFIDENTIAL

Engineering drawing — Sheet 5 of 5: SPLITTER PLATE

REVISIONS

REV.	DESCRIPTION	DATE	REV. BY	CHECK. BY	APPR. BY
A	INITIAL RELEASE	1/17/2012	BAS		

.025±.003

⌀ .005

A

SCALE 1:4

1.825±.010
4X 1.569
4X 1.569
1.825±.010

2.125 +.000 / -.005

.005 A
B

DETAIL E
SCALE 2 : 1

FULL RADIUS

8X 1±.005

8X .206±.005
⌖ .005 A B

GEORGIA INSTITUTE OF TECHNOLOGY -
SCHOOL OF AEROSPACE ENGINEERING

INCH

UNLESS OTHERWISE SPECIFIED
BREAK AND DEBURR ALL EDGES R/C 0.01
DO NOT SCALE DRAWING
DIMENSIONING AND TOLERANCING PER ASME Y14.5M 1994 & 843 1999

TITLE: SPLITTER PLATE

MATERIAL: AISI 1074

APPROVALS: DATE:
DRAWN: BAS 1/17/2012
CHECKED:

FINISH: NONE

SIZE: C   DWG. NO. STRAIGHTENER SECTION   REV: A

SCALE: 1:2 & NOTED   SHEET 5 OF 5

PROPRIETARY AND CONFIDENTIAL

المنارة للاستشارات   www.manaraa.com

GEORGIA INSTITUTE OF TECHNOLOGY - SCHOOL OF AEROSPACE ENGINEERING

TITLE: OVERVIEW

SIZE C | DWG. NO. STRAIGHTENER WELDMENT | REV A

SCALE: 1:1 & NOTED | SHEET 1 OF 9

INCH

SCALE 1 : 2

GEORGIA INSTITUTE OF TECHNOLOGY - SCHOOL OF AEROSPACE ENGINEERING

TITLE: BOTTOM WALL

SIZE C | DWG. NO. STRAIGHTENER WELDMENT | REV A

SCALE: 1:1 & NOTED | SHEET 2 OF 9

INCH

AISI 1020

152

Drawing 1 (top):

SCALE 1 : 2

.005 | A | B
C
2.125 +.000 / -.005
14.031 ±0.010
.002 | A
B
.002
.25±.0015
A

INCH

UNLESS OTHERWISE SPECIFIED:
BREAK AND DEBURR ALL EDGES R/C 0.01
SURFACE FINISH = 125
DO NOT SCALE DRAWING
DIMENSIONING AND TOLERANCING PER ASME Y14.5M 1994 & 843 1999

MATERIAL
AISI 1020

THIRD ANGLE PROJECTION

APPROVALS: DATE:
DRAWN BAS 2/7/2012
CHECKED
NONE

GEORGIA INSTITUTE OF TECHNOLOGY -
SCHOOL OF AEROSPACE ENGINEERING

TITLE:
TOP WALL

SIZE C | DWG. NO. STRAIGHTENER WELDMENT | REV A
SCALE: 1:1 & NOTED | SHEET 3 OF 9

Drawing 2 (bottom):

A

.002 | A | B
C

30°
45°
.02±.005
.1±.010

2X DETAIL A
SCALE 6 : 1

3.875 +.000 / -.005
.002 | A
A
1±.003
.25 +.000 / -.005
B

INCH

UNLESS OTHERWISE SPECIFIED:
BREAK AND DEBURR ALL EDGES R/C 0.01
SURFACE FINISH = 125
DO NOT SCALE DRAWING
DIMENSIONING AND TOLERANCING PER ASME Y14.5M 1994 & 843 1999

MATERIAL
AISI 1020

THIRD ANGLE PROJECTION

APPROVALS: DATE:
DRAWN BAS 2/7/2012
CHECKED
NONE

GEORGIA INSTITUTE OF TECHNOLOGY -
SCHOOL OF AEROSPACE ENGINEERING

TITLE:
SIDE WALL

SIZE C | DWG. NO. STRAIGHTENER WELDMENT | REV A
SCALE: 1:1 & NOTED | SHEET 4 OF 9

SECTION B-B

DETAIL C
SCALE 6 : 1

SECTION D-D

DETAIL E
SCALE 6 : 1

154

Drawing 1 (Sheet 7):

0
.25±.010
1.875±.010
.125
1.75±.010
.25±.010
AISI 1020
INCH

.266±.005
.003 | A | B
1.5 +.005/-.000
.5 +.000/-.005
FULL RADIUS R .125"
.25±.010

.002
.002 | A
.002 | A
B
A

UNLESS OTHERWISE SPECIFIED
BREAK AND DEBURR ALL EDGES R/C 0.01
SURFACE FINISH = 125
DO NOT SCALE DRAWING
DIMENSIONING AND TOLERANCING PER ASME Y14.5M-1994 & B4.3-1999

THIRD ANGLE PROJECTION

APPROVALS: DATE:
BAS 2/7/2012
DRAWN
CHECKED
NONE

GEORGIA INSTITUTE OF TECHNOLOGY -
SCHOOL OF AEROSPACE ENGINEERING
TITLE: RAIL
SIZE C | DWG. NO. STRAIGHTENER WELDMENT | REV A
SCALE: 1:1 & NOTED | SHEET 7 OF 9

REV. | DESCRIPTION | DATE | REV. BY | CHECK. BY | APPR. BY
A | INITIAL RELEASE | 2/7/2012 | BAS

PROPRIETARY AND CONFIDENTIAL

Drawing 2 (Sheet 8):

.002 | A | B
.002 | A | B
.002 | A | B
1.266±.005
6.766±.005
12.266±.005
.016
.003 | A | B | C
.003 | A | B | C
.003 | A | B | C
(1)
.003 | A | B | C
.003 | A | B | C
.003 | A | B | C
.002 | A | B
.005 | C
C

.005 | A
B
.005 | A
.01
A
.005 | B
3.625
3.375
.25
2.125
2.375
.002 | A | B

INCH

ITEM NO.	PART NUMBER	DESCRIPTION	QTY.
1	straightenerBottom	BOTTOM WALL	1
2	straightenerSideWall	SIDE WALL	4
3	straightenerTop	TOP WALL	1
4	straightenerFlangeUp	UPSTREAM FLANGE ON STRAIGHTENER	1
5	straightenerFlangeDown	DOWNSTREAM FLANGE ON STRAIGHTENER	1
6	rail	RAIL	6

UNLESS OTHERWISE SPECIFIED
BREAK AND DEBURR ALL EDGES R/C 0.01
SURFACE FINISH = 125
DO NOT SCALE DRAWING
DIMENSIONING AND TOLERANCING PER ASME Y14.5M-1994 & B4.3-1999

THIRD ANGLE PROJECTION

APPROVALS: DATE:
BAS 2/7/2012
DRAWN
CHECKED

GEORGIA INSTITUTE OF TECHNOLOGY -
SCHOOL OF AEROSPACE ENGINEERING
TITLE: ASSEMBLY
SIZE C | DWG. NO. STRAIGHTENER WELDMENT | REV A
SCALE: 1:1 & NOTED | SHEET 8 OF 9

REV. | DESCRIPTION | DATE | REV. BY | CHECK. BY | APPR. BY
A | INITIAL RELEASE | 2/7/2012 | BAS

PROPRIETARY AND CONFIDENTIAL

ITEM NO.	PART NUMBER	DESCRIPTION	QTY.
1	straightenerBottom	BOTTOM WALL	1
2	straightenerSideWall	SIDE WALL	4
3	straightenerTop	TOP WALL	1
4	straightenerFlangeUp	UPSTREAM FLANGE ON STRAIGHTENER	1
5	straightenerFlangeDown	DOWNSTREAM FLANGE ON STRAIGHTENER	1
6	rail	RAIL	6

REVISIONS

REV.	DESCRIPTION	DATE	REV. BY	CHECK. BY	APPR. BY
A	INITIAL RELEASE	2/7/2012	RAS		

GEORGIA INSTITUTE OF TECHNOLOGY - SCHOOL OF AEROSPACE ENGINEERING

TITLE: WELD GUIDE

INCH

THIRD ANGLE PROJECTION

UNLESS OTHERWISE SPECIFIED:
BREAK AND DEBURR ALL EDGES R/C 0.01
SURFACE FINISH = 125
DO NOT SCALE DRAWING
DIMENSIONING AND TOLERANCING PER ASME Y14.5M 1994 & B4.3 1999

APPROVALS: DATE:
RAS 2/7/2012

SIZE C DWG. NO. STRAIGHTENER WELDMENT REV A

SCALE: 1:1 & NOTED   SHEET 9 OF 9

156

www.manaraa.com

APPENDIX B

IGNITION PROBABILITY DATABASE

B.1 Hotwire Spectra
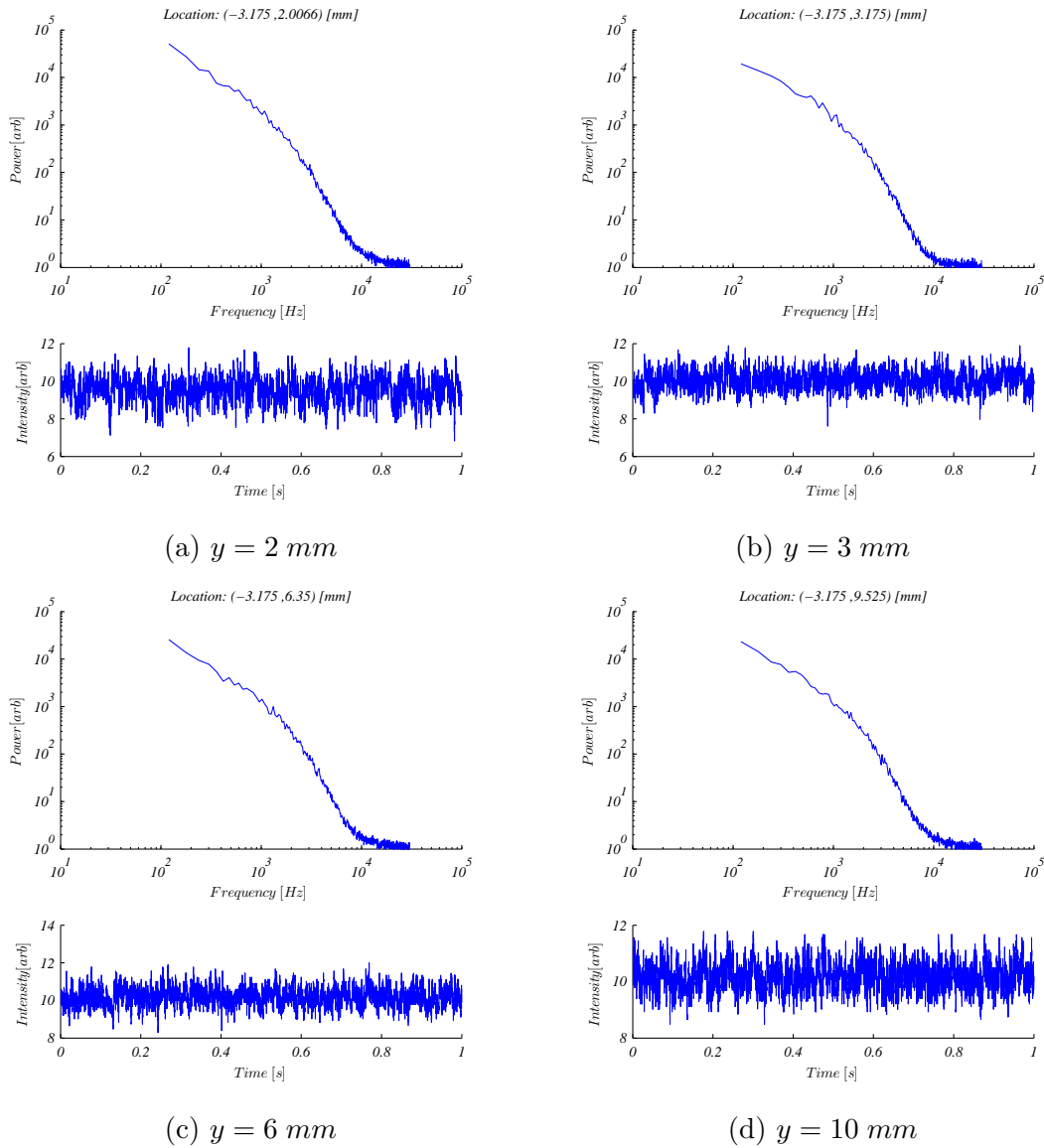
Figure B.1: *Velocity data and spectra recorded with hotwire.* $\bar{v} = 10 \, m/s$, $x = -3 \, mm$
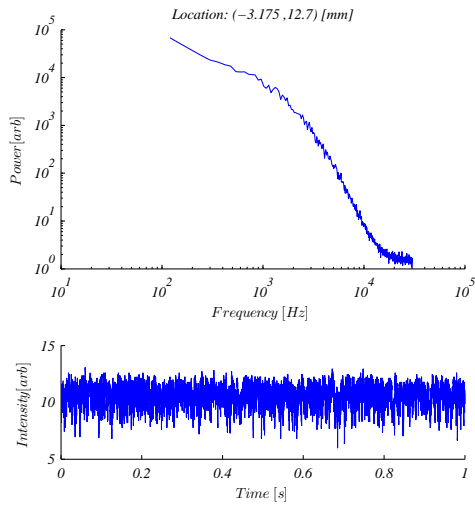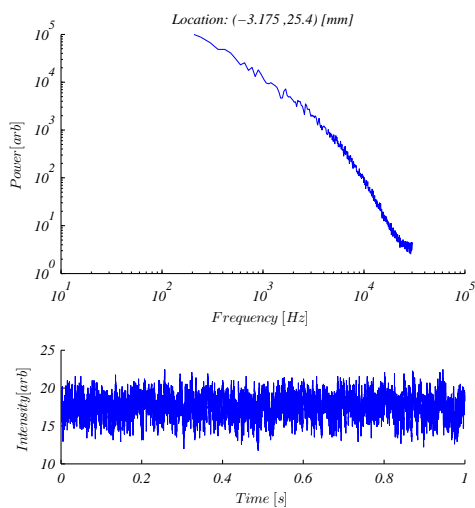
(a) $y = 13\ mm$ (b) $y = 19\ mm$
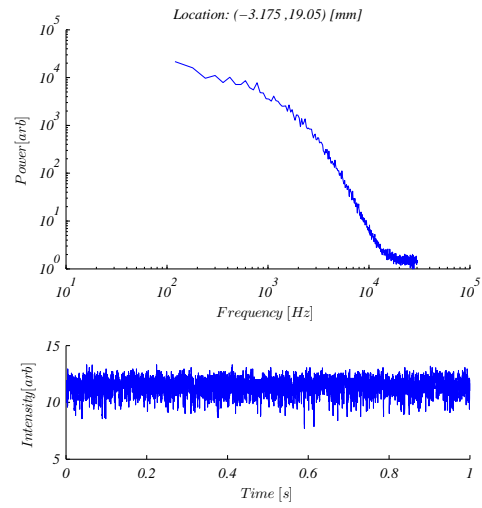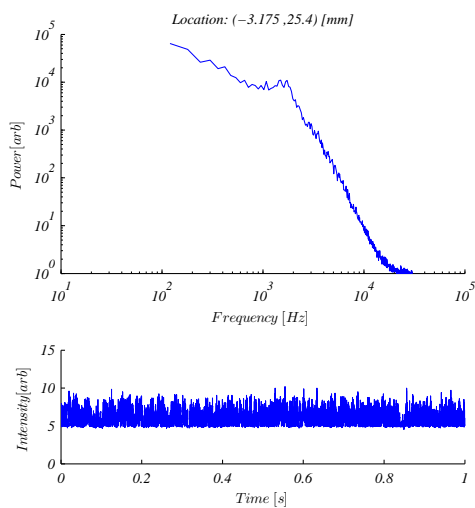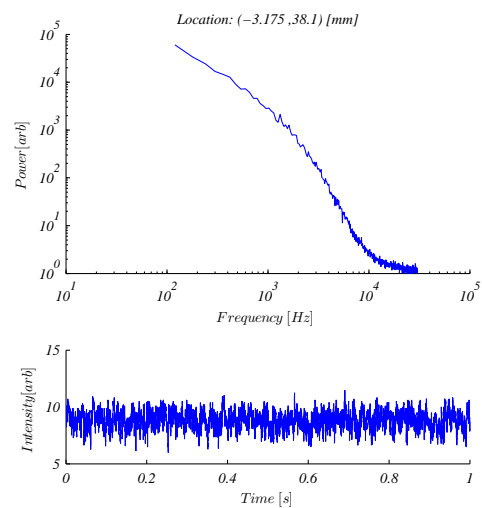
(c) $y = 25\ mm$ (d) $y = 38\ mm$

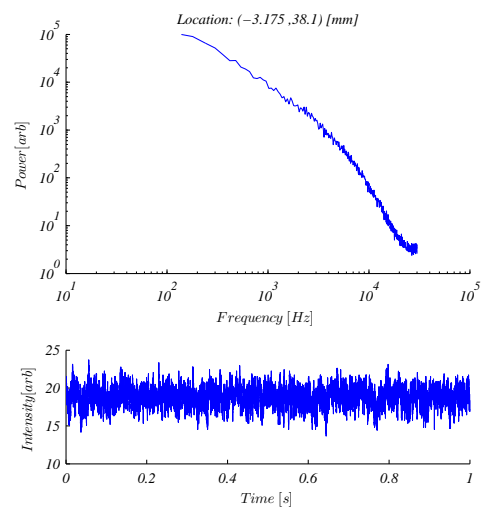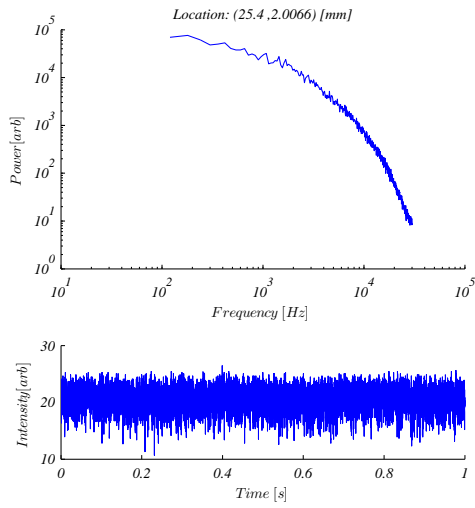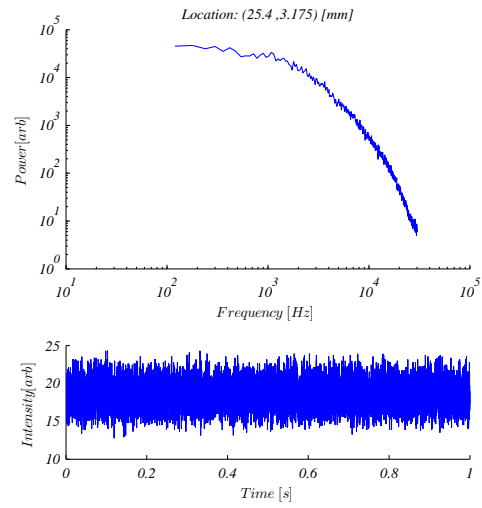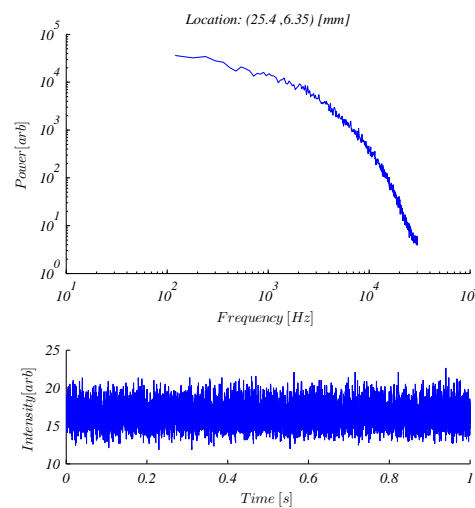Figure B.2: *Velocity data and spectra recorded with hotwire.* $\bar{v} = 10\ m/s$, $x = -3\ mm$
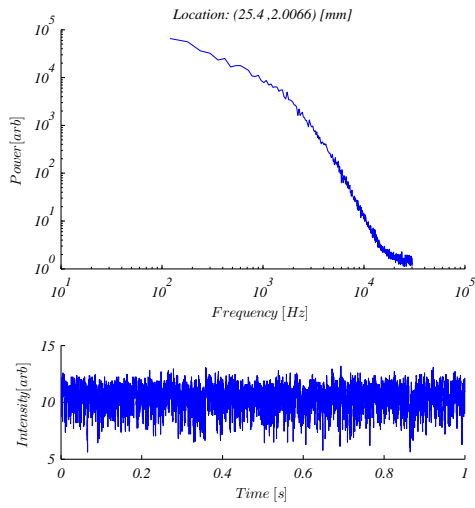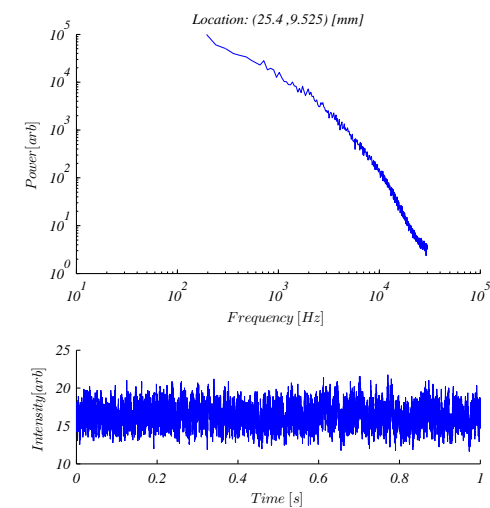
(a) $y = 2\ mm$
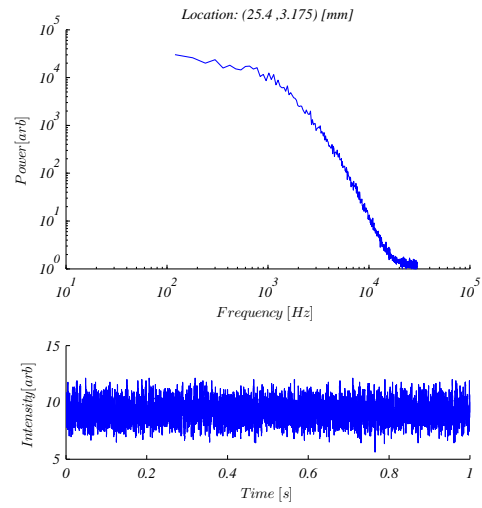
(b) $y = 3\ mm$
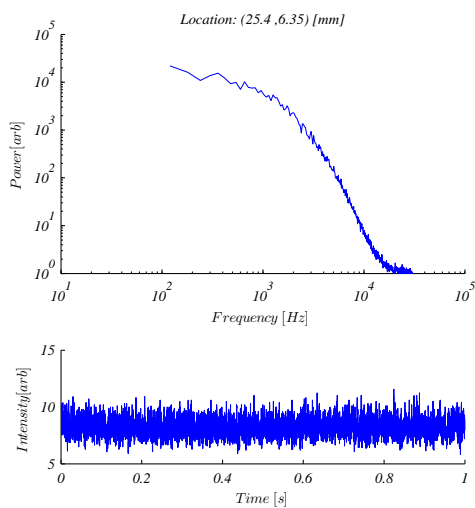
(c) $y = 6\ mm$
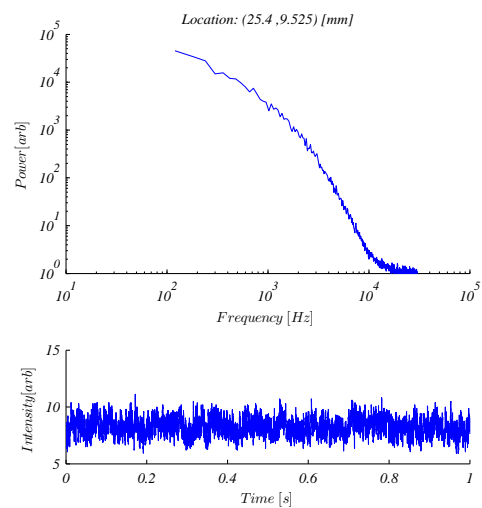
(d) $y = 10\ mm$

Figure B.3: *Velocity data and spectra recorded with hotwire.* $\bar{v} = 10\ m/s$, $x = 25\ mm$

159
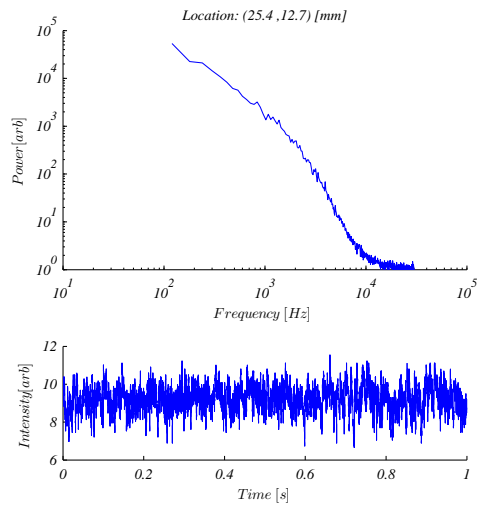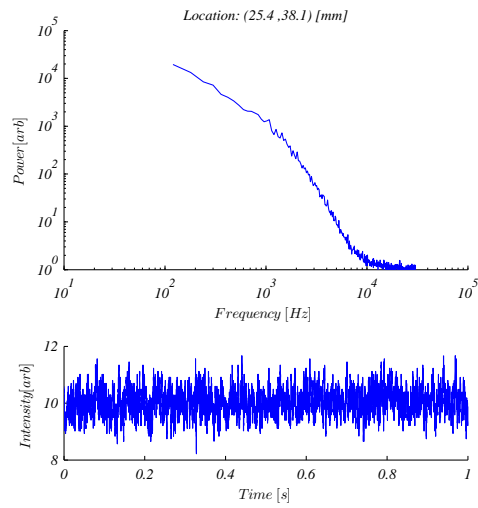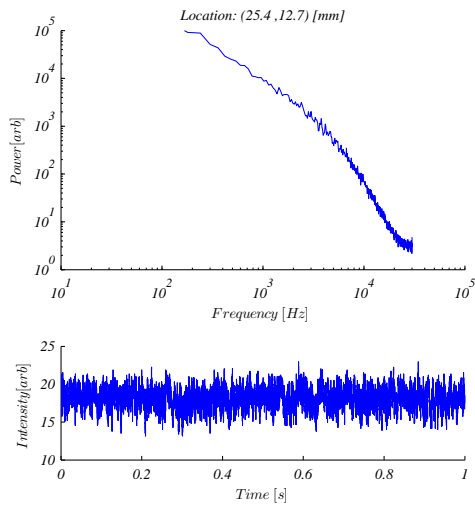
(a) $y = 13 \ mm$ (b) $y = 38 \ mm$

Figure B.4: *Velocity data and spectra recorded with hotwire.* $\bar{v} = 10 \ m/s$, $x = 25 \ mm$
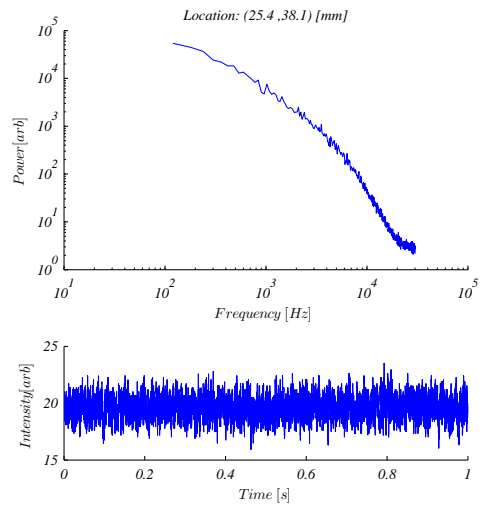
160
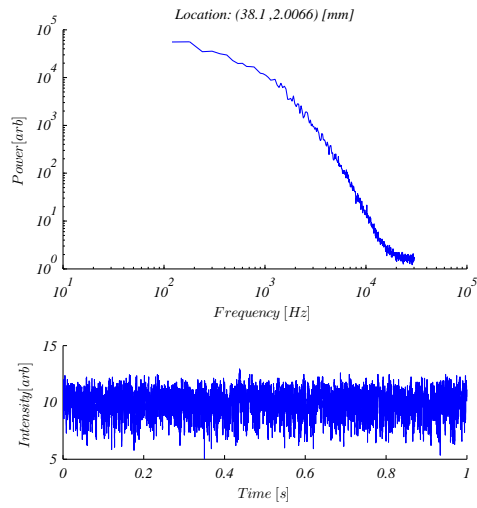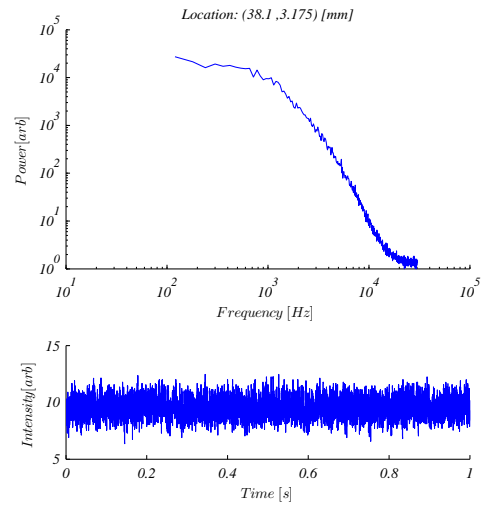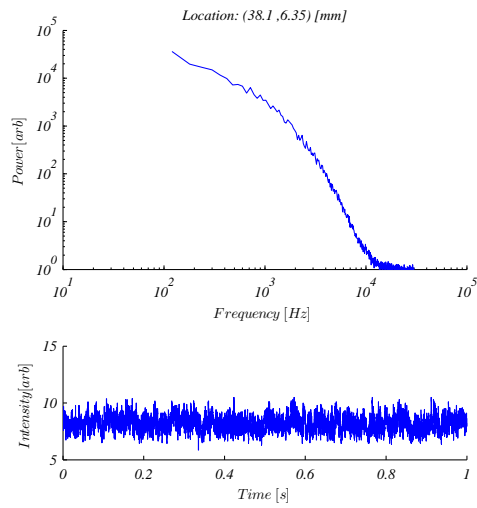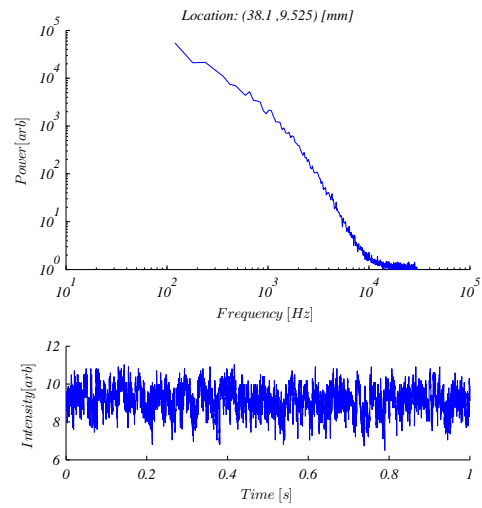
(a) $y = 2\ mm$

(b) $y = 3\ mm$

(c) $y = 6\ mm$

(d) $y = 10\ mm$

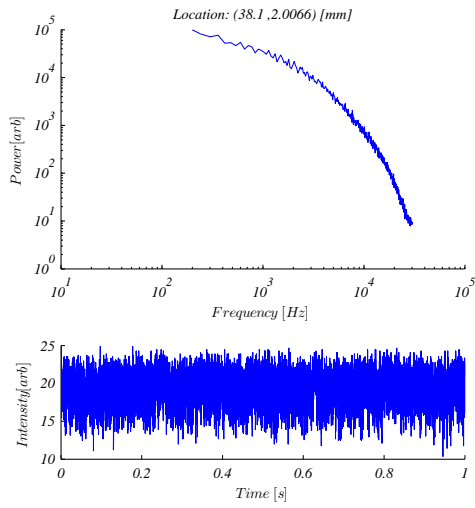Figure B.5: *Velocity data and spectra recorded with hotwire.* $\bar{v} = 10\ m/s$, $x = 38\ mm$
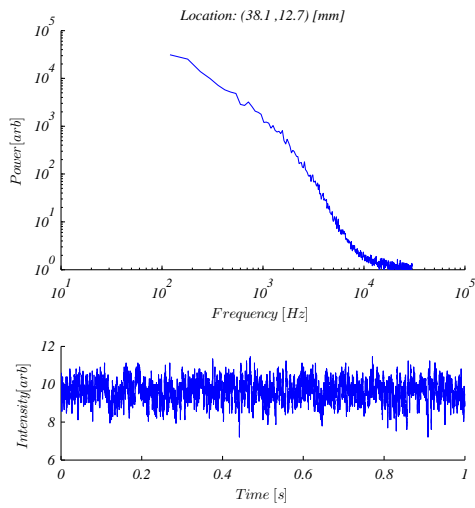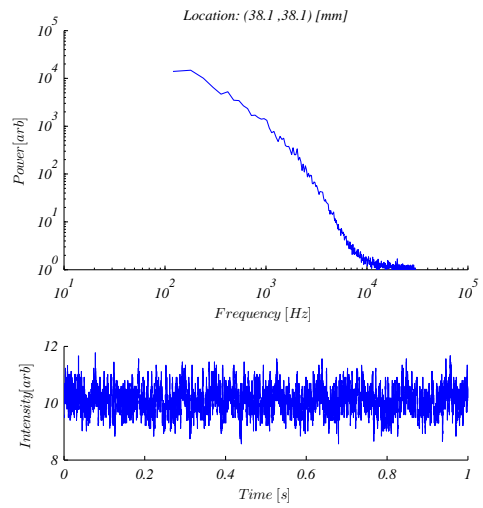
(a) $y = 13 \ mm$ (b) $y = 38 \ mm$

Figure B.6: *Velocity data and spectra recorded with hotwire.* $\bar{v} = 10 \ m/s$, $x = 38 \ mm$
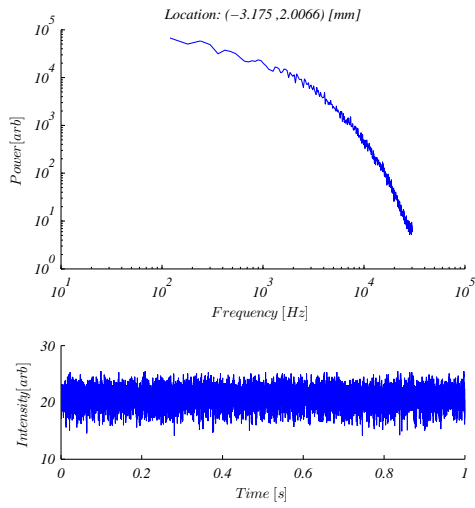
(a) $y = 2\ mm$
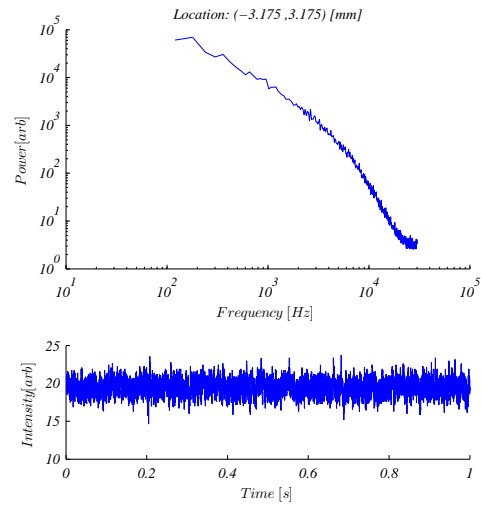
(b) $y = 3\ mm$
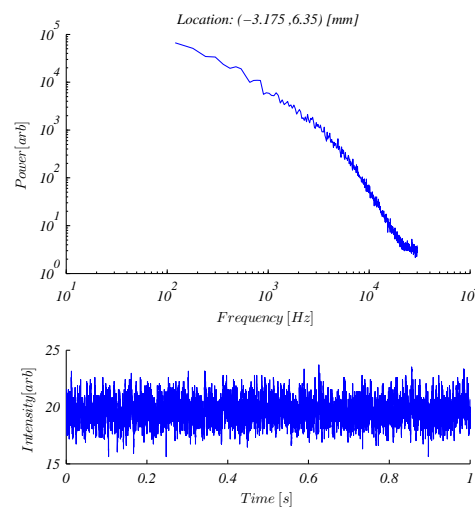
(c) $y = 6\ mm$
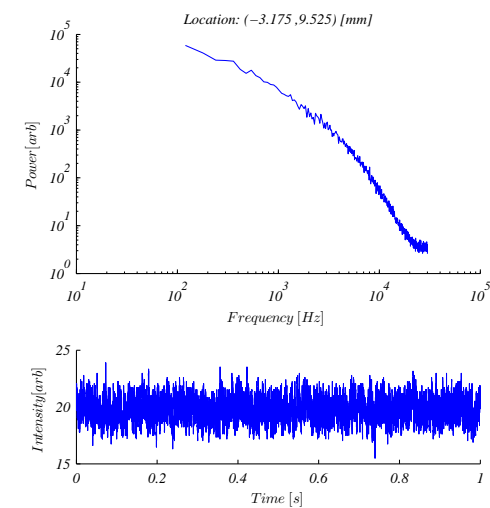
(d) $y = 10\ mm$

Figure B.7: *Velocity data and spectra recorded with hotwire.* $\bar{v} = 20\ m/s$, $x = -3\ mm$
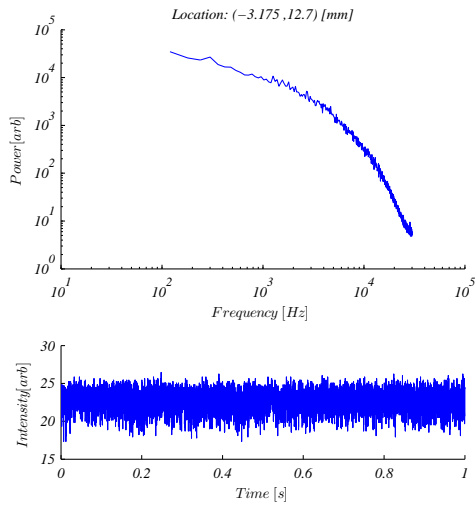
(a) $y = 13\ mm$
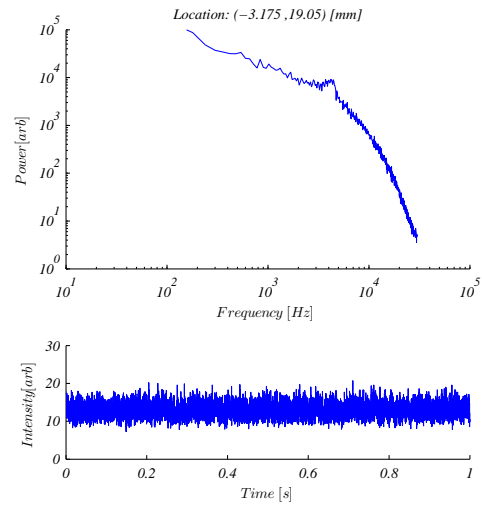
(b) $y = 19\ mm$

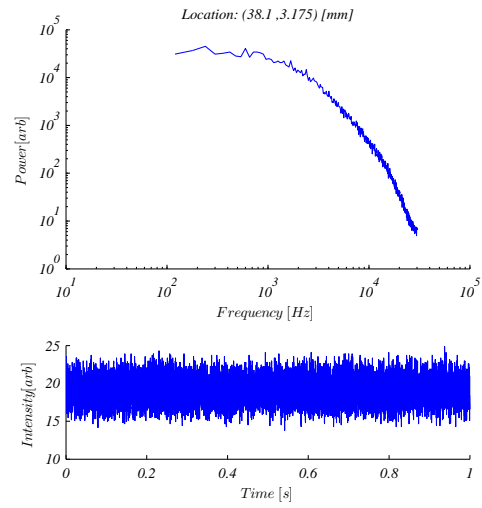(c) $y = 25\ mm$

(d) $y = 38\ mm$

Figure B.8: *Velocity data and spectra recorded with hotwire.* $\bar{v} = 20\ m/s$, $x = -3\ mm$

Figure B.9: *Velocity data and spectra recorded with hotwire.* $\bar{v} = 20\ m/s$, $x = 25\ mm$

(a) $y = 13\ mm$

(b) $y = 38\ mm$

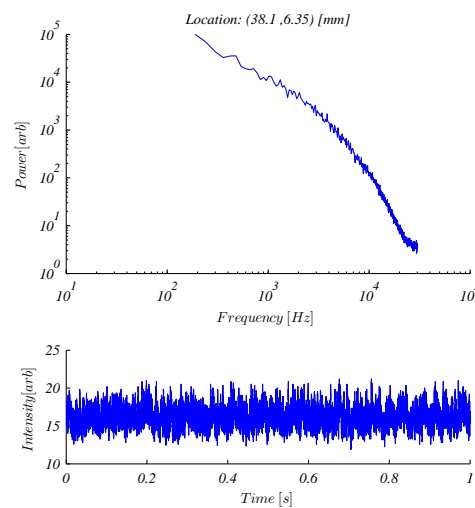Figure B.10: *Velocity data and spectra recorded with hotwire.* $\bar{v} = 20\ m/s$, $x = 25\ mm$

166

Figure B.11: *Velocity data and spectra recorded with hotwire.* $\bar{v} = 20 \ m/s$, $x = 38 \ mm$

(a) $y = 13\ mm$　　(b) $y = 38\ mm$

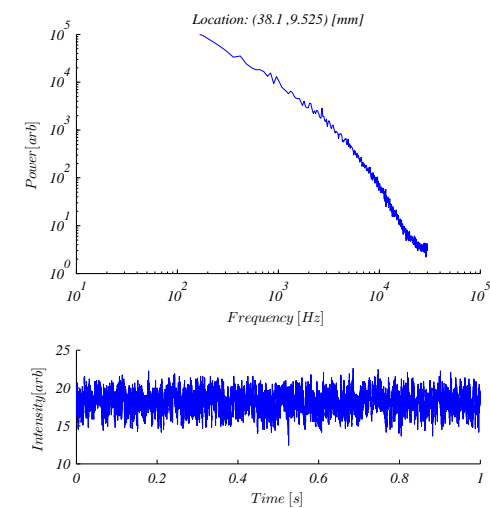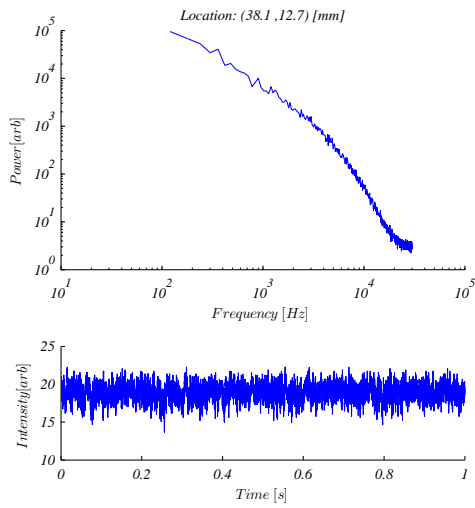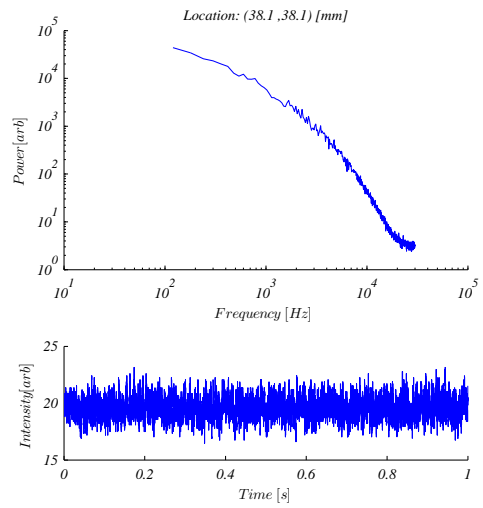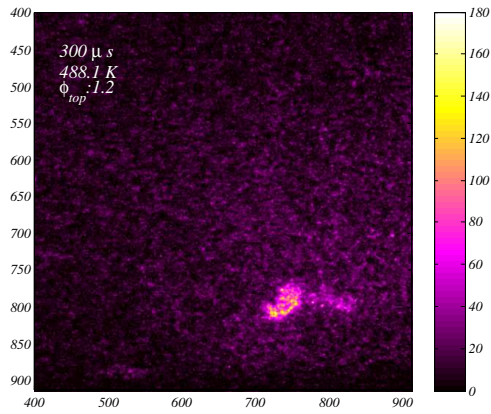Figure B.12: *Velocity data and spectra recorded with hotwire.* $\bar{v} = 20\ m/s$, $x = 38\ mm$

168

B.2 CH PLIF Images

(a) 300 μs, trial 15, event 15
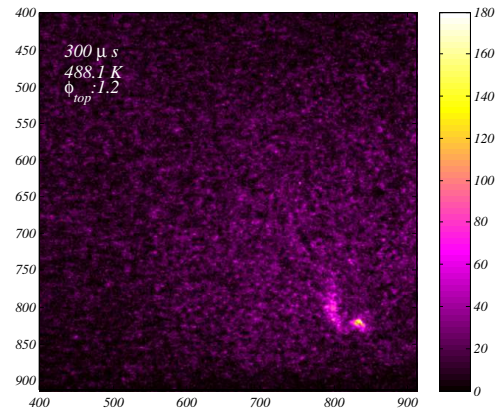
(b) 300 μs, trial 15, event 18

(c) 300 μs, trial 15, event 24

(d) 300 μs, trial 15, event 25

(e) 300 μs, trial 16, event 24

Figure B.13: 300 μs CH PLIF images

170

(a) 450 μs, trial 23, event 26

(b) 450 μs, trial 23, event 27

(c) 450 μs, trial 23, event 29
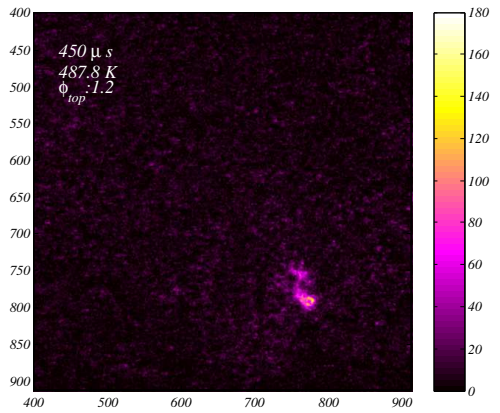
(d) 450 μs, trial 24, event 17

(e) 450 μs, trial 24, event 22

Figure B.14: 450 μs CH PLIF images

(a) 600 μs, trial 5, event 23
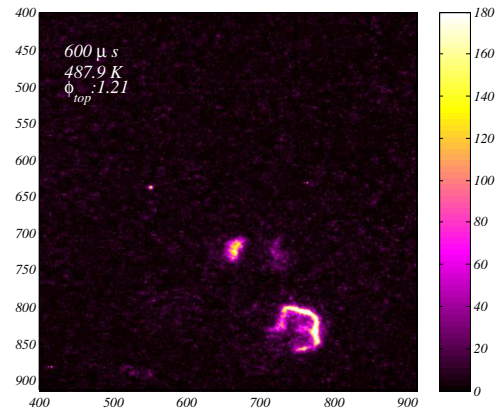
(b) 600 μs, trial 5, event 26
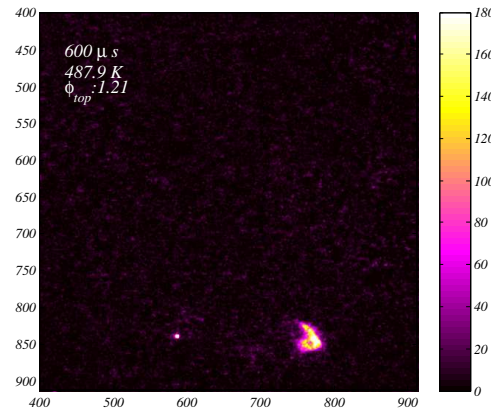
(c) 600 μs, trial 5, event 30

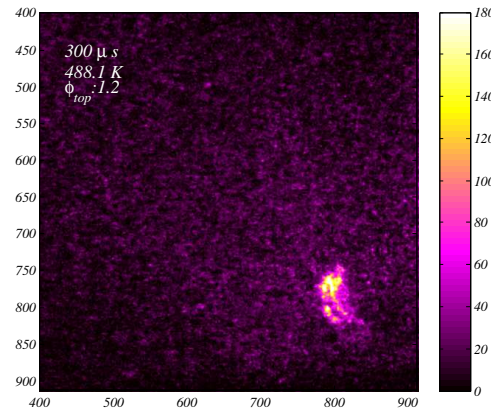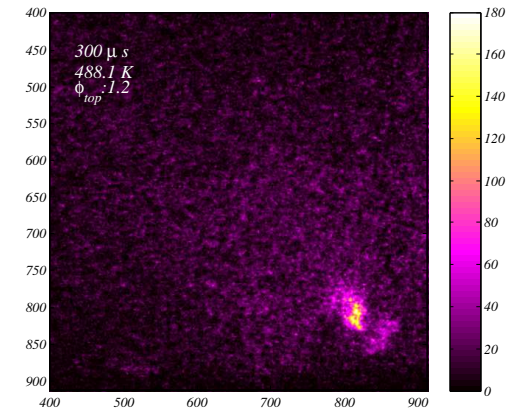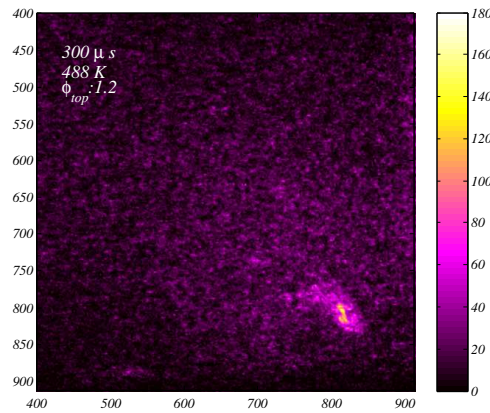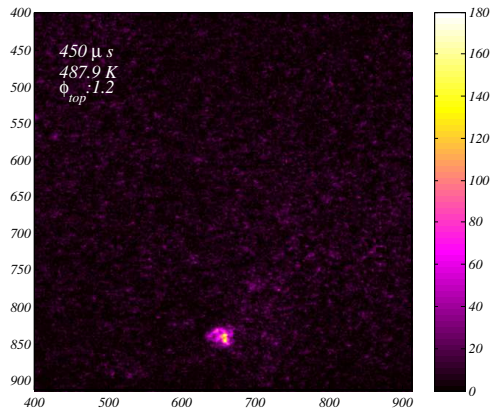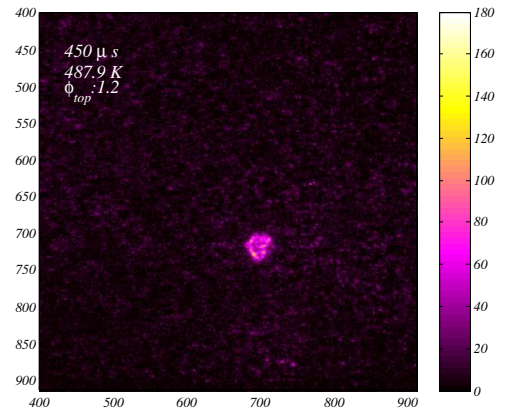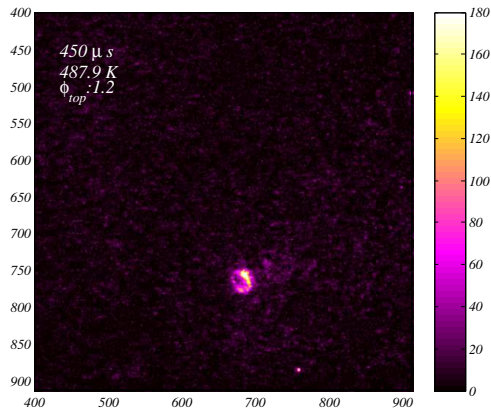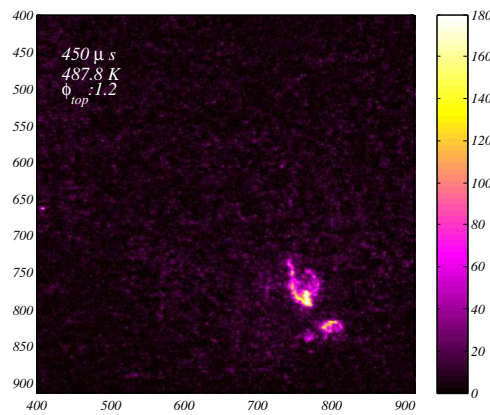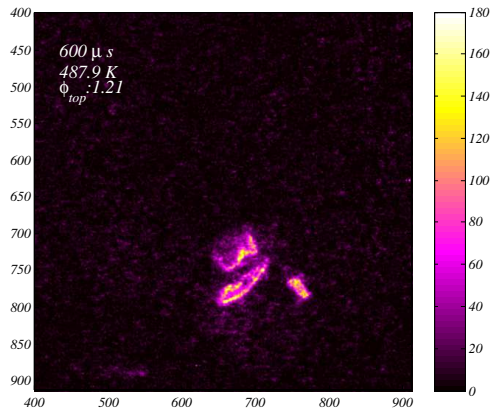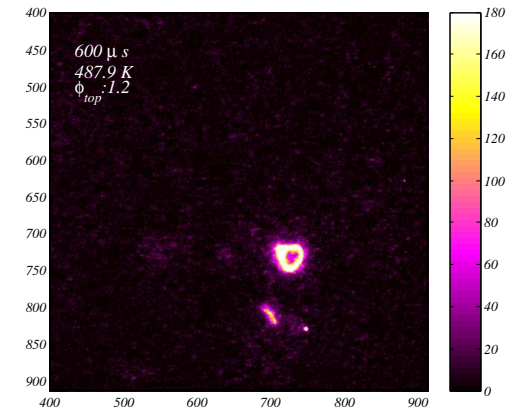(d) 600 μs, trial 8, event 13
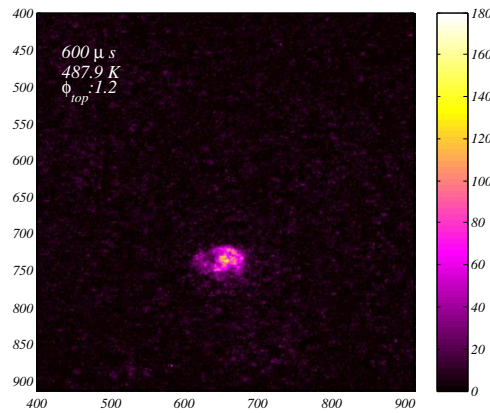
(e) 600 μs, trial 8, event 17

Figure B.15: 600 μs CH PLIF images

B.3 Ignition Probability Database

Table B.1: *Ignition probability testing conditions and results*

Date	$\bar{v}$ [m/s]	T_i [K]	h_s [mm]	ϕ_{top}	ϕ_{bottom}	Shots	Success	$P(ign)$
10/26/2012	20.0	294.3	12.70	1.50	0.00	135	0	0.000
10/26/2012	20.0	294.3	12.70	1.40	0.00	135	0	0.000
10/26/2012	20.0	294.3	12.70	1.30	0.00	135	0	0.000
10/26/2012	20.0	294.3	12.70	1.20	0.00	135	0	0.000
10/26/2012	20.0	294.3	12.70	1.10	0.00	135	0	0.000
10/26/2012	20.0	294.3	12.70	1.00	0.00	135	0	0.000
10/26/2012	20.0	294.3	12.70	0.90	0.00	135	0	0.000
10/26/2012	20.0	294.3	12.70	0.70	0.00	135	0	0.000
10/26/2012	10.0	294.3	12.70	1.50	0.00	135	0	0.000
10/26/2012	10.0	294.3	12.70	1.40	0.00	135	0	0.000
10/26/2012	10.0	294.3	12.70	1.30	0.00	135	0	0.000
10/26/2012	10.0	294.3	12.70	1.20	0.00	135	0	0.000
10/26/2012	10.0	294.3	12.70	1.10	0.00	135	0	0.000
10/26/2012	10.0	294.3	12.70	1.00	0.00	135	0	0.000
10/26/2012	10.0	294.3	12.70	0.90	0.00	135	0	0.000
10/26/2012	10.0	294.3	12.70	0.70	0.00	135	0	0.000
11/5/2012	20.0	294.3	9.53	1.40	0.00	136	0	0.000
11/5/2012	20.0	294.3	9.53	1.30	0.00	136	0	0.000
11/5/2012	20.0	294.3	9.53	1.20	0.00	136	1	0.007
11/5/2012	20.0	294.3	9.53	1.10	0.00	136	0	0.000
11/5/2012	20.0	294.3	9.53	1.00	0.00	136	0	0.000
11/5/2012	20.0	294.3	9.53	0.90	0.00	136	0	0.000

Continued on next page

Date	$\bar{v}$ [m/s]	T_i [K]	h_s [mm]	ϕ_{top}	ϕ_{bottom}	Shots	Success	P(ign)
11/5/2012	20.0	294.3	9.53	0.80	0.00	136	0	0.000
11/5/2012	20.0	294.3	9.53	0.70	0.00	136	0	0.000
11/5/2012	15.0	294.3	9.53	1.50	0.00	136	0	0.000
11/5/2012	15.0	294.3	9.53	1.40	0.00	136	0	0.000
11/5/2012	15.0	294.3	9.53	1.30	0.00	136	1	0.007
11/5/2012	15.0	294.3	9.53	1.20	0.00	136	0	0.000
11/5/2012	15.0	294.3	9.53	1.10	0.00	136	1	0.007
11/5/2012	15.0	294.3	9.53	1.00	0.00	136	0	0.000
11/5/2012	15.0	294.3	9.53	0.90	0.00	136	0	0.000
11/5/2012	10.0	294.3	9.53	1.40	0.00	136	0	0.000
11/5/2012	10.0	294.3	9.53	1.30	0.00	136	4	0.029
11/5/2012	10.0	294.3	9.53	1.20	0.00	136	2	0.015
11/5/2012	10.0	294.3	9.53	1.10	0.00	136	0	0.000
11/5/2012	10.0	294.3	9.53	1.00	0.00	136	0	0.000
11/5/2012	10.0	294.3	9.53	0.90	0.00	136	0	0.000
11/5/2012	10.0	294.3	9.53	0.80	0.00	136	0	0.000
11/5/2012	10.0	294.3	9.53	0.70	0.00	136	0	0.000
11/7/2012	30.0	294.3	7.94	1.06	0.00	135	1	0.007
11/7/2012	30.0	294.3	7.94	1.00	0.00	135	1	0.007
11/7/2012	30.0	294.3	7.94	0.90	0.00	135	0	0.000
11/7/2012	30.0	294.3	7.94	0.80	0.00	135	0	0.000
11/7/2012	30.0	294.3	7.94	0.70	0.00	135	0	0.000
11/7/2012	15.0	294.3	7.94	1.40	0.00	135	1	0.007
11/7/2012	15.0	294.3	7.94	1.30	0.00	136	2	0.015

Table B.1 – *Continued from previous page*

Date	$\bar{v}$ [m/s]	T_i [K]	h_s [mm]	ϕ_{top}	ϕ_{bottom}	Shots	Success	P(ign)
11/7/2012	15.0	294.3	7.94	1.20	0.00	136	10	0.074
11/7/2012	15.0	294.3	7.94	1.10	0.00	135	1	0.007
11/7/2012	15.0	294.3	7.94	1.00	0.00	136	1	0.007
11/7/2012	15.0	294.3	7.94	0.90	0.00	136	0	0.000
11/7/2012	15.0	294.3	7.94	0.80	0.00	135	0	0.000
11/7/2012	15.0	294.3	7.94	0.70	0.00	135	0	0.000
11/8/2012	25.0	294.3	7.94	1.28	0.00	135	0	0.000
11/8/2012	25.0	294.3	7.94	1.20	0.00	135	7	0.052
11/8/2012	25.0	294.3	7.94	1.10	0.00	135	2	0.015
11/8/2012	25.0	294.3	7.94	1.00	0.00	135	0	0.000
11/8/2012	25.0	294.3	7.94	0.90	0.00	135	0	0.000
11/8/2012	25.0	294.3	7.94	0.80	0.00	135	0	0.000
11/8/2012	25.0	294.3	7.94	0.70	0.00	135	0	0.000
11/8/2012	20.0	294.3	7.94	1.40	0.00	135	0	0.000
11/8/2012	20.0	294.3	7.94	1.30	0.00	136	15	0.110
11/8/2012	20.0	294.3	7.94	1.20	0.00	135	5	0.037
11/8/2012	20.0	294.3	7.94	1.10	0.00	136	6	0.044
11/8/2012	20.0	294.3	7.94	1.00	0.00	135	0	0.000
11/8/2012	20.0	294.3	7.94	0.90	0.00	135	0	0.000
11/8/2012	20.0	294.3	7.94	0.80	0.00	135	0	0.000
11/8/2012	20.0	294.3	7.94	0.70	0.00	135	0	0.000
11/8/2012	10.0	294.3	7.94	1.40	0.00	136	7	0.051
11/8/2012	10.0	294.3	7.94	1.30	0.00	136	7	0.051
11/8/2012	10.0	294.3	7.94	1.20	0.00	136	3	0.022

Continued on next page

Table B.1 – *Continued from previous page*

Date	$\bar{v}$ [m/s]	T_i [K]	h_s [mm]	ϕ_{top}	ϕ_{bottom}	Shots	Success	P(ign)
11/8/2012	10.0	294.3	7.94	1.10	0.00	136	0	0.000
11/8/2012	10.0	294.3	7.94	1.00	0.00	136	2	0.015
11/8/2012	10.0	294.3	7.94	0.90	0.00	135	0	0.000
11/8/2012	10.0	294.3	7.94	0.80	0.00	135	0	0.000
11/8/2012	10.0	294.3	7.94	0.70	0.00	135	0	0.000
11/9/2012	20.0	324.8	6.35	1.40	0.00	135	21	0.156
11/9/2012	20.0	324.8	6.35	1.30	0.00	136	31	0.228
11/9/2012	20.0	324.8	6.35	1.20	0.00	135	37	0.274
11/9/2012	20.0	324.8	6.35	1.10	0.00	135	4	0.030
11/9/2012	20.0	324.8	6.35	0.90	0.00	135	16	0.119
11/9/2012	20.0	324.3	6.35	1.00	0.00	135	5	0.037
11/9/2012	20.0	324.3	6.35	0.80	0.00	135	0	0.000
11/9/2012	20.0	323.7	6.35	0.70	0.00	135	0	0.000
11/9/2012	30.0	294.3	6.35	1.05	0.00	136	2	0.015
11/9/2012	30.0	294.3	6.35	1.00	0.00	271	5	0.018
11/9/2012	30.0	294.3	6.35	0.90	0.00	136	1	0.007
11/9/2012	30.0	294.3	6.35	0.80	0.00	135	0	0.000
11/9/2012	30.0	294.3	6.35	0.70	0.00	135	0	0.000
11/9/2012	25.0	294.3	6.35	1.28	0.00	270	2	0.007
11/9/2012	25.0	294.3	6.35	1.20	0.00	136	1	0.007
11/9/2012	25.0	294.3	6.35	1.10	0.00	135	11	0.081
11/9/2012	25.0	294.3	6.35	1.00	0.00	135	5	0.037
11/9/2012	25.0	294.3	6.35	0.90	0.00	135	1	0.007
11/9/2012	25.0	294.3	6.35	0.80	0.00	135	0	0.000

Continued on next page

Table B.1 – *Continued from previous page*

Date	$\bar{v}$ [m/s]	T_i [K]	h_s [mm]	ϕ_{top}	ϕ_{bottom}	Shots	Success	P(ign)
11/9/2012	25.0	294.3	6.35	0.70	0.00	135	0	0.000
11/9/2012	20.0	294.3	6.35	1.40	0.00	270	7	0.026
11/9/2012	20.0	294.3	6.35	1.30	0.00	271	14	0.052
11/9/2012	20.0	294.3	6.35	1.20	0.00	270	16	0.059
11/9/2012	20.0	294.3	6.35	1.10	0.00	271	16	0.059
11/9/2012	20.0	294.3	6.35	1.00	0.00	272	5	0.018
11/9/2012	20.0	294.3	6.35	0.90	0.00	135	0	0.000
11/9/2012	20.0	294.3	6.35	0.80	0.00	135	0	0.000
11/9/2012	20.0	294.3	6.35	0.70	0.00	135	0	0.000
11/9/2012	15.0	294.3	6.35	1.40	0.00	136	2	0.015
11/9/2012	15.0	294.3	6.35	1.30	0.00	135	17	0.126
11/9/2012	15.0	294.3	6.35	1.20	0.00	136	21	0.154
11/9/2012	15.0	294.3	6.35	1.10	0.00	136	16	0.118
11/9/2012	15.0	294.3	6.35	1.00	0.00	135	5	0.037
11/9/2012	15.0	294.3	6.35	0.90	0.00	135	1	0.007
11/9/2012	15.0	294.3	6.35	0.80	0.00	135	0	0.000
11/9/2012	15.0	294.3	6.35	0.70	0.00	135	0	0.000
11/9/2012	10.0	294.3	6.35	1.40	0.00	136	4	0.029
11/9/2012	10.0	294.3	6.35	1.30	0.00	271	35	0.129
11/9/2012	10.0	294.3	6.35	1.20	0.00	271	15	0.055
11/9/2012	10.0	294.3	6.35	1.10	0.00	272	6	0.022
11/9/2012	10.0	294.3	6.35	1.00	0.00	272	19	0.070
11/9/2012	10.0	294.3	6.35	0.90	0.00	272	4	0.015
11/9/2012	10.0	294.3	6.35	0.80	0.00	135	0	0.000

Table B.1 – *Continued from previous page*

Date	$\bar{v}$ [m/s]	T_i [K]	h_s [mm]	ϕ_{top}	ϕ_{bottom}	Shots	Success	P(ign)
11/9/2012	10.0	294.3	6.35	0.70	0.00	135	0	0.000
11/13/2012	20.0	533.2	6.35	1.10	0.00	136	111	0.816
11/13/2012	20.0	519.3	6.35	1.10	0.00	135	102	0.756
11/13/2012	20.0	502.6	6.35	1.10	0.00	136	93	0.684
11/13/2012	20.0	483.2	6.35	1.10	0.00	136	112	0.824
11/13/2012	20.0	464.8	6.35	1.10	0.00	136	97	0.713
11/13/2012	20.0	444.3	6.35	1.10	0.00	135	89	0.659
11/13/2012	20.0	422.0	6.35	1.10	0.00	135	35	0.259
11/13/2012	20.0	405.4	6.35	1.10	0.00	135	49	0.363
11/13/2012	20.0	380.4	6.35	1.10	0.00	135	35	0.259
11/13/2012	20.0	355.4	6.35	1.10	0.00	135	29	0.215
11/13/2012	20.0	335.9	6.35	1.10	0.00	135	17	0.126
11/13/2012	20.0	305.4	6.35	1.10	0.00	135	12	0.089
11/15/2012	20.0	455.4	6.35	1.40	0.00	136	88	0.647
11/15/2012	20.0	455.4	6.35	1.30	0.00	136	107	0.787
11/15/2012	20.0	455.4	6.35	1.20	0.00	136	111	0.816
11/15/2012	20.0	455.4	6.35	1.10	0.00	136	98	0.721
11/15/2012	20.0	455.4	6.35	1.00	0.00	136	70	0.515
11/15/2012	20.0	455.4	6.35	0.90	0.00	136	59	0.434
11/15/2012	20.0	455.4	6.35	0.80	0.00	136	31	0.228
11/15/2012	20.0	449.8	6.35	0.70	0.00	136	5	0.037
11/15/2012	20.0	455.4	6.35	0.60	0.00	136	0	0.000
11/15/2012	20.0	444.3	6.35	1.10	0.00	136	37	0.272
11/15/2012	20.0	422.0	6.35	1.10	0.00	136	56	0.412

Date	$\bar{v}$ [m/s]	T_i [K]	h_s [mm]	ϕ_{top}	ϕ_{bottom}	Shots	Success	$P(ign)$
11/15/2012	20.0	405.4	6.35	1.10	0.00	136	41	0.301
11/15/2012	20.0	388.7	6.35	1.10	0.00	136	56	0.412
11/15/2012	20.0	374.8	6.35	1.10	0.00	136	43	0.316
11/15/2012	20.0	349.8	6.35	1.10	0.00	136	36	0.265
11/15/2012	20.0	330.4	6.35	1.10	0.00	136	13	0.096
11/15/2012	20.0	306.5	6.35	1.10	0.00	136	4	0.029
11/19/2012	20.0	455.4	9.53	0.60	0.00	135	0	0.000
11/19/2012	20.0	455.4	9.53	0.70	0.00	135	2	0.015
11/19/2012	20.0	454.8	9.53	0.80	0.00	135	10	0.074
11/19/2012	20.0	454.3	9.53	0.90	0.00	136	5	0.037
11/19/2012	20.0	453.7	9.53	1.00	0.00	136	9	0.066
11/19/2012	20.0	453.2	9.53	1.10	0.00	136	15	0.110
11/19/2012	20.0	453.2	9.53	1.20	0.00	135	33	0.244
11/19/2012	20.0	453.2	9.53	1.30	0.00	135	13	0.096
11/19/2012	20.0	452.6	9.53	1.40	0.00	136	26	0.191
11/19/2012	20.0	452.6	9.53	1.50	0.00	135	5	0.037
11/20/2012	20.0	447.0	12.70	0.60	0.00	136	0	0.000
11/20/2012	20.0	449.8	12.70	0.70	0.00	136	0	0.000
11/20/2012	20.0	450.9	12.70	0.80	0.00	136	0	0.000
11/20/2012	20.0	452.0	12.70	0.90	0.00	136	0	0.000
11/20/2012	20.0	452.6	12.70	1.00	0.00	136	0	0.000
11/20/2012	20.0	452.6	12.70	1.10	0.00	136	6	0.044
11/20/2012	20.0	453.2	12.70	1.20	0.00	136	3	0.022
11/20/2012	20.0	453.7	12.70	1.30	0.00	136	2	0.015

179

Date	$\bar{v}$ [m/s]	T_i [K]	h_s [mm]	ϕ_{top}	ϕ_{bottom}	Shots	Success	P(ign)
11/20/2012	20.0	453.7	12.70	1.40	0.00	136	0	0.000
11/20/2012	15.0	449.8	12.70	0.60	0.00	136	0	0.000
11/20/2012	15.0	448.7	12.70	0.70	0.00	136	0	0.000
11/20/2012	15.0	447.6	12.70	0.80	0.00	136	0	0.000
11/20/2012	15.0	446.5	12.70	0.90	0.00	136	0	0.000
11/20/2012	15.0	446.5	12.70	1.00	0.00	136	0	0.000
11/20/2012	15.0	446.5	12.70	1.10	0.00	136	2	0.015
11/20/2012	15.0	446.5	12.70	1.20	0.00	136	0	0.000
11/20/2012	15.0	445.9	12.70	1.30	0.00	136	7	0.051
11/20/2012	15.0	445.4	12.70	1.40	0.00	136	0	0.000
11/27/2012	20.0	539.8	12.70	0.60	0.00	136	0	0.000
11/27/2012	20.0	533.2	12.70	0.70	0.00	136	2	0.015
11/27/2012	20.0	536.5	12.70	0.80	0.00	136	0	0.000
11/27/2012	20.0	538.2	12.70	0.90	0.00	136	2	0.015
11/27/2012	20.0	538.7	12.70	1.00	0.00	136	2	0.015
11/27/2012	20.0	539.8	12.70	1.10	0.00	136	3	0.022
11/27/2012	20.0	539.8	12.70	1.20	0.00	136	8	0.059
11/27/2012	20.0	539.8	12.70	1.30	0.00	136	10	0.074
11/27/2012	20.0	539.8	12.70	1.40	0.00	136	6	0.044
11/27/2012	20.0	539.8	12.70	1.50	0.00	136	2	0.015
11/27/2012	20.0	316.5	12.70	1.10	0.00	136	0	0.000
11/27/2012	20.0	344.3	12.70	1.10	0.00	136	0	0.000
11/27/2012	20.0	380.4	12.70	1.10	0.00	136	0	0.000
11/27/2012	20.0	413.7	12.70	1.10	0.00	136	0	0.000

Date	$\bar{v}$ [m/s]	T_i [K]	h_s [mm]	ϕ_{top}	ϕ_{bottom}	Shots	Success	P(ign)
11/27/2012	20.0	444.3	12.70	1.10	0.00	136	2	0.015
11/27/2012	20.0	472.0	12.70	1.10	0.00	136	0	0.000
11/27/2012	20.0	492.6	12.70	1.10	0.00	136	2	0.015
11/27/2012	20.0	513.7	12.70	1.10	0.00	136	2	0.015
11/27/2012	20.0	566.5	12.70	1.10	0.00	136	4	0.029
11/27/2012	20.0	574.8	12.70	1.10	0.00	136	7	0.051
6/19/2013	20.0	294.3	6.35	1.10	0.00	135	10	0.074
6/19/2013	20.0	294.3	6.35	1.10	0.00	135	9	0.067
6/19/2013	20.0	294.3	6.35	1.10	0.05	135	23	0.170
6/19/2013	20.0	294.3	6.35	1.10	0.05	120	29	0.242
6/19/2013	20.0	294.3	6.35	1.10	0.00	135	14	0.104
6/27/2013	20.0	295.6	9.53	1.10	0.00	135	2	0.015
6/27/2013	20.0	294.9	9.53	1.10	0.00	135	1	0.007
6/27/2013	20.0	294.8	9.53	1.10	0.05	135	3	0.022
6/27/2013	20.0	294.8	9.53	1.10	0.05	135	1	0.007
6/28/2013	10.0	294.3	9.53	1.40	0.05	135	0	0.000
6/28/2013	10.0	294.3	9.53	1.40	0.05	135	0	0.000
6/28/2013	20.0	533.2	9.53	1.10	0.00	135	68	0.504
6/28/2013	20.0	533.2	9.53	1.10	0.00	135	70	0.519
6/28/2013	20.0	533.2	9.53	1.10	0.05	135	73	0.541
6/28/2013	20.0	533.2	9.53	1.10	0.05	135	68	0.504
7/1/2013	30.0	294.3	9.53	1.05	0.00	135	0	0.000
7/1/2013	30.0	294.3	9.53	1.05	0.00	135	0	0.000
7/1/2013	10.0	533.2	9.53	1.10	0.00	135	42	0.311

Continued on next page

Table B.1 – *Continued from previous page*

Date	$\bar{v}$ [m/s]	T_i [K]	h_s [mm]	ϕ_{top}	ϕ_{bottom}	Shots	Success	P(ign)
7/1/2013	10.0	533.2	9.53	1.10	0.00	135	40	0.296
7/1/2013	30.0	533.2	9.53	0.80	0.05	135	18	0.133
7/1/2013	30.0	533.2	9.53	0.80	0.05	135	40	0.296
7/1/2013	20.0	533.2	9.53	0.80	0.00	135	13	0.096
7/1/2013	20.0	533.2	9.53	0.80	0.00	135	26	0.193
7/2/2013	20.0	294.3	6.35	0.80	0.05	135	0	0.000
7/2/2013	20.0	294.3	6.35	0.80	0.05	135	2	0.015
7/2/2013	10.0	294.3	6.35	0.80	0.00	135	0	0.000
7/2/2013	10.0	294.3	6.35	0.80	0.00	135	0	0.000
7/9/2013	30.0	527.6	6.35	1.30	0.05	135	121	0.896
7/9/2013	30.0	530.4	6.35	1.30	0.05	135	126	0.933
7/9/2013	10.0	527.6	6.35	1.10	0.05	135	116	0.859
7/9/2013	10.0	527.6	6.35	1.10	0.05	135	118	0.874
7/9/2013	20.0	527.6	6.35	1.40	0.00	135	117	0.867
7/9/2013	20.0	527.6	6.35	1.40	0.00	135	121	0.896
7/9/2013	30.0	527.6	6.35	1.10	0.00	135	104	0.770
7/9/2013	30.0	527.6	6.35	1.10	0.00	135	82	0.607
7/11/2013	30.0	294.9	12.70	1.10	0.05	135	0	0.000
7/11/2013	30.0	294.9	12.70	1.10	0.05	135	0	0.000
7/11/2013	20.0	294.3	12.70	1.10	0.00	135	0	0.000
7/11/2013	20.0	294.3	12.70	1.10	0.00	153	0	0.000
7/12/2013	10.0	524.8	12.70	1.40	0.00	135	0	0.000
7/12/2013	10.0	523.2	12.70	0.80	0.05	135	1	0.007
7/12/2013	10.0	522.0	12.70	0.80	0.05	135	11	0.081

Date	$\bar{v}$ [m/s]	T_i [K]	h_s [mm]	ϕ_{top}	ϕ_{bottom}	Shots	Success	P(ign)
7/12/2013	40.0	522.0	12.70	0.80	0.00	135	0	0.000
7/12/2013	40.0	523.2	12.70	0.80	0.00	135	0	0.000
7/12/2013	20.0	524.8	12.70	1.40	0.05	135	18	0.133
7/12/2013	20.0	524.8	12.70	1.40	0.05	135	26	0.193
7/30/2013	20.0	317.6	6.35	1.10	0.00	109	3	0.028
7/30/2013	20.0	382.6	6.35	0.60	0.00	135	0	0.000
7/30/2013	20.0	385.4	6.35	1.10	0.00	132	36	0.273
7/30/2013	20.0	427.6	6.35	0.80	0.00	135	62	0.459
7/30/2013	20.0	431.5	6.35	1.40	0.00	135	70	0.519
7/30/2013	20.0	516.5	6.35	0.80	0.00	135	30	0.222
7/30/2013	20.0	519.3	6.35	1.20	0.00	135	123	0.911
7/30/2013	20.0	518.2	6.35	1.20	0.00	135	90	0.667
7/30/2013	20.0	517.0	6.35	0.80	0.00	135	52	0.385
7/30/2013	20.0	425.9	6.35	1.40	0.00	135	83	0.615
7/30/2013	20.0	415.4	6.35	0.80	0.00	135	107	0.793
7/30/2013	20.0	385.4	6.35	1.10	0.00	135	42	0.311
7/30/2013	20.0	380.4	6.35	0.60	0.00	135	0	0.000
7/30/2013	20.0	316.5	6.35	1.10	0.00	135	9	0.067
7/30/2013	20.0	326.5	6.35	1.10	0.00	135	14	0.104
7/30/2013	20.0	327.6	6.35	1.10	0.05	135	28	0.207
7/30/2013	20.0	328.2	6.35	1.10	0.10	135	22	0.163
8/2/2013	20.0	294.3	7.94	0.90	0.00	135	0	0.000
8/2/2013	20.0	337.0	7.94	0.70	0.00	135	0	0.000
8/2/2013	20.0	338.7	7.94	1.30	0.00	135	4	0.030

183

Table B.1 – *Continued from previous page*

Date	$\bar{v}$ [m/s]	T_i [K]	h_s [mm]	ϕ_{top}	ϕ_{bottom}	Shots	Success	P(ign)
8/2/2013	20.0	360.9	7.94	0.91	0.00	135	1	0.007
8/2/2013	20.0	403.7	7.94	0.60	0.00	135	0	0.000
8/2/2013	20.0	405.4	7.94	1.00	0.00	135	5	0.037
8/2/2013	20.0	408.2	7.94	1.20	0.00	135	16	0.119
8/2/2013	20.0	450.4	7.94	1.21	0.00	135	31	0.230
8/2/2013	20.0	470.4	7.94	0.70	0.00	135	3	0.022
8/2/2013	20.0	474.3	7.94	0.90	0.00	135	18	0.133
8/2/2013	20.0	478.2	7.94	1.40	0.00	135	21	0.156
8/2/2013	20.0	538.7	7.94	0.91	0.00	135	38	0.281
8/2/2013	20.0	537.6	7.94	0.90	0.00	135	41	0.304
8/2/2013	20.0	470.4	7.94	1.40	0.00	135	44	0.326
8/2/2013	20.0	466.5	7.94	0.90	0.00	135	9	0.067
8/2/2013	20.0	462.6	7.94	0.70	0.00	135	2	0.015
8/2/2013	19.9	449.3	7.94	1.20	0.00	135	39	0.289
8/2/2013	20.0	406.5	7.94	1.20	0.00	135	23	0.170
8/2/2013	20.0	402.6	7.94	1.00	0.00	135	7	0.052
8/2/2013	20.1	398.7	7.94	0.60	0.00	135	0	0.000
8/2/2013	20.0	359.8	7.94	0.91	0.00	135	3	0.022
8/2/2013	20.1	341.5	7.94	1.30	0.00	135	0	0.000
8/2/2013	20.0	338.7	7.94	0.71	0.00	135	0	0.000
8/12/2013	20.0	315.4	9.53	0.80	0.00	30	0	0.000
8/12/2013	19.9	317.6	9.53	1.30	0.00	122	1	0.008
8/12/2013	20.0	335.9	9.53	0.60	0.00	135	0	0.000
8/12/2013	20.0	338.7	9.53	1.10	0.00	135	3	0.022

184

Table B.1 – *Continued from previous page*

Date	$\bar{v}$ [m/s]	T_i [K]	h_s [mm]	ϕ_{top}	ϕ_{bottom}	Shots	Success	P(ign)
8/12/2013	20.0	360.9	9.53	1.40	0.00	135	0	0.000
9/18/2013	20.0	449.8	9.53	1.10	0.00	135	4	0.030
9/18/2013	20.0	472.0	9.53	0.90	0.00	135	4	0.030
9/18/2013	20.0	494.3	9.53	0.60	0.00	135	0	0.000
9/18/2013	20.0	498.2	9.53	1.10	0.00	135	28	0.207
9/18/2013	20.0	500.9	9.53	1.30	0.00	135	39	0.289
8/19/2013	20.0	292.6	11.11	0.80	0.00	135	0	0.000
8/19/2013	20.0	292.6	11.11	1.30	0.00	135	0	0.000
8/19/2013	20.0	316.5	11.11	1.00	0.00	135	0	0.000
8/19/2013	20.0	360.9	11.11	1.30	0.00	135	1	0.007
8/19/2013	20.0	383.2	11.11	0.70	0.00	135	0	0.000
8/19/2013	20.0	405.4	11.11	1.10	0.00	135	0	0.000
8/19/2013	20.0	427.6	11.11	1.40	0.00	135	2	0.015
8/19/2013	20.0	448.2	11.11	0.70	0.00	135	0	0.000
8/19/2013	20.0	454.3	11.11	1.00	0.00	135	1	0.007
8/19/2013	20.0	515.4	11.11	0.80	0.00	135	0	0.000
8/19/2013	20.0	523.7	11.11	1.00	0.00	135	11	0.081
8/19/2013	20.0	538.7	11.11	1.20	0.00	135	27	0.200
8/20/2013	20.0	338.7	12.70	1.20	0.00	135	0	0.000
8/20/2013	20.0	369.3	12.70	0.90	0.00	135	0	0.000
8/20/2013	20.0	405.4	12.70	1.30	0.00	135	1	0.007
8/20/2013	20.0	427.6	12.70	0.80	0.00	135	0	0.000
8/20/2013	20.0	449.8	12.70	1.20	0.00	135	1	0.007
8/20/2013	20.0	492.6	12.70	0.70	0.00	135	0	0.000

185

Table B.1 – *Continued from previous page*

Date	$\bar{v}$ [m/s]	T_i [K]	h_s [mm]	ϕ_{top}	ϕ_{bottom}	Shots	Success	P(ign)
8/20/2013	20.0	497.0	12.70	1.00	0.00	135	1	0.007
8/12/2013	20.0	315.4	9.53	0.80	0.00	135	0	0.000
8/12/2013	20.0	317.6	9.53	1.30	0.00	135	2	0.015
8/12/2013	20.0	334.8	9.53	0.60	0.00	135	0	0.000
8/12/2013	20.0	339.3	9.53	1.10	0.00	135	1	0.007
8/12/2013	20.0	360.9	9.53	1.40	0.00	135	14	0.104
9/18/2013	20.0	377.6	9.53	0.70	0.00	135	1	0.007
9/18/2013	20.0	382.6	9.53	1.00	0.00	135	1	0.007
9/18/2013	20.0	449.8	9.53	1.10	0.00	135	10	0.074
9/18/2013	20.0	470.4	9.53	0.90	0.00	135	8	0.059
9/18/2013	20.0	492.6	9.53	0.60	0.00	135	0	0.000
9/18/2013	20.0	495.4	9.53	1.10	0.00	135	39	0.289
9/18/2013	20.0	498.2	9.53	1.30	0.00	135	42	0.311
8/19/2013	20.0	299.8	11.11	0.80	0.00	135	0	0.000
8/19/2013	20.0	299.8	11.11	1.30	0.00	135	1	0.007
8/19/2013	20.0	317.6	11.11	1.00	0.00	135	1	0.007
8/19/2013	20.0	360.9	11.11	1.30	0.00	100	0	0.000
8/19/2013	20.0	382.6	11.11	0.70	0.00	135	0	0.000
8/19/2013	20.0	405.4	11.11	1.10	0.00	135	1	0.007
8/19/2013	20.0	427.6	11.11	1.40	0.00	135	2	0.015
8/19/2013	20.0	448.2	11.11	0.70	0.00	135	0	0.000
8/19/2013	20.0	454.3	11.11	1.00	0.00	135	3	0.022
8/19/2013	20.0	514.8	11.11	0.80	0.00	135	1	0.007
8/19/2013	20.0	520.9	11.11	1.00	0.00	135	12	0.089

Continued on next page

186

Table B.1 – *Continued from previous page*

Date	$\bar{v}$ [m/s]	T_i [K]	h_s [mm]	ϕ_{top}	ϕ_{bottom}	Shots	Success	P(ign)
8/19/2013	20.0	539.3	11.11	1.20	0.00	135	19	0.141
8/20/2013	20.0	338.7	12.70	1.20	0.00	135	0	0.000
8/20/2013	20.0	360.4	12.70	0.90	0.00	135	2	0.015
8/20/2013	20.0	405.4	12.70	1.30	0.00	135	0	0.000
8/20/2013	20.0	426.5	12.70	0.80	0.00	135	4	0.030
8/20/2013	20.0	449.8	12.70	1.20	0.00	135	0	0.000
8/20/2013	20.0	482.0	12.70	0.70	0.00	135	0	0.000
8/20/2013	20.0	487.0	12.70	1.00	0.00	135	3	0.022

APPENDIX C

CANTERA CODE

C.1 "KernelReactor.m"

```matlab
% %%%%%%%%%%%%%%%%%%%%%%%%%%%%%%%%%%%%%%%%%%%%%%%%%%%%%%%%%%%%%%%%%%%%%%%%%%%%
% KERNEL REACTOR
% Created by Brandon Sforzo, updated July 2014
%
% PSR Stage 1: Zero-dimensional kinetics: adiabatic, constant pressure.
% Calculates the evolution of an air plasma kernel following a 1.25 J
% energy deposition. Uses deposition volumes approximated from experimental
% schlieren imaging.
% INPUT:     dt - time step for output of variables, [s]
%            endt - final evaluation time, [s]
%            mentrain - mass entrainment rate of environment gas, [kg/s]
%            Tin - initial temperature and of environment, [K]
%            pin - environment pressure [Pa]
%            Xin - mole fractions of composition after energy deposition
% OUTPUT:    Results - Structure of the following vectors at each timestep
%                        time - step time [s]
%                        Temperature - temperature [K]
%                        Pressure - pressure [Pa]
%                        Density - density [kg/m^3]
%                        Volume - volume [m^3]
%                        Mass - mass of reactor [kg]
%                        MoleFrac - array of mole fractions
% EXAMPLE EXECUTION: Results = KernelReactor(1e-8,150e-6,3e-5, 300,...
%                               oneatm, 'N2:79,O2:21');
% %%%%%%%%%%%%%%%%%%%%%%%%%%%%%%%%%%%%%%%%%%%%%%%%%%%%%%%%%%%%%%%%%%%%%%%%%%%%
function Results = KernelReactor(dt,endt,mentrain, Tin, pin, Xin)
% Spark initialization
Eign = 1.25; %J, obtained from experiments
Vign = (10e-3)*pi()/4*(5e-3)^2;% Initial reactor volume, 10mm* 5mm dia
gas = importPhase('SforzoairNASA9.cti', 'SforzoairNASA9');
```

```matlab
nsp = nSpecies(gas);
set(gas,'T',Tin,'P',pin,'X','N2:.79,O2:.21');
m = density(gas) * Vign;
Eign_mass = Eign / m; %Spark energy per mass (J/kg)
% Add spark energy density (per mass) to internal energy of air (per mass)
set(gas,'U', intEnergy_mass(gas) + Eign_mass, 'V', 1/density(gas),'X',Xin);
%Expand isentropically
set(gas,'P',pin);
equilibrate(gas,'SP');
% create a reactor, and insert the Kernel gas
Kernel = Reactor(gas);
%K Initial volume as determined by Schlieren regression
setInitialVolume( Kernel, 1.9e-8);
% Specify phase for the enviroment gas
envGas = importPhase('SforzoairNASA9.cti', 'SforzoairNASA9');
set(envGas,'T',Tin,'P',pin,'X','N2:.79,O2:.21');
% create a reservoir to represent the environment
env = Reservoir(envGas);
% Define a wall between the reactor and the environment and
% make it flexible, so that the pressure in the reactor is held
% at the environment pressure.
w = Wall;
% set wall area
setArea(w, 1.0);
install(w,Kernel,env);
% set expansion parameter. dV/dt = KA(P_1 - P_2)
setExpansionRateCoeff(w, 1.0e6);
% Create Mass flow controler regulating mass being entrained from the
% enviroment
entrain = MassFlowController(env,Kernel);
setMassFlowRate(entrain,mentrain);
% create a reactor network and insert the reactor:
network = ReactorNet({Kernel});
t = 0.0; %Initialize time
h = waitbar(0,'Please wait...'); %Create progress bar
steps = endt/dt;
%Pre-alocate memory for variables to be stored at each step
tim = zeros(round(steps),1);
temp = zeros(round(steps),1);
vol = zeros(round(steps),1);
mas = zeros(round(steps),1);
```

189

```matlab
pres = zeros(round(steps),1);
dens = zeros(round(steps),1);
x = zeros(round(steps),nsp);
for n = 1:round(steps)
    t = t + dt;
    % Perform time step and calculate the change in thermodynamic state
    advance(network, t);
    % Save kernel variables
    tim(n) = time(Kernel);
    temp(n) = temperature(Kernel);
    vol(n) = volume(Kernel);
    mas(n) = mass(Kernel);
    pres(n) = pressure(Kernel);
    dens(n) = density(Kernel);
    x(n,1:nsp) = moleFractions(gas);
    waitbar(n / steps) % Advance progress bar
end
close(h); %Close progress bar
%Save all variables into a structure for this run
Results = struct('time',tim,'Temperature',temp,'Pressure',pres,...
    'Density',dens,'Volume',vol,'Mass',mas,'MoleFrac',x);
```

190

C.2 "IgnitionReactor.m"

```matlab
% %%%%%%%%%%%%%%%%%%%%%%%%%%%%%%%%%%%%%%%%%%%%%%%%%%%%%%%%%%%%%%%%%%%%%%%%%%%%
% IGNITION REACTOR
% Created by Brandon Sforzo, updated July,30 2014
%
% PSR Stage 2: Zero-dimensional kinetics: adiabatic, constant pressure.
% Calculates the evolution of an ignition kernel, created in a previous
% reactor as it entrains flammable methane/air environment gas. The state
% from the first reactor acts as an input and the chemical composition is
% portaged into the new mechanism.
% INPUT:      dt - time step for output of variables, [s]
%             endt - final evaluation time of THIS reactor, [s]
%             mentrain - mass entrainment rate of environment gas, [kg/s]
%             kernelProps - result structure from ignition kernel simulation
%             tau - index of kernel structure to pull variables from, [s]
%             ER - Equivalence ratio of methane/air of environment
%             Tin - temperature of environment, [K]
%             pin - environment pressure [Pa]
% OUTPUT:     Results - Structure of the following vectors at each timestep
%                       time - step time [s]
%                       Temperature - temperature [K]
%                       Pressure - pressure [Pa]
%                       Density - density [kg/m^3]
%                       Volume - volume [m^3]
%                       Mass - mass of reactor [kg]
%                       MoleFrac - array of mole fractions
% EXAMPLE EXECUTION: Results = KernelReactor(1e-8,750e-6,3e-5,...
%                                 kernelStruct,15000, 1.1, 300, oneatm,...
%                                 'CH4:1');
% %%%%%%%%%%%%%%%%%%%%%%%%%%%%%%%%%%%%%%%%%%%%%%%%%%%%%%%%%%%%%%%%%%%%%%%%%%%%
function Results = IgnitionReactor_ER(dt,endt,mentrain, kernelProps,tau, ER, Tin,↵
    pin, fuelComp)
% Import and initialize ignition kernel Phase %%%%%%%%%%%%%%%%%%
% Specify phase for ignition kernel gas
gasKernel = importPhase('NOXcombined_mech.cti', 'NOXcombined_mech');
Tkernel = kernelProps.Temperature(tau);
Pkernel = kernelProps.Pressure(tau);
```

191

```matlab
Vkernel = kernelProps.Volume(tau);
% Set mole fractions in ucsd indices to the corresponding mole fractions
% from SforzoairNASA9 mechanism
Xkernel = nasa2ucsd(kernelProps.MoleFrac(tau,:));
nsp = nSpecies(gasKernel);
% set the initial conditions for the kernel gas as it is entering the
% flammable flow
set(gasKernel,'T',Tkernel,'P',Pkernel,'X',Xkernel);
% create a reactor, and insert the Kernel gas
Kernel = Reactor(gasKernel);
setInitialVolume(Kernel, Vkernel);


% %%%%%%%%%%%%%% Flammable Main Flow Environment Phase %%%%%%%%%%
% Create the oxidizer for the flammable mixture flow - Air
oxidizer = importPhase('NOXcombined_mech.cti', 'NOXcombined_mech');
set(oxidizer,'T',Tin,'P',pin,'X','N2:.79,O2:.21');


%% Create the fuel for the flammable mixture flow
fuel = importPhase('NOXcombined_mech.cti', 'NOXcombined_mech');
set(fuel,'T',Tin,'P',pin,'X',fuelComp);
fuel_X = moleFractions(fuel);
idx = find(fuel_X);
x = zeros(numel(idx),1);
y = zeros(numel(idx),1);
for j = 1:numel(idx)
    x(j,1) = nAtoms(fuel, idx(j), elementIndex(fuel, 'C'))*fuel_X(idx(j));
    y(j,1) = nAtoms(fuel, idx(j), elementIndex(fuel, 'H'))*fuel_X(idx(j));
end
x_eff = sum(x(:,1));
y_eff = sum(y(:,1));
a = x_eff + y_eff/4;


% Specify phase for the enviroment gas - Flammable Mixture
flamGas = importPhase('NOXcombined_mech.cti', 'NOXcombined_mech');
FlamComp = zeros(nSpecies(flamGas),1);
% Create mixture based on Mole fraction of oxidixer = 1
ox = a;
n2 = a.*3.76;
FlamComp(speciesIndex(flamGas, 'N2')) = n2;
FlamComp(speciesIndex(flamGas, 'O2')) = ox;
```

```matlab
for j = 1:numel(idx)
FlamComp(idx(j)) =fuel_X(idx(j))*ER;
end


set(flamGas,'T',Tin,'P',pin, 'X',FlamComp);


%% create a reservoir of the flammable gas to represent the environment
env = Reservoir(flamGas);
% Define a wall between the reactor and the environment and
% make it flexible, so that the pressure in the reactor is held
% at the environment pressure.
w = Wall;
% set wall area
setArea(w, 1.0);
install(w,Kernel,env);
% set expansion parameter. dV/dt = KA(P_1 - P_2)
setExpansionRateCoeff(w, 1.0e6);
% Create Mass flow controler regulating mass being entrained from the
% enviroment
entrain = MassFlowController(env,Kernel);
setMassFlowRate(entrain,mentrain);
% create a reactor network and insert the reactor:
network = ReactorNet({Kernel});
% setTolerances(network, 1e-9, 1e-15)
t = 0.0; %Initialize time
h = waitbar(0,'Please wait...'); %Create progress bar
steps = endt/dt;
%Pre-alocate memory for variables to be stored at each step
tim = zeros(round(steps),1);
temp = zeros(round(steps),1);
vol = zeros(round(steps),1);
mas = zeros(round(steps),1);
pres = zeros(round(steps),1);
dens = zeros(round(steps),1);
x = zeros(round(steps),nsp);
for n = 1:round(steps)
    t = t + dt;
    % Advances network and allows variables to be saved if a computation
    % error occurs.
    try
        % Perform time step and calculate the change in state
```

193

```matlab
            advance(network, t);
    catch exception %#ok<NASGU>
            tim(n) = time(Kernel);
            temp(n) = temperature(Kernel);
            vol(n) = volume(Kernel);
            mas(n) = mass(Kernel);
            pres(n) = pressure(Kernel);
            dens(n) = density(Kernel);
            x(n,1:nsp) = moleFractions(gasKernel);
            continue
    end
    % Save kernel variables
    tim(n) = time(Kernel);
    temp(n) = temperature(Kernel);
    vol(n) = volume(Kernel);
    mas(n) = mass(Kernel);
    pres(n) = pressure(Kernel);
    dens(n) = density(Kernel);
    x(n,1:nsp) = moleFractions(gasKernel);
    waitbar(n / steps)
end
close(h);
%Save all variables into a structure for this run
Results = struct('time',tim,'Temperature',temp,'Pressure',pres,...
    'Density',dens,'Volume',vol,'Mass',mas,'MoleFrac',x);
```

C.3 "nasa2ucsd.m"

```matlab
%%%%%%%%%%%%%%%%%%%%%%%%%%%%%%%%%%%%%%%%%%%%%%%%%%%%%%%%%%%%%%%%%%%%%%%%%%%%%%
% NASA 2 UCSD
% Created by Brandon Sforzo, updated July 2014
%
% Transfers the values of mole fractions from the NASA mechanism indexing
% convention to the UCSD mechanism. Ion values are combined with their
% neutral analogues
% INPUT:    Xnasa - mole fraction values indexed according to NASA9
% OUTPUT:   UCSD - same mole fraction values indexed according to UCSD
%%%%%%%%%%%%%%%%%%%%%%%%%%%%%%%%%%%%%%%%%%%%%%%%%%%%%%%%%%%%%%%%%%%%%%%%%%%%%%
function XSD = nasa2ucsd(Xnasa)
UCSD = importPhase('NOXcombined_mech.cti', 'NOXcombined_mech');
N2 = Xnasa(1) + Xnasa(6);    % XN2 + XN2+
O2 = Xnasa(2) + Xnasa(7);    % XO2 + XO2+
NO = Xnasa(3) + Xnasa(8);    % XNO + XNO+
N  = Xnasa(4) + Xnasa(9);    % XN  + XN+
O  = Xnasa(5) + Xnasa(10);   % XO  + XO+
% Sets all species mole fraction values to zero
XSD = zeros(nSpecies(UCSD),1);
% Applies mole fractions under new indices
XSD(speciesIndex(UCSD, 'N2')) = N2;
XSD(speciesIndex(UCSD, 'O2')) = O2;
XSD(speciesIndex(UCSD, 'NO')) = NO;
XSD(speciesIndex(UCSD, 'N')) = N;
XSD(speciesIndex(UCSD, 'O')) = O;
```

C.4 "monteNorm.m"

```matlab
function S = monteNorm(mu,sig,points)
% Function used to simulate a random event with a normal distribution using
% the sum of 100 independent random samples

% points: quantity of returned values
% mu: expected value desired for variable
% sig: the standard deviation for the variable

% points = 1000;
sums = 100;

M = rand([points,sums])-0.5;
S = sum(M,2);
S = (sig*S/std(S))+mu;
%   hist(S,20)
```

REFERENCES

[1] S. R. Turns, *An introduction to combustion: concepts and applications.* No. v. 1 in McGraw-Hill series in mechanical engineering, WCB/McGraw-Hill, 2000.

[2] I. Glassman, *Combustion.* Amsterdam ;: Elsevier, 4th ed. ed., 2008. Previous ed.: 1996.

[3] D. Topham, P. Smy, and R. Clements, "An investigation of a coaxial spark igniter with emphasis on its practical use," *Combustion and Flame*, vol. 25, no. 0, pp. 187 – 195, 1975.

[4] D. R. Ballal and A. H. Lefebvre, "The influence of flow parameters on minimum ignition energy and quenching distance," *Symposium (International) on Combustion*, vol. 15, no. 1, pp. 1473 – 1481, 1975. Fifteenth Symposium (International) on Combustion.

[5] E. Mastorakos, "Ignition of turbulent non-premixed flames," *Progress in Energy and Combustion Science*, vol. 35, no. 1, pp. 57–97, 2009.

[6] S. Bane, J. Shepherd, E. Kwon, and A. Day, "Statistical analysis of electrostatic spark ignition of lean h2/o2/ar mixtures," *International Journal of Hydrogen Energy*, vol. 36, no. 3, pp. 2344 – 2350, 2011. The Third Annual International Conference on Hydrogen Safety.

[7] S. F. Ahmed and E. Mastorakos, "Spark ignition of lifted turbulent jet flames," *Combustion and Flame*, vol. 146, no. 1–2, pp. 215–231, 2006.

[8] A. Lefebvre, *Gas Turbine Combustion.* Combustion: An International Series, Taylor & Francis Group, 1999.

[9] D. Sepulveda and E. E. Striebel, "Starting means for a gas turbine engine," November 1983.

[10] J. C. Armstrong and H. D. Wilsted, "Investigation of several techniques for improving altitude-starting limits of turbojet engines," Tech. Rep. NACA RM E52103, National Advisory Committee for Aeronautics, Washington, DC, 1952.

[11] A. D. Birch, D. R. Brown, and M. G. Dodson, "Ignition probabilities in turbulent mixing flows," *Symposium (International) on Combustion*, vol. 18, no. 1, pp. 1775–1780, 1981.

[12] K. A. Dooley, "Continuous plasma ignition system," December 1996.

[13] F. Williams, *Combustion theory.* Addison-Wesley series in engineering science, Addison-Wesley Pub. Co., 1965.

[14] J. A. Lovett, T. P. Brogan, D. S. Philippona, B. V. Keil, and T. V. Thompson, "Development needs for advanced afterburner designs," *AIAA paper*, vol. 4192, p. 2004, 2004.

[15] B. Lewis and G. Von Elbe, *Combustion, flames, and explosions of gases.* Academic Press, 1987.

[16] F. J. Weinberg, K. Hom, A. K. Oppenheim, and K. Teichman, "Ignition by plasma jet," *Nature*, vol. 272, pp. 341 – 343, 1978.

[17] D. R. Ballal and A. H. Lefebvre, "The influence of spark discharge characteristics on minimum ignition energy in flowing gases," *Combustion and Flame*, vol. 24, no. 0, pp. 99–108, 1975.

[18] K. Rao and A. Lefebvre, "Minimum ignition energies in flowing kerosine-air mixtures," *Combustion and Flame*, vol. 27, no. 0, pp. 1 – 20, 1976.

198

[19] C. C. Swett, "Spark ignition of flowing gases using long-duration discharges," *Symposium (International) on Combustion*, vol. 6, no. 1, pp. 523 – 532, 1957. Sixth Symposium (International) on Combustion.

[20] C. C. Swett, "Effect of gas stream parameters on the energy and power dissipated in a spark and on ignition," *Symposium on Combustion and Flame, and Explosion Phenomena*, vol. 3, no. 1, pp. 353 – 361, 1949. Third Symposium on Combustion and Flame and Explosion Phenomena.

[21] D. Spalding, *Combustion and mass transfer: a textbook with multiple-choice exercises for engineering students.* Pergamon International Library, Pergamon Press, 1979.

[22] O. Akindele, D. Bradley, P. Mak, and M. McMahon, "Spark ignition of turbulent gases," *Combustion and Flame*, vol. 47, no. 0, pp. 129 – 155, 1982.

[23] L. J. Blair, "Retractable igniter device for gas turbines," June 1981.

[24] C. S. Campbell and F. N. Egolfopoulos, "Kinetics paths to radical-induced ignition of methane/air mixtures," *Combustion Science and Technology*, vol. 177, no. 12, pp. 2275–2298, 2005.

[25] E. Watson, "Ignition research work carried out by the lucas organization with special reference to high altitude problems," Tech. Rep. L5988, Lucas Aerospace, Ltd., Hempstead, UK, 1954.

[26] S. Srinivasan, R. Pasumarti, and S. Menon, "Large-eddy simulation of pulsed high-speed subsonic jets in a turbulent crossflow," *Journal of Turbulence*, vol. 13, no. 1, pp. 1–21, 2012.

[27] A. Eroglu and R. E. Breidenthal, "Structure, penetration, and mixing of pulsed jets in crossflow," *AIAA journal*, vol. 39, no. 3, pp. 417–423, 2001.

[28] S. R. Shapiro, J. King, R. T. M'Closkey, and A. R. Karagozian, "Optimization of controlled jets in crossflow," *AIAA journal*, vol. 44, no. 6, pp. 1292–1298, 2006.

[29] N. Anikin, E. Mintoussov, S. Pancheshnyi, D. Roupassov, V. Sych, and A. Y. Starikovskii, "Nonequilibrium plasmas and its applications for combustion and hypersonic flow control," *AIAA Paper*, vol. 1053, p. 41, 2003.

[30] E. Mintoussov, S. Pancheshnyi, A. Y. Starikovskii, *et al.*, "Propane-air flame control by non-equilibrium low-temperature pulsed nanosecond barrier discharge," *AIAA paper*, vol. 1013, pp. 5–8, 2004.

[31] J. Zhang, R. Clements, and P. Smy, "An experimental investigation of the effect of a plasma jet on a freely expanding methane-air flame," *Combustion and Flame*, vol. 50, no. 0, pp. 99 – 106, 1983.

[32] D. Randolph and F. Silsbee, *Flame speed and spark intensity*. US Government Printing Office, 1924.

[33] E. I. Mintoussov, A. A. Nikipelov, S. S. Starikovskaia, and A. Y. Starikovskii, "Rapid combustion achievement by nanosecond barrier discharge," in *44th AIAA Aerospace Sciences Meeting and Exhibit, Reno, NV*, pp. 2006–614, 2006.

[34] I. Kosarev, N. Aleksandrov, S. Kindysheva, S. Starikovskaia, and A. Starikovskii, "Kinetics of ignition of saturated hydrocarbons by nonequilibrium plasma: Ch4-containing mixtures," *Combustion and Flame*, vol. 154, no. 3, pp. 569 – 586, 2008.

[35] K. Takita, G. Masuya, T. Sato, and Y. Ju, "Effect of addition of radicals on burning velocity," *AIAA journal*, vol. 39, no. 4, pp. 742–744, 2001.

[36] G. E. Georghiou, A. P. Papadakis, R. Morrow, and A. C. Metaxas, "Numerical modelling of atmospheric pressure gas discharges leading to plasma production," *Journal of Physics D: Applied Physics*, vol. 38, no. 20, p. R303, 2005.

[37] K. Eisazadeh-Far, F. Parsinejad, H. Metghalchi, and J. C. Keck, "On flame kernel formation and propagation in premixed gases," *Combustion and Flame*, vol. 157, no. 12, pp. 2211 – 2221, 2010.

[38] J. Han, H. Yamashita, and N. Hayashi, "Numerical study on the spark ignition characteristics of a methane-air mixture using detailed chemical kinetics: Effect of equivalence ratio, electrode gap distance, and electrode radius on mie, quenching distance, and ignition delay," *Combustion and Flame*, vol. 157, no. 7, pp. 1414–1421, 2010.

[39] M. Thiele, S. Selle, U. Riedel, J. Warnatz, and U. Maas, "Numerical simulation of spark ignition including ionization," *Proceedings of the combustion institute*, vol. 28, no. 1, pp. 1177–1185, 2000.

[40] G. Lacaze, E. Richardson, and T. Poinsot, "Large eddy simulation of spark ignition in a turbulent methane jet," *Combustion and Flame*, vol. 156, no. 10, pp. 1993 – 2009, 2009.

[41] S. Nakaya, K. Hatori, M. Tsue, M. Kono, D. Segawa, and T. Kadota, "Numerical analysis on flame kernel in spark ignition methane/air mixtures," *Journal of Propulsion and Power*, vol. 27, no. 2, pp. 363–370, 2011.

[42] R. Maly, *Fuel Economy in Road Vehicles Powered by Spark Ignition Engines*, ch. 3, pp. 91–148. Plenum Press, 1984.

[43] E. Sher and J. C. Keck, "Spark ignition of combustible gas mixtures," *Combustion and Flame*, vol. 66, no. 1, pp. 17 – 25, 1986.

[44] B. Sforzo, A. Lambert, J. Kim, J. Jagoda, S. Menon, and J. Seitzman, "Post discharge evolution of a spark igniter kernel," *Combustion and Flame*, no. 0, pp. –, 2014.

[45] M. Thiele, J. Warnatz, A. Dreizler, S. Lindenmaier, R. Schießl, U. Maas, A. Grant, and P. Ewart, "Spark ignited hydrogen/air mixtures: two dimensional detailed modeling and laser based diagnostics," *Combustion and Flame*, vol. 128, no. 1–2, pp. 74 – 87, 2002.

[46] J. Richards, "Puff motions in unstratified surroundings," *Journal of Fluid Mechanics*, vol. 21, no. 01, pp. 97–106, 1965.

[47] N. Didden, "On the formation of vortex rings: Rolling-up and production of circulation," *Journal of Applied Mathematics and Physics (ZAMP)*, vol. 30, no. 1, pp. 101–116, 1979.

[48] J. O. Dabiri and M. Gharib, "Fluid entrainment by isolated vortex rings," *Journal of fluid mechanics*, vol. 511, no. 1, pp. 311–331, 2004.

[49] T. Maxworthy, "The structure and stability of vortex rings," *J. Fluid Mech*, vol. 51, no. 1, pp. 15–32, 1972.

[50] A. B. Olcay and P. S. Krueger, "Measurement of ambient fluid entrainment during laminar vortex ring formation," *Experiments in Fluids*, vol. 44, no. 2, pp. 235–247, 2008.

[51] P. S. Krueger and M. Gharib, "The significance of vortex ring formation to the impulse and thrust of a starting jet," *Physics of Fluids (1994-present)*, vol. 15, no. 5, pp. 1271–1281, 2003.

[52] H. Johari, "Scaling of fully pulsed jets in crossflow," *AIAA journal*, vol. 44, no. 11, pp. 2719–2725, 2006.

[53] R. Sau and K. Mahesh, "Optimization of pulsed jets in crossflow," *Journal of Fluid Mechanics*, vol. 653, p. 365, 2010.

[54] H. Johari, M. Pacheco-Tougas, and J. Hermanson, "Penetration and mixing of fully modulated turbulent jets in crossflow," *AIAA Journal*, vol. 37, no. 7, pp. 842–850, 1999.

[55] Y. K. Chang and A. D. Vakili, "Dynamics of vortex rings in crossflow," *Physics of Fluids (1994-present)*, vol. 7, no. 7, pp. 1583–1597, 1995.

[56] R. M'closkey, J. King, L. Cortelezzi, and A. Karagozian, "The actively controlled jet in crossflow," *Journal of Fluid Mechanics*, vol. 452, pp. 325–335, 2002.

[57] J. Hermanson, A. Wahba, and H. Johari, "Duty-cycle effects on penetration of fully modulated, turbulent jets in crossflow," *AIAA journal*, vol. 36, no. 10, pp. 1935–1937, 1998.

[58] M. Gordon, J. E. Cater, and J. Soria, "Investigation of the mean passive scalar field in zero-net-mass-flux jets in cross-flow using planar-laser-induced fluorescence," *Physics of Fluids (1994-present)*, vol. 16, no. 3, pp. 794–808, 2004.

[59] A. Glezer and M. Amitay, "Synthetic jets," *Annual Review of Fluid Mechanics*, vol. 34, no. 1, pp. 503–529, 2002.

[60] Y. Kamotani and I. Greber, "Experiments on a turbulent jet in a cross flow," *AIAA journal*, vol. 10, no. 11, pp. 1425–1429, 1972.

[61] R. Pasumarti, J. Schulz, J. Seitzman, J. Jagoda, and S. Menon, "Large eddy simulation of pulsed jets in high speed turbulent crossflow," in *AIAA Paper*, AIAA, AIAA, 2010.

[62] M. Mohri, A. Rostamizadeh, and A. Talwalkar, *Foundations of machine learning.* MIT press, 2012.

203

[63] A. J. Smola and B. Schölkopf, "A tutorial on support vector regression," *Statistics and computing*, vol. 14, pp. 199–222, 2004.

[64] T. Hastie, R. Tibshirani, J. Friedman, T. Hastie, J. Friedman, and R. Tibshirani, *The elements of statistical learning*, vol. 2. Springer, 2009.

[65] C. Cortes and V. Vapnik, "Support-vector networks," *Machine Learning*, vol. 20, no. 3, pp. 273–297, 1995.

[66] B. E. Boser, I. M. Guyon, and V. N. Vapnik, "A training algorithm for optimal margin classifiers," in *Proceedings of the fifth annual workshop on Computational learning theory*, COLT '92, (New York, NY, USA), pp. 144–152, ACM, 1992.

[67] D. Holder, *Schlieren Methods.* Notes on applied science, H.M. Stationery Office, 1963.

[68] J. Kim, B. Sforzo, J. Seitzman, and J. Jagoda, "High energy spark discharges for ignition," in *Joint Propulsion Conferences*, American Institute of Aeronautics and Astronautics, American Institute of Aeronautics and Astronautics, July 2012.

[69] J. M. Hall and E. L. Petersen, "An optimized kinetics model for oh chemiluminescence at high temperatures and atmospheric pressures," *International Journal of Chemical Kinetics*, vol. 38, no. 12, pp. 714–724, 2006.

[70] B. Higgins, M. McQuay, F. Lacas, J. Rolon, N. Darabiha, and S. Candel, "Systematic measurements of {OH} chemiluminescence for fuel-lean, high-pressure, premixed, laminar flames," *Fuel*, vol. 80, no. 1, pp. 67 – 74, 2001.

[71] K. B. Periagaram, *Determination of flame characteristics in a low swirl burner at gas turbine conditions through reaction zone imaging.* PhD thesis, Georgia Institute of Technology, 2013.

[72] D. Goodwin, "Cantera: An object-oriented software toolkit for chemical kinetics, thermodynamics, and transport processes," *Caltech, Pasadena*, 2009.

[73] J. Schulz, K. Gottiparthi, and S. Menon, "Ionization in gaseous detonation waves," *Shock Waves*, vol. 22, pp. 579–590, 2012.

[74] D. Bose and G. V. Candler, "Thermal rate constants of the $N_2+O \rightarrow NO+N$ reaction using ab initio ^{3}A'' and ^{3}A' potential energy surfaces," *Journal of Chemical Physics*, vol. 104, no. 8, pp. 2825–2833, 1996.

[75] C. Park, J. Howe, R. Jaffe, and G. Candler, "Review of chemical-kinetic problems of future nasa missions," *Journal of Thermophysics and Heat transfer*, vol. 8, pp. 385–398, 1994.

[76] P. Teulet, J. P. Sarrette, and A. M. Gomes, "Calculation of electron impact inelastic cross sections and rate coefficients for diatomic molecules. application to air molecules," *Journal of Quantitative Spectroscopy and Radiative Transfer*, vol. 62, no. 5, pp. 549–569, 1999.

[77] B. J. McBride, M. J. Zehe, and S. Gordon, *NASA Glenn coefficients for calculating thermodynamic properties of individual species.* National Aeronautics and Space Administration, John H. Glenn Research Center at Lewis Field, 2002.

[78] "Chemical-kinetic mechanisms for combustion applications," *San Diego Mechanism web page, Mechanical and Aerospace Engineering (Combustion Research), University of California at San Diego (http://combustion.ucsd.edu).*

[79] I. M. Chakravarti, "Fractional replication in asymmetrical factorial designs and partially balanced arrays," *Sankhyā: The Indian Journal of Statistics (1933-1960)*, vol. 17, no. 2, pp. pp. 143–164, 1956.

205

[80] M. D. McKay, R. J. Beckman, and W. J. Conover, "A comparison of three methods for selecting values of input variables in the analysis of output from a computer code," *Technometrics*, vol. 21, no. 2, pp. pp. 239–245, 1979.

[81] L. Spadaccini and M. Colket, III, "Ignition delay characteristics of methane fuels," *Progress in Energy and Combustion Science*, vol. 20, no. 5, pp. 431 – 460, 1994.